NASA Contractor Report 165136

EFFECTS OF AXISYMMETRIC CONTRACTIONS ON TURBULENCE OF VARIOUS SCALES

Jimmy Tan-atichat, Hassan M. Nagib and Robert E. Drubka

Illinois Institute of Technology
Chicago, Illinois

September 1980

Prepared for

NATIONAL AERONAUTICS AND SPACE ADMINISTRATION
Lewis Research Center
Under Grant NSG-3220

TABLE OF CONTENTS

LIST OF SYMBOLS

Symbol	Definition
$A_0, A_1, \ldots, A_3$	Hot-wire calibration polynomial coefficients
C_a	Effective contraction area ratio = $\bar{U}_e/\bar{U}_i$
C0, C1, ..., C10	Contraction designation; See Figure 3
c	Contraction area ratio = (inlet area)/(outlet area)
D	Inside diameter of test section; inlet diameter of contractions
d	Wire diameter of screens
E	Anemometer output voltage
f^2	Hot-wire yaw dependence function
H	Hot-wire calibration function
J0, J1, ..., J5	Grid designation; See Figure 2
L	Contraction length
L_u	Longitudinal integral length scale = $\bar{U}T_u$
L_v	Lateral integral length scale = $\bar{U}T_v$
M	Grid mesh size
q'	RMS of total turbulent kinetic energy
R_M	Grid mesh Reynolds number = $\bar{U}_i M/\nu$
R_λ	Microscale Reynolds number = $u'\lambda/\nu$
r	Radial distance from axis of symmetry
$r_c(x)$	Radius of contraction contour at x
S_o	Separation distance between turbulence-generating grid and inlet to contraction
T_u	Integral time scale for velocity component in the streamwise direction

Symbol	Definition
T_v	Integral time scale for velocity component in the radial direction
t	Time; thickness of turbulence-generating grid (Figure 2)
U, U_∞	Nominal free-stream velocity
$\bar{U}, \bar{U}(x)$	Streamwise mean velocity
u'	RMS of velocity fluctuations in the streamwise direction
V	Radial velocity
v'	RMS of velocity fluctuations in the radial direction
$\overline{uv}$	Reynolds stress between streamwise component of velocity and a component normal to the axis of symmetry
x	Direction parallel to axis of symmetry of test section and contraction; origin is at contraction inlet, positive downstream
$\tilde{x}$	Direction parallel to axis of symmetry of test section and contraction; origin is at downstream end of turbulence-generating grid, positive downstream
x_o	Virtual origin of turbulence
y	Vertical axis, perpendicular to x direction; origin on axis of symmetry, positive up
z	Horizontal direction in a right-handed Cartesian coordinate system; origin on axis of symmetry
α	Angle between hot-wire sensor and arbitrary axis
γ	Instantaneous flow angle with respect to an arbitrary axis
η	Total turbulence reduction efficiency $= (q'/\bar{U})_e/(q'/\bar{U})_i$

Symbol	Definition
$\bar{\eta}$	Corrected total turbulence reduction efficiency = $\eta/(\eta)_{c=1}$
η_u	Streamwise turbulence reduction efficiency = $(u'/\bar{U})_e/(u'/\bar{U})_i$
$\bar{\eta}_u$	Corrected streamwise turbulence reduction efficiency = $\eta_u/(\eta_u)_{c=1}$
η_v	Radial turbulence reduction efficiency = $(v'/\bar{U})_e/(v'/\bar{U})_i$
$\bar{\eta}_v$	Corrected radial turbulence reduction efficiency = $\eta_v/(\eta_v)_{c=1}$
λ	Taylor microscale
μ	Total turbulence kinetic energy ratio = q'^2_e/q'^2_i
$\bar{\mu}$	Corrected total turbulence kinetic energy ratio = $\mu/(\mu)_{c=1}$
μ_u	Streamwise turbulence kinetic energy ratio = u'^2_e/u'^2_i
$\bar{\mu}_u$	Corrected streamwise turbulence kinetic energy ratio = $\mu_u/(\mu_u)_{c=1}$
μ_v	Radial turbulence kinetic energy ratio = v'^2_e/v'^2_i
$\bar{\mu}_v$	Corrected radial turbulence kinetic energy ratio = $\mu_v/(\mu_v)_{c=1}$
ν	Kinematic viscosity
ξ	Non-dimensional inflection-point location of the contraction in the x-direction = $(x/L)_{\text{zero curvature}}$
σ	Grid solidity = closed area/total area
τ	Time delay in auto- and cross-covariance functions
ζ	Damping factor of the op-amp low pass filters

Subscripts	Definition
e	Value at exit of contraction
i	Value at inlet to contraction
$\{\overline{\quad}\}$	Overbar = average value, time average value

SUMMARY

Recent intensified research in jet-engine noise abatement and in laminar flow control utilize facilities that can benefit a great deal from a better fundamental understanding of turbulent flow in contracting streams. Such understanding is vital for any attempts towards the management and control of turbulence in these and many other applications. Of particular importance is the question of how the variation of turbulence scales may affect the flow through and downstream of contractions.

The present study examines digitally acquired and processed results from an experimental investigation of grid-generated turbulence of various scales through and downstream of axisymmetric contractions for a wide range of initial conditions and contraction geometry. Parameters for this study include the contraction area ratio, the contraction length-to-diameter ratio, and the contraction shape. The effects of a contraction on turbulence were indicated by changes in the turbulent kinetic energy, its distribution among the velocity components, its characteristic length scales, and the Reynolds stress, as well as spectra, coherence and correlation functions. Key physical parameters and dominant mechanisms involved in the contraction process were established. By applying a first-order correction to account for the viscous dissipation, the subsequent comparison with the predictions

of rapid distortion theory led to far more consistent interpretations than those reached by the vast number of previous experiments.

In the course of this study, the effects of a contraction on grid-generated turbulence have been investigated with 9 matched-cubic contractions ranging in area ratio from 2 to 36, and in length-to-inlet diameter ratio from 0.25 to 1.50. In addition, a fifth-order contraction was utilized for studying the contour shape effect. Thirteen homogeneous and nearly isotropic test flow conditions were generated with streamwise turbulence intensities in the range 1.4 % $\leq u'/\bar{U} \leq$ 3.0 % and initial non-dimensional longitudinal and lateral integral length scales in the ranges of $0.02 \leq \bar{L}_{ui}/D_i \leq 0.082$ and $0.01 \leq \bar{L}_{vi}/D_i \leq 0.037$, respectively. The ratio between the longitudinal and lateral length scale was about 2.3 in all test flow conditions, rendering approximately isotropic initial turbulence conditions. Turbulence Reynolds numbers, R_λ, ranging from 2.3 to 31 were achieved using mesh Reynolds numbers in the range $270 \leq R_M \leq 8130$. Key features of this experiment include powering the wind tunnel with compressed air to eliminate minute extraneous velocity fluctuations caused by the blower fan blades which amplify in a contracting stream and affect the components of turbulent kinetic energy unequally, along with the use of both digital and analog instrumentation to achieve a higher quality of the recorded data. On-line analog signal processing was

used to monitor the flow conditions during digital data acquisition to ensure that only data of high quality were recorded. Digital processing of the data enabled the use of elaborate calibration and correction schemes for very high accuracy. Non-ideal probe characteristics and very low frequency velocity variations, which were easily corrected digitally, would have lead to substantial errors with the use of analog processing alone.

Results indicate that the extent to which the turbulence is altered by the contraction depends on the incoming turbulence scales, the total strain experienced by the fluid, as well as the contraction ratio and the strain rate. Varying the turbulence integral scale influences the transverse turbulence components more than the streamwise component. In general, the larger the turbulence scale, the lesser the reduction in the turbulence intensity of the transverse components. For any given contraction ratio, there is an optimum initial turbulence scale for maximum turbulence reduction. This optimum length scale decreases with increasing contraction ratios. Best agreement with rapid distortion theory is obtained for large-scale turbulence where viscous decay over the contraction length is negligible, even though small scale assumptions are utilized in the theory. When a first-order correction for the viscous decay is applied to the results, good agreement between experimental data and rapid distortion theory is obtained for the transverse components and the total

turbulent kinetic energy for turbulence of all scales. The streamwise component does not agree with theory primarily because of the turbulence production and inter-component energy transfer caused by the large difference between the lateral and streamwise fluctuating velocity components. This results in an increase in the energy of the streamwise component as the contraction ratio increases rather than the decrease predicted by rapid distortion theory, which is a linear theory. This investigation has extended our fundamental understanding of turbulence under strain and provided a library of detailed turbulence data for comparison with the computer modeling of such complex turbulent flows.

CHAPTER I

INTRODUCTION

The problems of reducing free-stream turbulence and of improving isotropy characteristics for grid-generated turbulence in wind tunnels have been the subjects of numerous research investigations over the past few decades. It is often desirable to improve the degree of isotropy of grid-generated turbulence by using a mild contraction in order to enhance the validity of comparisons between experiments on grid-generated turbulence and theories based on isotropic turbulence. On the other hand, attainment of a uniform flow with low turbulence intensities is of utmost importance in many experimental fluid dynamics and practical aeronautical problems. Experiments in transition to turbulence and on laminar flow control on airfoils are typical examples of situations that require the turbulence intensity to be at least below 0.1%. Such low turbulence levels could be achieved by careful selection of turbulence manipulators in the settling chamber[1-6]* and through the use of a carefully designed contraction ahead of the test section of the wind tunnel to further reduce the relative turbulence levels.

Many problems of practical importance can also benefit from an improved understanding of the effects of stream

*Number(s) in brackets refer to numbered references in the bibliography.

contraction or strain on turbulence. For example, recent intensified research in jet-engine noise abatement, employing simulations of in-flight conditions on test stands and in anechoic chambers utilizes facilities that can benefit immensely from a better fundamental understanding of turbulent flows in contracting streams. In particular, differences between measured noise spectra of jet-engine fan intakes recorded on test stands and those obtained from in-flight data cause a great deal of concern to intake fan designers who are trying to quiet these jet intakes by reducing the fan-generated noise. According to the recent excellent review by Feiler and Groeneweg[7] the main discrepancy appears to be due to the presence of high-energy pure-tone noise at the fundamental blade-passing frequency which only exists on static ground tests and can be reduced by increasing the forward speed in a wind-tunnel simulation. Broad-band noise emitted by the fans seemed to be controlled by different mechanisms and is not affected significantly by forward velocity.

In order to place correct emphasis on the design of noise suppression treatments to these fan intakes, or to optimize the fan and blades design, fundamental questions concerning the behavior of inflow characteristics will have to be answered. Several causes have been suggested for the discrepancy between flight noise measurements and ground tests. In flight, the inflow condition is clean and has a small effective contraction ratio so that ingested

atmospheric disturbances pass through the inlet with little scale or intensity changes. In ground static tests, however, the inflow undergoes a very large contraction. The disturbances created by the flow passing nearby protuberances and support structures, as well as any atmospheric turbulence, undergo tremendous distortion and elongate along the flow streamlines. Once inside the duct they interact with the fan rotor for a number of revolutions resulting in tone noise. Highly localized disturbances such as the presence of "ground" vortices has also been suggested as another possible cause of tone noise. Recent experiments at I.I.T. suggest that the proximity of any other surfaces in addition to the ground, e.g., walls and ceiling of anechoic chambers, where vorticity is generated can lead to the development of these vortices. The vortices are often unsteady and intermittent; i.e., they meander around the fan inlet plane near the side where vorticity is supplied by a neighboring surface.

Before successful methods or techniques for adequate simulation of flight behavior in ground static tests can be implemented, basic questions concerning inflow contraction and turbulence characteristics must be investigated in detail to determine the effects of contraction ratio (i.e., differences between flight and static conditions) on different scales of turbulence (i.e., scale effect of different inflow disturbances). Such understanding is also vital for any attempts toward management and control of

turbulence in this and numerous other applications. Of particular importance is the question of how the variation of initial turbulence scales affects the flow through and downstream of contractions.

Background and Motivation

Over the years a number of publications have dealt with the design and use of a contraction to reduce turbulence in wind tunnels[8-16]. More recently researchers have also utilized mild contractions to improve the isotropy of turbulence generated by grids[17-19], observed the decay of isotropic and anisotropic turbulence downstream of a contraction[35], and studied effects of different contraction shapes[20,21] as well as contraction ratios[22,23] on free-stream turbulence.

Uberoi and Wallis[17] found that the degree of isotropy of grid turbulence could be modified, so that turbulence would be nearly isotropic, by the use of a small contraction (c=1.25). However, at some distance downstream of the contraction, the u'/v' ratio tends toward its anisotropic pre-contraction value. Because measurements could be made only over a limited distance downstream of the contraction, they used grids of progressively smaller mesh sizes to extend the x/M range and found that for a fixed contraction, the effect of the contraction on turbulence decreases with decreasing mesh sizes and that in all three cases (3 grid mesh sizes), the u^2/v^2 ratio tends to return to its original

pre-contraction value. The turbulence generated by the small-mesh grid exhibited more of a return than those generated by the large-mesh grid. These results point to the important role of turbulence scales in affecting turbulence characteristics through a contraction since turbulence generated by different mesh grids contain different ranges of scales.

Their work[17] was contradicted by the experiment of Comte-Bellot and Corrsin[18] who used a similar contraction (c=1.27) to modify the distribution of turbulence energy for several grid-generated turbulent flows. Square-rod biplane grids with mesh sizes of 2.54, 5.08, and 10.16 cm and a round-rod biplane grid with a mesh size of 5.08 cm were used to generate the turbulence. In addition, a "disk grid" with a mesh size of 5.08 cm was also utilized to check the sensitivity of the turbulence generated to the geometry of the grid used. In all cases they found[19] that once altered by the contraction, the distribution of energy between the streamwise and the lateral components did not return to pre-contraction values with increasing downstream distance. Although the range of mesh and turbulence Reynolds numbers were overlapping between the experiments of Uberoi and Wallis[17] and of Comte-Bellot and Corrsin[19], no integral length scale information was available from Reference [17]. On the other hand, while extensive turbulence decay characteristics were shown, limited scale growth characteristics were reported by Reference [19].

Therefore, it is possible that differences in turbulence characteristics, especially the predominant turbulence scales, between the two experiments resulted in the conflicting conclusions.

A recent study of nearly isotropic turbulence in the "final period" of decay by Bennett and Corrsin[18] indicated that the effectiveness in modifying the degree of isotropy in grid-generated turbulence using mild contractions diminishes as the turbulence Reynolds number R_λ decreases. However, this result was based on limited experimental data. The main thrust of investigations discussed above was to improve the u'/v' isotropy of grid-generated turbulence by using mild contractions so that a more valid comparison between experiments on grid-generated turbulence and theories of isotropic turbulence can be made.

The effects of contraction geometry on non-isotropic free-stream turbulence were studied by Klein and Ramjee[20] using two families of axisymmetric contractions (Thwaites's contour[33] and Batchelor and Shaw's contour[34]) with four contractions each. All contractions had a contraction ratio of 10 but the length-to-inlet diameter varied from 0.5 to 1.5. Contractions designed with Thwaites's contour[33] had a gradual initial variation in cross-sectional area and a rather rapid change in the mid section followed by a gradual tapering off towards the exit plane. Those designed according to Batchelor and Shaw's contour[34] had a very rapid change in cross-sectional area at the inlet for the

sake of having a gradual variation towards the outlet. Inlet flow separation is more likely with the latter contractions[34], especially the short ones. In these experiments, non-isotropy of the initial turbulence resulted from the air flowing through a bellmouth entry and a high-solidity screen.

Their conclusions, based on a single and probably highly non-homogeneous initial upstream condition, were: For anisotropic turbulence with an initial $u'^2/v'^2=3$, the turbulent kinetic energy in both longitudinal and radial components increases substantially along the contractions; the degree of anisotropy at the contraction outlet was the same as that at the inlet; and that neither the contour shape nor the length-to-diameter ratio had any influence on the variation of the turbulent kinetic energy! We conjecture that extraneous fluctuations caused by the suspected flow separations may be contaminating some of their results. According to them[20], the only parameter of importance was the contraction ratio and in this respect Klein and Ramjee[20] concluded that non-isotropic turbulence behaved in a way predicted by linear theory which was derived using isotropic assumptions!

In a similar study on shape effects of a contraction on turbulence, Hussain and Ramjee[21] conducted an experiment with four axisymmetric contractions (all of them with c=11) of very different shapes and fairly short length-to-inlet diameter ratios ($0.3 \leq L/D \leq 0.7$). Three of them, namely,

Batchelor and Shaw contour[34], ASME high β series contour, and ASME low β series contour, had extremely rapid area variation near the inlet which as again likely to cause large upstream influence, flow separation and consequently increased turbulence levels. When normalized with its value at the inlet, the streamwise component of turbulence kinetic energy through the contraction, shown in Figure 10c of Reference [21], demonstrates this increased turbulence for the ASME low β nozzle which had the highest area variation at the inlet. The initial turbulence intensity in this experiment was also abnormally high (greater than 7% for both streamwise and radial components), thus the free-stream turbulence may not have been homogeneous. However, an important observation that Hussain and Ramjee[21] made pointed to the fact that the effects of a contraction appear to be directly related to pre-contraction turbulence intensity. They recommend that these effects warrant further systematic investigations since their experiment was conducted with a single upstream condition. We suspected that not only is the pre-contraction turbulence intensity relevant but also that the turbulence structure and scales play an extremely important role in affecting the post-contraction flow characteristics.

In studies which dealt with the contraction ratio as an independent parameter, Uberoi[22], who used three square cross-section contractions with area ratios of 4:1, 9:1 and 16:1, noted that because of differences in the mean velocity

gradient in the streamwise direction, it is not possible to predict the performance of all nozzles with contraction ratios between 1 and 16 from results obtained in the 16:1 contraction alone. This result is in contradiction with the finding of Klein and Ramjee[20], who reported that the change in turbulence energy depends only on the local contraction ratio.

In a more extensive study of contraction ratio effects, Ramjee and Hussain[23] investigated axisymmetric contractions with the large area ratios of 11, 22, 44.5, 64, and 100, fabricated according to the Batchelor and Shaw contour[34], thus risking flow separation and increased turbulence production near the upstream end of the nozzle. They found that both longitudinal and lateral components of turbulence energy increase with contraction ratio. In contrast with the prediction of classical linear theory (Batchelor-Proudman[24], Ribner-Tucker[25]), a monotonic increase of the longitudinal turbulent kinetic energy with increasing contraction ratio was obtained by them experimentally. However, they admitted that noise and pressure fluctuations which originated from the boundary layers and, particularly, from the blower fan blades, which contribute mainly to the measured longitudinal turbulence kinetic energy, were not accounted for in any way. The upstream turbulence-generating screen was of a very high solidity type (σ=0.75) which is generally known to produce non-homogeneous turbulence, e.g., see Reference [3]. For

one contraction (c=11), they also investigated the performance using five different upstream screens and found that the exit turbulence intensities were essentially independent of the mesh or wire-diameter Reynolds number of the upstream turbulence-generating screen. Because the wind tunnel was powered by a blower, it is likely that extraneous pressure-induced fluctuations caused by the fan blades, which amplify through contractions, contributed unequally to the measured streamwise and radial turbulence intensities. Since contractions reduce the streamwise component of vortical motions, i.e., turbulence, but amplify pressure-induced wave-like fluctuations, it is possible that downstream of the contraction, the measured u' fluctuations were primarily those caused by the blower fan blades and not genuine turbulence. Thus the disagreement with linear rapid distortion theory is not surprising. These conclusions lead us to question the validity of these results for a better fundamental understanding of turbulence under contraction.

Theoretical analyses of flow subjected to a rapid distortion have been carried out in the classical works of Batchelor and Proudman[24] and Ribner and Tucker[25] for the small-scale isotropic turbulence limit. Ribner and Tucker's analysis[25] was done for an axisymmetric contraction while Batchelor and Proudman[24] carried out the analysis to include any arbitrary three-dimensional distortion. Previous experiments have shown that predictions of this classical theory[24,25] have been generally poor because

assumptions crucial to the derivation of the analytical results are violated experimentally. A prime example would be the neglect of viscous dissipation in the analysis. One other example would be the assumption of asymptotically small-scale turbulence. However, Goldstein and Durbin[26] have recently extended the theory to include turbulence with scales comparable to the spatial scale of the mean flow for asymptotically large contraction ratios in two-dimensional contractions. Their results predicted a "blocking" effect of large scale turbulence so that the turbulence energy downstream of a contraction would be lower than the predictions of Batchelor and Proudman[24] and Ribner and Tucker[25] when the upstream turbulence scale is finite.

Another generalization of the theory of Batchelor and Proudman[24] has been developed by Sreenivasan and Narasimha[27] to estimate the effect of a sudden but arbitrary three-dimensional distortion on homogeneous, initially axisymmetric, rather than isotropic turbulence. They concluded that for large contractions, their results show no difference between axisymmetric and isotropic turbulence as far as the longitudinal energy component is concerned. However, the increase of radial-component energy during distortion is over-estimated by isotropic theory if the initial radial component energy is less than the longitudinal one.

To avoid difficulties due to non-linear viscous interactions, all the above mentioned theories were

developed to hold in very rapid distortions (i.e., no viscous dissipation). It should be pointed out that the word "rapid" signifies only that the flow velocity through the contraction leads to particle transit times small compared to the turbulence relaxation times. It does not signify any degree of gentleness of the rate of change of area through the contraction or any limitations on the length-to-diameter ratio of the contraction. These two aspects of contraction design are very important parameters for the quality of the mean flow, including boundary layer separation and mean flow uniformity, and in principle can be incorporated in the "rapid" distortion theory. The presence of separation and mean flow nonuniformities lead to the production of new turbulence which cannot be accounted for in such a theory. Therefore, Goldstein and Durbin[26] suggested that their theoretical results could be used to compare with experiments, contrary to Batchelor and Proudman's[24] contention that no practical experiments had a "rapid enough" distortion for linear theory to hold. Thus, it was interesting to compare the experimental results to theory, both classical rapid distortion[24,25] and extensions thereof[26,27]. The above comments may suggest ways of dealing with experimental results obtained in conditions for which some of the simplifying assumptions used in theoretical analyses cannot be met experimentally. It could also lead to improved correlations between theory and experiment and as a result may enhance our understanding

of turbulence.

Based on the above arguments we conclude that the two major limitations of the theory as used by Goldstein and Durbin[26] are the result of neglecting viscous dissipation and non-linear interaction, including any inter-component energy transfer. As the reader will discover from the later chapters, we have devised a first-order correction to account for the first of these which leads us to conclude that the remainder of the discrepancy with theory is caused by the latter. This approach provides us with a good estimate of the role of these different but important mechanisms in turbulent flows.

From the literature review of the more relevant experimental investigations, we concluded that the role played by upstream turbulence scales in controlling turbulence characteristics within and downstream of contractions must be important. While it was often hinted at, no comprehensive systematic investigation was undertaken to study the effects of vastly different initial turbulence scales on contracting flows. As a result, the following research was proposed. Since grid-generated turbulence in a uniform stream has been the subject of many investigations, both experimentally and theoretically, it was decided to study turbulence characteristics in a contracting stream using grid-generated turbulence and to specifically address the issue of turbulence scales by generating controlled test flow conditions that are documented in detail. To extend

the usefulness of the results, contraction length-to-diameter ratios as well as contraction ratios were varied over a wide range which included many cases found in practical applications. The range and number of parameters covered here are more comprehensive than in any previous investigation on the subject. It is hoped that this study will enhance our basic understanding of the role played by various turbulence scales when the flow is contracted. It also has a direct bearing on the attempted solutions to the design of flow manipulators for test-stand noise measurements of jet-engine intakes as well as providing information vital to the design of high performance wind tunnel contractions.

Objectives

The main objectives of the present investigation can be summarized as follows:

1) Generate using grids and document several selected, homogeneous turbulence test-flow conditions covering a range of length scales and Reynolds numbers for use as input conditions in various axisymmetric contractions. The documentation should include mean velocity and turbulence intensity information for both the streamwise and radial components, as well as their development in the streamwise direction. The turbulence decay rates, the integral scales, (both longitudinal and

lateral) and the Reynolds stresses should be determined along a constant area duct. Spectra, coherence, and correlation functions should also be calculated from the experimental measurements. These results may then be used as the reference conditions to separate the contraction effects from the measurements outlined in the second objective.

2) Investigate the sensitivity of turbulent flow through a wide range of contractions to the different, documented initial turbulence conditions, i.e., test-flow conditions. The wide range of contraction parameters should include variation of the contraction area ratio, the contraction length-to-diameter ratio, and the contraction contour shape. The resulting number and range of independent parameters is more comprehensive than that used in any previous single experimental investigation or than the combination of many of them. Centerline measurements of the two components of velocity (streamwise and radial) should be made and accompanied by their time-averaged statistics as well as some statistical functions i.e., the same ones calculated in the first objective. Selected off-axis and simultaneous two-probe data should also be collected. The results should be

summarized in a form useful for both practical applications as well as basic turbulence research.

3) Compare the experimental results with the rapid distortion theory to develop a better understanding of the mechanisms governing turbulence in contracting (or strained) streams.

CHAPTER II

EXPERIMENTAL FACILITIES AND INSTRUMENTATION

Wind-Tunnel Characteristics

The present investigation was conducted in an open-circuit wind tunnel, powered by a compressed air supply, with a 15.4 cm diameter circular test section. During the diagnostic phase of the present investigation, this wind tunnel was modified to improve its flow qualities. Some of these modifications were crucial to the success of the experiment and their details are discussed in Appendix B.

Compressed air enters the acoustically-treated upstream duct after passing through a control valve, and particulate and oil filters. The duct leads into a settling chamber. As the flow moves through the settling chamber, it encounters a series of flow manipulators of different types and mesh sizes. This array was designed according to Loehrke and Nagib[1] for flow uniformization and turbulence reduction before the flow passed through an axisymmetric 25:1 contraction. Complete information on the construction details can be found in the report by Ahmed *et al*[4]. The schematic in Figure 1 shows the arrangement of the test section, the turbulence generating grid, the contraction under test and the position of the X-wire probe. The test-section length is adjusted by attaching a number of sections together to form the required length. The sections

were designed to permit 2.54-cm increments in the length adjustment (ΔS_o) between the turbulence-generating grid and the inlet to the contraction, i.e., from S_o=0 to S_o=50 cm. This arrangement facilitates the adjustment of the grid-to-contraction distance for the different turbulence-generating grids in order to ensure that homogeneity and near-isotropy of turbulence are achieved at the contraction inlet for all test flow conditions. The values of S_o used with each grid are tabulated in Figure 2.

A right-handed Cartesian coordinate system is used in this experiment with the x-coordinate aligned with the axis of symmetry. The y-coordinate is oriented vertically and z is in the horizontal direction. The origin is located on the axis of symmetry at the inlet to the contraction. Positive x and y is in the downstream and upward directions, respectively.

A triaxial traversing mechanism that was used to hold and traverse the X-wire probe was located completely to one side of the test section so as to minimize any blockage or flow disturbance effects. The traversing mechanism was equipped with a digital position indicator and was capable of positioning the X-probe to within 0.2 mm of desired location.

Grid Characteristics

A large number of turbulence-generating grids were tested for turbulence decay, homogeneity and mean-velocity

uniformity characteristics before final selection of the grids was made. The characteristics of the turbulence generating grids used upstream of the contractions to establish the test flow conditions are given in Figure 2. Six grids, numbered J0 through J5, were selected to generate, in combination with different free-stream velocities, test flow conditions covering a wide range of mesh Reynolds numbers and integral length scales. Documentation of the test flow conditions is deferred until Chapters III and V.

Three basic types of "grids" were used. Type A grids, J0 and J1, were woven screens with small mesh sizes. Grid J2 of type B was a punched steel plate with square holes arranged in a square array. Grids J3 through J5, which have the largest mesh sizes, were of type C and were also manufactured by the punched-plate method. These grids have round holes arranged in a triangular array. The mesh size of all the grids ranged from 0.0847 cm for J0 to 2.54 cm for J5. All the grids were chosen to have low solidity ($0.33 \leq \sigma \leq 0.36$) so that there is no danger of them exhibiting anomalous behavior[3]. The thickness t (or the wire diameter of the screens), and the selected S_o along with x/M for the grids, are also tabulated in Figure 2.

Design and Construction of Contractions

Ten contractions were designed and constructed for the present investigation. All the contractions except one were

of the matched-cubic contour type. The matched-cubic is a more general case of the simple cubic equation in that the inflection point can be placed at an arbitrary position along the contour. In a single cubic-equation contour, the matching point is fixed at the midpoint between the inlet and the outlet of the contraction. This flexibility of locating the inflection point results in a higher performance contraction when properly used in the design. Details of the design and construction procedures for these contractions are presented in Appendix A and in Reference [16]. The contraction numbers, C0-C10, symbols used for plotting the results, the type of contraction (MC=matched-cubic, FO=fifth-order), the non-dimensional location of the inflection or cubic match point, ξ, the contraction area ratio, c, the length-to-inlet diameter ratio, L/D, and the exit diameter D_e, are all tabulated in Figure 3. The last column in Figure 3 lists the effective contraction ratio C_a. Note that for short contractions, C_a is very different from c as in C8 and C9. Upstream influence of these contractions is very pronounced and the flow starts to accelerate far upstream of the inlet. Profile shapes of the contours are shown in Figure 4 for contractions with an L/D of 1. Contractions with different length ratios but with an area ratio of 9 are shown in Figure 5. In addition to the matched-cubic contractions, a fifth-order contraction was designed and constructed for the experiment. Its profile was designed to have zero curvature

(2nd derivative) at both the inlet and exit sections. This subtle shape difference between the matched-cubic and the fifth-order contraction (see Figure 6) may have a significant influence on the performance of contractions if effects are very sensitive to the strain rate.

Instrumentation

Two independent systems of electronic instruments were utilized to acquire and process the X-wire probe outputs. The analog signal processing circuitry converts the hot-wire outputs to signals proportional to the U and V velocity components. The digital acquisition system, which consists of an analog front-end signal pre-processing circuitry and a digital data acquisition system[32], records digitized hot-wire signals for later off-line processing. Signals from the X-wire probe to the two systems were separated at the output of the anemometers, i.e., only the X-probe and the hot-wire anemometers are common to both.

Analog Signal Processing. The electronic circuitry used in converting the X-wire signals to U and V velocity signals is shown schematically in Figure 7. The hot-wire probe was mounted on a 3-dimensional traversing mechanism[4,29] capable of positioning the probe to within 0.2 mm of the required coordinates. The power supply energized the position indicator potentiometers and DVM 1 was used to monitor the reference supply voltage. Another digital voltmeter was used for position indication. The

coordinates of the different axes can be read from this position indicator by switching the x, y or z-axis selector. The position signal was also provided as an input to one of the axes of the x-y recorder for synchronization.

The X-probe was operated by a pair of DISA constant-temperature anemometers at an overheat ratio of 1.7. The anemometer outputs were linearized by exponential-type DISA linearizers using a value of 2.2 for the exponent. DISA auxiliary units functioned as low-pass filters to reduce electronic noise above 20 kHz. The signals were then fed into an op-amp sum-and-difference circuit to separate the U and V velocity components which were then monitored on a dual-trace oscilloscope and a 2-channel real-time spectrum analyzer. Either U or V can be selected for a mean-value display on DVM 2 or processed through the DISA true-rms voltmeter. These signals could then be recorded on the x-y recorder to obtain direct profiles in the radial or axial direction of the mean or rms velocity of either component.

Signal-Conditioning for Digital Data Acquisition. Analog pre-processing of the X-wire probe signals was necessary in order to achieve maximum signal-to-noise ratios and to prevent aliasing when the sampled digital signals were transformed into spectra and correlations. Circuitry for processing the X-wire signals into an optimized form for digitizing is shown in Figure 8. Since the

analog-to-digital (A-D) converter of the acquisition computer covers a range of $\pm$ 10 V with 12 bits, the smallest increment in voltage it can discern is about 5 mV. The output from hot-wire probes in a typical flow situation consists of a mean dc component of several volts and a small superimposed ac (turbulence) component of only a few millivolts. If turbulence statistics were computed from digitized but unprocessed hot-wire signals, a poor signal-to-noise ratio will result because of the quantization. The solution adopted here was to bias out the dc component of the hot-wire signal and to apply gain to the ac component so that the ac signal utilized most of the $\pm$ 10 V range of the A-D converter. This minimizes the effect of quantization error. The pre-processing described above is accomplished by the op-amps shown on the left top and bottom of Figure 8. These op-amps provide dc bias which is subtracted from the X-wire voltages to cancel out their dc components. The next two op-amps provide two stages of amplification with the gain of the second stage being adjustable by changing the values of R_{G1} and R_{G2}. The circuitry was calibrated so that the bias and gain applied to the signals were precisely known for each file of data acquired. This allowed the accurate reconstruction of the original signals on the UNIVAC-1100/81 computer prior to linearization and processing. The 4th-order Butterworth low-pass filters, required to prevent signal aliasing, were set to a cut-off frequency of 8 kHz. The filtered signals

were monitored on a dual-trace oscilloscope to ensure proper bias and gain adjustments before being fed to the A-D converters on the acquisition computer (DAPS) for recording onto industry-standard, 9-track digital tape. The sampling rate was set at 18.66 kHz and the beginning of each record was triggered on the same phase of the power line. This scheme enabled the removal of all periodic power-line related noise when the acquired data were processed[32].

Two additional channels of identical instrumentation except for the anti-aliasing filters were used when signals from two X-wire probes were acquired. These additional 4th-order filters, shown in Figure 9, were constructed with low-noise op-amps. Care was taken to match both the amplitude and phase characteristics of all four channels of instrumentation. Tests revealed that the processed signals matched within 0.07dB and the phase difference between them did not exceed 5^{o} throughout the frequency range of interest (i.e., at least to 10 kHz). When four channels of signals were being acquired, the maximum sampling rate available was 11.36 kHz. Therefore, all 4 anti-aliasing filters were set to low-pass at 5 kHz.

CHAPTER III

PRELIMINARY INVESTIGATIONS

Mean-Velocity and Turbulence-Intensity Profiles of Test Flow Conditions

Prior to making the final selection of the turbulence-generating grids to be used in the present investigation, a large number of them, spanning a wide range of mesh sizes and solidities, were tested in the uniform cross-sectional area duct. Mean velocity and the two components of turbulence intensity were measured along the centerline of the test section to determine the turbulence decay rates. Radial profiles of mean velocity and turbulence intensity were also recorded at several $\tilde{x}/M$ positions using analog signal-processing instrumentation to check the transverse uniformity of both the mean velocity and turbulence intensity. Streamwise turbulence decay rates of the grids were tabulated for both the longitudinal and radial components. Although these preliminary results are not shown here, it was discovered that some grids with solidities between 44% and 49% exhibited turbulence decay rates that were substantially lower than others with solidities below 40%. These were suspected of having some anomalous behavior[1,3] and were, therefore, excluded from further consideration.

The lateral profiles of the streamwise velocity and the two components of turbulence intensity for some of the test flow conditions are shown in Figures 10 through 14 in order

of increasing turbulence length scales. Flow conditions having the same "T" numbers but with a, b, or c suffixes have similar lateral length scales. However, the condition with the "a" suffix has a smaller longitudinal length scale than the one with a suffix "b". The flow condition with a "c" suffix has an even larger longitudinal length scale. This will become clear in Chapter V when the test flow conditions are presented. Note that the scales of these, as well as many other figures shown here, are expanded and have a shifted datum to render them more accurate for the reader.

For the small-scale turbulence conditions T1 and T2b, Figures 10 and 11 indicate that the turbulence intensities are very uniform for both the streamwise and radial components except for the flow very close to the test section wall. The mean streamwise velocity shows some small undulations in these relatively low turbulence cases ($u'/\overline{U} \approx$ 1.7% in T1 and $u'/\overline{U} \approx$ 2.5% in T2b).

Figure 12 shows the velocity profiles for a flow condition similar to T4. The turbulence intensity exhibits a small amount of nonuniformity in the u' component across the test section. The mean flow is uniform except again in the boundary layers near the walls. In the central portion of the duct ($r \leq 5$ cm), the flow quality is certainly sufficient for use as a medium scale test flow condition.

In the larger-scale turbulence flow conditions, the mean streamwise velocity profiles exhibit a remarkable uniformity in the central portion. However, effects of the

sidewall boundary layer are felt farther towards the center of the duct when these results are compared with the smaller-scale test flow conditions. An increase in the turbulence intensity near the wall is witnessed in Figures 13 and 14. As one would expect, this rise is more rapid and occurs at a smaller radial distance for the u' component. Turbulence levels at radial distances less than about 5 cm are very flat in both u' and v' components for the large-scale test flow conditions T7a and T8, thus indicating a high degree of homogeneity of the turbulence. This is a very important criterion for the selection of all test flow conditions that are used for this investigation.

Mean-Velocity and Turbulence-Intensity Profiles Downstream of Contractions

Turbulence and mean flow velocities were also measured downstream of the contractions during an early phase of this investigation after the fabrication of some contractions. Effects of using different contraction area ratios, length-to-inlet diameter ratios, and strain histories were examined utilizing lateral profiles of streamwise and radial components of mean velocity and turbulence intensity in the jet immediately downstream of the contraction exit. Ultimately it is the flow characteristics downstream of the contraction that would be of primary interest in many applications such as in test sections of wind tunnels. Documentation of these various effects is discussed in the following.

Contraction-Ratio Effect. In these preliminary measurements, contractions with area ratios of 9, 16, and 23.5 were used to examine the mean velocity uniformity and turbulence homogeneity in the flow downstream of the contractions. All the contractions used here have an L/D = 1. When the streamwise and radial mean velocities are normalized using the exit diameter and centerline mean velocity, the top portion of Figure 15 is obtained. It reveals that the shapes of the exit profiles downstream of these different contractions are identical. The mean radial velocity profiles for the different contractions involved also follow the same curve. A small amount of velocity overshoot near the walls is visible from the streamwise mean velocity profile. The flow is still contracting slightly at this streamwise position, therefore, $\overline{V}$ is zero only at the center but is non-zero with opposite signs to either side of the centerline. The u' component increases slightly with increasing contraction ratio. In contrast, the v' component does not show a monotonic trend since the level is slightly higher with c=16 than with the contraction ratios of either 9 or 23.5.

Length-to-Diameter Ratio Effect. To investigate the effects of the strain rate on turbulence, contractions with the same area ratio but different length-to-diameter ratios were used. Velocity and turbulence profiles downstream of three c=9 contractions with L/D ratios of 0.5, 1.0 and 1.5

are shown in Figure 16. The amount of mean flow nonuniformity decreases for the relatively longer contractions. In fact, for the L/D = 1.5 contraction, $\bar{U}$ is practically flat across the entire cross section. The radial mean velocity curves also indicate an absence of $\bar{V}$ for this long contraction. However, with an L/D of 0.5 there is substantial overshoot in the streamwise mean velocity. A significant value of radial velocity also exists off-axis. Turbulence levels are not substantially different downstream of the three contractions although the long (L/D = 1.5) contraction has a larger homogeneous portion which is unaffected by the shear layers.

Contraction-Shape Effect. Another interesting effect stems from the question of whether turbulence characteristics would be sensitive to its strain history when exposed to the same amount of total strain with the average strain rate kept approximately equal. To investigate this effect the mean and turbulence velocity profiles of a fifth-order contour contraction are compared in Figure 17 to the ones obtained from a matched-cubic contraction with equal area contraction and length-to-inlet diameter ratios. Because the fifth-order contour has zero curvature in addition to zero slope at the exit, mean velocity overshoot and radial velocity magnitude are minimal downstream of it. When the contraction process is considered as a whole, the average strain rate imposed on

the flow by both the matched-cubic and the fifth-order contractions is about the same, although instantaneously during the contraction process, a higher peak strain rate is imposed on the flow by the fifth-order contraction at equal inlet velocities. However, the flow is subjected to a much lower strain rate at the beginning and towards the end of the contraction. This allows more time for the turbulence to relax and the mean flow to adjust to the presence of boundaries (i.e., closer confinement) as the flow approaches the end of the contraction. A comparison of mean and turbulence velocity profiles with the ones from a longer matched-cubic contraction (L/D = 1.5) indicates that the resulting profiles are practically identical. Therefore, to obtain a more uniform downstream velocity profile for a contraction with a given length, a fifth-order contour can be used instead of the matched-cubic. The effect of using a dissimilar strain history on turbulence is not readily visible form the u' or v' profiles shown on the bottom of Figure 17 and will require more detailed statistics to reveal its subtle consequences.

Streamwise Development of Mean Velocity and Turbulence through a Contraction

To aid in planning the final experiment, extensive preliminary data were collected for various contractions using many different flow conditions. Mean streamwise velocity and rms turbulence velocities for both the streamwise and radial components were measured along the

contraction centerline with an X-wire probe. The results were plotted by an x-y recorder after being processed through the analog circuitry shown on Figure 7. Photographs of velocity spectra obtained from a 2-channel real-time spectrum analyzer were recorded for many preliminary runs but will not be presented here in lieu of more accurate results from the digitally acquired data. As an illustration of the very important issue of turbulence scales in this study, two figures demonstrating this effect are presented and briefly discussed in the following.

Small-scale Turbulence. Figure 18 shows the mean streamwise velocity and the rms u' and v' turbulence velocities along the centerline of a fifth-order contraction with a c=9 and an L/D = 1. The cross-sectional area starts contracting at x = 0 reaching its final value at x = 15.4 cm. The mean velocity increases monotonically from the inlet to the exit section with very little influence upstream. It should be pointed out that the mean velocity is still increasing slowly at the physical end of the contraction.

The viscous decay of turbulence in a uniform duct is shown by the u' and v' traces on the left side of the figure. For the flow conditions used in this investigation, the rms of fluctuating velocities is such that in a uniform duct u' is always greater than v'. Documentation of this test flow condition using a straight duct (c=1), indicates

that the viscous decay of turbulence is unaffected by the presence of the contraction for all streamwise positions upstream of x = -2 cm. Once the flow has started contracting, the v' downstream decay decreases and at about 6 cm into the contraction ($x/L \simeq 0.4$) it levels off and starts to increase. On the other hand, the longitudinal u' component continues to decay until $x \simeq 9$ cm ($x/L \simeq 0.6$) before its value begins to rise. At the exit section, v' is only slightly greater than u'. The contraction appears not to have a very significant effect on small-scale turbulence.

Large-scale Turbulence. Instead of the flow condition with small turbulence scales of Figure 18, another which had very large scales was used with the same contraction to produce the results shown on Figure 19. The mean streamwise velocity development is the same in both cases. However, the turbulence velocity traces show a remarkable difference. The difference is primarily in the v' component. Immediately upon encountering the contraction, the v' component is amplified to a much higher value than its initial condition at the inlet section. This trend leads to a substantial difference by the time the flow reaches the exit of the contraction. The u' development through the contraction is very similar to the case of small-scale turbulence. The incoming turbulence levels are about the same for the two cases but the turbulence-flow structure is very different. This dramatic difference in the response of

turbulence to a strain could be the key to some of the contradictory results obtained by different investigators working on the problems of contractions and contracting flows. This will be examined in detail in the following chapters.

To summarize these preliminary investigations, one can state that turbulence behavior through a contraction is affected differently in the longitudinal and the lateral components. The extent of this difference is contigent upon characteristics of the incoming turbulent flow and in particular its scales. In order to fully appreciate the various effects discussed in the present chapter, a more thorough investigation has been performed. Results are presented in subsequent chapters of this report.

CHAPTER IV

DIGITAL DATA ACQUISITION AND PROCESSING TECHNIQUES

The final measurements were acquired and processed using digital techniques. The acquired data were processed on a UNIVAC-1100/81 mainframe computer to obtain the results presented in the following chapters. Many quantities that were calculated digitally could not be reliably determined if conventional analog processing had been used. The digital results are much more reliable since the X-wire probe was calibrated more accurately with a squared third-order polynomial and corrections for non-ideal probe geometry were applied. Quantities such as the Reynolds stress and integral scales, that would have been inaccurate and very difficult to obtain with analog circuitry, were calculated with relative ease from the digital data since only multiplication and averaging (summation) operations were involved.

One other advantage of using digital data acquisition is that all the data were stored on magnetic tapes in a form that would permit reprocessing them in the future for additional corrections or with new processing schemes. The experiment could then be "recreated" exactly at no additional cost.

Data Acquisition

After extensive diagnostic runs (digital as well as analog) were made to insure data quality, final measurements

were acquired digitally onto magnetic tapes. From preliminary measurements, it was decided that data would be acquired at 9 streamwise locations along the centerline for each contraction and test flow condition combination. These positions are schematically depicted in Figure 20 for the different length-to-diameter ratio contractions and for the constant-area (c=1) reference flow conditions.

To study turbulence relaxation downstream of a contraction (see L/D=1 case on Figure 20), 8 additional positions of centerline data were acquired during a separate run for each case tested. Three overlapping positions were utilized so that the downstream data could be related to the ones acquired through the contraction. The maximum probe length allowable to minimize probe vibration contamination (see Appendix D for details) and the need to minimize support blockage effects prevented the acquisition of all the positions during a single run. The length of the downstream duct was changed between the two separate runs to accommodate this.

Data were taken upstream of the position where area contraction begins so that the upstream influence of the contraction on the mean flow as well as on turbulence can be estimated. For short contractions (L/D = 0.25 and 0.50), where the upstream influence is substantial, data were collected starting farther upstream from the contraction inlet position. The first data position was either 1 or repositioned to 1A if the X-wire probe could not reach

position 1, in order to prevent any interference with an attached constant-diameter downstream tube with a length equal to 1.5 times the exit diameter. This problem only occurs for mild contractions (large D_e), because the tube is physically longer than for those that have higher contraction ratios. In the L/D = 1.0 case, only the c=2 contraction required 1A as the starting position.

For the constant-area duct case, the choice of the value of x/M at which the location of the contraction inlet would be placed limits the distance upstream which the probe could traverse. Therefore, the first data point for grids J4 and J5 was located at position 1A. Throughout the entire final data collection period, the X-wire probe was never dismounted from the traversing mechanism which was aligned in all directions to the test section of the wind tunnel with a dial indicator. The position where the contraction begins was always at point 2 or 3 as shown on Figure 20. The location at which the cross-sectional area reached its final value in each contraction are also noted on this figure. However, this did not coincide exactly with a point where data was acquired.

The final selection of test flow conditions consists of 13 different cases. Coupled with 10 contractions and a reference case, the amount of data collected would have been astronomical and unnecessary if all combinations of contractions and flow conditions were utilized. Based on the preliminary studies, a judicious choice was made on

which cases to run. A table containing cases that were actually used is shown in Figure 21. The 13 test flow conditions are arranged in order of increasing turbulence length scales from left to right. Conditions with the same "T" number but with different suffixes indicate that these flow conditions have the same lateral length scale but a slightly different longitudinal scale. Conditions with the suffix "a" have the smallest L_u while those with suffix "c" have the largest one, for that particular L_v.

Contractions were designated with "C" numbers. However, C0 is the constant-area duct reference case. The characteristics of all these contractions are tabulated in Figure 3 and their contour shapes are shown in Figures 4 through 6. Selected cases were marked with an "X" in Figure 21 for data acquisition and circled if detailed plots of streamwise development are presented in the following chapters. Supplemental cases were run to study the effects of turbulence relaxation downstream of a contraction and some off-axis data were also collected. These cases are summarized in Figure 22. Positions where off-axis data were collected are shown in the next figure. At the contraction exit, off-axis data were acquired at three radial positions with a separation of 7 mm between points. For other streamwise positions, only the "DY3" radial position (21 mm off-axis) was used. At both the inlet and exit sections, reference on-axis data were also collected.

In addition to single probe data acquisition, digital

samples were also acquired simultaneously with two X-wire probes placed at the same streamwise location but using 6 different radial separation distances with one probe always located on the centerline of the C2 contraction in flow condition T7a. The two probes' separation distance ranged from 0.64 cm to 1.91 cm in 0.25-cm increments. Data were acquired from four streamwise positions. These data are essential in establishing the relationship between the lateral integral length scale of the radial velocity component in the streamwise direction (single-probe measurements) and the lateral length scale of the radial velocity component in the radial direction (two-probe measurements) for contracting flows. Measurements of this type are of interest to theoreticians and have not been available or reported in the literature.

The acquisition procedure begins with setting-up the required test flow condition and contraction, centering the X-probe on the axis of symmetry and calculating the 9 streamwise locations of the run which would be monitored on the digital position indicator. A reference run was then made to record the centerline mean streamwise velocity on the x-y recorder. During digital acquisition, the mean velocity was constantly compared with the reference run. Detection of any slight drift in the velocity was corrected before data were recorded onto magnetic tape. Collected data were immediately discarded if the drift occurred during the acquisition.

The bias and gain of signal-conditioning circuitry were adjusted and recorded for each channel of the X-wires for reconstruction of the original signal during data processing. The details of the circuitry are presented in Chapter II.

Digital sampling and recording were accomplished with a customized fast-acquisition program which simultaneously samples the hot-wire channels, converts them to 12-bit numbers, and writes them onto industry-standard 9-track tapes at a sequence rate of 18.66 kHz for 2-channel acquisition and 11.36 kHz for 4-channel acquisition. The program was executed on a PDP-11/10 based, portable acquisition and processing system designed by Way[32] and previously used by Wigeland[29]. Both analog and digital instrumentation systems, described in detail in Chapter II, were active during the data acquisition. The analog processing instrumentation was used to monitor the U and V signals and their spectra on a 2-channel real-time spectrum analyzer, while the digital acquisition was in progress, to ensure data of high quality. One hundred records of digital data, each with 2048 samples per channel, were recorded at 9 positions for each case. In all, over 300 million samples of final X-wire data points were collected and processed for this investigation. The original data are stored on a total of 32 reels of magnetic tapes.

Data Processing

The 100 digital data records that make up a data file for one position in a run were first converted to U and V velocity information by the efficient and highly accurate calibration and linearization procedure described in Appendix C. While the results were still in the computer's core memory, an FFT spectra computing program was called as a subroutine to compute the power spectra of the velocity data. The same program which computed the spectra also calculated other desired information such as time scales and the Reynolds stress, then computed commonly used quantities, e.g., turbulence intensities, length scales, etc., and printed them out. The power spectrum, cross-spectrum, coherence and phase functions, auto and cross-covariances, co- and quad-spectra were recorded on an output tape. These functions can be plotted using appropriate software which generate displays on a Tektronix 4010-1 graphic display unit or pen-plots them on a Calcomp drum plotter.

Sample plots of spectra, coherence and correlations are shown in Chapter XI. The subroutine which makes integral time scale calculations was modified by Wigeland[29] to improve the accuracy of the time-scale computation as well as the calculated rms values. The data reduction took a total of 7 hours of CPU time on an UNIVAC-1100/81 and the final results are stored on 2 reels of magnetic tapes.

CHAPTER V

TEST FLOW CONDITIONS

Before describing the contraction effects on turbulence characteristics, it is important to know how the turbulence behaves in the absence of any contraction (or strain) so that effects due solely to the contraction can be isolated and assessed. The purpose of this chapter is to document, in detail, the 13 different test flow conditions used to generate input turbulence to the contractions. These results are very important in forming a basis for comparisons between the different experimental cases and theory by establishing reference conditions. Such reference flow conditions were either unavailable or unreported by previous investigators leading to difficulty in obtaining valid comparisons with the present investigation since it was not possible to correct their results for viscous dissipation using the present scheme. Such difficulty may have also lead to the controversy in the previous results discussed in the Introduction.

In planning the present experiment, flow conditions with the widest possible range of turbulence scales were generated and documented. Test conditions with various turbulence scales were selected from those that exhibited homogeneous characteristics and well-behaved turbulence decay. In addition to the very wide range of turbulence scales exhibited in these flow conditions, a condition which

has very low turbulence intensity was also selected. To assure homogeneity and isotropy, the highest total turbulence intensity in any of the test flow conditions was limited to about 5%. During the planning and acquisition phase, flow conditions were identified by the grid number (J1, J2, J3, etc.) and the velocity used in generating them. In the results presented here, test flow conditions are identified in this manner. After the analyses of the data, "T" numbers were assigned to flow conditions such that larger numbers correspond to larger length scales. This scheme is designed to aid the reader in interpreting data from different flow conditions. Flow conditions with the same "T" number but different suffixes have approximately equal lateral length scales but different longitudinal length scales. A cross reference is given in Figure 36 for corresponding "T" designation of the flow conditions with equivalent grid number-velocity designation.

Turbulence-Energy Decay

An important criterion used in making the selection of the test conditions is "proper" turbulence energy decay. To qualify as well-behaved conditions, the turbulence must decay axially and the decay rate should be relatively independent of velocity, i.e., the Reynolds number. Turbulence energy decay of the streamwise and radial components plotted as a function of the axial distance along the centerline of the uniform-area test section are shown in

Figures 24 and 25, respectively. Total turbulence-energy decay is shown in Figure 26.

These figures indicate that the turbulence decay rates for the different flow conditions vary over a very wide range. Results show that the decay rate is primarily a function of the grid mesh and is quite insensitive to the mean velocity used. This velocity independence is a highly desirable quality to look for in the selection of flow manipulators because it will assure predictable performance over a range of Reynolds numbers. In general, turbulence generation and decay of fine-mesh grids tend to be more dependent on the velocity because they are operated closer to the critical Reynolds numbers[3]. Such operating conditions should be avoided whenever possible. When the axial decay rates are normalized by the mesh, the values obtained from the various size grids are approximately equal for most of the test flow conditions. These values are tabulated in Figure 37. Exceptions include the small-scale test flow condition T1, flow condition T3c which was operated close to but above the critical Reynolds number, and a very low turbulence flow condition T5b. Because of the higher decay rates, turbulence decay data for these flow conditions are shown separately in Figures 27-29. At about $\tilde{x} \approx 16$ cm ($\tilde{x}/M \approx 113$) for T3c, the decay rate increases significantly indicating that the turbulence is going through its final decay stages. This position is downstream of the exit station for all contractions with an L/D equal

to one or less so that it is of no concern here.

In the low turbulence flow condition, T5b, the fluctuation energy increases slightly in the downstream distance for both the streamwise and radial components. At such low "turbulence" levels, potential fluctuations induced by vorticity in the boundary layer on the test section wall could be sensed by the X-probe. These induced fluctuations increase slightly in the downstream direction due to boundary layer growth on the walls. The streamwise turbulence intensity, $u'/\bar{U}$ is less than 0.2% and the radial component, $v'/\bar{U}$ is below 0.1%. From these turbulence intensity figures, one concludes that the turbulence in this flow condition is hardly energetic. Bennett and Corrsin[18] also reported an increase in their free-stream turbulence intensity with axial distance. These extraordinary flow conditions were used sparingly and the results treated cautiously in the present experiment.

Isotropy, Integral Length Scales and Reynolds Stresses

The documentation of test flow conditions for this investigation goes beyond measurements of mean velocities and turbulence intensities. Integral length scales and Reynolds stresses were also computed along with spectra and correlations. A major advantage of using digital data processing is that these quantities are not more difficult to obtain than the mean velocity or turbulence intensity once the programs required for computing them are available.

Figure 30 shows the downstream development of u'/v' for all test flow conditions except the very low turbulence condition T5b which exhibited high anisotropy. Except for T5b, all the grid-generated test flow conditions have a u'/v' value slightly greater than 1. Perfect isotropy is practically impossible to achieve for naturally decaying grid-generated turbulence. A few investigators[17,18,19] have reported some success in improving isotropy of grid turbulence by using a mild contraction to increase v' thereby modifying the partition of turbulence energy in the free-stream. Small-mesh grids with u'/v' values of up to 1.34, show more departure from isotropy than large-mesh grids.

In general, the data show that turbulence tends very slightly towards isotropy with increasing downstream distance for large-mesh grids and away from isotropy for the fine-mesh grids. Such changes in the values of u'/v' are small when compared with changes resulting from the contraction so that u'/v' can be treated as essentially constant for the reference conditions.

To study the effects of turbulence scales on contracting flows, homogeneous and approximately isotropic turbulence flow conditions were generated to cover the widest possible range of integral scales in the present facility. Streamwise development of the longitudinal and lateral length scales of the test flows are shown in Figures 31 and 32, respectively. These integral length scales were

calculated from the integral time scale obtained from the autocovariance functions using the local mean streamwise velocity and assuming validity of Taylor's hypothesis in relating length scales with time scales.

For the longitudinal length scale this is fairly straight-forward, but for the lateral component, the quantity obtained is the lateral length scale in the streamwise direction. This length scale is simply related to the lateral length scale in the radial direction in grid-generated turbulence, i.e., homogeneous and approximately isotropic. Whether this relation holds or not, for contracting flow situations, will be answered when data acquired with two X-probes separated laterally are processed. It would be interesting to compare these results with those of Bennett and Corrsin[18] to see the effect of a contraction on the two-point space time correlations. Although the streamwise development of the longitudinal length scales shows more scatter than the lateral scales, a definite trend of a slow growth in the length scales with increasing time during the decay is apparent. The range of length scales for these flow conditions at the location of the contraction inlet varies from about 0.31 cm to 1.3 cm for the longitudinal scale and from 0.17 cm to 0.57 cm for the lateral scales.

Reynolds stress development profiles in the streamwise direction are also shown for the same flow conditions in Figures 33 and 34. The low turbulence condition, T5b (open

circles in Figure 33), shows an effectively zero $\overline{uv}$ Reynolds stress. Turbulence in this flow condition is very weak. For most flow conditions the magnitude of $\overline{uv}/\bar{U}^2$ decreases in the downstream direction and approaches zero by about x = 20 cm. As expected, turbulence generated by large-mesh grids is more energetic and produces higher Reynolds stresses that decay rather slowly as shown in Figure 34. The Reynolds stress is generally associated with turbulence production due to the exchange of momentum in the turbulent mixing process. The reasoning behind the behavior of the Reynolds stress profiles in Figure 33, which are positive for some flow conditions and negative for others, is not clearly understood at the present time. The Reynolds stress concept is difficult to comprehend physically except in idealized situations and is an extremely difficult quantity to measure accurately in experiments.

A straight line relationship between longitudinal and lateral length scales for all the flow conditions at the inlet position of the contractions is shown in Figure 35. Data on this graph reveal that L_{u_i} is typically 2.3 times L_{v_i} rendering these turbulent flow conditions approximately isotropic. Von Kármán and Howarth[36] showed that perfectly isotropic turbulence would exhibit an $L_u = 2\ L_v$ relationship. The "T" number for each test flow condition was assigned based on these length scales and subsequently used to identify the various flow conditions. To aid in the interpretation of data from various flow conditions,

turbulence of larger scales is denoted with increasing "T" numbers. Suffixes are used to distinguish flow conditions with approximately equal lateral length scales.

To fully characterize the 13 test flow conditions, pertinent quantities such as the initial turbulence intensity, mesh Reynolds number, average initial length scales, turbulence decay slope (streamwise component), virtual origin, and the initial turbulence Reynolds number, R_{λ}, are tabulated in Figures 36 and 37. Arrows indicating largest (arrow points to the right) and smallest (arrow points to the left) values of certain parameters are also shown on the figures. These two figures and Figure 38, which relates the turbulent Reynolds number to the mesh Reynolds number for each flow condition, show some of the widest ranges of test condition parameters used in an experiment on contracting flows.

CHAPTER VI

EFFECTS OF TURBULENCE SCALES ON FLOW DURING AND AFTER A CONTRACTION

This chapter is devoted to the study of the effects of different turbulence scales on the flow through and downstream of a 9:1 matched-cubic contraction. A similar investigation was conducted by Ramjee and Hussain[23] using 4 screens of different mesh sizes and a round-rod, biplanar grid for a contraction ratio of 11. Results that were presented by them covered only the contracting section. Here we are also interested in what happens to the turbulence in the uniform duct downstream of the contraction. The relative initial turbulence scale range, L_{u_i}/D_i, varies by a factor of approximately 2 in their study[23] while in the present experiment it covers a range of more than 3 using flow conditions T1, T4, and T7a. The constant-diameter duct length on the downstream end of the contraction was 4.2 times the exit diameter D_e.

Results are presented in the form of turbulence quantities through and downstream of the contraction starting with the flow condition with the smallest length scales. Before delving into the turbulence characteristics, streamwise mean velocity development along the centerline is shown in Figure 39 for flow conditions having different turbulence scales. The mean velocity is shown to increase monotonically reaching a constant value in the constant area duct downstream of the contraction. These axial mean

velocity profiles indicate very small differences in $\overline{U}(x)$ between the flow conditions with widely differing turbulence scales. Even though two of the conditions shown here, namely T5a and T7b, were not the ones chosen for the investigation summarized in this chapter, their turbulence characteristics were representative of the medium and large-scale conditions T4 and T7a, respectively. The dimension L on the figure indicates the length and the physical location of the contraction. The inlet of the contraction is always located at x = 0. Included on this figure are axial mean velocity profiles for two other contractions and the uniform cross-sectional area duct. These will be discussed in conjunction with contraction ratio effects in the next chapter.

Turbulence Energy Components

The longitudinal component of turbulent kinetic energy for the small scale condition T1, normalized with its initial value at x = 0 is shown in Figure 40 as a function of downstream distance for the 9:1 contraction and the 1:1 reference condition. The turbulent energy in the constant-area duct decays monotonically in the downstream direction, while for the flow through the contraction, the energy decays at a slightly higher rate over the first half of the contraction as predicted by rapid distortion theory. However,with continued contraction, the kinetic energy rises sharply reaching a peak value of about 0.9 $u_i'^2$ at the exit

position. This level is about 3.5 times higher than the corresponding unstrained turbulence which has decayed in a uniform duct up to this position. Downstream of the contracting section in the constant-diameter duct, the turbulence energy again decays at approximately the same rate as that for unstrained turbulence as the reader can verify by comparing results of contracted and non-contracted flows.

The radial turbulence energy development through and downstream of the contraction in this flow condition, shown in the next figure, indicates a similar trend. The shape of the curve is similar to the longitudinal component but now the decay rate is slower than the reference case, even at the initial stages of contraction. This increase in the v' component relative to the unstrained flow is predicted qualitatively by theory. A peak value of about 1.2 times the incoming radial component energy is reached at the exit section. The decay rate downstream of the contracting section is again approximately that of the unstrained turbulence. Therefore, the total turbulent kinetic energy through and downstream of the contraction should behave similarly. Figure 42 shows this to be the case.

Tucker and Ali[35] showed that downstream of a contraction in an anisotropic turbulence field, the streamwise energy component decays slower but the radial component decays faster than in isotropic turbulence. The turbulence was generated by placing a perforated grid

(σ=0.47) either at the inlet to a 5.75:1 contraction to generate anisotropic turbulence or at the outlet section to generate isotropic turbulence. However, no attempt was made to match the mesh Reynolds number between the two conditions. It has been shown[1,3] that grids with solidities greater than about 40% exhibit highly Reynolds-number dependent turbulence decay rates. Therefore, these results should be taken cautiously.

It is interesting to note that for the present results, the total kinetic energy does not show a higher decay rate behavior during the initial stages of contraction. This is the case because the radial component of turbulent energy is increased substantially by the contraction relative to the unstrained flow and is weighted more towards the total turbulent kinetic energy contribution in an axisymmetric geometry.

For flow conditions with larger turbulent length scales, attenuation of the streamwise component of energy is increased during the initial straining of the fluid. This is demonstrated by comparing Figure 40 to Figures 43 and 46. The increase in u'^2 with continued straining is lower for the turbulence with larger scales. For both flow conditions, T4 and T7a, this energy rise does not exceed the values attained by the naturally decaying turbulence. Again, the decay rates for u'^2 downstream of the contraction approximate those of the corresponding unstrained flow conditions. Only the turbulence in the large-scale T7a

condition seems to show a slight increase in the decay rate after the contraction in both the streamwise and radial components as indicated on Figures 46 and 47, but this difference is within experimental uncertainty.

An increase in the turbulence scales of incoming flow conditions results in higher turbulence amplification in the radial component as shown in plots on Figures 41, 44, and 47. The peak value of $v'^2/v_i'^2$, which is attained at the end of the contraction, increases from 1.2 for T1 to 2.8 and 3.4 for T4 and T7a, respectively. This produces a corresponding increase in the total turbulent kinetic energy downstream of a contraction for larger-scale turbulence conditions, as indicated on Figures 42, 45, and 48. Thus, the turbulence intensity reduction efficiency of a contraction is highly dependent on the incoming turbulence scales. This is not predicted by the rapid distortion theory of Batchelor and Proudman[24] and Ribner and Tucker[25] because of the intrinsic assumption of asymptotically small-scale turbulence used in the derivation. Goldstein and Durbin's analysis[26], which included finite-scale effects, predicted an opposite behavior but was done for asympotically large two-dimensional contractions.

Ramjee and Hussain[23] reported in their study on the effect of upstream screens that the exit values of turbulent intensities were independent of changes in the incoming turbulence intensities (and the integral length scales) especially for the streamwise component. This was not found

to be the case in the present experiment. The present data show higher values of the exit turbulence intensity for incoming turbulence of larger scales and coincidently higher turbulence intensity in these selected flow conditions. We conjecture that in their experiment[23] the problem could be due to large contributions of pressure fluctuations from the blower fan blades which affect the measurement accuracy of streamwise component of turbulence. What they were measuring as the asymptotic value of $(u'/\bar{U})_e$ could be mostly fan-induced fluctuations that get amplified through the contraction and not true grid-generated turbulence. The present experiment has avoided this problem by powering the wind tunnel with a compressed air supply instead of a blower. See Appendix B for details of this modification.

Isotropy and Integral Length Scales

Axial developments of u'/v' through the contraction for 3 flow conditions are shown in Figures 49-51. For the small-scale turbulence, Figure 49 shows a decrease in u'/v' ratio as the flow gets contracted. At $x/L \simeq 0.6$ a minimum value of 0.8 is reached after which there is an increase in u'/v' with further straining. At the end of the contracting section, turbulence is again nearly isotropic, i.e., $u'/v' \simeq 1.0$. Further downstream in the constant-area duct, the turbulence remains isotropic. The value of u'/v', however, is lower than that of the corresponding unstrained turbulence condition.

For test conditions with larger turbulence scales, shown in Figures 50 and 51, disparity between u' and v' is greater after the contraction, causing the flow to be more anisotropic. Moreover, the uneven partition between the longitudinal and lateral components of the fluctuation velocity does not lead to a return to the isotropic state of the unstrained flow. The u'/v' ratio remains at the value attained near the end of the contracting section even for the flow far downstream in the constant-area duct. This is in sharp contrast to the behavior of small-scale turbulence shown earlier.

Uberoi and Wallis[17] and Comte-Bellot and Corrsin[19] have utilized mild contractions to modify the isotropic state of grid-generated turbulence. Their goal, to improve the validity of comparisons between experiments on grid-generated turbulence and theories of isotropic turbulence by improving the degree of isotropy in the turbulent flows, was met with varying degrees of success. Results from the present experiment have also shown that the degree of isotropy (or anisotropy) introduced by a contraction can persist downstream for large-scale incoming turbulence but not for small-scale turbulence. Therefore, in experiments which require altering the degree of isotropy by utilizing a contraction, whether to improve it or to generate an even more anisotropic test flow condition, the selection of incoming turbulence scale characteristics plays a key role in the success of such an endeavor. For example,

while Uberoi and Wallis[17] reported a return to the initial precontraction isotropic state for the flow downstream of a contraction, Comte-Bellot and Corrsin[19] found the opposite to be true in a very similar experiment. This points to the fact that incoming or background turbulence characteristics play an important role in determining the results of such "similar" experiments. The details of the unstrained initial conditions for these two experiments are not available to analyze this any further.

The next three figures show the resulting length scales, both longitudinal and lateral, for the 3 flow conditions that were strained through the contraction. First, it is noted that both length scales grow when the turbulence is subjected to an axisymmetric contraction. The resulting length scales downstream are as much as almost 20 times their initial values in the present results. In Ramjee and Hussain's study[23], they reported that the longitudinal length scales downstream of an axisymmetric 11:1 contraction were between 90 and 170 times the initial length scales. However, they were unable to explain this large increase in the length scale, but suggested that this could be due to the large uncertainty in the calculated Eulerian integral time scale from experimental measurements of the autocorrelation function. Since the measured values were consistently high for all their screens, statistically it is unlikely that this is due to experimental uncertainty. From our previous experience, a likely cause of this problem

is the low-frequency contribution from the blower. This results in abnormally large values of the calculated integral time and length scales. This effect could be eliminated by utilizing the digital data acquisition and processing techniques described by Wigeland[29]. The present experiment does not suffer from this problem because the wind tunnel was powered by a compressed-air supply.

For the small-scale flow condition T1, the longitudinal length scale was 19 times larger at the downstream end of the contraction than at the inlet, while the lateral length scale increased only 6-7 times. When flow condition T4 was used, the longitudinal length scale, L_{ui}, increased only to about 8 times its initial unstrained value, while the lateral length scale reached almost 12 times its initial value. When flow condition T7a, which has the largest scales, was used, the growth in L_u amounted to less than 5 times its unstrained value but L_v attained a length of 10 times L_{vi}, its initial length scale. Despite some scatter of data in Figures 52-54, a clear trend emerges for the various turbulence conditions of initially different scales subjected to the same contraction. The longitudinal length scale increases more than the lateral length scale for initially small scale turbulence. The reverse is true for initially large turbulence scales. For an intermediate-scale turbulence condition, the growth in the integral length scales is approximately equal. These findings are clearly demonstrated in Figures 52-54.

CHAPTER VII

CONTRACTION RATIO EFFECTS

The effects of using turbulence of different scales through a fixed contraction ratio were demonstrated in Chapter VI. In this chapter the effects of varying the contraction ratio on incoming turbulence of different scales will be examined. Results from mild and moderate contractions are presented first, followed by those with high contraction ratios.

Streamwise mean velocity profiles through the mild and moderate matched-cubic contractions are shown in Figure 39 for test flow conditions representing small (T1), medium (T5a), and large (T7a) scale turbulence conditions. The centerline mean velocity varies only slightly for the different flow conditions due to differences in the boundary layer condition at the contraction inlet as well as in the boundary layer development through the contraction. The differences in the boundary layers along the upstream duct are caused by the differences in the grids and the free-stream velocities used in the various test flow conditions, and have been documented in Chapter III. The difference is slightly more pronounced in the c=4 contraction than either in the 9:1 or the 2:1 contractions. The axial mean velocity profiles for the high contraction ratios are presented in Figure 75. The difference in the mean velocity resulting from incoming turbulence of

different scales increases with increasing contraction ratio. The centerline mean velocity downstream of the contraction is slightly higher for the small-scale turbulence condition. However, in all cases, the axial profile shape differences are practically negligible, in particular, when considering the range of initial free-stream velocity and turbulence involved.

Small-scale Turbulence Flow Conditions

The axial turbulence energy development of the longitudinal and lateral components are shown in Figures 55 and 56. The total turbulence energy at the end of the contraction increases monotonically with the contraction ratio as shown on Figure 58. This increase is reflected more closely by the lateral energy component. According to theory[24,25] the streamwise component of the fluctuation energy should decrease as the contraction ratio is increased. Figure 55 shows this to be true during the early part of the contraction for mild contractions ($c \leq 4$). For the 9:1 contraction, even though the initial decay rate of the streamwise fluctuation energy is faster than that of the unstrained turbulence, the turbulence reduction is not higher than the 4:1 contraction as would be predicted by linear theory[24,25].

Instead of further reduction in the streamwise component of energy with continued contraction, an increase is noted beginning at $x/L \simeq 0.8$ for the mild contractions and

earlier at $x/L \doteq 0.6$ for the moderate contractions. This non-linear behavior is much more pronounced for the 9:1 contraction than for mild contractions. The peak values of the turbulence energy ratios attained at the exit section are less than the initial value for these contractions in the longitudinal, component but reaches 1.2 in the lateral component for the 9:1 contraction.

When higher contraction ratios (c=16, 23.5 and 36) are used in T3a, a flow condition with relatively small length scales, the axial development of the streamwise turbulence component shown in Figure 76 behaves like results from the very small-scale T1 for the mild and moderate contractions. In both cases, this component of energy initially decays faster than unstrained turbulence but with continued straining, the turbulence stops decaying and its energy increases. The maximum energy level reached at the end of the contracting section is higher than the level at the contraction inlet. This net production of turbulence through the contraction increases with contraction ratio.

Qualitatively, the increase in the lateral component of turbulent kinetic energy for higher contraction ratios is in agreement with rapid distortion theory. This is shown in Figure 56 for the mild through moderate contractions and can be inferred from the total turbulence energy plot in Figure 78 for higher contraction ratios.

The u'/v' plots presented in Figures 57 and 77 indicate that as the flow is contracted, its velocity fluctuations

deviate from isotropy. In accordance with theory, it was shown in the turbulence energy ratio plots that this imbalance between the streamwise and lateral components is due to a relative increase in the lateral component energy with increasing contraction. A behavior not predicted by theory is the return towards a more isotropic state with continued contraction shown in the results for the moderate and high contraction ratios. The amount of increase in the value of the u'/v' ratio, after reaching a minimum somewhere midway along the contraction, increases with the area ratio of the contraction. This is due to a non-linear inter-component energy transfer from the lateral component to the streamwise component which increases with the total strain. This mechanism of turbulent energy transfer does not manifest itself in the flow through mild contractions. Therefore, the values of u'/v' remain low downstream of the contracting sections.

Both the longitudinal and lateral length scales increase through the contractions. Growth of initially small turbulence scales through the contractions are shown in Figures 59 and 60 for the mild and moderate contractions and in Figures 79 and 80 for higher contraction ratios. The longitudinal length scale development in Figure 59 indicates a slightly faster growth rate with increasing strain for the c=2 contraction than for either of the other ones shown on that figure. The length scale near the end of the contracting section for this mild contraction is also

slightly larger than the 4:1 or 9:1 contractions. The longitudinal length scale development in the small-scale turbulence flow condition shown in Figure 79 for high contraction ratios reveals that the maximum length scale attained is not monotonic with increasing or decreasing contraction ratios. The maximum longitudinal length scale after straining for the contraction with an area ratio of 36:1 is larger than that of a 16:1 contraction but less than for the 23.5:1 contraction. In the T1 test condition, increasing the contraction ratio seems to decrease the maximum streamwise length scale attained in mild and moderate contractions. However, the net length scale growth is always large compared to the unstrained turbulence, which exhibited only a small growth over the same downstream distance; see Figures 31 and 32.

The lateral length scale increase is monotonic with increasing contraction ratios as demonstrated in Figures 60 and 80. Larger axial strains from higher contraction ratios produce a "bigger" lateral length scale at the downstream end of the contraction. For example, a maximum lateral scale of over 30 times its initial unstrained value is reached at the end of the contracting section in the 36:1 contraction. Both L_u and L_v of the highly strained turbulence tend to become smaller in the constant-area duct downstream of the contractions.

The axial development of the Reynolds stress shown in Figure 61 for the mild and moderate contractions indicates

that for the mild 2:1 contraction a slight increase in the Reynolds stress occurs during the early phase of contraction. It then decreases to its initial value and remains constant through the remainder of the contraction. At a higher contraction ratio, c=4, the Reynolds stress behaves like unstrained turbulence, decaying in the downstream direction; except there is a bit more scatter in the data. For the 9:1 contraction, the Reynolds stress decreases with increasing downstream distance into the contraction but does not asymptote to zero. Instead it keeps on decreasing with an eventual sign change at $x/L \simeq 0.8$. The trend continues with increasing downstream distance up to and slightly beyond the contracting section. In the constant-diameter section the Reynolds stress tends to return to zero but data on this figure do not extend far enough downstream to locate this zero Reynolds stress position. The higher magnitude of the Reynolds stress at the downstream end of the 9:1 contraction is probably associated with the turbulence "production" by the inter-component transfer of turbulent energy from the lateral component to the streamwise component. This inter-component transfer of energy causes the streamwise turbulent kinetic energy to rise at the downstream end of the 9:1 contraction as shown earlier in Figure 55. It will be proven in Chapter XI that the streamwise and radial velocity fluctuations are indeed interrelated and Chapter XIII shows that this gain in the streamwise component is

reflected as a loss of some energy in the lateral component.

Medium-scale Turbulence Flow Conditions

Results from two medium-scale turbulence flow conditions are shown in Figures 62-67 for the mild and moderate contractions. Even though the two flow conditions have approximately the same length scales, the other turbulence characteristics, as shown in Figures 36 and 37, are very different. Flow condition T5a is a typical energetic turbulent flow condition while T5b has vanishingly low turbulence intensity. In Figures 65 and 66 it is shown that for the very low turbulence flow condition, the contractions amplify the turbulence energy tremendously in both streamwise and lateral components. Downstream of the contraction, the total turbulence energy (Figure 67) is much higher than the energy entering the contractions. Even the relative turbulence intensities are not appreciably reduced by the contractions. It is evident that contractions cannot be used to reduce very low level turbulence because the inter-component transfer leads to higher energy in both components of turbulence.

The streamwise and lateral components of turbulence energy and the isotropy plots for a typical medium-scale turbulence condition, T5a, are shown in Figures 62 to 64, respectively. Comparing these figures with the corresponding ones for the small-scale flow condition T1 (Figures 55 to 57), one finds that the plots are

qualitatively similar for both streamwise and lateral components of turbulence energy. This large-scale turbulence flow condition has a slower viscous decay rate than the smaller-scale T1 condition; see Figures 36 and 37. Therefore, one of the crucial assumptions of rapid distortion theory (no viscous dissipation) is violated to a lesser degree in flow condition T5a, so that we should expect a better agreement with theory.

Figure 62 shows that in accordance with the theory the streamwise component of energy is reduced by the contractions. This reduction increases with the contraction ratio, except no further increase in reduction is shown by increasing the contraction ratio from 4 to 9. It is suspected that some non-linear transfer of energy into the streamwise turbulence energy component inhibits further decay enhancement and causes the rise in u'^2 close to the downstream end of the 9:1 contraction. Non-linear interaction has not been incorporated in any of the theories to date. When this figure is compared with Figure 55, the corresponding one for the small-scale turbulence, it is noted that during the initial stages of straining, the contraction area ratio has a stronger influence on the turbulence energy reduction for larger-scale turbulence. Despite the rise in u'^2, its level at the downstream end of the contraction is below that of the naturally-decaying unstrained turbulence. This is contrary to results from the small-scale test condition, where there is a net gain in u'^2

energy downstream of the contraction over unstrained turbulence. The lateral component of turbulence energy shows a monotonic increase with higher contraction ratios. When compared to the small-scale condition, the amount of increase for each corresponding contraction is higher in this medium-scale turbulence.

The degree of isotropy variation through the contractions in this turbulence condition is plotted in Figure 64. For each of the corresponding contractions, the increase of v' relative to u' is amplified more for this turbulence condition than for the small-scale turbulence examined earlier. The tendency for the turbulence to return towards a more isotropic state during the latter stages of straining, which is present when small-scale turbulence is used in the 9:1 contraction is notably absent here.

Large-scale Turbulence Flow Conditions

Streamwise developments of turbulence kinetic energy are presented in Figures 68, 69, and 71 for the mild and moderate contractions using the large-scale flow condition T7b, similar to the ones displayed for higher contraction ratios in Figures 81 and 83 in flow condition T7a. A comparison of the results obtained in these large-scale turbulence conditions with results obtained in the medium- and small-scale turbulence indicate that, with increasing turbulence scales, the streamwise component of turbulence energy is attenuated more acutely for each corresponding

contraction ratio during the initial straining process. For contractions with area ratios of 9 or greater, there is an increase in the u'^2 energy due to non-linear inter-component energy transfer to the streamwise component. This energy increase relative to the minimum value is greater for turbulence of small scales. The non-linear transfer process increases with increasing contraction ratios for a fixed flow condition as shown by Figures 68 and 81 in the case of large-scale flow condition and in Figures 55, 62, 65, and 76 for turbulence with smaller scales. The lateral component and total turbulence energy, shown in Figures 69 and 71, respectively, exhibit an increase with contraction ratio. A large increase in the peak values attained is noted between the 4:1 and 9:1 contractions. Results at higher contraction ratios in Figure 83 show further increase in the total turbulence energy. Maximum values attained downstream of the contracting section in large-scale turbulence are higher than for small-scale turbulence flow conditions.

The development of isotropy through contractions in Figures 70 and 82 resembles that of the medium-scale flow condition in which there is a tendency to "recover" to a more isotropic state after substantial straining. This tendency starts near the exit but still within the contracting section. This "isotropic recovery" is more prominent at higher contraction ratios and not noticeable for the 4:1 and 2:1 contractions. Final values of u'/v' downstream of the contractions are correspondingly lower for

these large-scale flow conditions than for the medium- or small-scale conditions.

The longitudinal and lateral integral length scales for these large-scale flow conditions are shown in Figures 72-73 and Figures 84-85 for mild to moderate and for high contraction ratios, respectively. Development trends are similar to those of the small-scale turbulence condition T3a. Longitudinal length scales downstream of contractions increase with contraction ratio. However, the largest longitudinal scale is attained by the 23.5:1 instead of the 36:1 contraction. This is the same order found using flow condition T3a. Lateral length scales downstream of the contractions increase with the contraction ratio. These large-scale turbulence flow conditions show peak values that are higher than those of the medium-scale flow conditions. The Reynolds stress plots for contractions with c=2, 4, and 9 are shown in Figure 74. For the 9:1 contraction, the curve shows an increase in the production of turbulence as the flow goes through the contraction.

Summary of Contraction Ratio Effects

A short summary of the effects of contraction ratio variation on incoming turbulence conditions of various scales is presented here to establish the major results. These results are referenced to flow characteristics of the constant-area duct using the same test flow conditions as for the contractions under investigation.

The streamwise component of kinetic energy decreases during initial passage through the contractions. In general, for a given flow condition, this attenuation increases with increasing contraction ratio. At a fixed contraction ratio, this energy attenuation increases when the incoming turbulence scales are increased. An exception to the above observations occurs when the turbulence level of the free-stream flow is vanishingly low. In such cases, the streamwise turbulence energy and relative turbulence intensity get amplified tremendously when the flow is contracted. The amount of amplification increases with the contraction ratio. Towards the downstream end of the contracting section, u'^2 rises because of non-linear energy transfer to the streamwise component. This non-linear increase is higher for larger contraction area ratios in a given flow condition. However, upstream turbulence with larger scales reduces the peak level of this increase in u'^2 at the downstream end of the contraction. Depending on the contraction ratio and the upstream turbulence scales, the non-linear increase in u'^2 near the end of the contraction may or may not exceed levels found for naturally decaying turbulence in a constant-area duct. At high contraction ratios, the streamwise turbulence energy can be several times higher than its level entering the inlet of the contraction.

The lateral component of turbulence energy always increases through a contraction. This increase is higher

for larger contraction ratios and for turbulence of larger scales. Past investigations have always indicated that rapid distortion theory underpredicts this rise in the lateral turbulence energy component and over predicts the attenuation of the streamwise component of turbulence intensity. Present results show that the predictions by classical rapid distortion theory are approached for both components of turbulence intensity during the initial stages of flow contraction when the upstream turbulence scales are large. However, the increase in u'^2 at the downstream end of contractions cannot be accounted for by linear rapid distortion theory[24-27]. It is suspected that this non-linear effect is due to an inter-component energy transfer from the lateral to the streamwise component. The non-linear transfer mechanism is more effective for turbulence of smaller scales and at higher contraction ratios.

Turbulence length scales increase through the contractions. Large values are observed downstream of contractions with large area ratios. In general, these length scale increases are higher for turbulence of larger scales. This behavior is more systematic for the lateral length scale. However, relative growth between the longitudinal and lateral length scales shows the ratio L_u/L_v at the downstream end of the contraction to decrease with increasing turbulence scales.

CHAPTER VIII

TURBULENCE SCALE EFFECTS

The effects of varying the contraction area ratio on free-stream turbulence with different integral length scales are presented in Chapter VII. In the present chapter, three representative contractions are chosen for investigation of effects of free-stream conditions with a wide range of turbulence scales on the performance of a mild (2:1), a moderate (9:1), and a high (16:1) contraction.

Mild Contraction Ratio

Axial development of streamwise and lateral components of turbulence kinetic energy through a mild contraction are shown in Figures 86 and 87. The streamwise component of turbulent kinetic energy in Figure 86 indicates that for the medium- and large-scale turbulence conditions, decay rates and energy ratios downstream of the contraction are approximately equal. The radial component of turbulence energy for these flow conditions, in Figure 87, reveals that the fluctuation energy remains relatively constant throughout the contracting section. This is brought about because the natural (viscous) decay is offset by the amplification effect of the contraction. Amplification due to contraction and vortex stretching matches viscous decay almost exactly for the large-scale condition T6 starting near the inlet section. For the medium-scale condition T3b, this does not come about until farther downstream into the

contraction. Therefore, the lateral turbulence energy remains relatively constant, although at a different level in the contracting section.

For the fine-scale condition T1, rapid decay of turbulence energy in the axial direction is noted for both the streamwise and radial components through the contraction. This is primarily due to a naturally faster-decaying turbulence condition i.e., more viscous dissipation. The amplification by this mild contraction does not have enough of an effect on the turbulence to sustain or increase the radial component in this small-scale condition. Therefore, viscous dissipation dominates and the v'^2 energy decays through the contraction. Compared to the uncontracted turbulence, it is noted in Figure 55 that during the initial straining of the flow, the streamwise component decays slightly faster. However, at the downstream end, its energy level is approximately equal to that of the unstrained turbulence. This is caused by a relatively slower net decay, as compared to the corresponding unstrained case in Figure 56; i.e., amplification by the contraction is off-setting the viscous decay effect.

Even for this mild 2:1 contraction ratio, present results demonstrate that turbulence characteristics downstream of such a contraction are dependent on the incoming turbulence scales. In view of these results, the discrepancy between the results of Uberoi and Wallis[17] and

Comte-Bellot and Corrsin[19] should not be surprising. While their grids, wind-tunnel size and free-stream velocities were comparable, background turbulence conditions in the two wind tunnels may have contained different characteristic scales; see Loehrke and Nagib[1]. Since they do not have the details for the development of the upstream conditions, we can only speculate regarding this issue.

Moderate Contraction Ratio

With moderate contraction ratios, significant differences in the behavior of turbulence characteristics through a contraction can be discerned when turbulence conditions of various scales are used. A contraction area ratio of 9 is chosen for this study. Total turbulence energy ratio plots through the contraction in Figure 89 indicate that the amount of turbulence-energy increase through the contraction is directly related to the size of the incoming turbulence scales. Large initial turbulence scales produce high levels of total turbulence energy downstream of the contraction; i.e., more net turbulence production.

The streamwise component of turbulence energy is attenuated through the first half of the contracting section. According to linear rapid distortion theories, both classical[24,25] and the recently extended analysis including finite scale effects[26], this enhanced turbulence decay should continue through the whole contraction.

However, experimental results shown on Figure 88 indicate a rise of energy near the downstream end of the contraction. This non-linear increase of u'^2 is attributed to inter-component energy transfer from the radial to the streamwise component. Free-stream turbulence conditions with small-scales show more of this non-linear interaction. Thus, more energy is transferred into the streamwise component by the contraction, resulting in higher u'^2 levels downstream, when small-scale turbulence conditions are utilized. An exception to the above is obtained from flow condition T3b. If the scale trend is consistent, this would have incorrectly implied that T3b has a larger turbulence scale than flow condition T8. However, after a careful examination of the other characteristics of this and other test flow conditions in Figure 36 and 37, it is evident that this non-linear effect also increases with higher incoming free-stream velocity, i.e., higher Reynolds number and shorter transit time. The two trends are acting concurrently and the results are consistent only when both of them are considered.

The degree of turbulence isotropy through the contraction, developed using the various flow conditions shown in Figure 90, indicates that the radial component of fluctuation velocity is influenced by a greater amount relative to the streamwise component as the initial size of the turbulence scales is increased. For all the results shown here, except possibly that of flow condition T8, a

distinct minimum in the u'/v' curves is reached inside the contracting section with subsequent recovery downstream. These plots indicate that the minimum is reached at higher x/L values, i.e., closer to the end of the contracting section, when larger initial turbulence scales are used. The amount of isotropic recovery also decreases for free-stream turbulence of increasing scales. For example, the large-scale flow condition T8 exhibits no appreciable return towards a more isotropic state downstream of the contraction as noted at the farthest downstream position where data were collected. Axial development of turbulence length scales in Figures 91 and 92 reveals that while growth of the lateral length scales through the contractions increases with the size of the initial turbulence scales, the longitudinal scale growth decreases. This trend was observed and discussed in previous chapters. A study of Figures 36 and 37 suggests that the growth in the longitudinal length scales through the contraction is small for turbulence conditions with initially high R_λ.

Figure 93 shows Reynolds stress development for flow conditions with a range of length scales similar to the ones discussed above. Except for the small-scale flow condition T1 and the large-scale condition T7b, the two extremes in initial turbulence scales, the Reynolds stress decays gradually through the contraction. When turbulence conditions of very small- or large-scales are contracted, the magnitude of the Reynolds stress shows an increase with

higher strain, indicating greater turbulence production in the flow through the contraction.

High Contraction Ratio

Unlike the streamwise component of turbulence energy for the moderate contraction, the present results from a contraction with an area ratio of 16, shown in Figure 94, reveal that data from turbulence conditions of different scales do not produce large differences as observed in the previous case. From an earlier result, the increase in energy level downstream of the contraction in the streamwise component was shown to be controlled by the turbulence length scales as well as the upstream velocity. It should be pointed out that flow conditions utilized for this high contraction area ratio study were generated using a small range of free-stream velocity upstream of the contraction. Conclusions drawn in the previous section, concerning the relative levels of u'^2 downstream, were consistent with additional data shown here, i.e., an increase in the upstream turbulence scale size decreases the amount of non-linear energy transfer towards the end of the contraction. However, as discussed in Chapter VII and confirmed with the present data, this non-linear energy transfer to the streamwise component increases with higher contraction area ratios.

The degree of turbulence isotropy and the total turbulence kinetic energy increase are controlled by the

size of the upstream turbulence length scales when the contraction ratio is held constant. Isotropic recovery during the final phase of straining in the contraction is minimal for large-scale turbulence as shown in Figure 95. Comparing Figure 90 to Figure 95 demonstrates that this isotropic recovery is greater for higher contraction ratios.

The total turbulence energy level at the downstream end of the contraction increases with larger scales of upstream turbulence, as noted in Figure 96. By comparing this figure with the results of Figure 89, it is clear that the total turbulence kinetic-energy level downstream of the contracting section also increases at higher contraction ratios.

Integral length scale development through the 16:1 contraction, plotted in Figures 97 and 98 in different flow conditions, indicates that the peak values of the longitudinal scale are approximately equal, while the maximum lateral length scale is higher for initially large-scale turbulence conditions.

The Reynolds stress for flow conditions T4 and T6, plotted in the next figure, increase in magnitude through the contraction. However, these results are shown to have opposite signs. Reasons for such behavior are still unclear at the present time. However, a comparison of Figures 93 and 99 points to the fact that higher stress values are present for a contraction with a higher area ratio.

CHAPTER IX

CONTRACTION LENGTH AND SHAPE EFFECTS

Two other parameters examined in the present experiments are the length-to-inlet diameter ratio and the shape of the contraction contour. For this portion of the experiment, a contraction area ratio of 9:1 was selected for the investigation. Preliminary studies showed that this contraction ratio produces a sufficiently large effect on the turbulence characteristics such that definitive conclusions could be made while alleviating experimental instrumentation difficulties due to an excessive flow velocity range if a higher contraction ratio were used. Many typical applications of contractions also call for contraction area ratios of about 9 or 10.

In a similar experiment, Klein and Ramjee[20] investigated the effects of contraction geometry on non-isotropic free-stream turbulence using two families of contractions with an area ratio of 10 and utilizing one flow condition. Their findings were discussed in the Introduction. The length-to-inlet diameter ratios in that study ranged from 0.5 to 1.5 while the range in the present study is from 0.25 to 1.5. However, the effects of length and shape are studied separately here with the aid of two families of contraction profiles. The present experiment also utilizes upstream flows with both small- and large-scale turbulence conditions.

Length Ratio Effect

Experiments on the effect of contraction length-to-diameter ratio were conducted for matched-cubic contractions with length-to-inlet diameter ratios (L/D) of 0.25, 0.50, 1.0 and 1.5. Corresponding lengths of the nozzles are 3.85, 7.70, 15.4, and 23.1 cm, respectively. The contours are presented in Figure 5.

Streamwise mean velocity profiles through the short, L/D = 0.25 and 0.50 contractions are presented in Figure 100. Figure 112 shows similar profiles for the longer contractions. Only a small difference exists in axial mean velocity profiles between small-scale and large-scale turbulence flow conditions due to slight differences in the boundary layers. The large-scale flow condition T7a produces a slightly higher mean velocity through the contractions than the small-scale condition, except for the L/D = 1 matched-cubic contraction where the reverse is true. This axial profile difference in the streamwise mean velocity is more pronounced and significant only in short contractions. In the long contraction, L/D = 1.5, it is shown, in Figure 112, to be completely negligible.

Due to a high degree of upstream influence of short contractions (L/D = 0.25 and 0.50), mean velocity acceleration through the contracting section is much less than values predicted by geometrical considerations. Streamlines start to show mean flow acceleration far

upstream of the contraction inlet. At the downstream end, flow acceleration is still significant in the constant diameter duct.

When mean velocities at the geometrical inlet and exit sections are used to define an effective or actual contraction ratio, C_a, a value of 5.6 is obtained for the L/D = 0.50 contraction. The very short contraction (L/D = 0.25) has an effective contraction ratio of only 3.3 over its length even though its area ratio is equal to 9. For the L/D = 1 contraction, a C_a value of 7.6 is obtained. The long contraction (L/D = 1.5) exhibits an effective contraction ratio approximately equal to the geometrical ratio because almost all the flow velocity acceleration occurs within the contracting section. Fluid mechanically it is very difficult, if not impossible, to achieve large contraction ratios in a very short axial distance.

Small-scale Incoming Turbulence. Turbulence energy developments through the short contractions for the small-scale flow condition T1 are shown in Figure 101 for the streamwise component and in Figure 103 for the total turbulence kinetic energy. Turbulence at the inlet of the contracting section is affected by the presence of these contractions. Because of this significant upstream influence, little or no decay in the streamwise turbulence energy component is observed within the contraction as shown in Figure 101. As a matter of fact, the minimum in u'^2 for

the very short contraction is reached at the inlet location of the contracting section with the u'^2 turbulence energy showing a subsequent increase downstream, which is in sharp contrast with the predictions of linear theory. The u'^2 energy rise at the outlet of contractions is attributed to a non-linear mechanism of energy transfer from the lateral to the streamwise component. In these short contractions, unavoidable flow separation due to high adverse pressure gradients near the inlet could be contributing significantly to additional turbulence production.

Klein and Ramjee[20] also reported flow separation for their short nozzles, although they chose to believe that these separations had no appreciable effect on the turbulence distributions. These points will be explored in a later chapter. The peak values of u'^2 and q'^2 after the contraction are inversely related to the contraction length as shown by comparisons of Figure 101 with 113 and Figure 103 with 115. When examining the peak values of u'^2 and q'^2, it is interesting to note that for the short contractions, u'^2 peaks are comparatively higher than q'^2 peaks while the opposite is true for the turbulence energy profiles of the longer contractions. It is indicative of a larger increase in the streamwise energy component relative to the radial component for flow through these short contractions. This result is partially due to the selection of the initial reference point and the fact that the mean and turbulence characteristics suffer from an early upstream

effect caused by the presence of these short contractions.

In the present experiments, the upstream reference point is always located at the geometrical inlet to the contraction. Although this choice may not seem to be the most suitable in all situations, practical applications such as the design of compact contractions could benefit from an easy determination of the information concerning the actual flow acceleration achieved in the contracting section, the minimum upstream and downstream distance required for proper operation of such contractions, and changes in the turbulence characteristics due to the straining that occur within the contractions. In previous investigations, the choice of this initial reference point has been quite arbitrary as pointed out by Ramjee and Hussain[23]. This has made consistent, objective interpretations and comparisons between different experiments quite difficult.

The "isotropy" plots in Figure 102 demonstrate only a small decrease of the u'/v' ratio with subsequent recovery, indicating almost perfect isotropy in the velocity fluctuation downstream of the short contractions. This "recovery" is shown in earlier chapters to be a characteristic of small-scale upstream turbulence. A greater amount of u'/v' decrease is shown in Figure 114 for the long contractions. Recovery downstream of the minimum u'/v' point is not as high in these contractions and the most anisotropic turbulence is found downstream of the longest contraction. This is due to the least non-linear

increase of u'^2 during the final phases of straining.

The integral length scale development in Figures 104, 105, 116 and 117 suggest that a slightly larger scale growth through the contractions is associated with long contractions, for both longitudinal and lateral length scales. The length scales typically range from 5 to 7 times the initial scales downstream of the contractions for T1.

Figure 106 exhibits substantial scatter in the Reynolds stress values for the short contractions, especially in the L/D = 0.50 contraction. The curves drawn here merely act as guides through some of the data points. The data in this figure seem to suggest an increase in the magnitude of $\overline{uv}$ with increasing strain for both short contractions. Data from the contraction with an L/D = 0.50 also suggest a sharp increase in the magnitude of the Reynolds stress upstream of the contraction. For longer contractions (L/D = 1 and 1.5), Figure 118 indicates a relaxing of the Reynolds stress through the initial portion of both matched-cubic contractions. As the total strain is further increased, the magnitude of the stress increases again for both contractions, but with opposite signs. Presently such behavior is not fully understood. Near the junction between the contracting section and the constant-area duct, the magnitude of the Reynolds stress increases sharply as turbulence adjusts to the new boundary condition. This sharp increase is even more pronounced for the fifth-order contour contraction. Downstream in the constant-area duct,

the Reynolds stress relaxes and ultimately tends towards a zero value.

Large-scale Incoming Turbulence. Turbulence fluctuation energy and isotropy plots through the different contractions for the large-scale flow condition T7a are shown in Figures 107 to 109 for short contractions and in Figures 119 to 121 for long contractions. When Figures 107 and 119 are compared with Figures 101 and 113 it is apparent that the u'^2 component of turbulence energy of the large-scale turbulence decreases more rapidly during the initial phase of straining, as compared to corresponding values obtained in small-scale turbulence. Non-linear energy transfer to the streamwise component of turbulence energy is also less for initially large-scale turbulence. However, the total fluctuation energy, q'^2, amplifies more through the contraction when large-scale upstream turbulence is utilized, as shown by comparing Figure 103 to 109 for the short contractions and Figure 115 to 121 for the long contractions.

This highly non-isotropic partition of turbulence energy between the streamwise and radial components for this large-scale condition T7a, brought about by contraction, is also reflected in the data on the u'/v' ratio. After straining, the u'/v' ratio shows very little tendency to return to its original upstream distribution. It is instructive to contrast these results with those of the

small-scale condition T1, shown in Figures 102 and 114 for both short and long contractions, respectively.

When these results are compared to rapid distortion theory, data from the large-scale free-stream condition for both short and long contractions compare more favorably with predictions of theory than data from the small-scale turbulence condition, where viscous decay is too rapid for the contraction. If a comparison is made between theory and the results from either the short or the long contractions, the theory is better in predicting the outcome from a long contraction because of the smaller extent of upstream influence due to the pressure gradient brought about by the presence of the contraction and the smaller non-linear effects which occur near the end of the contracting section. In fact, the behavior of turbulence energy within short contractions seems to be completely dominated by this non-linear inter-component transfer. Linear theories[24-27] cannot predict the rise of u'^2 at the downstream end of the contracting section (or almost throughout the very short contraction) because it is governed by a non-linear mechanism. One of the main conclusions of Klein and Ramjee[20], suggesting that the length-to-diameter ratio has no influence on the variation of turbulent kinetic energy and turbulence intensity at the outlet, is refuted by the present results.

Integral scale growths, through different length-to-diameter ratio contractions of longitudinal length

scales, are shown in Figures 110 and 122 for the short and long contractions, respectively. Corresponding lateral length scales are plotted in Figures 111 and 123. They show that the lateral length scales increase more than the longitudinal length scales for flow through the various length-to-diameter ratio contractions when initially large-scale turbulence is utilized. For the small-scale turbulence condition shown in the previous section, approximately equal longitudinal and lateral length scales exist downstream of short contractions, but slightly larger longitudinal length scales are found in the longer contractions. Part of this result is also presented in Chapter VI.

Matched-Cubic versus Fifth-Order

Effects of using large-scale and small-scale upstream turbulence on contractions with different shapes are discussed in the present section. Comparison is made between a matched-cubic and a fifth-order contour nozzle, both with a contraction ratio of 9 and an L/D = 1. These contours are shown in Figure 6. The significant difference between the two is that in addition to requiring a zero slope in the radius function at the inlet and exit sections, the second derivative, i.e. curvature of the radius function with respect to the x-direction, is also zero at both inlet and exit sections for the fifth-order contour. This additional requirement is crucial to theoretical rapid

distortion analyses for obtaining a uniform flow downstream of the contraction when the contour is prescribed as a boundary condition.

For contractions with the same length and contraction area ratio, the absolute value of the maximum slope in the contour, viz. $|dr/dx|$, is greater for a fifth-order contraction. One minor difference between the two contours is the location of the inflection point. For the fifth-order contour, this occurs at an $x/L = 0.50$ while its location for the matched-cubic contour is placed at an $x/L \doteq 0.56$, according to design considerations given by Morel[16]. In view of the shape variations used in other studies[20,21], this difference can be considered miminal. Gross flow features are not expected to be significantly different. However, the object of this experiment is to introduce a different strain history on the turbulence as the flow goes through the contraction and to observe the effects of using both small-scale and large-scale upstream turbulence.

Test Flow Condition: Small-scale Turbulence. Qualitatively, the turbulence kinetic energy and isotropy plots in Figure 113 to 115 show similar behavior in both contractions. The attenuation of u'^2 during the initial area contraction is higher for the fifth-order, but the minimum u'^2 value is reached at slightly smaller x/L value. This minimum value is practically identical for both

contractions. However flow through the matched-cubic contraction may have a slightly higher degree of the subsequent non-linear interaction between turbulence components, which is also shown for the total turbulent kinetic energy in Figure 115. Isotropy plots in Figure 114 show that the decrease in the u'/v' ratio is practically identical down to a minimum value of 0.8. Further straining results in recovery towards a more isotropic state, which occurs sooner in the fifth-order contraction.

Length scale growth through the contractions is similar between the two contraction shapes as demonstrated in Figures 116 and 117. Ultimately similar turbulence scales are reached near the exit of the contracting section. However enhanced growth in turbulence scales resulting from area reduction is noticed at smaller x positions for the fifth-order contraction as a result of the greater amount of area reduction in the central portion of this nozzle.

The Reynolds stress data shown in Figure 118 demonstrate that for the most part it is unaffected by the shape or strain history difference. It is only significant at the junction between the contracting sections and the constant area duct, where a sharp increase in the magnitude of the Reynolds stress is more prominent in the fifth-order contraction as the flow adjusts to the downstream boundary condition.

Test Flow Condition: Large-scale Turbulence. When

results obtained from the large-scale turbulence condition are compared with the corresponding ones from the small-scale condition, some shape effect differences are accentuated while others are diminished. These differences and similarities are noted below.

Figure 119 indicates that during the initial contraction of the flow, attentuation of u'^2 with increasing area reduction is practically identical for the two contraction shapes in this large-scale turbulence. In Figure 113, when the small-scale turbulence condition is utilized, the fifth-order contour data shows a more rapid attenuation in u'^2. Non-linear transfer into u'^2 near the downstream end of the contraction is shown to be substantially less for large-scale turbulence. Relative to results obtained from the matched-cubic contraction, it seems that large-scale turbulence produces a slightly higher u'^2 energy increase at the exit of the fifth-order contraction. The opposite is true if small-scale turbulence is used instead, as noted by an examination of Figure 113.

Typical large-scale turbulence behavior in the isotropy plots is exhibited in Figure 120, where the anisotropic distribution of u' and v' does not show a strong tendency to return towards a more isotropic state during and after the final phase of the contraction process. Differences in the u'/v' ratio between the two contractions are slight and the apparent shift between the two curves is caused by differences in the contraction cross-sectional areas at the

same streamwise position.

The total turbulence kinetic energy in Figure 121 shows a significantly earlier q'^2 increase for the fifth-order contraction with a higher maximum value attained at a smaller x/L. Comparing these results to the ones in the small-scale condition T1, the total turbulence kinetic energy of the contracted flow is approximately twice as high for initially large-scale turbulence. Greater total turbulence energy increases due to the contraction of large-scale upstream turbulence have been demonstrated in earlier chapters to be a direct result of higher turbulence production in the lateral energy component.

Figures 122 and 123, which present the integral length-scale growth through the contractions, reveal an earlier growth in the longitudinal length scale for the fifth-order contraction, which resulted in a slightly larger longitudinal length scale. However lateral scales downstream of the contraction increase to about the same size for both contractions even though the scale growth through the fifth-order contraction starts increasing sooner. Results from large- and small-scale turbulence conditions reveal that the longitudinal length scales increase more than the lateral length scales in small-scale turbulence conditions. The opposite is true when large-scale turbulence conditions are utilized. The result previously established applies equally to both fifth-order and matched-cubic contractions investigated here.

Results presented in this section show that differences in the behavior of turbulence characteristics resulting from these different contraction contours are minor in both small- and large-scale free-stream turbulence conditions. Previous investigators[20,21] studying contour effects reported similar conclusions. However, for effects on the boundary and shear layers, even small differences in the contour shapes produce drastically different results. Therefore, the shape of the contraction should be based mainly on mean flow consideration, i.e. separation in the early part and uniformity of the exit flow. In addition, care must be taken in the design to control the boundary layer growth on the walls, which often leads to anomalous behavior in the shear layers downstream of the contraction. As far as the free-stream turbulence is concerned, the area ratio and the length-to-diameter ratios are the key factors involved, to be discussed in detail in Chapter XIII.

CHAPTER X

OFF-AXIS DATA OF FLOW THROUGH A CONTRACTION

In addition to data that have been collected on-axis and presented thus far, off-axis data were also acquired in the L/D = 1, matched-cubic, 9:1 contraction using three different upstream flow conditions, namely T1, T4, and T7a. These test conditions represent turbulence with small, medium, and large scales, respectively. These measurements are valuable for checking theoretical predictions of turbulence behavior through a contraction away from the axis of symmetry. Review of the literature reveals that heretofore, such data have not been available.

Data acquisition locations are shown in Figure 23. The sensing volume of the X-wire probe was positioned, to simplify the measurements and increase their reliability, at a fixed distance of 2.1 cm off-center and traversed along the length of the contraction. At the downstream end of the contraction, data were also collected for two other off-center positions with the probe sensors located at 1.4 and 0.7 cm off-axis. For reference purposes, data were also collected on the axis of symmetry at the inlet and exit planes of the contracting section. Sample plots showing streamwise and transverse components of turbulence fluctuation energy and integral length scales are presented in Figure 124 through 127. Additional detailed statistics are given in the next chapter. Measured quantities are

compared with the corresponding data that were acquired on the axis of symmetry to assess the influence of the lateral position on the turbulence characteristics for upstream turbulence of different scales.

When the streamwise and radial components of turbulence energy are contrasted against centerline measurements, Figures 124 and 125 show that the axial turbulence energy development off the axis assumed values similar to those recorded along the centerline up to an $x/L \approx 0.8$ except for the streamwise energy component for T4 and T7a which indicate a slight increase. Farther downstream, at an axial position 90% through the length of the contraction, the off-axis turbulence kinetic energy increases rapidly and is significantly higher than the centerline value. At this x/L, the probe sensing volume is located at an off-center position about 78% of the total radial distance between the axis of symmetry and the contraction wall, well away from the boundary layer.

At the exit of the contraction, where data were gathered for additional radial positions, results show that when the off-center distance is reduced to 1.4 cm, i.e., $r/r_c = 0.55$ (symbols with 2 flags), turbulence kinetic energy for both components is not altered from centerline values, except for the streamwise component of the medium-scale T4 and the large-scale T7a conditions which still indicate slightly higher values when compared with on-axis measurements.

The increase in turbulence energy at radial positions relative to results obtained on-axis is predicted by analysis and reported in Goldstein and Durbin[26]. According to theory, this effect should be more pronounced in turbulence conditions with small scales for the normal component and vice versa for the streamwise component. Present results show that this effect is most accentuated for the medium-scale T4 and least pronounced in the small-scale condition T1 for both streamwise and radial components. However, Goldstein and Durbin's analysis[26] was done for asymptotically large two-dimensional contractions with assumed turbulence scales that are much larger than those found in the present experiment.

Evolution of the turbulence length scales both on- and off-axis through the contraction is shown in Figures 126 and 127 for the longitudinal and lateral scales, respectively. No significant differences in the sizes of the length scale between data collected on- and 2.1 cm off-axis are noted for x/L less than 0.8, except for the lateral length scale of the small-scale turbulence condition. Farther downstream, when the flow has traversed through 90% of the contraction's length, L_v for the small-scale flow condition shows a large increase over its on-axis value, while the growth of the longitudinal scale at this location has not been affected by the probe's off-center displacement.

Turbulence conditions with larger length scales show a small deviation between on-and off-axis length scales at

this downstream position. The lateral length scales obtained off-axis at the contraction's exit plane reveal that the highest growth is found for the initially smallest turbulence scales, with the growth decreasing for the larger-scale turbulence conditions. In contrast, when data are collected with the probe centered on the axis of symmetry, initially large-scale turbulence conditions show a higher growth in L_v through the contraction than for small-scale flow conditions. The opposite trend is true for the longitudinal length scales growth as demonstrated previously in Chapter VI. However, off-axis L_u data in Figure 126 show that the smallest growth among the test flow conditions utilized in this part of the investigation is found for the medium-scale T4 flow condition.

A comparison between length scales obtained on- and those recorded off-axis reveals that downstream of the contraction, values of both length scales are larger than the corresponding ones obtained on the centerline. The difference is larger for the L_v scales. From the practical application standpoint, this documentation of turbulence behavior off-axis is valuable in contraction design optimization, where turbulence characteristics are required to be uniform over a large portion of the cross-sectional area in the test section.

CHAPTER XI

SAMPLES OF DETAILED STATISTICAL DATA

The data processing program utilized in the present investigation calculates a number of statistical functions as part of the computations to obtain time-averaged results such as means, variances, integral time and length scales, Reynolds stress, etc. While these time-averaged quantities have been presented and discussed in earlier chapters, this chapter concentrates on exposing and discussing these functions for the reader. Statistical functions such as spectra, cross-spectra, auto- and cross-covariances, coherence, are available at every position where data were acquired. While integrated results such as means and variances are printed out, the detailed statistical functions are recorded on magnetic tape. Consequently, they can be plotted at any future time by appropriate software, either on a drum plotter or on a graphics terminal. Sample plots of these functions are included here to demonstrate the turbulence scale effects, the contraction ratio effects, and to compare some of the resulting statistical functions with the X-probe located either on or off the axis of symmetry for different flows through the contractions.

As an introduction to the functions computed at every position, a set of them obtained from one data file, i.e., at one point for a single case, is presented and discussed first. A total of 742 files were recorded during this

investigation and all their statistical functions are available on 2 magnetic tapes. The set of sample functions are plotted from data obtained in the small-scale flow condition T1 upstream of a contraction, i.e., for homogeneous grid turbulence. Spectra of the streamwise and radial velocity components are shown in Figures 128 and 129, respectively. Note that the amplitude spans almost five decades on these plots and covers a frequency range from below 10 Hz to over 9 kHz. These spectra are very smooth with a resolution of approximtely 9 Hz per point. Four or five narrow-band peaks from above 1 kHz to about 6.5 kHz can be seen in each graph. It was determined that these peaks are the remnants of probe-related vibrations. However, the contribution from these peaks to the fluctuating turbulence energy can be completely neglected without introducing any significant error. For a discussion of the probe vibration problem and attempts at eliminating it, refer to Appendix D.

Figure 130 is a plot of the cross-spectrum function of the uv velocity signal. Notice that the function covers about twice the number of decades present in either the u or v velocity spectrum. This function is not as smooth. As shown on this figure, the plot contains only half of the information required to characterize the cross-spectrum. A phase function associated with it has been computed but is not displayed on this plot because of its highly random nature. Alternatively, the same information can be represented by the co-spectrum and the quad-spectrum. These

were also calculated and again not plotted because of difficulty in plotting them in a meaningful way for typical turbulence data. However, the cross-spectral density function is usually computed as an intermediate step in obtaining other useful functions such as the coherence function, which is a real-valued quantity with a range from 0 to 1.

Significance of the coherence function can be described as follows: When the coherence is zero at a particular frequency, two signals, such as u and v, are said to be incoherent at that frequency or in other words, they are uncorrelated. Conversely, if the coherence function is 1 at some frequency, then the two signals are perfectly correlated, i.e., identical, at that frequency. For the present experiment, the coherence function can be thought of as the correlation between the two components of velocity, u and v, at each particular frequency. Figure 131 demonstrates that except for five peaks related to probe vibration, the u and v velocity signals in homogeneous, nearly isotropic turbulence show very little coherence. High coherence at frequencies related to probe vibrations is evident because "half" of the signal for both u and v comes from the same X-wire sensor. Even though the coherence function emphasizes the effect of probe vibration, the contributions from these peaks to the integrated quantities are very small; e.g., their contribution to the variances, which is proportional to the area under the spectral plots,

is negligibly small.

The autocovariance functions for u and v are shown in Figures 132 and 133, respectively. These two figures demonstrate that a larger time scale is associated with the streamwise component. From results shown in previous chapters, it has been estimated that the streamwise scales are about twice the radial scales, indicating nearly isotropic conditions. After the first decrease of the autocovariance function to zero at small time delays, the autocovariance for the radial component shows a significant dip in the negative direction. This pronounced negative portion is absent from the u autocovariance. This behavior is predicted theoretically from continuity considerations because there should be no net mass flux in the radial direction. It is also reported by experimental investigators using two-point spatial correlation techniques. This provides supporting evidence to the validity of Taylor's hypothesis in homogeneous, nearly isotropic turbulence, where it has been checked satisfactorily. However, for flow through a contraction, validity of Taylor's hypothesis will have to be verified with 2-probe data, which were also acquired during this investigation. The results from those 2-probe measurements will be presented in a future report as an addendum to this work.

Two other functions that were calculated are the uv and vu cross-covariance functions plotted on Figures 134 and

135, respectively. Theoretically, these two functions should look identical for homogeneous and isotropic turbulence, but the plots show significant differences. However, a similarity between them exists especially if the first few peaks after the initial dip in the vu cross-covariance are increased to values above zero. The general characteristic observed in these functions is the presence of large variations at non-zero time delays. Effects of a contraction and other key parameters on some of these statistical functions will be highlighted in the following sections.

The effect of a typical 9:1 contraction on the u and v spectra is demonstrated for small-scale turbulence by comparisons of Figure 128 to Figure 136 and Figure 129 to Figure 138. Two main features are evident. First, downstream of the contraction there is a large relative increase in the energy at high frequencies, particularly above 2.5 kHz. It should be pointed out, however, that the sharp roll-off above 6-7 kHz is due to the effect of anti-aliasing filters. Second, the slope of the spectral decay in the inertial subrange of turbulence energy downstream of the contraction is not as steep in both the streamwise and, in particular, the radial component. A few narrow-band probe-vibration peaks remain visible downstream but they have very small contribution to the energy and are confined to a few specific frequencies.

It has been suggested in earlier chapters that the

increase in u'^2 energy downstream of a contraction is due to a non-linear inter-component energy transfer from the v'^2 component. Strong evidence in favor of such a conjecture can be found by comparing the coherence functions upstream and downstream of the contraction shown in Figures 131 and 140, respectively. Unstrained homogeneous turbulence upstream of the contraction exhibits very little coherence between the streamwise and radial components. Ignoring the narrow-band peaks on Figures 131 and 140, which are related to probe vibration, Figure 140 shows broad-band coherence of the u and v velocities downstream of the contraction. This is undeniable evidence that u'^2 and v'^2 components are related downstream of the contraction and therefore, strongly supports the idea of an inter-component energy transfer concept advanced in earlier chapters. A comparison between Figures 140 and 141 reveals that downstream of a contraction there is somewhat less coherence for initially large-scale than for small-scale turbulence, which is also in agreement with results presented in earlier chapters.

Turbulence-scale Effects

Having documented important gross effects of initial turbulence scales on flow through contractions, it is interesting and instructive to show how initial turbulence scales affect some of the detailed statistical functions. Spectra of u and v downstream of a contraction for initially small and large scale turbulence are shown in Figures 136

through 139. These figures indicate that spectral decay of both u and v for incoming large-scale turbulence downstream of a contraction is lower than for small-scale turbulence but the energy roll-off occurs at a lower frequency.

It was noted earlier that the coherence between u and v downstream of a contraction is higher for small-scale turbulence rather than large-scale turbulence due to more inter-component energy transfer. This is evident in the plots on Figures 140 and 141 for initially small-scale and large-scale turbulence, respectively. Figures 142 and 143 demonstrate typical cross-covariance functions for small- and large-scale turbulence flow conditions downstream of a contraction. A persistent turbulence interaction between velocity components downstream of a contraction not found in unstrained homogeneous isotropic turbulence can be inferred from these two plots. The periodic high frequency undulations in Figure 142 are probe related and not an artifact associated with turbulence in the flow.

Contraction Ratio Effects

Effects of varying the area ratio for flow through a contraction are demonstrated through spectra and coherence functions for a medium-scale turbulence condition in Figures 144 through 149. Examination of the velocity spectra reveals that when the contraction ratio is increased from 4 to 16, a substantial increase in the turbulence energy at frequencies above 700 or 800 Hz is evident. This high

frequency energy increase occurs in both streamwise and radial components of turbulence fluctuations. However, this evidence of "new" turbulence is stronger in the u component. At frequencies below 800 Hz, the corresponding spectral distributions of the mild and high contractions are virtually identical. At frequencies above 7 kHz, the sharp spectral roll-off is a result of the anti-aliasing filters' settings. Narrow-band peaks in the spectral and the coherence functions are associated with minute probe vibration but they do not contribute significantly to the turbulence energy. A detailed documentation of the problem and its solution is given in Appendix D.

It was documented in earlier chapters that for a given flow condition, as the contraction ratio is increased, the streamwise component of turbulence energy, which should decrease according to rapid distortion theory, increases instead. An explanation which involves non-linear inter-component energy transfer from the radial to the streamwise component is further supported by plots of coherence function in Figures 148 and 149. With an increase in the contraction ratio, coherence between u and v increases. For the 4:1 contraction, there appears to be very small coherence at the exit, indicating very small influence by the inter-component transfer. This is supported by the results of earlier chapters on the streamwise energy development. This evidence proves that a relationship between the two components definitely exists

downstream of a highly contracted flow since homogeneous, isotropic turbulence does not show such high coherence values. As a reminder, the isolated narrow peaks on these two figures are identified with probe vibration and should be ignored.

Statistical Data On- and Off-Axis

Turbulence kinetic energy ratios obtained on- and off-axis are compared in Chapter X. Towards the downstream end of the contraction, significant differences in turbulence energy ratios are demonstrated. In this section, a sample of statistical functions obtained near the downstream end of a 9:1 contraction both on- and off-axis are presented to provide additional insight into the previous results. The medium-scale free-stream condition was chosen and off-axis data were acquired at a radial position r/r_c=0.78.

A comparison of u and v velocity spectra, shown in Figures 150 through 153, indicates that the slope of spectral decay during the inertial subrange in both velocity components is significantly lower for data collected off-axis. In the low frequency region, i.e., up to 400 Hz for u and 500 Hz for v, the velocity spectra show no appreciable difference whether data were collected on or off the axis of symmetry. Therefore, the turbulence measured off-axis has relatively more energy at high frequencies in both u and v. A plot of the uv cross-spectrum using

off-axis data is also shown in Figure 156. The coherence functions of Figures 154 and 155 also indicate that the streamwise and radial velocity components are more interrelated at positions away from the axis of symmetry.

A very interesting feature is revealed when the on-axis and off-axis uv cross-covariance plots are compared in Figures 157 and 158. The on-axis cross-covariance function infers a persistent u-v interrelated turbulence structure typical of turbulence immediately downstream of a contraction, as demonstrated in Figures 142 and 143. By contrast, the off-axis cross-covariance of Figure 158 suggest a non-persistent turbulence structure. Also note that the zero time delay correlation, i.e. Reynolds stress, for the off-axis data is an order of magnitude larger than that for the on-axis data. From these two figures, the predominant turbulence scales implied by these cross-covariance functions are about the same regardless of whether data were collected on or off the axis of symmetry but the persistence characteristics are dramatically different.

An important difference betwen the on- and off-axis conditions is related to the orientation of the principal stress axes. While the axes are aligned in the u and v directions on the centerline, away from the axis of symmetry they are not. This difference can be used to explain many of the phenomena observed here. The reader is referred to the recent paper by Goldstein and Durbin[26] for a more

detailed discussion of this and some theoretical predictions related to it.

CHAPTER XII

ATTEMPTS AT NORMALIZING THE DATA

Results presented in Chapters VI through IX emphasize specific effects, treating other independent variables involved in the experiment as parameters. Diversity of these outcomes was clearly demonstrated in those chapters. Although each effect was clearly identified when all other parameters involved were held constant, results taken collectively were quite difficult to comprehend because the effects were interrelated. In an effort to consolidate the outcome of these different effects, thus extending the usefulness of the results by reducing the complexity in data interpretation and at the same time trying to gain better insight into the physical phenomena, attempts were made to regress the data using simple yet rational normalizations. Occasionally, these attempts were guided by theoretical considerations but often they were based on simple empirical correlations. The modest but gratifying outcome of these attempts is outlined in this chapter.

An important assumption made in the derivation of rapid distortion theories, whether classical[24,25] or extended[26,27], is the ignoring of viscous dissipation in the flow. Conceptually, this assumption is valid only if the distortion occurs very rapidly such that the characteristic time scale of viscous decay is much greater than the time scale of the flow distortion imposed by

geometry. Batchelor and Proudman[24] pointed out that in most experiments conducted on flow distortions and contractions, straining is not sufficiently rapid for this linear theory to hold. Experimental investigations[20-23] have shown that predictions of the turbulence kinetic energy development through a contraction by rapid distortion theory are in fact inaccurate and thus quickly dismissed further considerations into its usefulness. Although inherent deficiencies of this linear theory are apparent, it is possible to obtain useful predictions if some of the analytical assumptions violated in experiments, e.g., the viscous decay, could be properly compensated in the experimental results through a better understanding of the turbulence mechanisms involved. Comparison with theory can lead to better assessment of the importance of other mechanisms and terms in the governing equations, such as the non-linear terms.

To the best of our knowledge, no correction for viscous dissipation had ever been attempted by previous experimental investigators of contracting flows. Some attempts to include viscous decay were made in recent extensions of the theory. Although test flow conditions were thought to be similar among different investigators, documentation of these flow conditions was usually limited, at best, to mean velocity and turbulence intensity profiles, which are shown to be insufficient in uniquely characterizing the free-stream condition. Differences in turbulence scales and

decay rates could have existed, therefore the widespread disagreement among experimental investigators that has been noted in "nominally" similar experiments should not be totally surprising. This also led to poor agreement between theoretical predictions and experimental results.

The present experiment, for the first time, attempts to correct for the effect of viscous decay by obtaining turbulence data in a non-contracting duct and using these results as reference conditions when studying the effects of contractions. This will provide at least a first-order dissipation correction for test flow conditions with different turbulence decay rates. The success of this scheme depends on two important factors; that is, the turbulence decay or dissipation rate must not vary significantly with the convection velocity and it must also be somewhat insensitive to the strain rate. Results presented in Chapters V and VI indicate that the first of the above requirements is generally met in the present experiment. However, possible exceptions will be noted in the discussion. Very complex measurements, assumptions and calculations are required to verify the second of the above requirements. In any case, it is expected that the outcome of the following will be very instructive.

Thus, viscous decay correction requires that the turbulence energy ratios of both radial and streamwise components through the contractions be normalized by the corresponding quantities at the same streamwise positions

using the same initial flow condition but with the flow unstrained. These results are presented in the following sections. The symbols used in the figures of this and following chapters are consistent with the keys given in Figures 3 and 36, depending on the parameter being held constant, i.e., initial condition or contraction, respectively.

Normalizing the Radial Component

A first attempt at normalizing the radial component of turbulence energy is shown in Figure 159, where the results utilizing "fixed" incoming turbulence scales, namely flow condition T7a, are plotted for all contractions. The ordinate of this graph shows the non-dimensional radial component of turbulence kinetic energy through the contractions, $v'^2/v_i'^2$, normalized by its value at the same axial position through a constant-area (c=1) duct. This normalization compensates for the effect of viscous dissipation such that, if the evolution of $v'^2/v_i'^2$ through a contraction is the same as for a uniform cross-sectional area duct, the value of this normalized ordinate would have been unity, thus, indicating that the contraction has no effect on this component of turbulence kinetic energy. However, deviation from unity in this plot indicates a contraction effect over and above the effect of "natural" viscous decay.

The parameter used in the abscissa can be broken up

into two groups each relating to a different physical effect encountered by the flow. The first quantity, $(\bar{U}(x)/\bar{U}_i - 1)$, is the total axial strain the fluid has experienced from a reference point x = 0 to any point x. The amount of straining is referenced to the condition at point i, the inlet location. The second quantity which is the geometrical contraction area ratio (raised to an empirically determined one-third power) accounts for the pressure field and resulting mean flow effects due to the presence of a contraction with an area ratio of c.

The resulting graph shows an excellent collapse of the data points onto a straight line with a positive slope. It indicates that the corrected radial component of turbulence energy increases linearly with the total amount of strain through a given contraction. The data plotted here include the 9:1 contractions with various L/D's, ranging from the very short L/D = 0.25 to the long L/D = 1.5 contractions, and the fifth-order contour contraction, as well as contractions with area ratios ranging from 2:1 to 36:1. The data correlation demonstrates that normalization in this manner can practically account for all the variations encountered in the radial component of turbulence kinetic energy for a given initial flow condition. This evidence strongly suggests that within the limits of accuracy shown by the present data, v'^2 is insensitive to the strain rate and strain history, but is a linear function of the total integrated axial strain and has a weak one-third power

relation with the contraction area ratio, i.e., pressure field.

Generalizing the plot to include data from turbulence conditions having different initial scales, an additional factor, $(Lv_i/D_i)^{1/3}$, relating effects of turbulence scales relative to a characteristic dimension of the experimental apparatus, is added to the parameter in the abscissa. This correlation is first limited to conditions tested through a single contraction. The results showing variation of the lateral component of turbulence kinetic energy through a 9:1 contraction for incoming turbulence of different scales are plotted in Figure 160. To demonstrate the implications of this result, the following examples are given. First, as in Figure 159, when a particular contraction ratio and an initial turbulence condition are chosen, the corrected radial component of turbulence energy varies linearly with the amount of axial strain. Equivalently, for a chosen contraction ratio and total strain, the radial turbulence energy increases linearly with the relative initial lateral scale raised to the empirically determined one-third power.

By including data from all contractions and flow conditions used in the present investigation (a total of approximately 200 points), the resulting plot on Figure 161 is produced. The parameters on the horizontal and vertical axes are identical to corresponding ones on Figure 160. The regression of the data onto a straight line is simply remarkable considering the diversity of conditions and

contractions utilized. Therefore, with these results we are able to provide an explanation of how the radial component of turbulence kinetic energy of the flow subjected to a contraction behaves when different scales of turbulence as well as different contraction area and length ratios are used.

Normalizing the Streamwise Component

The streamwise component of turbulence kinetic energy ratio, corrected for viscous decay by the method discussed in the previous section, is plotted in Figure 162 as a function of the total strain for all contractions utilizing flow condition T7a. Except for the short contractions (L/D<1), data points for the streamwise turbulence energy are shown to collapse on a single curve. The streamwise turbulence energy decreases slightly during the initial flow contraction, reaching a minimum at a total axial strain of about 4, after which it then rises with increased straining.

Solid symbols, showing data from the fifth-order contraction in Figure 162, also follow the above trend indicating insensitivity to small differences in the strain history between its contour and that of the matched-cubic contractions. Depending on the amount of strain, the streamwise component of turbulence energy can be three to four times the unstrained value. This energy rise downstream of the minimum is attributed to non-linear inter-component energy transfer mechanisms since the linear

rapid distortion theories[24-27] only predict monotonically decreasing streamwise energy level with increasing flow contraction. The comparison with theory is now more valid and valuable after application of a first-order correction for viscous decay to the experimental results.

For short (L/D<1) contractions, the streamwise component of turbulence energy attains higher values than longer contractions when subjected to the "same" amount of strain. As demonstrated by the flagged symbols on Figure 162 for the L/D = 0.50 and 0.25 contractions, the shorter the length ratio of the contraction, the more pronounced the effect. This is due primarily to the large upstream effect of these short contractions and the choice of initial reference point. For these contractions the flow has been significantly accelerated by the time it passes the geometrical inlet section which is chosen as the initial reference point. In this situation the total amount of strain experienced by the fluid is greater than values indicated on Figure 162. However, the value shown in Figure 162 represents the additional strain that takes place inside the contracting section, starting at the inlet. Accounting for the upstream strain, a difficult task in many practical cases, could account for the non-collapse of the data from L/D<1 on the same correlation curve in Figure 162.

If no appreciable upstream influence occurs, such as for long contractions, then the straining which takes place inside the contraction is also the total axial strain

experienced by the fluid. The convention for the location of the initial reference point adopted in the present experiment is a consistent one and is useful in determining the actual amount of flow acceleration through the contracting section. The choice of the initial point has been quite arbitrary in most previous experimental investigations[22,23] making objective comparisons between results from different researchers rather difficult. In principle, the present data can be reprocessed using a criterion of the initiation of strain to detect the fluid mechanical initial position, e.g. see the discussion in Loehrke and Nagib[1].

To generalize the plot of Figure 162 so that data from all the flow conditions can be included, a parameter which accounts for the effects of different turbulence scales is introduced in the form of a turbulence energy decay slope of the unstrained flow condition. This quantity, $\partial/\partial x(\bar{U}/u')^2\Big|_{c=1}$, can be shown to be inversely proportional to the integral length scale L_{v_i} by comparing tabulated L_{v_i} data in Figure 37 with the results on Figure 24. Thus, the effect of initial scales on turbulence kinetic energy is very relevant. The turbulence length scales are normalized by a characteristic dimension of the experimental set-up, e.g., test section diameter D_i. The test condition decay slope is introduced into the correlation through a quantity analogous and proportional to the square root of D_i/L_{v_i}.

To reconcile data that exhibit considerable upstream

influence, i.e., acquired in short contractions, terms containing length-to-diameter ratios are applied to both the ordinate and abscissa of Figure 163. This normalized plot for the general case includes over 200 points and represents the evolution of the viscous-decay corrected streamwise component of turbulence energy during the straining process for all contractions and all flow conditions utilized in this experiment.

During the initial straining, there is a small decrease in the streamwise turbulence energy component, but with continued straining, this turbulence energy increases rapidly. The decrease is predicted by the rapid distortion theory through vortex stretching and tilting mechanisms, but the increase is attributed to turbulence production and inter-component transfer caused by non-linear effects that are not accounted for in any theory to date. By examining the effects of individual parmeters, we have a better understanding of turbulence behavior under strain. As an example, if a particular free-stream condition is chosen, i.e., for a known relative turbulence scale and therefore a fixed value of $\{D_i \; \partial/\partial x(\bar{U}/u')^2|_{c=1}\}^{1/2}$, the u'^2 turbulence energy first decreases slightly, attains a shallow minimum, and rises rapidly with increasing strain. Now, for a given amount of strain, i.e., setting $(\bar{U}(x)/\bar{U}_i - 1)$ at some required value, it may then be possible to select upstream free-stream flow conditions that produce the lowest streamwise turbulence energy. Depending

on the amount of strain, there is an optimum range of initial turbulence scales which would yield low u'^2 values. This minimum corresponds to a total strain less than that leading to inter-component transfer. The smaller the initial scale, the faster its decay and the smaller the total strain, i.e., contraction ratio, that leads to maximum turbulence reduction.

For a constant strain value, increasing the relative incoming turbulence scales, in Figure 163, shifts the parameter on the abscissa to the left and vice versa. Because of the steep rise of u'^2 towards the right of the optimum range, it is therefore better to have larger-scale freestream conditions if the objective is to reduce the streamwise component of turbulence energy as much as possible by substantial flow contraction. This is a concept which is somewhat related to the "blocking" effect of Goldstein and Durbin[26].

As shown by the solid symbols in Figure 163, only the data from T1, a flow condition with very fine scales, show significant departure from the trend discussed above. The initial drop in u'^2 with increasing strain is absent and its rise at high strain values is lower than for other conditions. In general, this fine-scale turbulence seems to be less affected by the contraction process.

The ability to summarize results obtained from a diverse set of turbulence flow conditions for a wide range of contraction parameters provides us with a comprehensive

overall view of turbulence behavior under strain. It is a key to a better understanding of the turbulence mechanisms that are important during the contraction process. This chapter demonstrates the use of simple yet physically relevant parameters to normalize the streamwise and radial turbulence kinetic energy components of all the data from the present investigation in order to provide a unified explanation of turbulence behavior under axisymmetric contraction.

CHAPTER XIII

DISCUSSION AND SUMMARY RESULTS

Details of flow through contractions have been documented in previous chapters. In Chapter XII, attempts were made to normalize the streamwise and radial components of turbulence kinetic energy using simple yet physically relevant parameters. These attempts met with a high degree of success, enhancing our understanding of the role various parameters play in determining the behavior of turbulence through a contraction. The important question of how the performance of contractions is affected by different design parameters and by incoming turbulence scales will be discussed in the present chapter. A simple yet effective correction for viscous dissipation is applied to the results to improve the correlation between experimental results and theory. Comparisons to predictions of classical rapid distortion theory[24,25] and to pure vortex stretching[37] will be made to show when non-linear effects cannot be neglected. Finally, for scientists and engineers who will use these results as a guide in designing high performance contractions, simple empirical relations are suggested. The symbols used in the figures of this and the previous chapter are consistent with the keys given in Figures 3 and 36, depending on the parameter being held constant, i.e. initial condition or contraction, respectively.

Turbulence Reduction Efficiency of Contractions

The primary use of contractions in wind tunnels is to reduce the relative turbulence intensity of the free-stream flow entering the test section. Numerous investigations have been conducted in the past detailing design and construction of wind tunnel contractions. Most of these investigations were initiated because of specific needs for specialized wind tunnel contractions. Results from these studies are not sufficiently general due to cumbersome and involved analytical design methods. Many of these approaches are also inaccurate in predicting turbulence behavior in actual contractions primarily because of the lack of accurate contracting turbulence data that can be used in the design of high performance contractions.

As discussed in the Introduction, there have been some recent attempts[20-23] at studying behavior of turbulence under contraction by systematically investigating relevant physical parameters such as the contraction area ratio, the length-to-diameter ratio, and the contraction contour shape. A few of them[17,19,23] included some form of free-stream turbulence variation, i.e. sensitivity to upstream conditions. However to date, no single investigation on turbulence through contractions has included the number and range of parameters utilized in the present experimental study. Of particular importance here is the scope and experimental rigor of the systematic probing of effects of initial turbulence scales on the performance of

contractions. These results will certainly shed light on the effectiveness of proposed solutions to unresolved problems of the documented differences in noise data between in-flight measurements and static ground tests. Some details of these problems were presented in the Introduction.

Length-to-Diameter Ratio Effects. An important criterion in judging the performance of a wind tunnel contraction is its ability to reduce the relative turbulence intensity of the free-stream. Turbulence reduction efficiency, defined as turbulence intensity at the exit of the contraction divided by its value at the inlet, is a quantitative measure of contraction performance as a turbulence reduction device. Precise definitions of turbulence reduction efficiencies for the different components and the total rms of turbulence are given in the List of Symbols. In general, smaller η values represent greater turbulence reduction through the contraction and thus higher contraction performance.

For this study of length-to-diameter ratio effects, contractions with an area ratio of 9:1 and L/D_i ratios ranging from 0.25 to 1.50 were used. Turbulence reduction efficiencies of the streamwise and radial components, η_u and η_v respectively, are plotted as a function of length ratios in Figures 164 and 165. The turbulence reduction efficiency is improved substantially when the ratio of length-to-inlet diameter of the contractions is increased

from 0.25 to 1.00. Additional performance improvement are reduced as the length ratio is further increased. Only a small incremental gain is achieved by increasing the length ratio from 1.00 to 1.50.

Another important performance criterion is the uniformity of mean velocity downstream of the contraction. For most wind tunnels, it is highly desirable to have the flow entering the test section with a uniform mean velocity profile in addition to low turbulence intensities. It is shown in Chapter III, Figure 16, that lateral profiles of the streamwise mean velocity immediately downstream of contractions are more uniform for contractions with longer length-to-diameter ratios. Whether this small increase in turbulence reduction performance and an improved mean velocity uniformity, obtained by using a very long contraction (L/D_i = 1.50), is justified by having to deal with the higher cost of fabrication, additional space requirements and the existence of a slightly thicker exit boundary layer will depend upon each particular application.

Turbulence scales of the incoming flow also play an important role in the turbulence intensity reduction capability of contractions. Figure 164 shows that for the streamwise component, initially large-scale turbulence is reduced by a slightly greater amount than small-scale turbulence. However, the opposite is true for the radial component of turbulence intensity plotted in Figure 165. Symbols identifying the test flow conditions in these two

figures are defined in Figure 36. Comparison between Figures 164 and 165 indicates that there is greater sensitivity to the variation of incoming turbulence scales in the radial turbulence reduction efficiency. This is demonstrated in axial plots of turbulence kinetic energy development through contractions in Chapter VIII. From these results, it is shown that maximum turbulence intensity reduction in the radial component is achieved by using flow conditions with small-scale turbulence. As demonstrated in Figure 89, total turbulence energy production will also be minimized for free-stream flow conditions with small scales.

Area Ratio Effects. Perhaps the most important physical parameter in controlling turbulence intensity reduction of flow through contractions is the contraction area ratio. Plots of η_u and η_v for different contractions and data obtained from uncontracted flows are shown as a function of the effective contraction ratio, $C_a = \overline{U}_e/\overline{U}_i$ in Figures 166 and 167, respectively. It is very evident that as the contraction ratio increases, both η_u and η_v are decreased, indicating higher reduction in the relative turbulence intensity of the incoming flow at the exit of the contraction. A fair amount of scatter is seen in data taken from various test flow conditions. Therefore, by using different free-stream conditions, varying amounts of turbulence intensity attenuation through the same contraction can be realized. This sensitivity manifests

itself more prominently in the radial turbulence component (Figure 167) than in the streamwise component (Figure 166).

A crude estimate of the turbulence levels for flows subjected to a contraction can be made by considering simple vortex stretching of vorticity components[37] initially aligned with, and perpendicular to the mean flow. Applying conservation of mass and angular momentum, it can be shown that $\eta_u = 1/c^2$ and $\eta_v = 1/\sqrt{c}$. These curves are shown in Figures 166 and 167 along with those obtained from classical rapid distortion theory[24,25] and some empirical fits through the data. The main mechanism incorporated in rapid distortion theory over simple vortex stretching, is the tilting of the vortices by the mean flow and the resulting transfer of energy, which is a linear effect and syphons energy mainly to the streamwise velocity fluctuations from the transverse ones.

Calculated η_u from vortex-stretching considerations alone decreases very rapidly and is below the experimental values for contraction ratios greater than about 2. It grossly over-predicts streamwise turbulence attenuation. On the other hand, the radial component of turbulence intensity reduction η_v decreases very slowly with increasing contraction ratio according to this simple model, thus substantially under-predicting turbulence attenuation. Experimental data in Figure 167 show much lower η_v values at corresponding contraction ratios. The poor correlation between experimental data and this simple estimate[37] is

due to the fact that no mean flow or turbulence considerations were utilized in the analysis to predict turbulence intensities downstream of contracted flows.

Comparison with Classical Rapid Distortion Theory. A more sophisticated model that has been used in predicting the turbulence characteristics downstream of flow contractions is the classical rapid distortion theory of Batchelor and Proudman[24] and Ribner and Tucker[25]. This theory was developed for homogeneous, initially isotropic, low level, and asymptotically small-scale turbulence through a contraction or flow distortion. In order to complete their analysis[24,25], non-linear effects and viscous dissipation were neglected. The viscous effects were assumed negligible by omitting turbulence dissipation and asserting that the time scale of the mean flow variation is much smaller than that of turbulence, so that viscous interactions could also be neglected; hence the name "rapid distortion" theory. Results predicted by this asymptotic theory are shown by the solid curves in Figures 166 through 173.

Comparison of experimental data with theory shows that for contraction ratios greater than about 4, η_u predicted by theory is below experimental values. The discrepancy increases at higher contraction ratios because theoretical values become vanishingly small, viz. $\eta_u = \{.75c^{-4}[\log 4c^3 - 1]\}^{0.5}$ while experimentally, very small decreases in η_u are

associated with increasing the contraction ratio beyond approximately 10. These discrepancies occur because crucial assumptions made in the derivation of rapid distortion theory are not applicable to actual flow situations. However, as demonstrated in Chapter XII, it is possible to compensate for some effects by applying a simple first-order correction and/or using flow conditions with different characteristic turbulence scales, thereby, rendering better correlations between experiment and theory.

Comparison with the extended rapid distortion theory of Goldstein and Durbin[26] is not presented here because the analysis was done for a two-dimensional rather than axisymmetric contraction. It would be interesting to do a similar analysis for the axisymmetric case for direct comparison with the present experiment. Such an analysis is well on its way at I.I.T.

A First-Order Correction for Viscous Dissipation

It is evident from an examination of the experimental values of η_u and η_v for the constant-area duct in Figures 166 and 167, that "natural" viscous dissipation effects cannot be ignored when comparing the experimental results to theory. Actual flow conditions vary in their turbulence decay characteristics, which must be accounted for if reasonable agreement between experiment and theory is to be expected.

A simple first-order correction is applied to

compensate for viscous dissipation effects in the turbulence energy ratios with a high degree of success in the normalizations of data presented Chapter XII. A similar correction, based on the same arguments, can also be applied here to remove effects of different viscous decay rates from various flow conditions, thus establishing a common reference for the turbulence reduction efficiency at c=1. To accomplish this, all η_u and η_v values through contractions are normalized with the corresponding values of the same flow condition through a c=1 contraction (i.e. constant-area duct), thus defining the dissipation-corrected values as $\bar{\eta}_u = \eta_u/\eta_u|_{c=1}$ and $\bar{\eta}_v = \eta_v/\eta_v|_{c=1}$. The validity of such a correction hinges upon two implied assumptions; namely, turbulence decay rates are insensitive to changes in either the mean convection velocity or the strain rate. For the present experiment, these assumptions appear to be valid, except possibly for the short (L/D<1) contractions. In fact, the first of these two assumption is verified by the measurements of Chapter V where the decay of the test flow conditions appears to be insensitive to the free-stream velocity for the various grids; see next to last column in Figure 37.

Viscous-dissipation corrected results are shown on Figures 168 and 169 for the streamwise and radial components, respectively. It does not appear that this dissipation correction improves the agreement between theory[24,25] and the experimental streamwise turbulence

reduction efficiency. However, differences in the "natural" turbulence decay rates of various flow conditions have been removed and a more consistent picture emerges. Figure 168 shows that as the flow is contracted, η_u decreases but experimental values are always greater than predictions of rapid distortion theory[24,25]. This implies the presence of "extra" turbulence not accounted for by the theory.

It was shown previously that the excess of u' is a result of non-linear inter-component energy transfer from the radial component. As the flow is contracted, the radial component of turbulence energy increases relative to the streamwise component. This leads to inter-component energy transfer through the pressure strain terms causing some of the radial turbulence energy to "leak" into the streamwise turbulence energy. The radial turbulence intensity will be slightly lower but the streamwise turbulence intensity will be higher than predicted values because such non-linear energy transfer is not taken into consideration by linear rapid distortion theory. Experimental data in Figures 168 and 169 seem to support the argument given above.

In addition to the inter-component transfer through pressure strain terms, the continued increase in v' and decrease in u', as the flow is strained through the contraction, leads to new turbulence production. This production comes through the terms $(v'^2-u'^2)\,\partial U/\partial x$ in the turbulence energy equation. Therefore, not only the increased anisotropy of turbulence contributes to it but

also the larger local strain rate. This production mechanism does not require any shear in the flow. Off the centerline of the contraction, additional production is probably going on through shear controlled terms like $\overline{uv}\ \partial U/\partial y$. The radial gradient in mean velocity away from the centerline is substantial, in particular, in the middle part of the contraction. The added turbulence production off-axis is reflected in the turbulence energy data of Chapter X and in the spectra of Chapter XI.

For the radial turbulence intensity reduction, applying the viscous decay correction does a remarkable job of bringing experimental values to closer agreement with predictions of rapid distortion theory. The only exceptions are results obtained from short, L/D_i = 0.25 and 0.50, contractions as demonstrated on Figure 169. Many investigators in the past have uncorrectly assumed that short, i.e. non-gentle, contractions represent "rapid" distortion. In fact the rapidity of the distortion depends more on the scales of the initial turbulence with respect to the size of the contraction. A combination of large upstream effects exhibited by these short contractions and the adopted convention for defining the initial and exit locations, render these results uncorrectable with the present scheme. If the definitions of the initial and exit locations are such that the total contraction influence is included, a better agreement will result but the points so chosen would be quite arbitrary and highly dependent on

contraction shapes.

These results strongly suggest that in order to compare experiment and rapid distortion theory, viscous dissipation cannot be simply neglected as was done in previous experiments on contractions. When viscous dissipation is accounted for by the present scheme, the radial turbulence intensity reduction efficiency data agreed remarkably well with theory except when short contractions were utilized. Application of this correction also offers a plausible explanation for the observed behavior of streamwise turbulence intensity reduction efficiency even though dissipation-corrected experimental results are not brought closer to agreement with theory.

Turbulence Energy Ratio of Contractions

Although relative turbulence intensity considerations are more appropriate for performance evaluation of contractions in practical applications, traditionally, contraction turbulence data are often plotted up as turbulence energy ratios especially for comparison with theory. These ratios are not weighted by any variation in mean velocity through the contraction.

Area Ratio Effects. The data of Figures 166 and 167 are replotted as longitudinal and lateral components of turbulence kinetic energy ratios in Figures 170 and 171, respectively. The longitudinal turbulence energy ratio in Figure 170 shows a slight decrease as the contraction ratio

is increased for mild contractions. Contractions with area ratios greater than approximately 5 show sharp turbulence energy ratio increases with higher area ratios, though theory predicts a monotonic decrease. This radical departure from theory is also shown by all similar previous experimental investigations[20,21,23]. However, no explanation was attempted in those reports except to note the importance of non-linear effects in "large" contractions. Present findings strongly suggest a specific non-linear inter-component transfer mechanism which "feeds" energy to the streamwise component from the radial component, causing μ_u to rise with increasing contraction ratios.

The radial turbulence kinetic energy ratio obtained experimentally follows the same trend predicted by rapid distortion theory, although the magnitude of turbulence energy rise at increasing contraction ratios is not as high as theory predicts. This behavior has also been observed by other investigators[20-22]. For example, Hussain and Ramjee[21] reported that theory over predicts this energy rise by as much as 100%.

Present findings in Figures 171 and 172 show that initial turbulence scales play an important role in determining the amount of energy increase in the radial component. After correcting for viscous decay, initially large-scale turbulence shows closer agreement with rapid distortion theory than small-scale turbulence. This is

expected and can be visualized as follows. One crucial assumption made in the derivation of rapid distortion theory[24,25] presumes that the time-scale of turbulence is large compared to the time-scale imposed by the geometrical distortion. Therefore, for a given time scale in the distortion, e.g. t-t', turbulence has a greater effect in distorting (or deforming) the smaller eddies than the larger ones relative to a reference configuration at time t. For example, in a given flow contraction situation, larger eddies will be deformed to a lesser degree than the smaller eddies. Thus, it will appear that the distortion took place more rapidly for the larger eddies than for smaller eddies. Rapid distortion theory should appear to be more applicable to large-scale turbulence than to small-scale turbulence in terms of predicting the behavior of turbulence energy components, even though small-scale assumptions were used in the derivation. This argument is supported by the present data. However, the total turbulence kinetic energy ratio on Figure 173 suggests that turbulence energy production in the flow through contractions is relatively independent of the initial turbulence scales. Therefore, only the distribution among the components is highly influenced by the different initial scales. All results presented thus far strongly support the inter-component energy transfer concept suggested in earlier discussions.

As pointed out earlier, when a first-order correction for viscous dissipation is employed, the linear rapid

distortion theory correctly predicts the behavior of the streamwise turbulence energy ratio for contractions of area ratios less than five. A similar conclusion can be made based on Figure 172 for the radial component. Therefore, the theory appears to be adequate for predicting the behavior of turbulence in mild contractions with c<5, since the viscous decay rate of turbulence required for our first-order correction is well-established empirically. In addition, the deviation for c>5 from the theory appears to be consistent with earlier comments on inter-component transfer through the pressure strain terms. As one would expect, the linear theory does not account for this mechanism correctly by underpredicting the streamwise component and overpredicting the radial velocity fluctuations.

In Figure 173, the simple vortex-stretching and the linear rapid-distortion theories are compared to all experimental results after they have been corrected for "simple" viscous dissipation. The linear theory appears to correctly predict the total turbulence production for mild contractions, c<5, and overpredicts the increase in turbulence energy for large contractions, i.e. c>10. Earlier in this chapter mechanisms for transfer of energy from the mean flow to the turbulence and from one component to the other have been discussed. From this figure it appears that the first of these, which is based on non-linear interaction, is either negligible or

non-existent. Evidence to this appears also in the discussion of the spectra and coherence functions in Chapter XI. Transfer of energy from the mean flow to turbulence occurs usually at the large scale eddies, i.e. low frequencies. The change in spectra in the downstream part of the contraction appears as an increase in the high frequency range and is accompanied by high coherence between u and v at the same frequencies. This is in support of the inter-component non-linear transfer mechanism.

To explain the overprediction of the theory for large contractions in Figure 173, one of the following mechanisms may be conjectured. The first-order viscous dissipation correction may be invalid for large contractions, indicating that viscous dissipation during large strain is higher than that under no or mild strains. Alternatively, the non-linear turbulence production terms, discussed earlier, may lead to negative production of turbulence, i.e. transfer of energy from turbulence to the mean flow through the largest eddies. Another possible mechanism may be the inefficiency of the pressure strain terms in transferring the energy from the radial to the streamwise component, which could also lead to energy transfer to the mean flow. Finally, the recent work of Sreenivasan and Narasimha[27] predicts less production by the rapid distortion theory for axisymmetric rather than isotropic turbulence. This may be the case here since as shown in Chapter V the grid generated turbulence is approximately 15% away from isotropy in the

direction that would lead to the trend of Figure 173 from the theory of Sreenivasan and Narasimha[27].

A detailed examination of the current results with the aid of theoretical calculations like those of Goldstein and Durbin[26] is required before one can decide which of the mechanisms may be responsible for governing conditions in strong contractions, i.e. c>10. This should lead to very important practical consequences and we hope that it can be carried out. In fact, if these mechanisms, singly or in combination, are strong enough, the turbulence production discussed earlier may not be as negligible as assumed.

Finally, it should be stated that this type of understanding of coupled experiments and theories of turbulence may be our best approach to a better understanding of turbulence.

Turbulence Length Scale Effects. Figures 174 and 175 show that, in general, the turbulence energy ratio downstream of the contraction increases with higher contraction ratios. The behavior of the radial component of turbulence energy ratio also indicates that for a given contraction, as the initial turbulence scales increase so does the energy ratio. This sensitivity to the initial turbulence scales is stronger for larger contraction ratios.

The longitudinal component exhibits a different turbulence scale dependence. Data of Figure 175 seem to suggest a minimum streamwise energy ratio at some

intermediate initial turbulence scale. After compensating for the viscous decay effects, this minimum is emphasized as shown in Figure 176. An interesting point to note in this figure is that the initial turbulence scale, at which the minimum turbulence energy ratio occurs, tends to shift towards smaller scales as the contraction ratio increases. If the initial scale of turbulence is normalized by the exit diameter of the contraction, rather than D_i, the trends of Figure 176 would be different, indicating a small positive rather than the negative slope of the almost vertical line used to guide the eyes of the reader.

If maximum turbulence reduction is the primary objective, results presented in these last three figures suggest a possibility of finding an optimum initial turbulence scale which would produce a minimum increase of turbulence energy downstream of the contraction. Therefore, in the design of high performance contractions, the scale of free-stream turbulence entering the contraction should be given due attention.

Summary of Empirical Formulas

Experimental results presented in this chapter have been compared with predictions of Prandtl's vortex-stretching arguments[37] and classical rapid distortion theory[24,25]. When the correction for viscous decay effects were applied, one finds that some quantities agree very well with theory while others do not. Whenever

possible in critical applications, it is imperative to use known experimental results rather than rely on crude or inaccurate theoretical predictions. To facilitate the use of these contraction performance summary data, simple empirical relationships suggested for figures in this chapter are summarized below. They should be only used with care for immediate practical design problems and their validity should not be overemphasized.

In the design of wind tunnels, turbulence intensity reduction efficiencies are of primary concern. To achieve a desired turbulence intensity reduction, a certain amount of flow contraction is required. The results shown in Figures 168 and 169 can be used in this phase of the design. For the streamwise component, two simple relations for determining $\bar{\eta}_u$ are given below depending on the range of effective contraction ratios.

$$\bar{\eta}_u = C_a^{-1} \quad , \qquad 1 \leq C_a \leq 15 \qquad \text{(XIII-1)}$$

$$\bar{\eta}_u = C_a^{-0.9} \{(C_a-5)/6\}^{0.5}, \qquad 15 \leq C_a \leq 30 \qquad \text{(XIII-2)}$$

The viscous-corrected radial turbulence reduction efficiency data are predicted very well by classical rapid distortion theory[24,25], so the theoretical expression for $\bar{\eta}_v$ can be ultilized up to at least an effective

contraction ratio of 30.

$$\bar{\eta}_v = \{0.75\ C_a^{-1} + 0.75\ C_a^{-4}\ (0.5\ \alpha^{-2} - \frac{1-\alpha^2}{4\alpha^3} \log \frac{1+\alpha}{1-\alpha}\ )\}^{0.5}$$

$$1 \leq C_a \leq 30 \qquad \text{(XIII-3)}$$

where $\alpha^2 = 1 - C_a^{-3}$

Short contractions are best avoided whenever possible because of large upstream influence and non-uniform mean velocity downstream. Turbulence reduction is also harder to predict for these contractions.

The relations given above are for turbulence intensity reduction efficiencies "corrected" for viscous decay, which effectively eliminates extraneous effects due to differences in the turbulence decay rate of different flow conditions. To employ the above equations for design, an estimate of the viscous dissipation of the upstream conditions must be made based on empirical information or on measurements.

Uncorrected turbulence reduction efficiencies are given in Figures 166 and 167 for the streamwise and radial components, respectively. These can be used to estimate the combined effects of a "natural" viscous decay and flow contraction. For the streamwise component,

$$\eta_u = C_a^{-1.5}, \qquad 2 \leq C_a \leq 4 \qquad \text{(XIII-4)}$$

$$\eta_u = C_a^{-1} \{(C_a-5)/6\}^{0.5}, \qquad 6 \leq C_a \leq 30 \qquad \text{(XIII-5)}$$

The uncorrected radial turbulence intensity reduction efficiency is shown to be a function of the initial turbulence scales. For small-scale turbulence,

$$\eta_v = C_a^{-1}, \qquad 2 \leq C_a \leq 8 \qquad \text{(XIII-6)}$$

The relation for initially large-scale turbulence is;

$$\eta_v = C_a^{-0.75}, \qquad 2 \leq C_a \leq 30 \qquad \text{(XIII-7)}$$

Estimates for the longitudinal and the corrected total turbulence energy ratios are given in Figures 170 and 173, respectively. These are less frequently needed for contraction design. Empirical relations summarized above are merely suggestions and as such, caution should be exercised in their use for design purposes. As with any empirical relationship, extrapolations outside the suggested range of applicability are risky and should be avoided.

CHAPTER XIV

SUMMARY AND CONCLUSIONS

Important findings of the present investigation are re-emphasized in this chapter. Detailed summary results and discussion were presented in Chapter XIII as well as in earlier chapters which focused on specific aspects of the investigation. Major contraction effects on turbulence quantities are summarized first in this chapter. A composite behavior of the various components of the turbulence kinetic energy is then presented from results of normalizing the turbulence kinetic energy data in Chapter XII.

The success of the present experiments is attributed to several key design features and experimental techniques incorporated during the early diagnostic phases of the investigation. The most important factor is the wind tunnel modification employed to eliminate extraneous minute streamwise velocity fluctuations caused by blower fan blades, which amplified differently through the various contractions. Apparently this was a prevalent problem which plagued some earlier investigations on flow through contractions[21-23]. Details of this wind tunnel modification are given in Appendix B.

In order to isolate and correctly assess turbulence behavior due solely to the contraction, it is important to document the detailed turbulence characteristics of the test

flow conditions in a uniform free-stream without the contraction. This is another crucial aspect of the experiment that is performed for the first time here in an extensive investigation on contractions. Thirteen different grid-generated test flow conditions are employed in the present study, with R_M ranging from 270 to 8100. The corresponding turbulence Reynolds number, R_λ , ranges from 2.3 to 31. To assure homogeneity and isotropy, the total turbulence intensity is limited to a maximum of about 5%.

The only reported free-stream longitudinal length scales in a similar experiment are found in Reference [23] with an L_u/D_i range of 0.017-0.032. A much wider range of 0.020-0.083 is generated for the present experiment and is perhaps the widest turbulence scale range possible with the present experimental configuration while retaining homogeneity and near isotropy of the flow conditions. Present data also reveal that the longitudinal length scale is typically 2.3 times the lateral length scale in all test flow conditions, rendering them approximately isotropic; $L_u = 2L_v$ for perfectly isotropic turbulence.

Test conditions with well-behaved turbulence decay characteristics are used here so that turbulence decay rates are relatively Reynolds number independent. Turbulence energy decay of the streamwise and radial components in Figures 24 and 25, respectively, indicate variation over a very wide geometrical range. Since they are primarily a function of the grid mesh size and rather insensitive to the

mean velocity, we are assured predictable performance of the turbulence-generating grids over a range of Reynolds numbers. Except for a couple of flow conditions, when the axial decay rates are normalized by the mesh size of the various grids, they fall in the narrow range of $70 < \partial/\partial(x/M)[\overline{U}/u']^2 < 85$.

Streamwise development of integral length scales indicate that both the longitudinal and lateral length scales remain relatively constant in the uniform cross-sectional area test section. All test flow conditions show a u'/v' slightly greater than one, corresponding to values typically found in grid-generated turbulence. Small-mesh grids exhibit more departure from isotropy than large-mesh grids with u'/v' ratios of up to 1.34. In general, the data show that for large-mesh grids, turbulence tends very slightly towards isotropy with increasing downstream distance and away from isotropy for fine-mesh grids, where the decay is closer to its final period. However, such variations are very small when compared with the effect imparted by a contraction, so that the u'/v' ratio can be treated as essentially constant for these reference flow conditions. The Reynolds stresses of the flow conditions decrease in magnitude with increasing downstream distance, although their signs vary from one flow condition to the next. Reasons for such behavior are not clearly understood at the present.

The above documented variation of the homogeneous and

almost isotropic test flow conditions (for further details see Chapter V), are coupled with the wide range of contraction geometrical parameters and powerful digital data acquisition and processing techniques to obtain the detailed results of Chapters VI through XI. In the following, a summary of the effects of contraction ratio variation on incoming turbulence of various scales is presented first to establish the major results on turbulence characteristics. The contraction area ratio ranges from a mild 2:1 to a high 36:1 in the present investigation. A length-to-inlet diameter ratio of one is utilized for all the contractions in this part of the experiment. To isolate and correctly assess the contraction effects, results from the constant-diameter test section (c=1) are used as a basis for comparison.

During initial straining of the flow through the contractions, the streamwise component of kinetic energy decreases. In general, for a given flow condition, this attenuation increases with increasing contraction ratio. At any particular contraction ratio, this energy attenuation is enhanced by increasing the scales of incoming turbulence. An exception to the above observation occurs when the turbulence level of the incoming flow is vanishingly low, such as in flow condition T5b. For such cases, this streamwise energy component is amplified as soon as the flow is contracted. This amplification increases with the contraction ratio. Therefore for turbulence already with

small scale and intensity, like in many wind-tunnel settling chambers, the reduction in the turbulence intensity achieved by the contraction is that corresponding to the acceleration of the mean flow only. Often this reduction is decreased because of the increase in streamwise turbulence energy discussed here.

At sufficiently high contraction ratios, u'^2 increases towards the downstream end of the contracting section for all test flow conditions. Turbulence spectra of both velocity components indicate that this rise in energy occurs primarily at high frequencies, e.g. above 2.5 kHz for a 9:1 contraction. It appears to be a consequence of non-linear inter-component energy transfer from the radial to the streamwise component through the pressure strain terms. This conjecture is supported by measurements of high coherence between u and v downstream of these contractions. This energy increase, relative to its minimum value, is higher at larger contraction area ratios for a given flow condition. Upstream turbulence of larger scales reduces the maximum level of this u'^2 energy at the downstream end of contractions. This is contrary to the extended rapid distortion theory of Goldstein and Durbin[26] which predicts lower u'^2 and v'^2 for turbulence with larger scales due to the blocking effect of solid boundaries. However, their analysis was done for a 2-D contraction rather than an axisymmetric one and the assumed turbulence scales are much larger than is realized in the present experiment.

Depending on the contraction ratio and the upstream turbulence scales, the u'^2 near the end of the contraction may or may not exceed levels found in naturally decaying turbulence in a constant-area duct of the same length. At high contraction ratios, the streamwise component of turbulence energy at the nozzle exit can be several times higher than the energy level at its inlet, causing a deterioration in the performance of the contraction as a turbulence reducer.

The lateral component of turbulence energy always increases through a contraction as predicted by theory based on vortex stretching and tilting. This increase is higher for larger contraction ratios. It is also higher at a fixed contraction ratio for turbulence of larger scales which is again contrary to theoretical predictions[26]. Past investigations[20-23] have indicated that rapid distortion theory[24,25] over-predicts this rise in the lateral turbulence energy component and under-predicts the attenuation of the streamwise component of turbulence intensity. Present results show that predictions by rapid distortion theory can be approached for both components of turbulence intensity during the initial stages of flow contraction or if the upstream turbulence scales are large. However the increase in u'^2 at the downstream end of contractions cannot be accounted for by the classical linear rapid distortion theory of Batchelor and Proudman[24], and Ribner and Tucker[25], or by the extended theory of

Goldstein and Durbin[26]. It is suspected that this discrepancy in behaviorial trend is due to a non-linear inter-component energy transfer from the lateral to the streamwise component. Evidence of this is suggested by the broad-band coherence of u and v velocity fluctuations downstream of the contraction as shown in Figure 140. This non-linear transfer mechanism is stronger for turbulence of smaller scales and at higher contraction ratios. However, as pointed out in Chapter XIII, when a first-order correction for viscous dissipation is applied to the experimental data, the linear rapid distortion theory correctly predicts the behavior of the streamwise and radial turbulence energy for mild contractions with area ratios less than five. Therefore the theory appears to be very useful for predicting the behavior of turbulence under mild strain, since the viscous dissipation rate required for our first-order correction is well-established empirically. This is a very important conclusion and should be quite useful for ongoing activities in computer modeling.

In addition, the predictions of the extended theory of Goldstein and Durbin[26], regarding the blocking of larger scales of turbulence through strong contractions, are realized in the streamwise energy component for the lower range of scales, e.g. see Figure 176. However for even larger initial scales of the turbulence, as well as for all scales in the case of the radial component, the results display a trend opposite to the extended theory

predictions[26]. This discrepancy may be caused by the non-linear inter-component transfer found in the experiment and neglected in the theory, or because of the extremely large initial scales considered by Goldstein and Durbin[26], as compared to the range utilized in this study.

Turbulence length scales calculated from the integral time scales using the local mean streamwise velocity show an increase through the contractions. Large values are observed downstream of contractions with large area ratios. In general, these length scale growths are also higher for turbulence of larger scales. This behavior tends to be more systematic for the lateral length scale. For example, turbulence scales downstream of a 36:1 contraction for an initially large-scale turbulence condition can be as much as 15 and 45 times the incoming length scales for the longitudinal and lateral scales, respectively. However relative growth between the longitudinal and lateral length scales indicates that the L_u/L_v ratio at the downstream end of the contraction decreases with increasing turbulence scales.

This extreme extension of the streamwise correlation times for the lateral velocity components can contribute significantly to noise production by jet-engine fans in static ground tests. The turbulence through a large contraction with large-scale initial conditions can be described as predominantly "sloshing" in the transverse directions. In fact what happens is that the turbulence

memory retains approximately the same integral time scales in this "rapid" contraction, but the flow is convected over a much larger streamwise distance by the accelerated flow downstream of the contraction. Preliminary visualization experiments at I.I.T. have already confirmed this trend for laboratory-model fan intakes.

Effects of initial turbulence scales on typically mild (2:1), moderate (9:1), and high (16:1) contractions indicate that even at a mild contraction ratio of 2, the downstream turbulence kinetic energy characteristics are influenced by the incoming turbulence scales. At higher contraction ratios, the non-linear increase in u'^2 with increasing strain which occurs near the downstream end of the contraction, is highly affected by incoming turbulence scales.

Velocity spectral data immediately downstream of the contraction point to the fact that the spectral decay slope in the inertial subrange is much lower for turbulence with larger scales and the roll-off occurs at a lower frequency. As pointed out earlier, initially small-scale turbulence exhibits the most u'^2 energy rise near the exit of the contraction, while large-scale turbulence displays the least. The coherence function for the u and v fluctuations also shows higher coherence for small-scale turbulence conditions. However the total turbulence energy level at the downstream end increases with incoming turbulence of larger scales. Higher incoming velocities, i.e. higher

Reynolds numbers, also increase the amount of u'^2 rise near the downstream end of the contraction.

Growth of the length scales through the contraction is lower for turbulence conditions with initially high turbulence Reynolds numbers. The degree of isotropic recovery during the final phase of straining in the contraction is minimal for large-scale turbulence but increases as the turbulence scales get smaller as well as with increasing contraction ratio. This tendency towards or away from isotropy appears to be governed by the amount of inter-component transfer as much as by the initial ratio of u'/v'. Therefore it is strongly affected by the scales and the viscous decay rates of the initial turbulence. This conclusion may be the key to the long-standing contradiction between experiments of Comte-Bellot and Corrsin[19] and those of Uberoi and Wallis[17]. Unfortunately, the details of their upstream conditions are not available in order to fully investigate our conjecture. However the present results should be of great value for future attempts at utilizing contractions to improve the isotropy of turbulence.

For the investigation of length-to-inlet diameter effects, the range of L/D_i is varied from a very short 0.25 to a rather long 1.50. Major differences in the turbulence characteristics for flows through short (L/D_i = 0.25 and 0.50) and long ($L/D_i \geq 1.00$) contractions are due primarily to the large upstream influence and possible flow

separation, especially near the inlet of the short contractions. Because of this high degree of upstream influence, mean velocity acceleration through the physical contracting section of short nozzles is much less than values predicted by geometrical considerations. A significant amount of flow acceleration occurs upstream and downstream of these contractions. Fluid mechanically, it is probably impossible to achieve large incompressible-flow acceleration in a very short axial distance.

For these short contractions, unavoidable flow separation due to high adverse pressure gradients contributes significantly to increased streamwise turbulence. Turbulence reduction and exit flow uniformity for both large- and small-scale initial turbulence improves substantially when the length-to-inlet diameter ratio of the contractions is increased from 0.25 to 1.00. Only a small incremental gain is achieved by increasing the length ratio from 1.00 to 1.50. Results also show that for a given contraction ratio, the streamwise component of turbulence intensity of initially large-scale turbulence is reduced by a slightly greater amount than for small-scale turbulence, but an opposite trend applies to the radial component.

Turbulence characteristics obtained from a matched-cubic and a fifth-order contraction with the same area and length-to-diameter ratios reveal insignificant differences in the behavior of turbulence energy and length scale growth characteristics. However downstream of the

contraction, the mean velocity profile is more uniform for the fifth-order contraction. Differences are noted in the $\overline{uv}$ Reynolds stress only at the exit end of the contraction where a sharp increase in the $\overline{uv}$ stress magnitude results from the flow adjusting to the constant-area downstream boundary condition. This sharp "spike" is more prominent for the fifth-order contraction.

In addition to data acquisition on-axis, data were also collected at several off-axis radial positions for the 9:1 matched-cubic contraction with an L/D = 1.00 using three upstream flow conditions representing small, medium and large-scale turbulence. Results show that the turbulence energy ratios increase dramatically starting at $x/L \simeq 0.8$ with the X-probe sensing volume at $r/r_c = 0.64$. At the contraction exit section, where the probe is relatively farther from the axis of symmetry, at $r/r_c = 0.82$, the turbulence energy ratios for both streamwise and radial components can be more than 3.5 times the corresponding on-axis values. This behavior is partly due to the fact that the principal stress axes are no longer aligned with the u and v directions, a result correctly predicted by Goldstein and Durbin[26]. It may also be caused by the larger production of new turbulence due to the radial gradient of the mean flow away from the centerline.

The medium-scale turbulence exhibits the highest energy increase off the centerline, while small-scale turbulence displays the least increase over on-axis turbulence kinetic

energy ratios. Detailed statistical functions, obtained from the medium-scale turbulence near the downstream end of the contraction, indicate a significantly lower spectral decay slope in the inertial subrange at frequencies above 400 - 500 Hz for the off-axis turbulence data. But below the roll-off frequency, the velocity spectra show no appreciable difference whether data are collected on- or off-axis. Therefore the turbulence spectra off-axis have relatively more energy at higher frequencies.

The coherence function also indicates that the streamwise and radial velocity components are more interrelated off-axis. The on-axis cross-covariance function infers a somewhat persistent turbulence structure typical of both small- and large-scale turbulence conditions downstream of a contraction, while the off-axis cross-covariance function suggests a non-persistent structure. The Reynolds stress $\overline{uv}$ can be an order of magnitude larger away from the centerline. Predominant turbulence scales implied by the cross-covariance functions are about the same regardless of whether data were collected on or off the axis of symmetry.

To interrelate the different parameters affecting the behavior of turbulence kinetic energy through contractions, as well as to gain insight into the physical mechanisms, data regressions are carried out using simple yet rational normalizations. For the first time, the present investigation attempted a first-order correction for the

effect of viscous decay which resulted in remarkable success. This correction relies on data obtained in non-contracting but otherwise identical flow conditions as reference conditions.

Using this scheme, the corrected radial component of turbulence kinetic energy ratio, from all the different cases, is shown to vary linearly with the total axial strain $(\bar{U}(x)/\bar{U}_i - 1)$, as well as to an empirically determined one-third power of the geometrical contraction ratio c, and the ratio L_{v_i}/D_i which is a measure of turbulence scales relative to some characteristic scale in the experimental set-up; see Figure 161. Similarly, behavior of the streamwise turbulence kinetic energy under axisymmetric strain can be better understood by examining the basic parameters used in the normalization; see Figure 163. For example, given a contraction geometry and a particular free-stream condition, the value of the $\{D_i\ \partial/\partial x\ (\bar{U}/u')^2|_{c=1}\}^{1/2}$ parameter, which is related to the relative scale of turbulence, is a constant. Therefore, as the axial strain is increased, the viscous-corrected streamwise turbulence energy ratio first decreases slightly because of vortex stretching, attains a shallow minimum, and then rapidly rises with increasing strain because of inter-component transfer. Now if the turbulence-scale related parameter is allowed to vary, and assuming that the flow has undergone a particular amount of axial strain, that is setting the quantity $(\bar{U}(x)/\bar{U}_i - 1)$ to some constant value, the present

results show that depending on the chosen amount of axial strain, there is an optimum range of initial turbulence scales which yield the lowest u'^2 turbulence energy ratios downstream of the contraction. Because of the steep rise in the streamwise turbulence energy ratio when initial turbulence scales are smaller than optimum, it is better to have a slightly larger-scale turbulence free-stream condition than one with a scale smaller than optimum from the standpoint of minimizing the u' turbulence intensity. From the wind-tunnel design standpoint, this means longer settling chambers downstream of turbulence manipulators and ahead of the contraction.

Streamwise turbulence energy ratio for the very fine scale turbulence condition T1 seems less affected by the contraction process. The initial decrease in the u'^2 ratio is absent with increasing strain using this flow condition and the rise at high axial strain is at a slower rate than in other flow conditions. For the streamwise component, the length-to-diameter ratio of the contraction also plays an important role in the performance, but this parameter cannot be varied arbitrarily because it appears as part of quantities on both the abscissa and the ordinate of Figure 163.

Therefore by using simple yet physically relevant parameters to normalize the streamwise and radial turbulence kinetic energy ratios, a composite effect of turbulence energy behavior is presented in flows through axisymmetric

contractions involving different initial turbulence scales, as well as different area and length ratios. This ability to summarize results obtained from a diverse set of turbulence flow conditions for a wide range of contraction parameters is a result of compensating for the different rates of viscous dissipation. The different decay rates occur in the flow conditions involving different turbulence scales. As a result, the contraction effects are separately and properly assessed with the aid of simple theories. To the best of our knowledge, this scheme is being applied for the first time to investigations of homogeneous turbulent flows through contractions. It is the key to a better understanding of mechanisms which are important during the contraction process.

Non-linear inter-component energy transfer is shown to be the major cause of discrepancy between experimental results and classical or other extended linear rapid distortion theories. As discussed in Chapter XIII, it may be that very little "new" turbulence production is going on through all the contractions used here, $2 \leq c \leq 36$. The inter-component transfer of energy by the pressure strain terms, between the amplified radial component and the suppressed streamwise component, may be the only mechanism in addition to viscous dissipation that is not accounted for by the rapid distortion theory. Therefore we feel that the revival of this theory in recent works deserves the attention of the turbulence researchers. The present

experiments also demonstrate conditions under which this non-linear mechanism governs the turbulence behavior in axisymmetric contractions for initially different free-stream conditions.

APPENDIX A

DESIGN AND CONSTRUCTION OF TEST SECTIONS AND CONTRACTIONS

Measurements were made in the test section downstream of the settling chamber and a 25:1 contraction shown schematically in Figure 1. Circular plexiglas sections of different lengths were bolted together to form the required separation distance between the turbulence-generating grid and the inlet to the contraction under investigation. The section lengths were designed to permit a 2.54 cm increment in the separation distance, S_o, starting from no separation (i.e., grid mounted at inlet of contraction) to a separation distance of 58 cm. The ability to adjust S_o is crucial to this investigation because each grid required a different decay distance for the generated turbulence to become homogeneous and approximately isotropic. Figure 2 lists the grid-to-contraction inlet distances utilized in the present experiment. These distances were chosen after careful probing of the mean streamwise velocity and both components of the turbulence velocity. To assure minimum flow disturbance when using a different number of sections to form the required S_o, all the sections were machined both inside and outside to produce sections of uniform inside diameter and to remove any slight eccentricity normally found in cast acrylic tubes. The machined tube sections were then finished to a tolerance of $\pm$ 0.05 mm and fitted with matched mounting flanges on both ends.

Nine of the contractions used in this investigation

were of the matched-cubic contour type and one was a fifth-order contraction. The matched-cubic contractions were designed according to the charts provided by Morel[16] whenever possible. According to him, the matched-cubic is most suitable for designs calling for the shortest non-separated nozzle. Hussain and Ramjee[21] had also found that of the four contours of axisymmetric contractions that they tested, the cubic profile was the best. Optimum design for a given contraction ratio is achieved by allowing the minimum coefficient of pressure near the inlet, C_{pi}, to attain a value just below incipient flow separation as determined by Stratford's criterion[28]. The maximum coefficient of pressure near the exit, C_{pe}, is selected based on the amount of nonuniformity in the mean velocity that can be tolerated. The design charts then give the shape of the contour by establishing the location of the inflection point, ξ, and the length of the contraction. The above procedure will produce the shortest contraction that meets the specified criteria.

When the length-to-inlet diameter ratio must also be specified along with the contraction ratio, the only remaining design parameter is the location of the inflection point and it may not be possible to avoid separation at the inlet. In addition, the degree of velocity nonuniformity at the contraction exit cannot be arbitrarily chosen if short contractions are required. The selection of the range of contraction area ratios and length-to-diameter ratios for

the present experiment was made to provide a wide spectrum of contractions that bracket the various typical cases encountered in practice as well as the optimum contractions predicted by design approaches like Morel's[16].

Once the parameters of the contractions were determined, a computer program was used to plot the contraction shapes for either the matched-cubic or the fifth-order type nozzles. The program permitted viewing the output on a Tektronix 4010-1 graphics terminal as well as printing out the contraction profile coordinates which were used to make contour templates for use on a tracer lathe. A brief description and a listing of the program is given in Appendix E. Contractions were then machined from solid blocks of plexiglas using these templates on a hydraulically-controlled tracer lathe to produce highly accurate contraction shapes with a tolerance of better than $\pm$ 0.05 mm. The constant-diameter tubes downstream of the contractions' exits were fabricated with the same degree of precision for perfect matching to each of the 10 contractions constructed for this investigation.

APPENDIX B

WIND-TUNNEL MODIFICATIONS

During the diagnostic phase of the present investigation the wind tunnel had to undergo several modifications that were vital to the ultimate success of this experiment. This open-circuit wind tunnel was previously used by Ahmed et al.[4] and by Wigeland[29]. Initially, the wind tunnel was powered by a centrifugal blower capable of providing up to a 20 m/s throughflow velocity in the test section. Preliminary results revealed that when low-level free-stream turbulence was used as a test flow condition, the streamwise component of velocity fluctuations could only be reduced slightly by a contraction. Results from earlier investigations[21-23] led us to suspect that the blower fan blades may have been introducing minute streamwise velocity fluctuations through the unsteady pressure field of the blower exhaust. These fluctuations amplify in a contracting stream and are measured by the hot-wire probe as part of turbulence. These non-vortical fluctuations can be easily identified because of their high correlation along transverse planes.

A simple experiment employing compressed air as an alternative power source convinced us that these extraneous "potential" fluctuations were not negligible, especially in low-level turbulence test flow conditions. The wind tunnel was subsequently modified to derive its power from a compressed-air supply. Comparative tests showed a very

significant reduction in the streamwise component of the fluctuating velocity for data taken when the compressed-air supply was utilized. The radial component was not affected at all. This confirmed our suspicion of the blower as the cause for unusually high "turbulence" fluctuations in the streamwise component measured during the preliminary work. This is often the case when contractions are used in the flow facility, since such streamwise fluctuations are amplified through a contraction, rather than decreased as in the case of the vortical turbulent velocity fluctuations.

A 5-micron particulate filter and a coalescing-type oil removal filter were installed at the exit of the air supply to protect the hot-wire probes against physical damage and to minimize calibration drifts. The maximum steady flow velocity that can be achieved by the compressed air supply in the large test section ahead of the contraction is approximately 6 m/s.

A final modification involved installing an assembly of three acoustic foam-lined baffles in the duct section at the compressed air inlet to absorb acoustic noise. The duct section was also lined with 19-mm thick sound absorbing "Scott-Pyrell" acoustic foam. This acoustic treatment was designed to prevent any valve, shear-flow, or separated-flow noise from propagating into the settling chamber and contaminating the turbulence measurements.

APPENDIX C

DATA CALIBRATION AND LINEARIZATION

The final digital hot-wire data were recorded directly from the anemometers after signal pre-processing (see Instrumentation section in Chapter II) to prevent aliasing and to utilize the maximum range of the analog-to-digital converter. Since the digital data recorded on tape were time-dependent raw-voltage signals from the output of constant-temperature anemometers, data calibration and linearization was necessary to transform voltages from the X-wire probe into U and V velocity components. Other statistics can then be computed from these velocity data.

Conversion of output voltages into appropriate velocities was performed on a UNIVAC-1100/81 computer. Several features of the present scheme produced results with higher accuracy than would have been possible with analog processing techniques. An essential part of this digital linearization was the availability of complete and sufficiently dense calibration data that covered all conditions encountered during the experiment. A squared third-order polynomial (Equation C-1) was used to relate the voltage to the velocity

$$U(E) = (A_0 + A_1E + A_2E^2 + A_3E^3)^2 \qquad (C\text{-}1)$$

when the sensor is normal to the flow. A_0 through A_3 are

constants obtained from calibration. It has been found by Drubka and Wlezien[30] that this method is computationally efficient because it does not involve taking logarithms or doing exponentiations on the data. The calibration curve is represented by only four constants. Furthermore, it fits the data more accurately over a wider range of velocity than the modified King's Law. Average errors of 0.006 m/s (standard deviation = $\pm$ 0.0082 m/s) for the low velocity range $0.94 \leq \bar{U} \leq 19.5$ m/s, and of 0.064 m/s (standard deviation = $\pm$ 0.088 m/s) for the high velocity range $20 \leq \bar{U} \leq 59$ m/s were obtained from the calibration of the X-wires.

Since the sensors in an X-array probe were inclined to the flow in its normal operation, Equation (C-1) is written as

$$H(E) = (A_0 + A_1E + A_2E^2 + A_3E^3)^2 \qquad (C\text{-}2)$$

where H(E) can be related to the true velocity through the yaw dependence of the hot-wire as shown in Equation (C-3).

$$H(E) = Uf^2(\alpha - \gamma) \qquad (C\text{-}3)$$

The function $f^2(\alpha-\gamma)$ expressed the yaw dependence of the hot-wire with respect to some arbitrary axis. The angle of

the wire with respect to this axis is α while γ is the flow angle with respect to the chosen axis. The simplest relation for the f function is the cosine law, viz.

$$f^2(\alpha - \gamma) = \cos(\alpha - \gamma) \qquad \text{(C-4)}$$

When dealing with large variations in the yaw angle, this relation should be changed to a more general one as suggested by Drubka et al.[31] in order to yield more accurate results. However, for the type of hot-wires used here, the corrections to the cosine law were small as long as the axis of the X-wire was aligned with the direction of the mean streamline or close to it. Hence, the cosine relation could be used without any loss of accuracy in the present investigation. Substituting Equation (C-4) into Equation (C-3), setting $\gamma = 0$ by choosing an appropriate reference axis, and writing the equation for each of the two sensors of the X-wire probe, the relations for determining the two velocity components are:

$$U = [\sin(\alpha_1 + \alpha_2)]^{-1}\{\sin \alpha_2 \, H(E_1) + \sin \alpha_1 \, H(E_2)\} \qquad \text{(C-5)}$$

$$V = [\sin(\alpha_1 + \alpha_2)]^{-1}\{\cos \alpha_2 \, H(E_1) - \cos \alpha_1 \, H(E_2)\} \qquad \text{(C-6)}$$

Subscripts 1 and 2 denote the values for each wire. Equations (C-5) and (C-6) are equivalent to Equations (III-5) and (III-6), respectively, in Drubka et al.[31]. This ability to correct for non-ideal probe construction enabled the data used for obtaining the two velocity components to be processed far more accurately by this scheme than through analog means.

Temperature compensation of the X-wires was not necessary in the present experiment because the compressed air temperature remained relatively constant (within $\pm$ 1°C). However, this scheme is very amenable to the simple incorporation of such corrections.

In summary, the values of the constants A_0 through A_3 in Equation (C-2) were obtained for each sensor from calibration data using a polynomial data-fitting routine on a microcomputer for the two ranges of velocities. These polynomial coefficients and the geometrical constants of the particular X-probe were among inputs to the UNIVAC-1100/81 program. Data calibration, linearization and processing were achieved in one pass through the computer making this scheme highly efficient in addition to being very accurate. All of the final data were collected for this experiment using the same probe and pair of hot-wire sensors.

APPENDIX D

PROBE VIBRATION REDUCTION

In order to minimize blockage effects of the probe body when high contraction ratios were employed, a 4.76 mm diameter, 41 cm long hot-wire probe body was used. At exit velocities above 25-30 m/s, the jet that impinges on the support of the probe created a very small vibration which was transmitted through the probe body to the prongs of the X-wires. While using low-turulence test flow conditions, the velocity spectra showed several distinct low-amplitude narrow-band peaks ranging from about 1 kHz to over 10 kHz that were caused by very slight prong vibrations. These vibrations lead to minute vibrations and strain-gaging of the hot-wire sensor itself, causing this contamination of the signal.

Oscilloscope traces of the fluctuating velocities, which were continuously monitored, did not indicate any periodic signal content that would suggest the existance of these vibrations because of the small noise to signal ratio. This problem was brought to light when early diagnostic digital data were processed and spectra plots of them obtained. Since the spectra were not computed and displayed on-line, identifying the cause and implementing a solution to the problem was very difficult and time-consuming; i.e., there was no immediate feedback to any modifications made.

Acquisition of a dual-channel real-time spectrum analyzer proved to be crucial in the solution of this

problem. The X-wire voltages were connected to an HP Model 3582A unit which computes the spectra via an FFT and outputs them on its built-in CRT display in a fraction of a second. This real-time spectral analysis capability allowed effective diagnosis of the X-wire vibration problem and provided immediate feedback on the success of attempted solutions.

Strain-gaging of the wires was eliminated by mounting the sensors with a small amount of slack and fixing the prongs' separation distance with 0.1 mm diameter glass fiber elements that were glued midway along the prongs to each pair of wire supports in the X-array. This resulted in the elimination of the high frequency peaks associated with strain-gaging of the wires.

The nature of the experiment dictated that the X-probe be capable of measurements over an extremely wide range of velocities. For example, the mean streamwise velocity increases by a factor of over 30 for one of the contractions,C7, with the velocity at the exit of the contraction reaching as high as 65 m/s. In addition, extremely low turbulence intensities had to be measured in this experiment near the exit of many of the contractions. The vibration of the prongs contaminates the spectra with several narrow-band peaks as shown for typical cases in Figures 177(a) and (c). In Figure 177(a) a spectrum of the hot-wire signal is displayed to 5 kHz on the annotated CRT of the real-time spectrum analyzer. Note that the amplitude

is in log while the frequency axis is linear with scale factors, marker frequency and reference levels shown on the display. A computer plot of the normalized U velocity spectrum on a more customary log-log scale is shown in Figure 177(c). The vibrational peaks are clearly visible in both figures. The logarithmic amplitude scaling makes the energy content associated with these peaks appear to be a significant fraction of the total energy even though the highest peaks in Figure 177(c) are more than an order of magnitude lower than the turbulence energy of the energetic lower frequencies. It would have been possible to ignore these vibrations without introducing appreciable errors in the turbulence energy or the rms of the fluctuating velocities. On the other hand, detailed statistics such as correlations and coherence functions would be affected to a greater extent. The quest for the cleanest possible signals led us to take great pains in trying to eliminate or reduce these vibrational contaminations from the turbulence energy.

A truss-like structure was constructed with 0.1 mm glass fiber rods to stabilize all four prongs about half way between the tips and the base. This resulted in added rigidity of the probe tip assembly thereby reducing the vibrations substantially. However, the glass fibers tend to shed vortices at the Strouhal frequency which is velocity dependent. Careful arrangement of the glass fibers minimized this effect by delaying the shedding process as the velocity is increased.

An enormous improvement was made by attaching small spherical balls of soft clay around each of the prongs that act as tuned-mass vibration dampers. The size of the clay spheres and their location on the prongs were optimized to produce maximum damping with minimum disturbance to the flow. This clay was also used at the base of the prongs to damp out vibrational energy through dissipation. The degree of success is clearly demonstrated by comparing the spectra on the CRT display of the spectrum analyzer, Figures 177(a) and 177(b), or the digitally processed U velocity spectra from another diagnostic run, Figures 177(c) and 177(d), before and after using the clay dampers, respectively. Most peaks have been totally eliminated with the remaining ones substantially reduced in amplitude and width. The real-time spectrum analyzer proved to be an indispensible tool for obtaining the solution to this problem.

APPENDIX E

CONTRACTION DESIGN PROGRAM

Description

This BASIC program calculates the nozzle contour according to either a 5th-order polynomial or a pair of matched cubic equations. Derivation of the equations is not given here but some interesting points will be made to give a better insight into the choice of the optimum contour. A knowledge of computer programming is not necessary to use this routine but it is nevertheless helpful.

For the cubic contour, equations E-11 and E-12 were derived using 8 boundary and matching conditions given by E-3 through E-10.

$$R_1(x^*) = a_o + a_1 x^* + a_2 x^{*2} + a_3 x^{*3} \quad , \quad 0 \leq x^* \leq \xi \qquad \text{(E-1)}$$

$$R_2(x^*) = b_o + b_1 x^* + b_2 x^{*2} + b_3 x^{*3} \quad , \quad \xi \leq x^* \leq 1 \qquad \text{(E-2)}$$

$$R_1(0) = D_1/2 \qquad \text{(E-3)}$$

$$\left.\frac{dR_1}{dx^*}\right|_{x^*=0} = 0 \qquad \text{(E-4)}$$

$$R_2(1) = D_2/2 \tag{E-5}$$

$$\left.\frac{dR_2}{dx^*}\right|_{x^*=1} = 0 \tag{E-6}$$

$$R_1(\xi) = R_2(\xi) \tag{E-7}$$

$$\left.\frac{dR_1}{dx^*}\right|_{x^*=\xi} = \left.\frac{dR_2}{dx^*}\right|_{x^*=\xi} \tag{E-8}$$

$$\left.\frac{d^2R_1}{dx^{*2}}\right|_{x^*=\xi} = 0 \tag{E-9}$$

$$\left.\frac{d^2R_2}{dx^{*2}}\right|_{x^*=\xi} = 0 \tag{E-10}$$

Applying these boundary and matching conditions leads to the final form of the contour equations given in E-11 and E-12 below.

$$R_1(x^*) = D_1/2 - \frac{3(D_1 - D_2)}{4\xi} x^{*2} + \frac{(D_1 - D_2)}{4\xi^2} x^{*3} \quad , \quad 0 \leq x^* \leq \xi \tag{E-11}$$

$$R_2(x^*) = D_2/2 - \frac{(D_1 - D_2)(3\xi - 2)}{4(\xi - 1)^2} + \frac{3(D_1 - D_2)(2\xi - 1)}{4(\xi - 1)^2} x^* - \frac{3(D_1 - D_2)\xi}{4(\xi - 1)^2} x^{*2} + \frac{(D_1 - D_2)}{4(\xi - 1)^2} x^{*3} \quad , \quad \xi \leq x^* \leq 1 \tag{E-12}$$

where

D1	= Inlet diameter
D2	= Outlet diameter
R1 & R2	= Contraction contour functions
x^*	= Non-dimensional axial distance = $x/L\|_\xi$
L	= Contraction length
ξ	= Non-dimensional location of inflection point

For the special case when = 0.5, the two contour functions reduce to a single equation (E-13) for the nozzle shape.

$$R(x^*) = D_1/2 - \frac{3(D_1 - D_2)}{2} x^{*2} + (D_1 - D_2) x^{*3} \quad , \quad 0 \leq x^* \leq 1 \tag{E-13}$$

One of the features of using a pair of cubic equations rather than a single one is that the location of the inflection point can be arbitrarily chosen to provide different contour shapes. This has a bearing on the flow

quality at the outlet of the nozzle. An optimum location of the inflection point for a given contraction ratio and length ratio can be found. Details are discussed in Morel[16].

A higher-order equation is needed to impose zero second derivatives at both ends of the nozzle. This 5th-order contour is given by Equation E-14 and is also incorporated in the computer program. For the same area ratio and L/D ratio, this contour gives a more uniform velocity profile downstream of the contraction as compared to the matched-cubic contour. The inflection point is fixed at $\xi = 0.5$ and is not a user selectable option as in the cubic contours.

$$R(x^*) = D_1/2 - 5(D_1 - D_2)\, x^{*3} + 7.5(D_1 - D_2)x^{*4} - 3(D_1 - D_2)x^{*5}, \qquad 0 \leq x^* \leq \xi \qquad \text{(E-14)}$$

User Instructions

Some Preliminary Remarks. The program was written in PDP-11 BASIC version GEO8D with the external function written for plotting on the Tektronix 4010-1 graphic display unit. This routine requires a minimum of 8k of memory space on a PDP-11 computer. The results can be presented either in tabulated form or the shape of the nozzle can be shown on the graphic display unit.

Program prompts are placed at input points to the program. Users may find it helpful to become familiar with

the GEO8D version of BASIC although it is not a requirement in using this program.

Using the Program. A brief explanation of the required inputs to the routine is available when the program prompts with "NEED HELP?" Answer all prompts with numbers only because this version of BASIC does not support string inputs. A non-zero number, normally a "1", signifies a "YES" answer and a "0" means "NO". Simply typing a carriage return <CR> will siffice for a "NO" since BASIC will assume a zero for that input. Disregard of the aforementioned will result in an error message ending with a "?". To continue, type in the correct response. Improper inputs can also cause the program to prompt for a valid input before it will continue. To quit the program and start over again type <CTRL-P> and rerun the program with a "RUN" command.

The program can be "tricked" into doing strange things such as calculating not enough points and then plotting the result. The contour displayed will not be an accurate representation of the nozzle shape.

When the program is used to plot, it is finished when a "BELL" is heard. The program is designed to "hang" in an infinite loop so that the BASIC prompt "STOP AT LINE...." is not displayed on the plot when a hard copy is made. Use the <CTRL-P> to halt the program after the hard copy is made. The program will "hang" in the plot mode only.

A listing of the program is shown at the end of this

appendix. We hope that this program is of some use in obtaining the contour of high performance nozzles.

PROGRAM LISTING

```
1 REM  NOZZLE DESIGN PROM W/PLOTTING (3RD &5TH ORDER) VER.2.3 120178
2 REM  WRITTEN BY JT FOR PDP-11 BASIC & TEKTRONIX 4010-1 GDU.
3 REM  REVISION 0 120278
10 PRINT,"AXISYMMETRIC NOZZLE DESIGN PROGRAM     VER. 2.3":PRINT
15 PRINT"PLEASE REPLY PROMPTS WITH:":PRINT" YES=NO.#0 & <CR>"
20 PRINT" NO=0 & <CR>":PRINT:PRINT"NEED HELP";:INPUT Z1
25 IF Z1<>0 GOTO 3000
30 PRINT:PRINT:PRINT"PLEASE TYPE IN THE FOLLOWING:":PRINT:PRINT
35 PRINT"MATCHED-CUBIC";:INPUT Z3
40 IF Z3<>0 THEN LET Z5=0:GOTO 60
45 PRINT"5TH ORDER";:INPUT Z5
50 IF Z5<>0 THEN LET M1=0:LET Z3=0:GOTO 60
55 GOTO 35
60 PRINT"D1=";:INPUT D1
65 IF D1<=0 THEN PRINT"INVALID INPUT: D1>0 ONLY":GOTO 60
70 PRINT"D2=";:INPUT D2
75 IF D2<0 THEN PRINT"INVALID INPUT: D2>0 PLEASE":GOTO 70
80 IF D2<>0 GOTO 100
85 PRINT"CONTRACTION AREA RATIO=";:INPUT C1
90 IF C1<=0 THEN PRINT"INVALID INPUT: C.R.>0 ONLY":GOTO 85
95 LET D2=D1/SQR(C1)
100 PRINT"L/D1=";:INPUT L1
105 IF L1<0 THEN PRINT"INVALID INPUT: L/D1>0 ONLY":GOTO 100
110 IF L1<>0 GOTO 130
115 PRINT"NOZZLE LENGTH=";:INPUT L2
120 IF L2<=0 THEN PRINT"INVALID INPUT: NOZZLE LENGTH>0 ONLY":GOTO 115
125 LET L1=L2/D1
130 IF Z5<>0 GOTO 150
135 PRINT"MATCH POINT=";:INPUT M1
140 IF M1<=0 THEN PRINT"INVALID INPUT: M.P.>0 ONLY":GOTO 135
145 IF M1>=1 THEN PRINT"INVALID INPUT: M.P.<1 ONLY":GOTO 135
150 PRINT"NO. OF INTERVALS REQUIRED=";:INPUT K
155 IF K<2 THEN PRINT"MINIMUM IS 2":GOTO 150
160 LET K=INT(K)
165 LET I=1/K
170 LET L2=L1*D1
175 LET M2=(M1-1)*(M1-1)
180 LET C1=(D1/D2)*(D1/D2)
185 LET D=D1-D2
190 PRINT"PRINT OUT COORDINATES";:INPUT Z2
195 IF Z2=0 GOTO 280
200 FOR L=1 TO 6
205 PRINT
210 NEXT L
215 PRINT,"NOZZLE CHARACTERISTICS:":PRINT
217 IF D=0 THEN PRINT"STRAIGHT CIRCULAR DUCT":GOTO 230
219 IF M1=.5 THEN PRINT"3RD ORDER";:GOTO 225
221 IF Z3<>0 THEN PRINT"MATCHED-CUBIC";:GOTO 225
223 PRINT"5TH ORDER";
225 IF C1>1 THEN PRINT" NOZZLE":GOTO230
227 PRINT" DIFFUSER"
230 PRINT"INLET DIA.=";D1;"IN."
235 PRINT"OUTLET DIA.=";D2;"IN."
240 PRINT"CONTRACTION AREA RATIO =";C1
245 PRINT"NOZZLE LENGTH =";L2;"IN."
250 PRINT"LENGTH RATIO, L/D1 =";L1
255 IF Z3<>0 THEN PRINT"MATCH POINT, XM/L =";M1
260 PRINT:PRINT:PRINT
265 PRINT,"  NOZZLE COORDINATES":PRINT
270 PRINT," X(IN.)          R(X)"
```

```
275 GOTO 340
280 PRINT"";
285 IF D=0 THEN PRINT,,,"STRAIGHT DUCT":GOTO 305
287 IF M1=.5 THEN PRINT,,,"3RD ORDER":;:GOTO 293
289 IF Z3<>0 THEN PRINT,,,"MATCHED-CUBIC":;:GOTO 293
291 PRINT,,,"5TH ORDER";
293 IF C1>1 THEN PRINT" NOZZLE":GOTO 305
295 PRINT" DIFFUSER"
305 PRINT:PRINT,,,,"D1 =";D1;"IN"
310 PRINT,,,,"D2 =";D2;"IN"
315 PRINT,,,,"C.R.=";C1
320 PRINT,,,,"L =";L2;"IN"
325 PRINT,,,,"L/D1 =";L1
330 IF Z3<>0 THEN PRINT,,,,"XM/L =";M1
335 GOSUB 1000
340 LET X=0
345 LET X1=X
350 LET R1=D1/2
355 IF Z2=0 GOTO 365
360 PRINT,X1,R1:GOTO 370
365 GOSUB 2000
370 LET X=X+I
375 LET X1=X*L2
380 LET X2=X*X:LET X3=X2*X:LET X4=X3*X:LET X5=X4*X
385 IF Z3=0 GOTO 490
390 IF X>M1 GOTO 430
395 LET R1=.25*D*X3/(M1*M1)
400 LET R1=R1-.75*D*X2/M1
405 LET R1=R1+D1/2
410 IF Z2=0 GOTO 420
415 PRINT,X1,R1:GOTO 370
420 GOSUB 2000
425 GOTO 370
430 IF X<=1 GOTO 445
435 IF Z2=0 GOTO 515
440 GOTO 525
445 LET R1=.25*D*X3/M2
450 LET R1=R1-.75*D*M1*X2/M2
455 LET R1=R1+.75*D*(2*M1-1)*X/M2
460 LET R1=R1-.25*D*(3*M1-2)/M2
465 LET R1=R1+D2/2
470 IF Z2=0 GOTO 480
475 PRINT,X1,R1:GOTO 370
480 GOSUB 2000
485 GOTO 370
490 LET R1=D1/2-(D*(5*X3-7.5*X4+3*X5))
492 IF X>1 GOTO 510
495 IF Z2=0 GOTO 505
500 PRINT,X1,R1:GOTO 507
505 GOSUB 2000
507 GOTO 370
510 IF Z2<>0 GOTO 525
515 PRINT"":REM  PLOT DONE
520 GOTO 520 :REM HANG UP PRGM TO SUPPRESS "STOP AT LINE..."
525 PRINT:PRINT:PRINT"":STOP
```

```
1000 LET S1=122.45 :REM HOR. SCALE FACTOR
1005 LET S2=124.64 :REM VERT. SCALE FACTOR
1010 LET O1=13     :REM HOR. OFFSET FROM LEFT
1015 LET O2=390    :REM VERT. OFFSET TO CENTER
1020 LET Q=EXF(1,0,O2,0)  :REM  POSITION BEAM
1025 LET C0=1.5*S1
1030 FOR L=1 TO 5
1035    LET Q=EXF(1,C0,O2,1)  :REM  DRAW LINE SEGMENT
1040    LET C0=C0+S1/8
1045    LET Q=EXF(1,C0,O2,0)  :REM  SKIP A SMALL SEGMENT
1050    LET C0=C0+S1/4
1055    LET Q=EXF(1,C0,O2,1)  :REM  DRAW SHORT SEGMENT
1060    LET C0=C0+S1/8
1065    LET Q=EXF(1,C0,O2,0)  :REM  SKIP A SMALL SEGMENT
1070    LET C0=C0+1.5*S1
1075 NEXT L
1080 LET D3=D1:LET D4=D2:LET L3=L2
1085 LET S=1
1090 IF D3/S>6.18 GOTO 1105
1095 IF D4/S>6.18 GOTO 1105
1100 IF L3/S<8.25 GOTO 1115
1105 LET S=S+1
1110 GOTO 1090
1115 LET S1=S1/S:LET S2=S2/S
1120 LET X=780:LET Y=13:LET Q=EXF(1,X,Y,0)
1125 PRINT"SCALE  1 :";S;
1130 RETURN
2000 LET A1=(X1*S1)+O1
2005 LET B1=(R1*S2)+O2
2010 LET B3=(-R1*S2)+O2
2015 IF X1=0 GOTO 2040
2020 LET Q=EXF(1,A0,B0,0)  :REM POSITION PLOT BEAM
2025 LET Q=EXF(1,A1,B1,1)  :REM DRAW UPPER SIDE OF NOZZLE
2030 LET Q=EXF(1,A0,B2,0)  :REM POSITION BEAM TO LOWER SIDE
2035 LET Q=EXF(1,A1,B3,1)  :REM DRAW LOWER CONTOUR
2040 LET A0=A1
2045 LET B0=B1
2050 LET B2=B3
2055 RETURN
3000 PRINT:PRINT:PRINT"  THIS PRGM WILL PRINT OR PLOT A NOZZLE OR";
3005 PRINT" DIFFUSER PROFILE USING A PAIR"
3010 PRINT"OF CUBIC EQNS. OR A 5TH ORDER EQN.  THE INFLECTION POINT";
3015 PRINT" ON THE CONTOUR"
3020 PRINT"CAN BE SPECIFIED IN THE CUBIC CASE BY GIVING THE MATCH-";
3025 PRINT"POINT WHEN THE"
3030 PRINT"PROGRAM PROMPTS FOR INPUTS."
3035 PRINT:PRINT"INPUTS TO PRGM INCLUDE:":PRINT:PRINT" D1=INLET DIA."
3040 PRINT" D2=OUTLET DIA."
3045 PRINT" C.R.=CONTRACTION AREA RATIO CAN BE SPECIFIED INSTEAD OF D2"
3050 PRINT"      BY TYPING <CR> WHEN D2 IS ASKED FOR."
3055 PRINT" L/D1=LENGTH RATIO"
3060 PRINT" L=NOZZLE LENGTH CAN BE SPECIFIED INSTEAD OF L/D1"
3065 PRINT" MATCH POINT=X/L AT INFLECTION PT. (3RD ORDER ONLY) 0<M.P.<1"
3070 PRINT" NO. OF INTERVALS=NO. OF POINTS - 1."
3075 PRINT" PRINT OR PLOT OPTION"
3080 GOTO 30
3085 END
READY
```

APPENDIX F

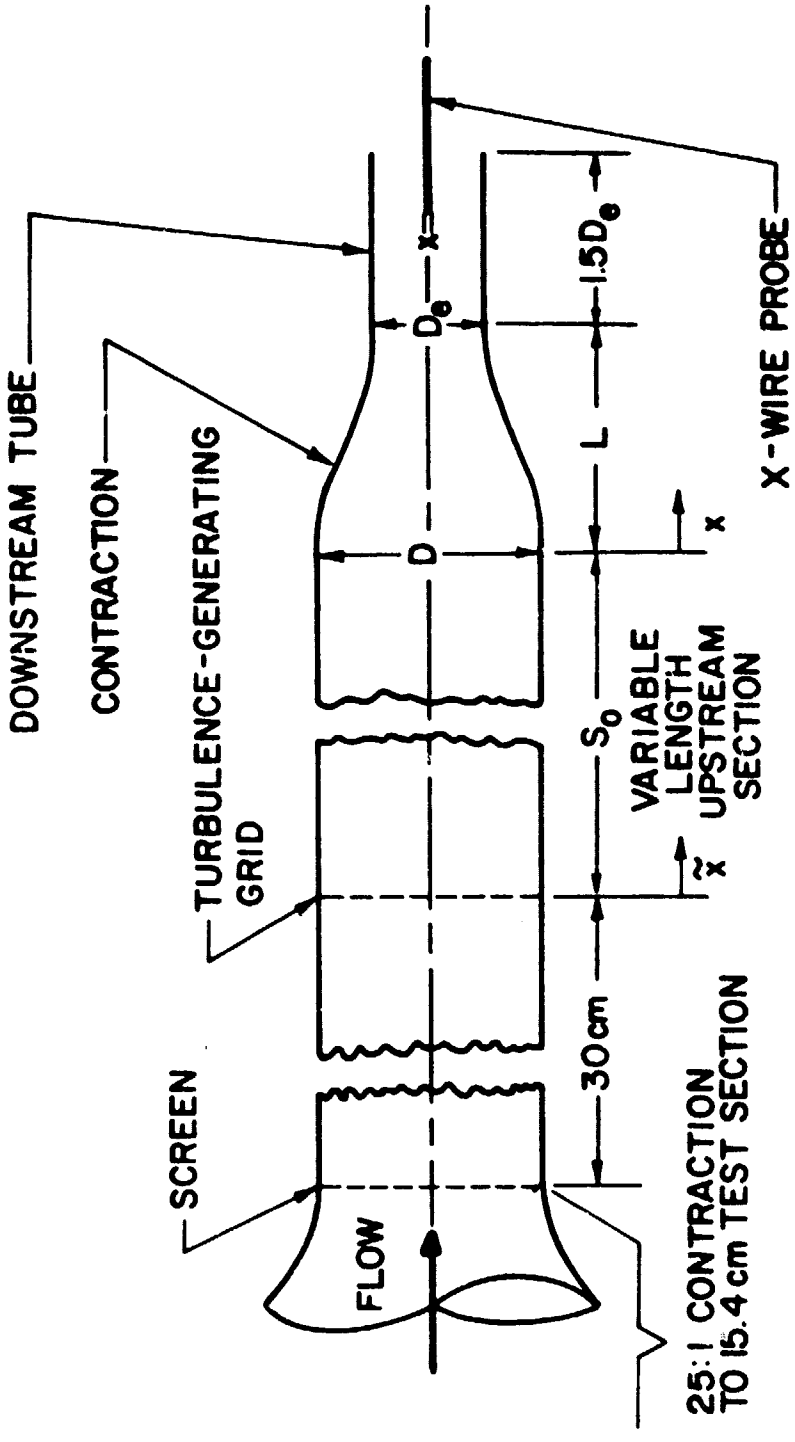

Figure 1. Schematic of Test Section

GRID	M [cm]	σ	t [mm]	S_o [cm]	$\tilde{X}/M$	TYPE *
J0	0.0847	0.33	$d^*=0.15$	7.6	90	A
J1	0.254	0.36	$d^*=0.64$	12.7	50	A
J2	0.635	0.34	1.19	22.9	36	B
J3	1.270	0.35	1.52	38.1	30	C
J4	1.746	0.36	1.40	43.2	25	C
J5	2.540	0.35	2.10	58.4	23	C

* A - SCREENS: WIRE DIA. = d
B - SQUARE HOLES IN SQUARE ARRAY } PUNCHED STEEL PLATES
C - ROUND HOLES IN TRIANGULAR ARRAY }

Figure 2. Characteristics of Grids

CONTRAC-TION	SYMBOL	TYPE	ϵ	ζ	L/D	D_e - [cm]	$C_d \equiv \bar{U}_e / \bar{U}_i$
C0	+	—	—	1	—	15.41	0.992
C1	□	MC	0.349	2	1	10.89	1.84
C2	◇	MC	0.447	4	1	7.70	3.48
C3	○	MC	0.557	9	1	5.14	7.64
C4	□	FO	0.500	9	1	5.14	7.95
C5	▷	MC	0.641	16	1	3.85	13.5
C6	△	MC	0.694	23.5	1	3.18	19.6
C7	▽	MC	0.753	36	1	2.57	29.6
C8	▷	MC	0.492	9	0.25	5.14	3.30
C9	△	MC	0.512	9	0.50	5.14	5.60
C10	▽	MC	0.594	9	1.50	5.14	8.40

Figure 3. Characteristics of Contractions

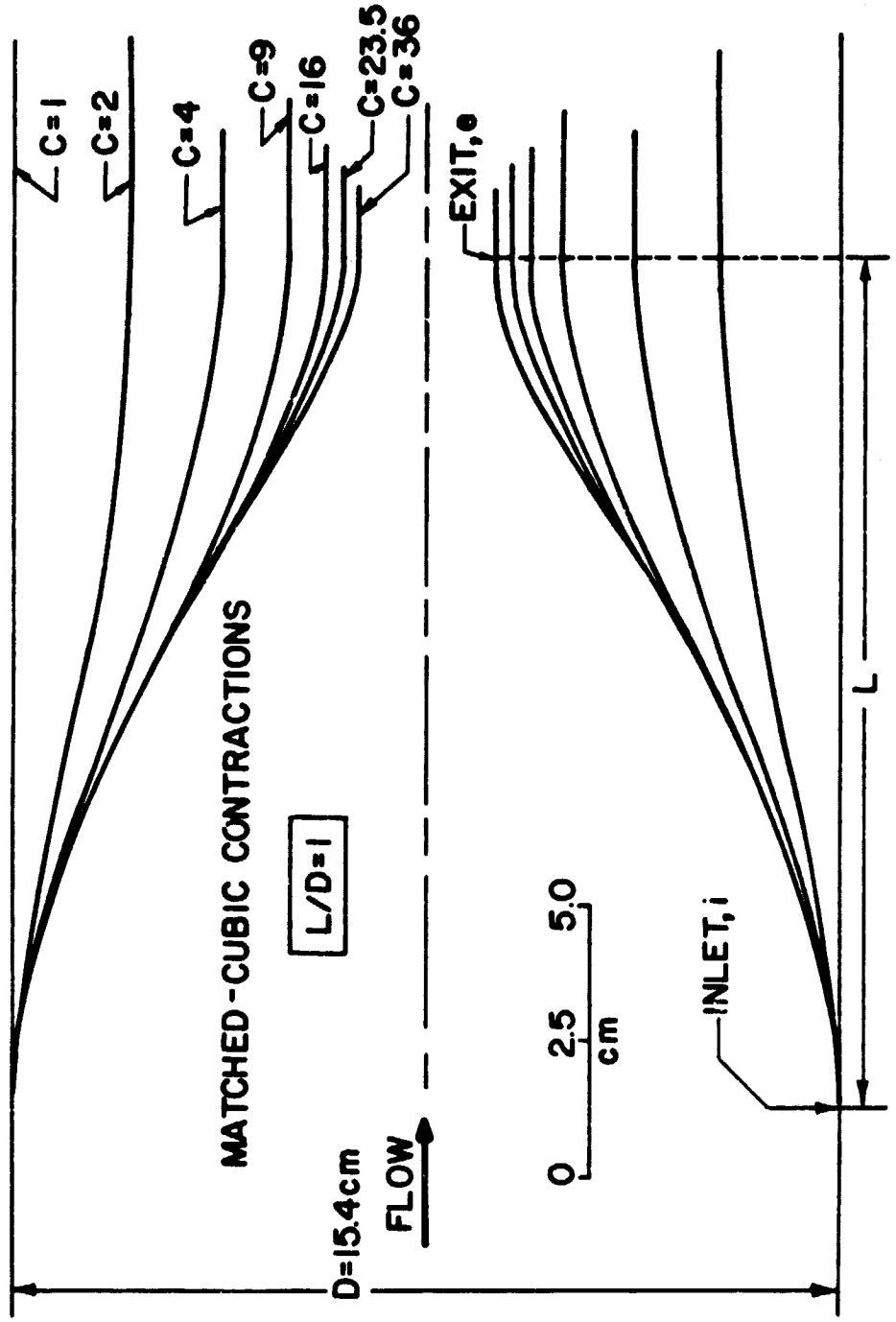

Figure 4. Contraction Shapes for Various Contraction Ratios; L/D = 1

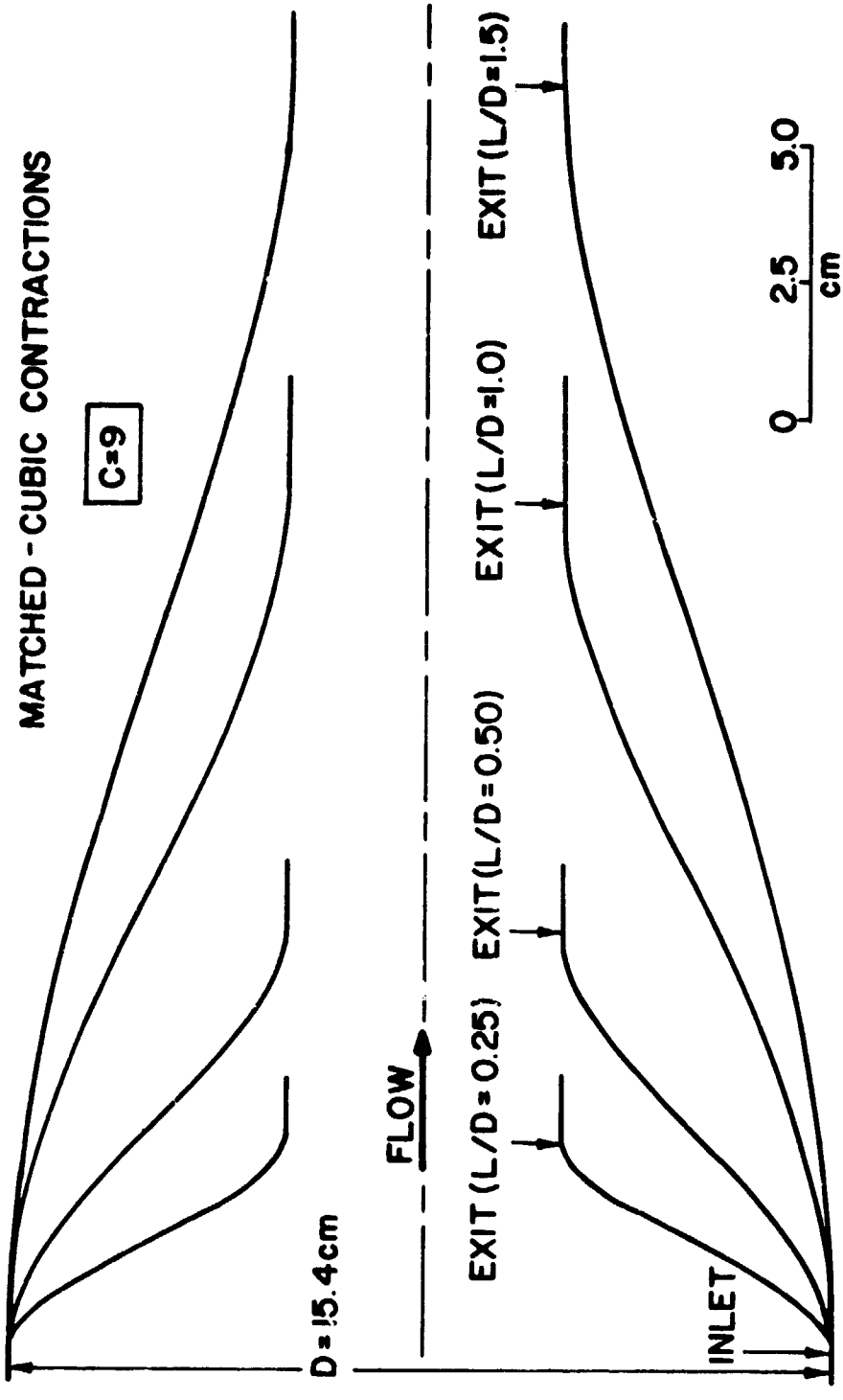

Figure 5. Contraction Shapes for Various Length-to-Diameter Ratios

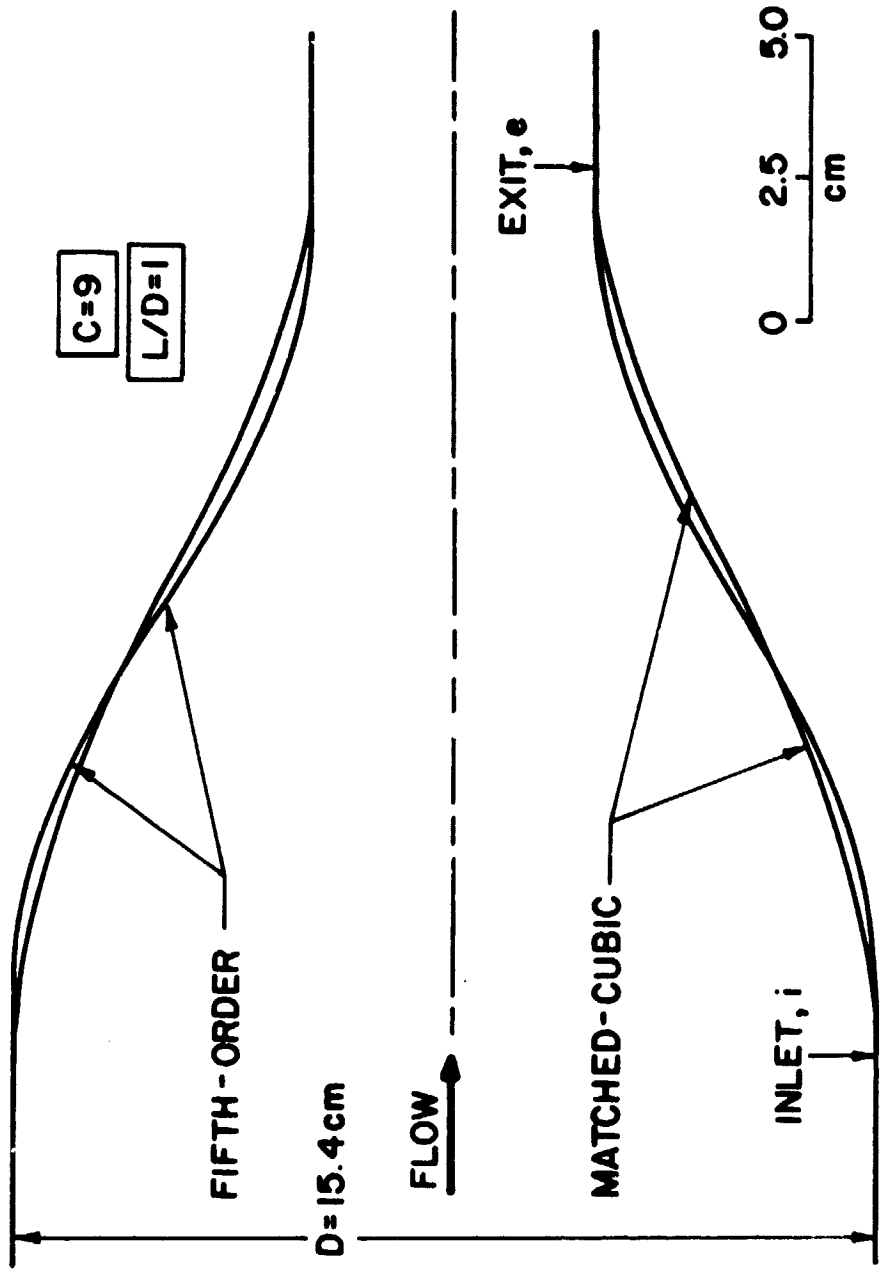

Figure 6. Shape Comparison Between Matched-Cubic and Fifth-Order Contractions

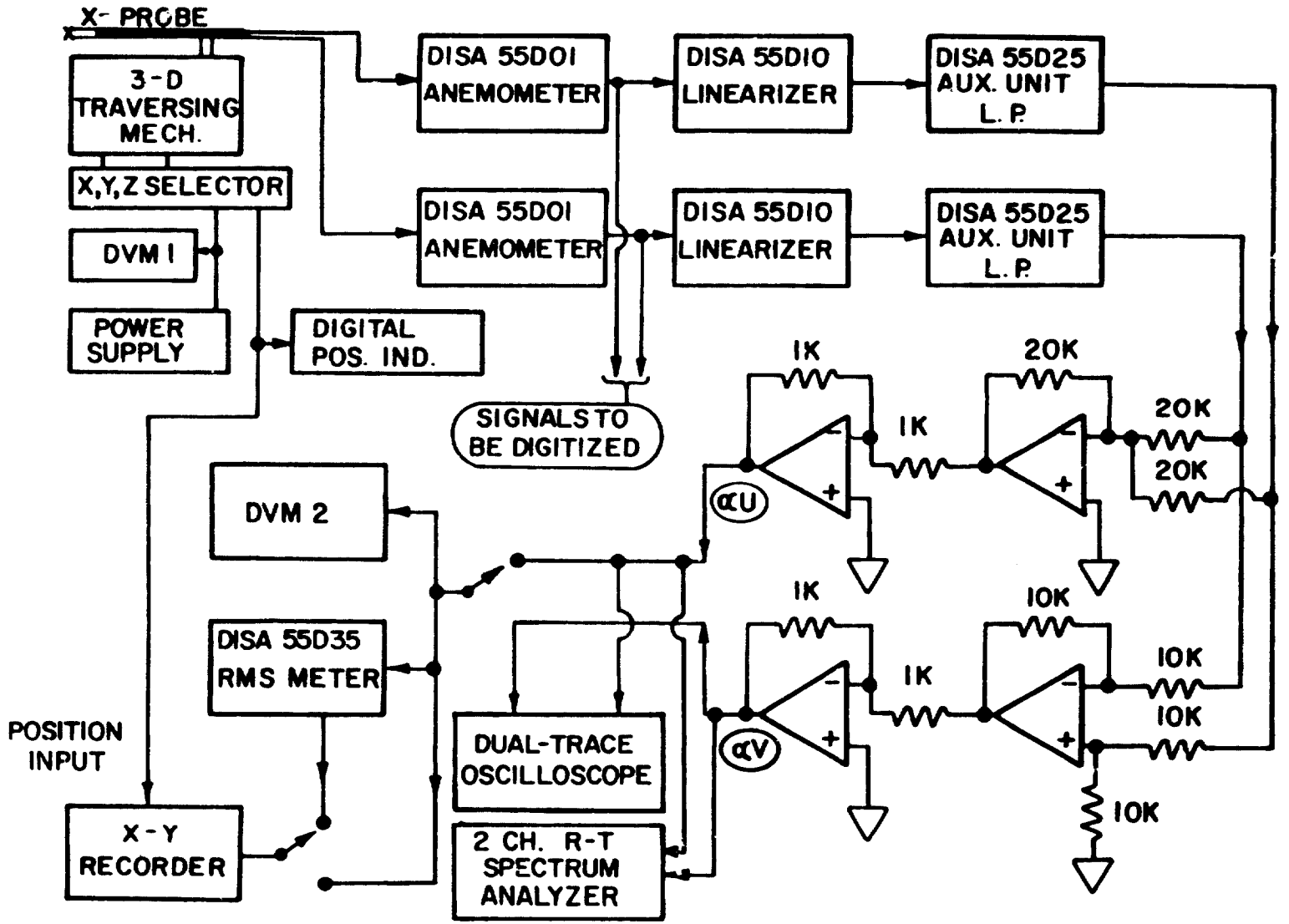

Figure 7. Instrumentation Schematic for Analog Signal Processing

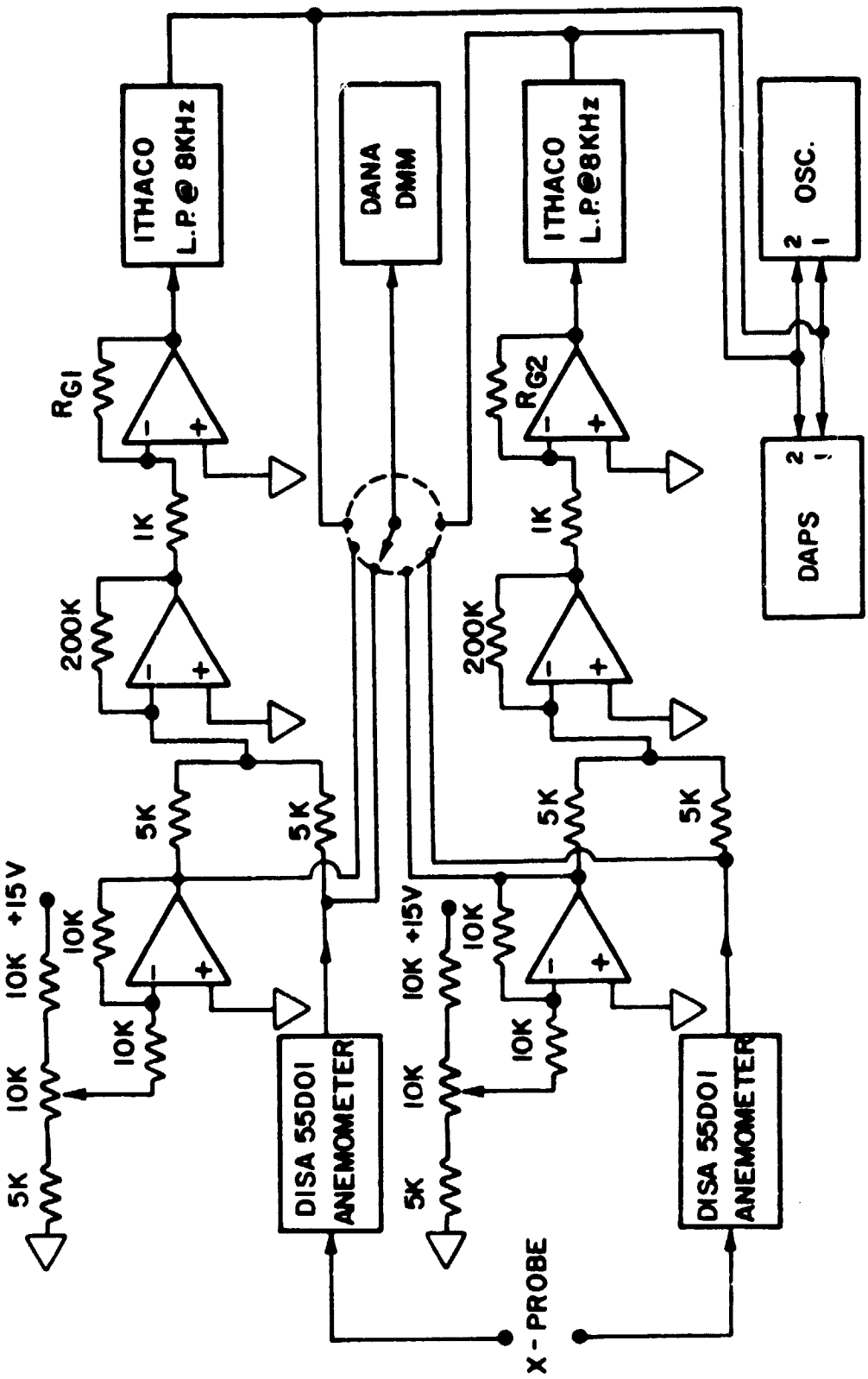

Figure 8. Instrumentation Schematic for Digital Data Acquistion

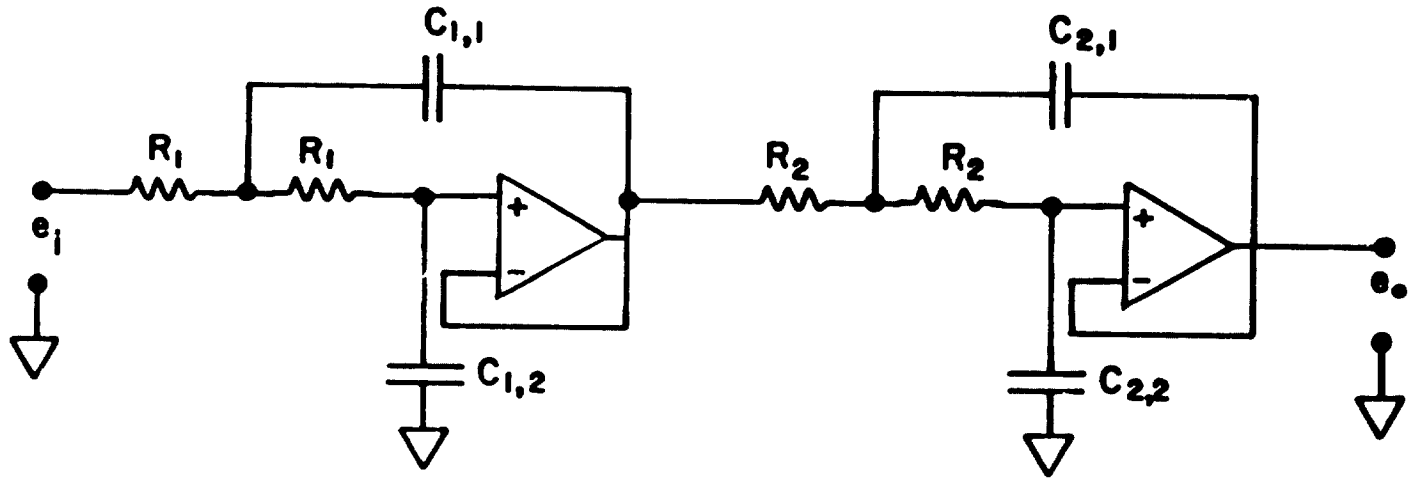

STAGE 1: $R_1 = 3145\Omega$

$C_{1,1} = .022\mu F$

$C_{1,2} = .0047\mu F$

$f_c = 5$ kHz

$\zeta = 0.46$

STAGE 2: $R_1 = 4647\Omega$

$C_{2,1} = .01\mu F$

$C_{2,2} = .0047\mu F$

$f_c = 5$ kHz

$\zeta = 0.69$

Figure 9. Schematic of a Fourth-Order Low-Pass Filter

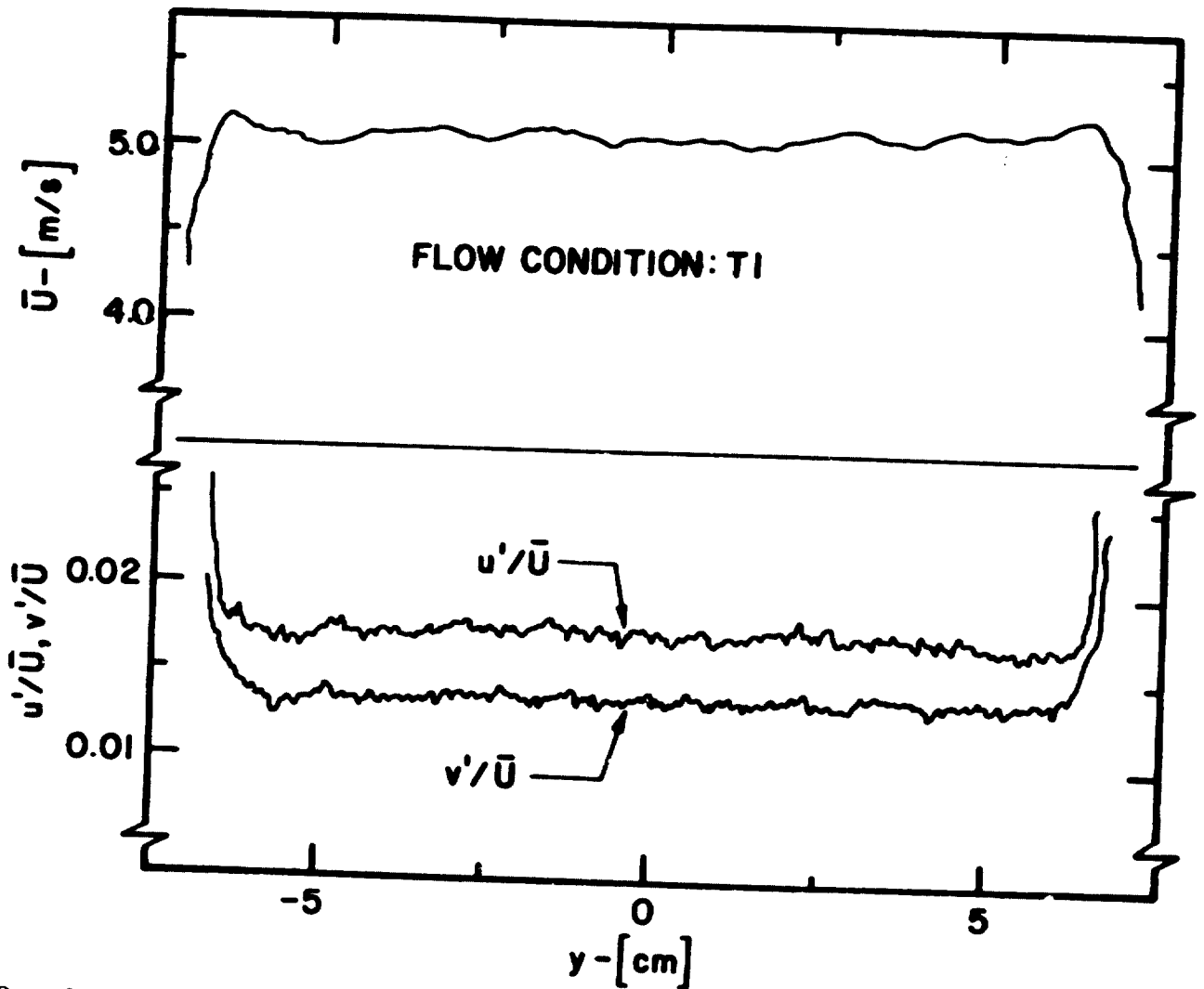

Figure 10. Lateral Profiles of Mean-Velocity and Turbulence Intensities for Flow Condition TI

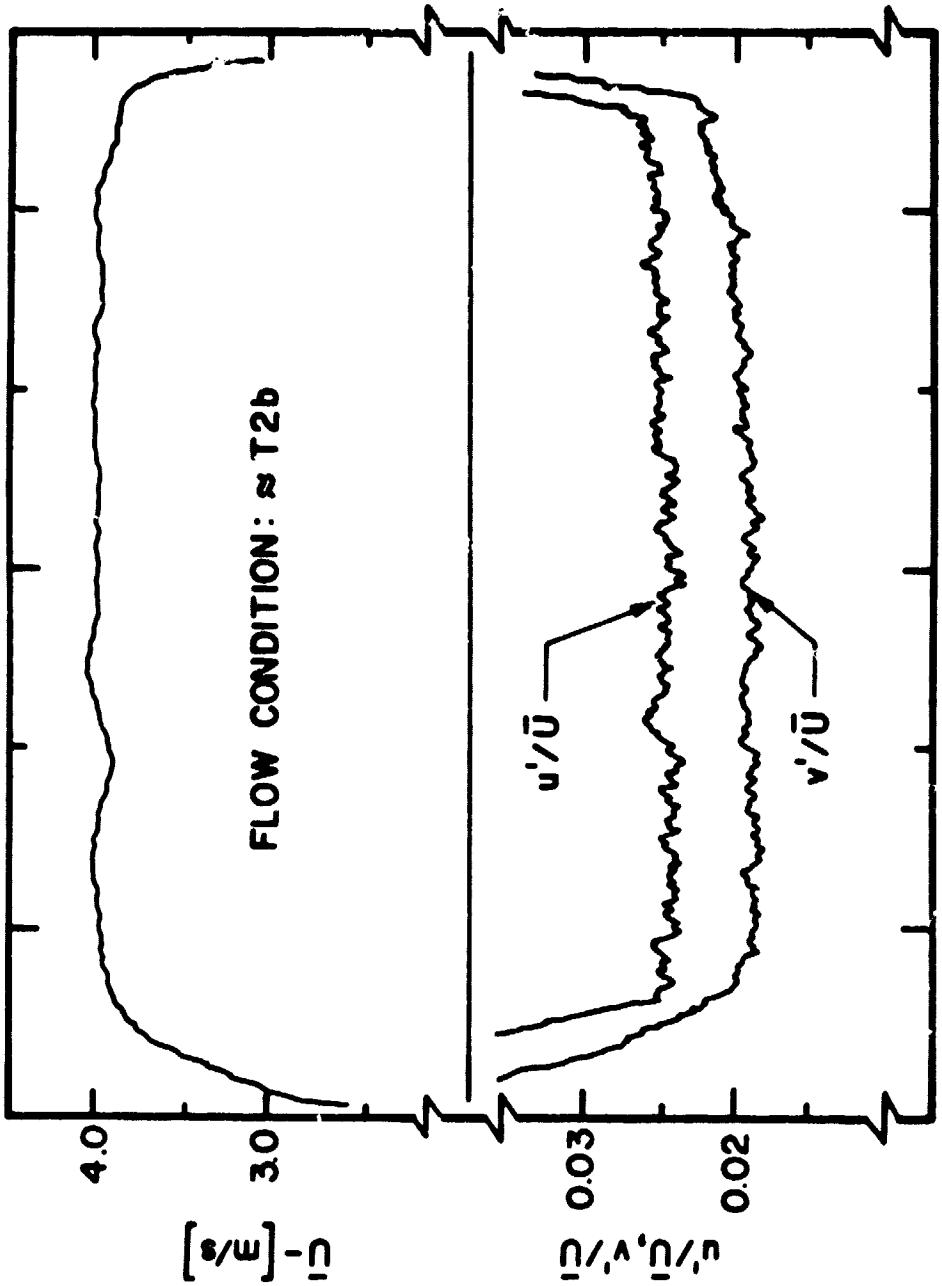

Figure 11. Lateral Profiles of Mean-Velocity and Turbulence Intensities for Flow Condition T2b

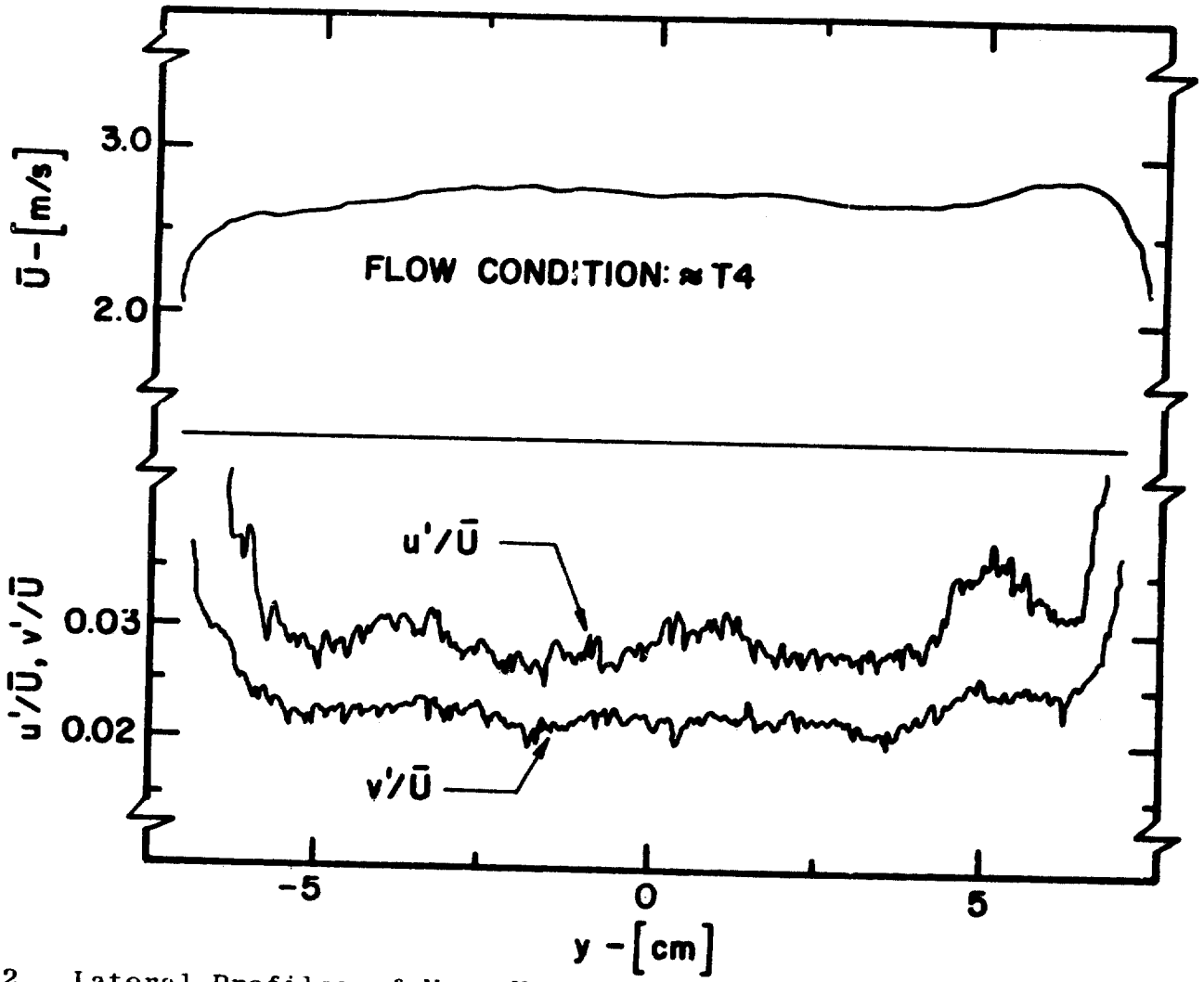

Figure 12. Lateral Profiles of Mean-Velocity and Turbulence Intensities for Flow Condition T4

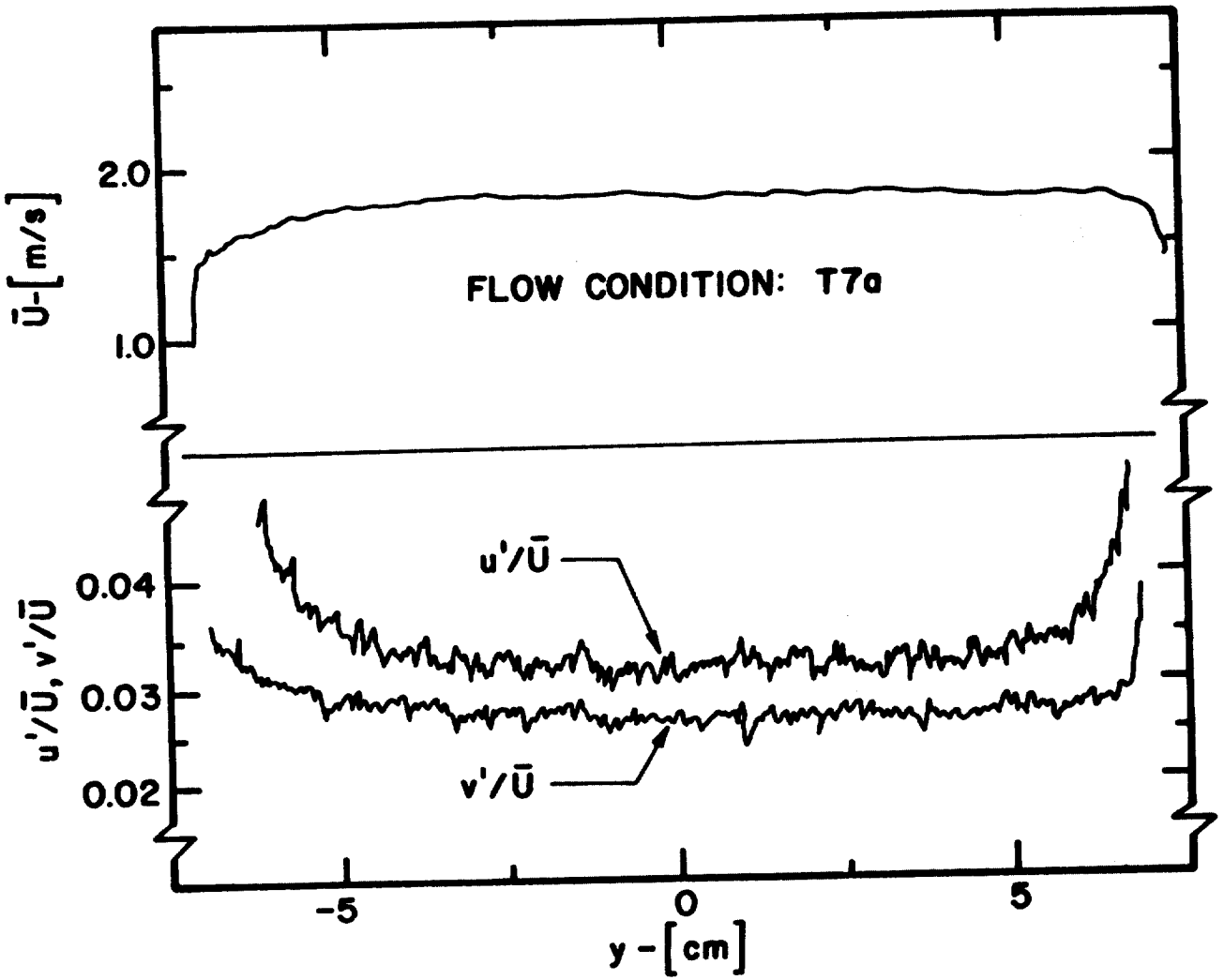

Figure 13. Lateral Profiles of Mean-Velocity and Turbulence Intensities for Flow Condition T7a

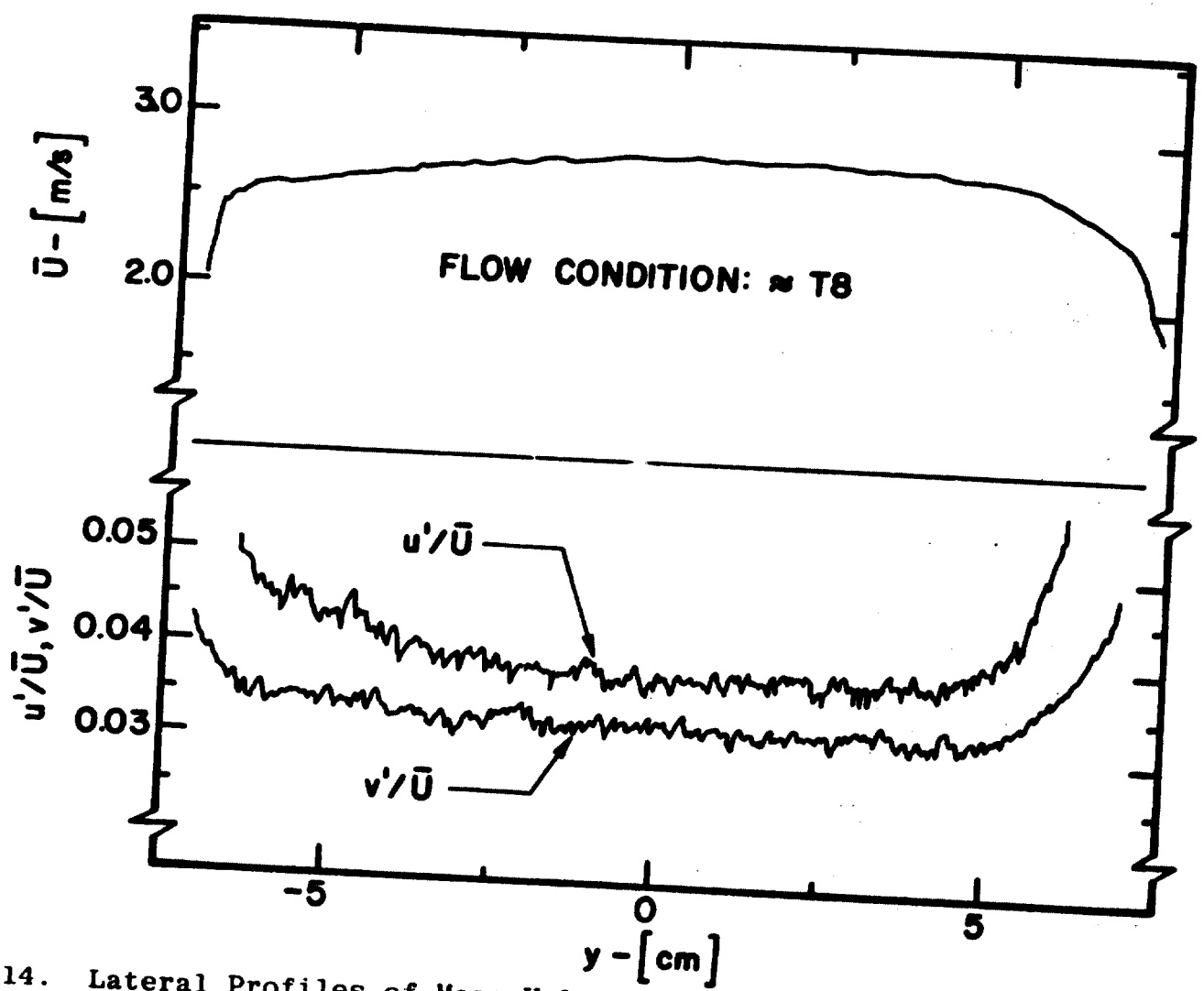

Figure 14. Lateral Profiles of Mean-Velocity and Turbulence Intensities for Flow Condition T8

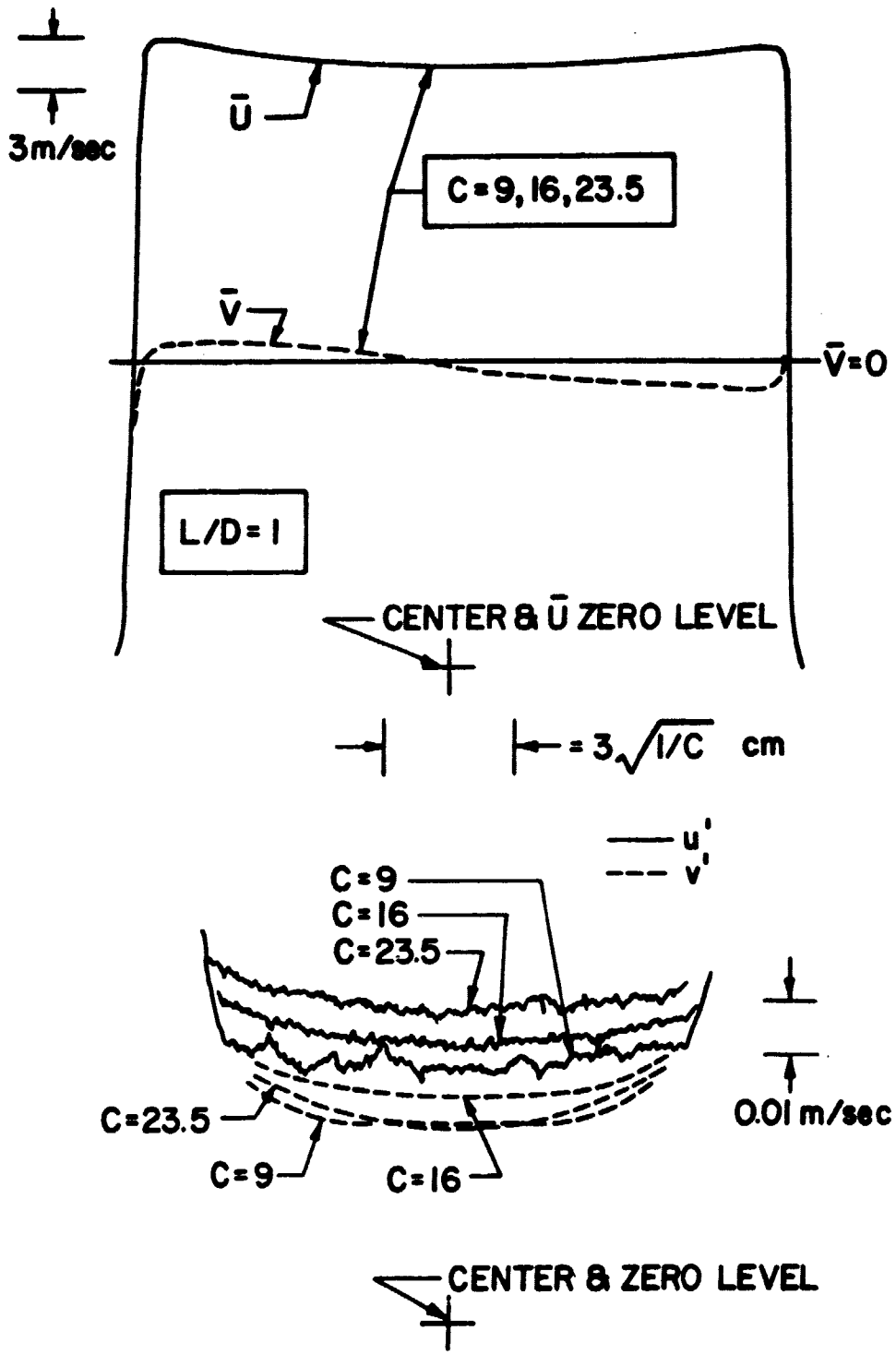

Figure 15. Normalized Lateral Profiles of Mean and Turbulence Velocities Downstream of Contractions with Different Contraction Ratios

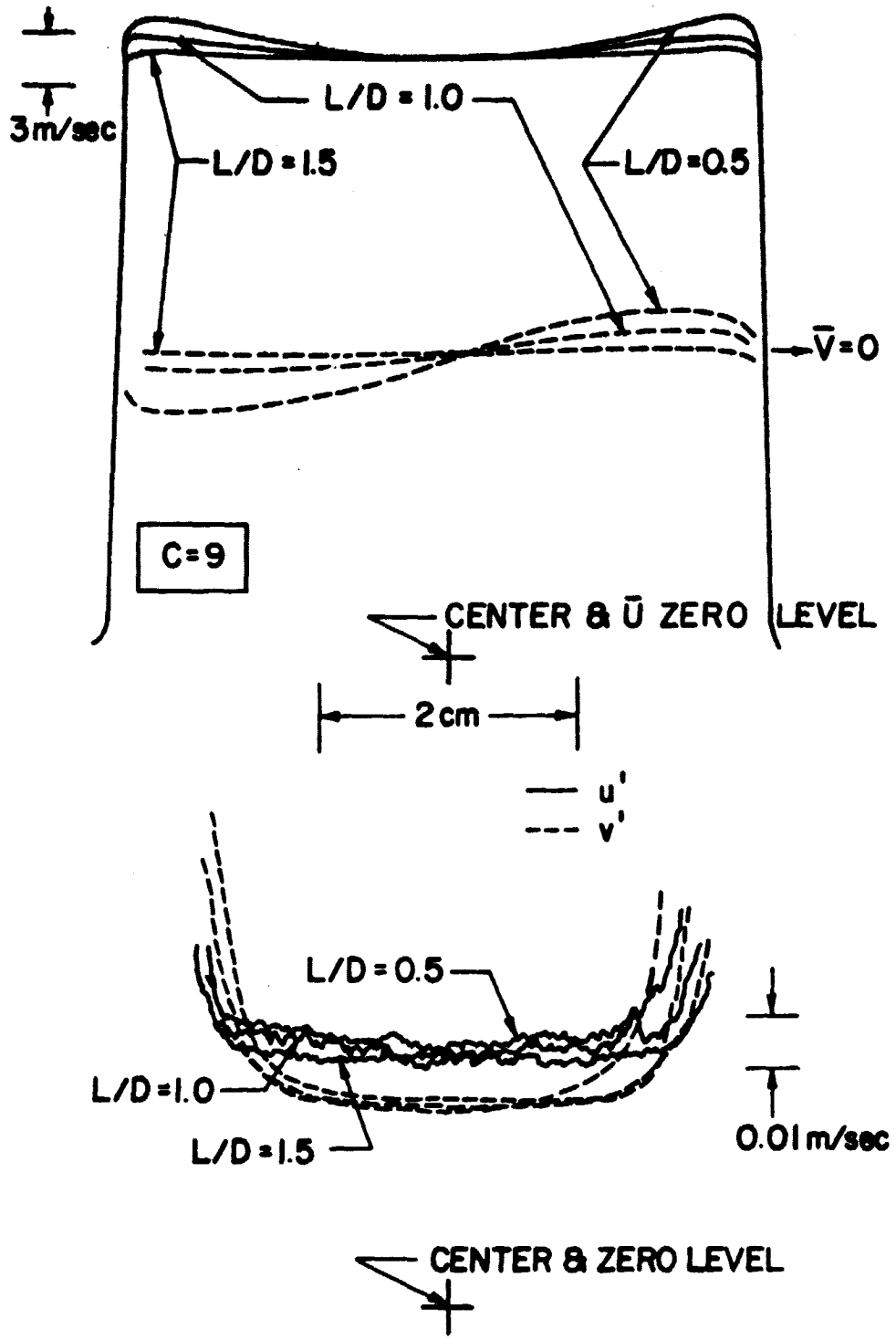

Figure 16. Normalized Lateral Profiles of Mean and Turbulence Velocities Downstream of Contractions with Different L/D Ratios

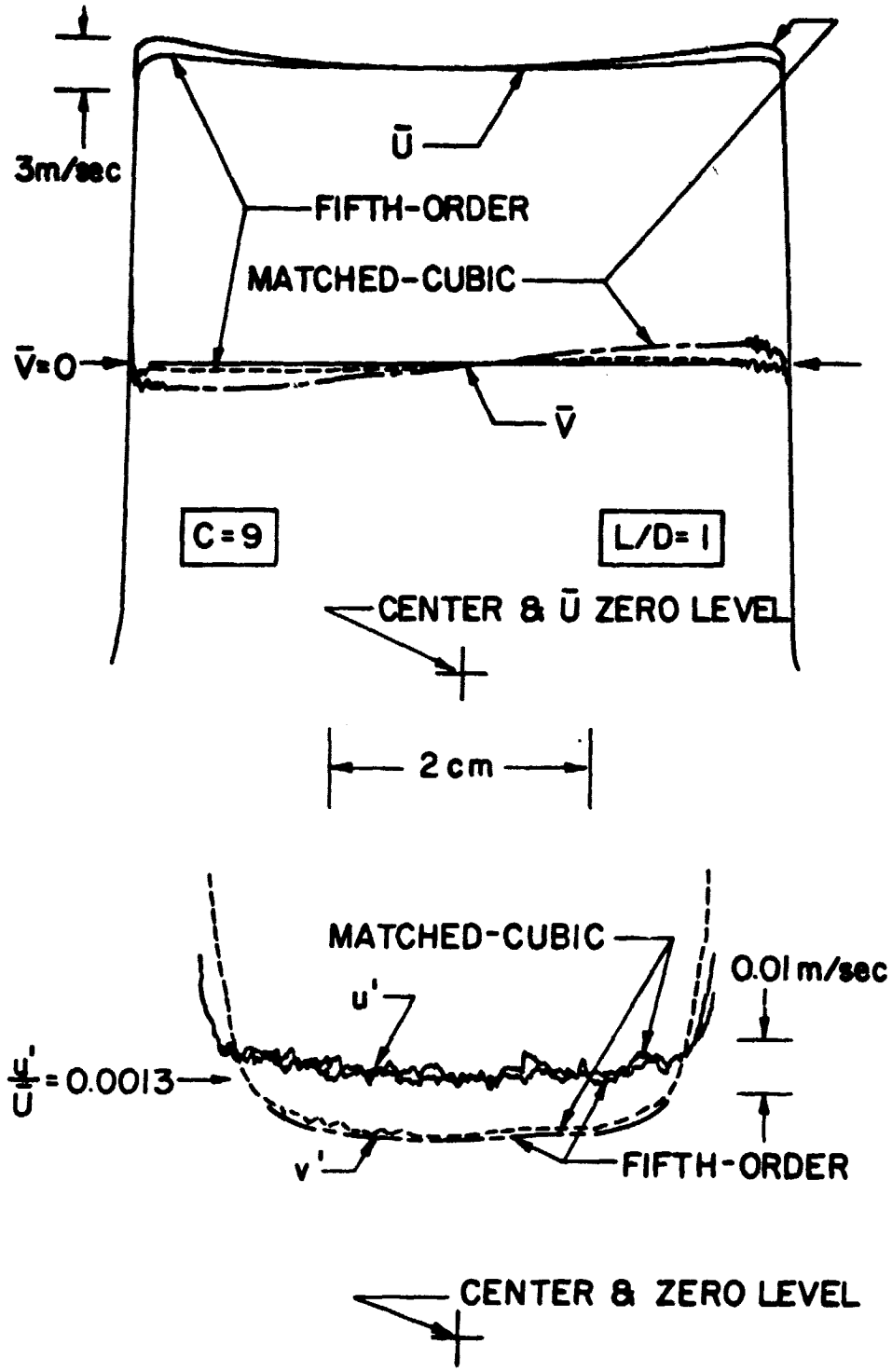

Figure 17. Normalized Lateral Profiles of Mean and Turbulence Velocities Downstream of Matched-Cubic and Fifth-Order Contractions

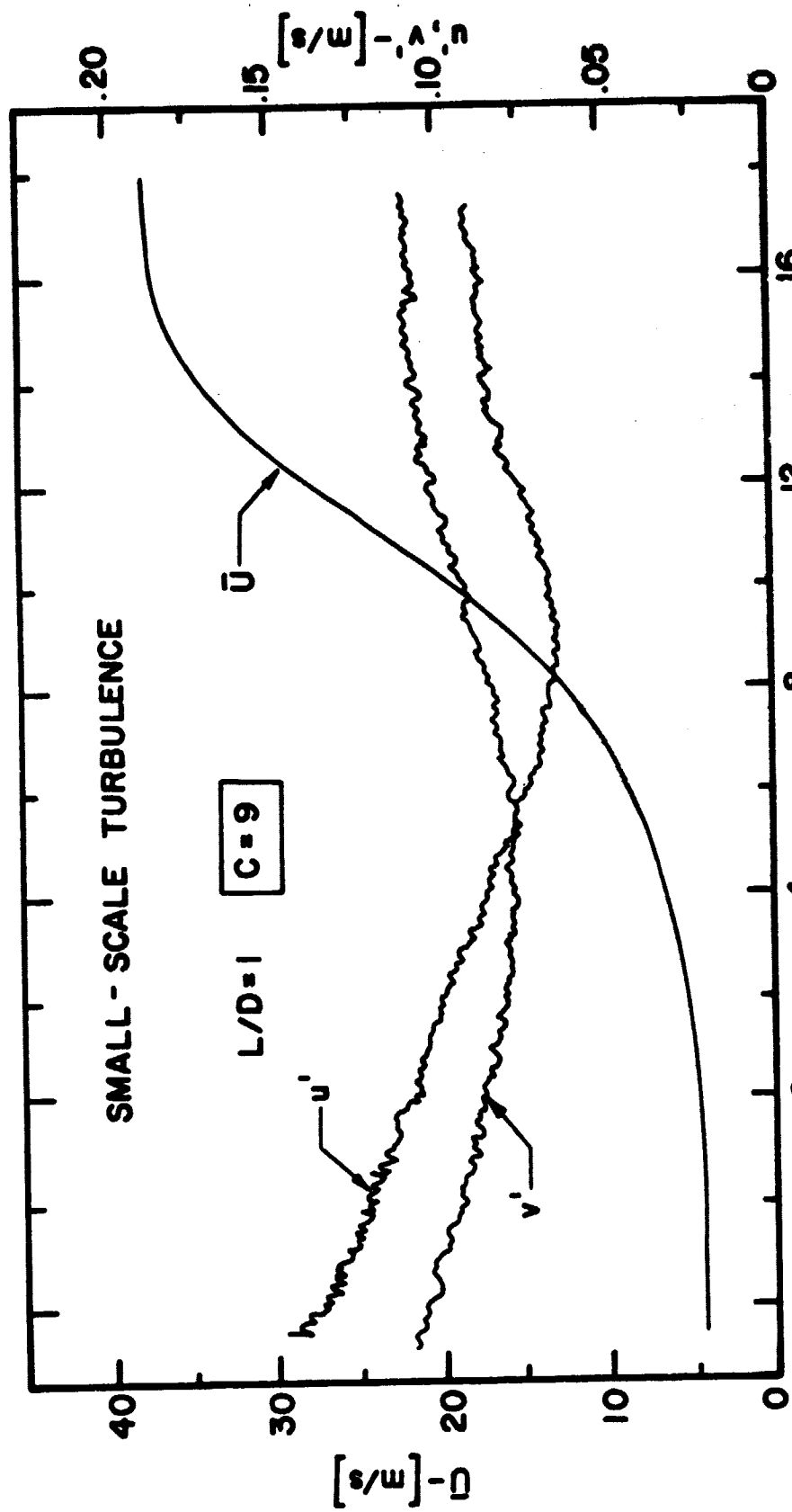

Figure 18. Streamwise Profiles of Mean and Turbulence Velocities through a Contraction for Small-Scale Turbulence

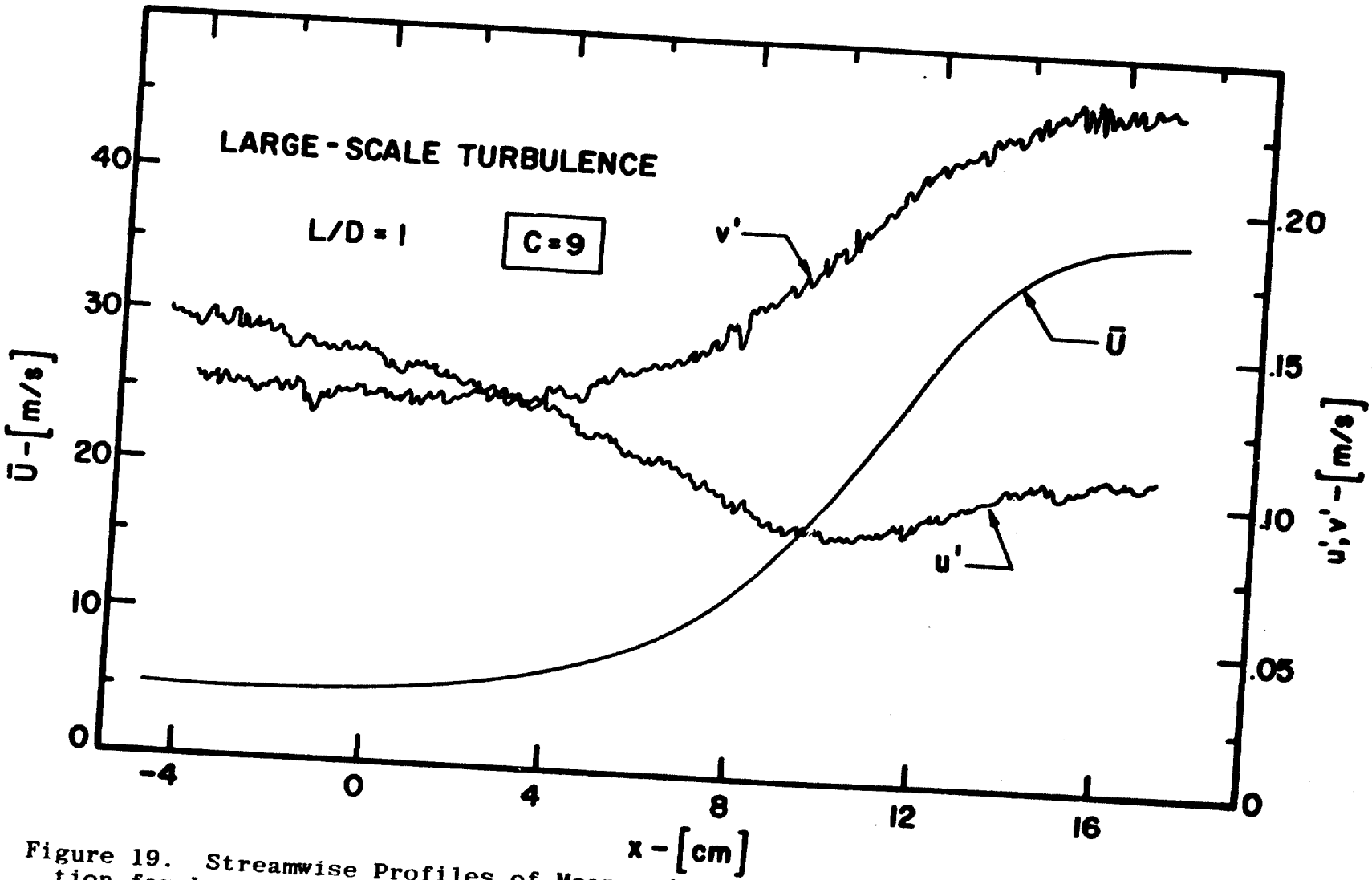

Figure 19. Streamwise Profiles of Mean and Turbulence Velocities through a Contraction for Large-Scale Turbulence

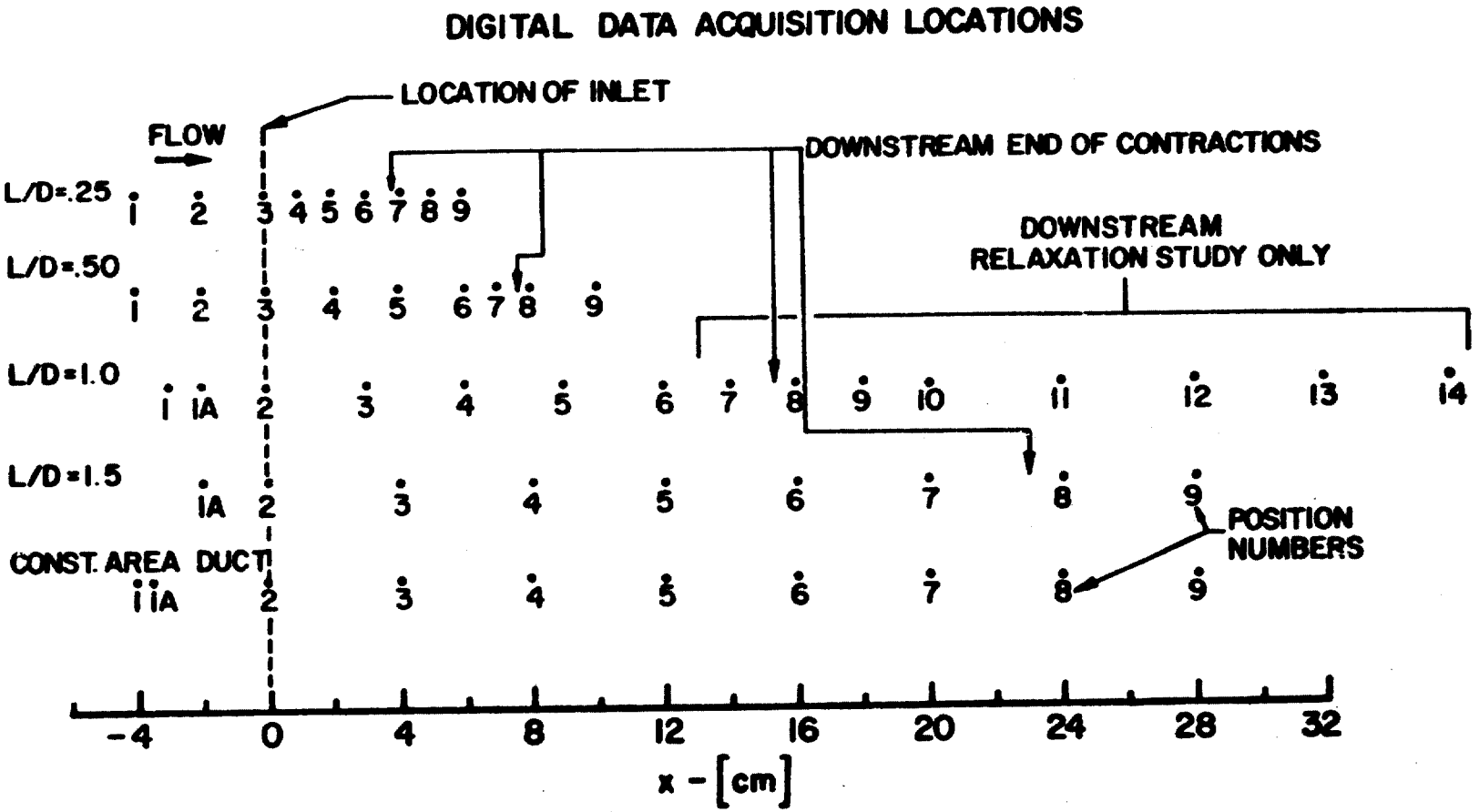

Figure 20. Schematic of On-Axis Digital Data Acquisition Positions

CON-TRACTION \ TEST FLOW CONDI-TION	T1	T2a	T2b	T3a	T3b	T3c	T4	T5a	T5b	T6	T7a	T7b	T8
C0	⊗	⊗	⊗	⊗	⊗	⊗	⊗	⊗	⊗	⊗	⊗	⊗	⊗
C1	⊗	X	X	⊗	⊗	–	X	⊗	–	⊗	X	⊗	–
C2	⊗	X	X	X	X	X	X	⊗	⊗	X	X	⊗	X
C3	⊗	X	X	⊗	⊗	X	⊗	⊗	⊗	⊗	⊗	⊗	⊗
C4	⊗	–	X	–	–	–	–	–	–	–	⊗	–	–
C5	–	–	⊗	⊗	–	–	X	X	–	⊗	⊗	–	⊗
C6	–	–	–	⊗	–	–	–	X	–	–	⊗	–	–
C7	–	–	–	⊗	–	–	–	X	–	–	⊗	–	–
C8	⊗	–	X	–	–	–	–	–	–	–	⊗	–	–
C9	⊗	–	X	–	–	–	–	–	–	–	⊗	–	–
C10	⊗	–	X	–	–	–	–	–	–	–	⊗	–	–

X - DATA FILES ACQUIRED AT 9 POSITIONS ALONG CENTERLINE. EACH FILE CONTAINS 100 RECORDS OF 2048 SAMPLES/CH. FOR TWO CHANNELS OF X-WIRE PROBE DATA.

O - DETAILED PLOTS OF STREAMWISE DEVELOPMENT ARE PRESENTED HERE.

Figure 21. Combinations of Contractions and Flow Conditions Used in Present Investigation

CONTRACTION / TEST-FLOW CONDITION	C2	C3	
		OFF-AXIS DATA	DOWNSTREAM RELAXATION DATA
T1	–	Ⓧ	Ⓨ
T4	–	Ⓧ	Ⓨ
T7a	Ⓩ	Ⓧ	Ⓨ

Ⓧ – DATA FILES ACQUIRED AT 7 OFF-AXIS POSITIONS AND 2 ON-AXIS POSITIONS.

Ⓨ – DATA FILES ACQUIRED AT 8 POSITIONS ALONG CENTERLINE, INCLUDING 5 POSITIONS FARTHER DOWNSTREAM OF CONTRACTION EXIT IN CONSTANT-AREA DUCT.

Ⓧ & Ⓨ – EACH FILE CONTAINS 100 RECORDS OF 2048 SAMPLES/CH. FOR TWO CHANNELS OF X-WIRE PROBE DATA.

Ⓩ – TWO-PROBE DATA ACQUIRED AT 4 STREAMWISE POSITIONS WITH ONE PROBE ON CENTERLINE, EACH WITH 6 DIFFERENT PROBES' SEPARATION. EACH FILE CONTAINS 100 RECORDS OF 2048 SAMPLES/CH. FOR 4 CHANNELS OF DATA FROM 2 X-WIRE PROBES.

Figure 22. Contractions and Flow Conditions Used for Off-Axis and Downstream Relaxation Study

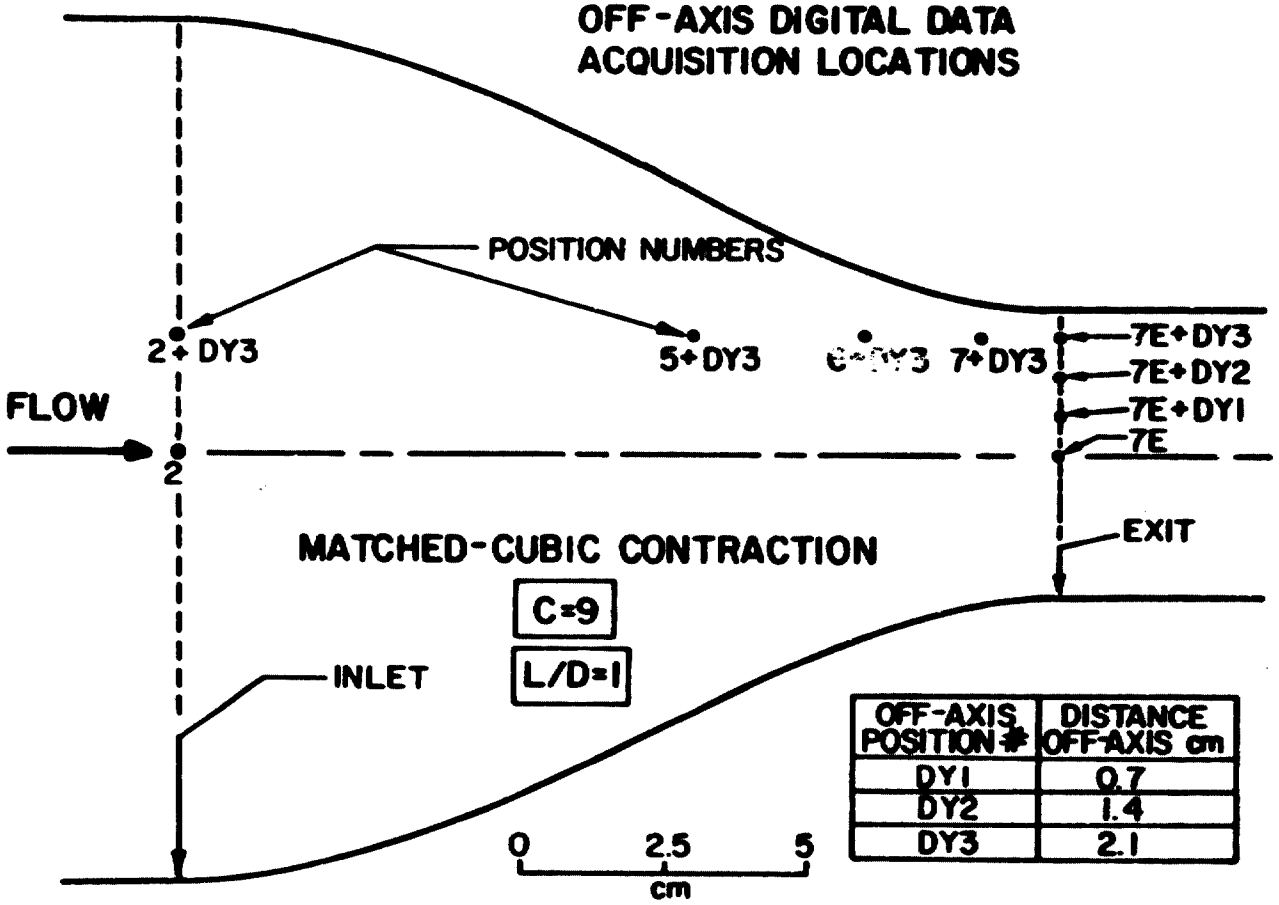

OFF-AXIS POSITION #	DISTANCE OFF-AXIS cm
DY1	0.7
DY2	1.4
DY3	2.1

Figure 23. Off-Axis Digital Data Acquisition Positions

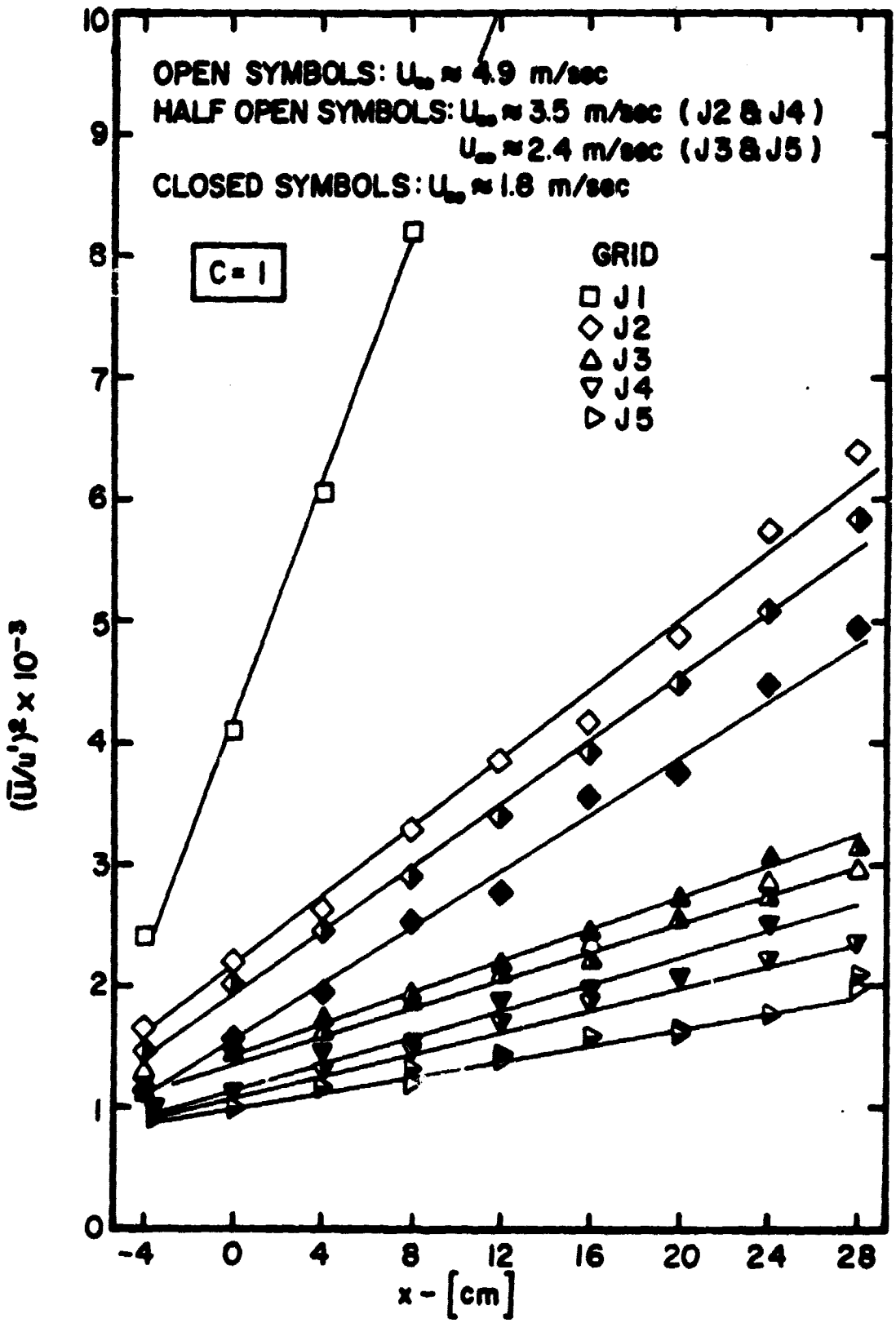

Figure 24. Turbulence-Energy Decay of Streamwise Component of Test Flow Conditions

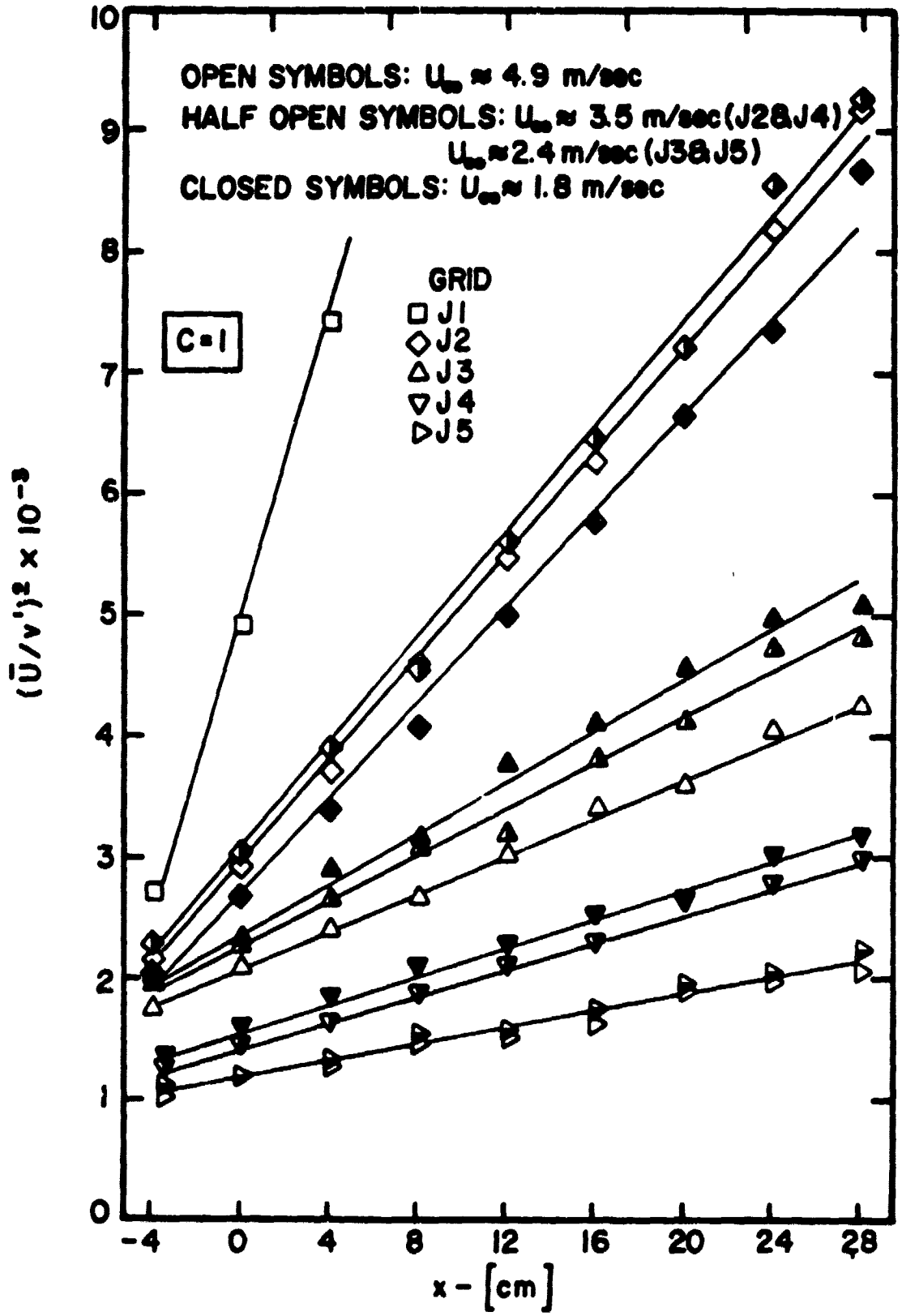

Figure 25. Turbulence-Energy Decay of Radial Component of Test Flow Conditions

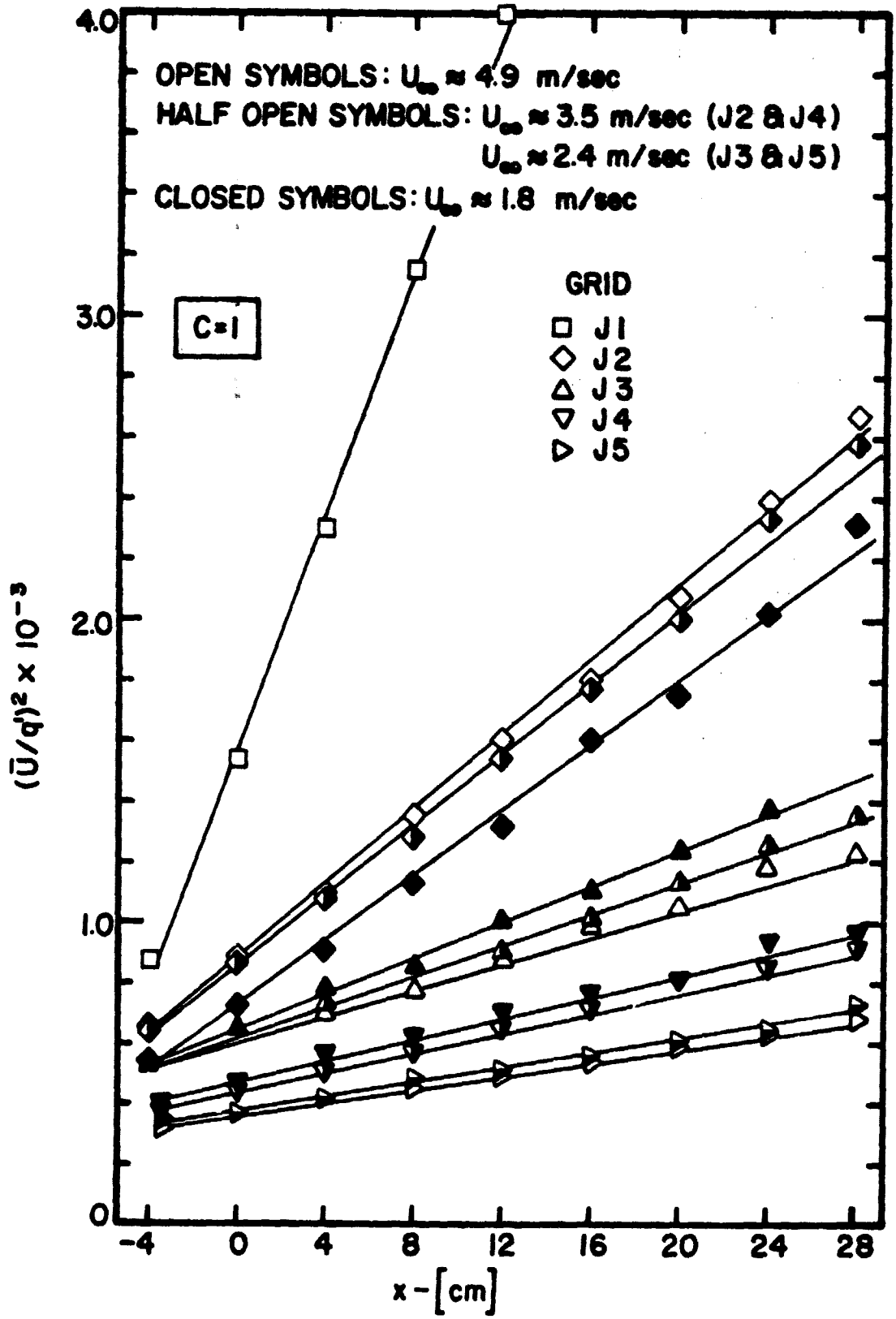

Figure 26. Total Turbulence-Energy Decay of Test Flow Conditions

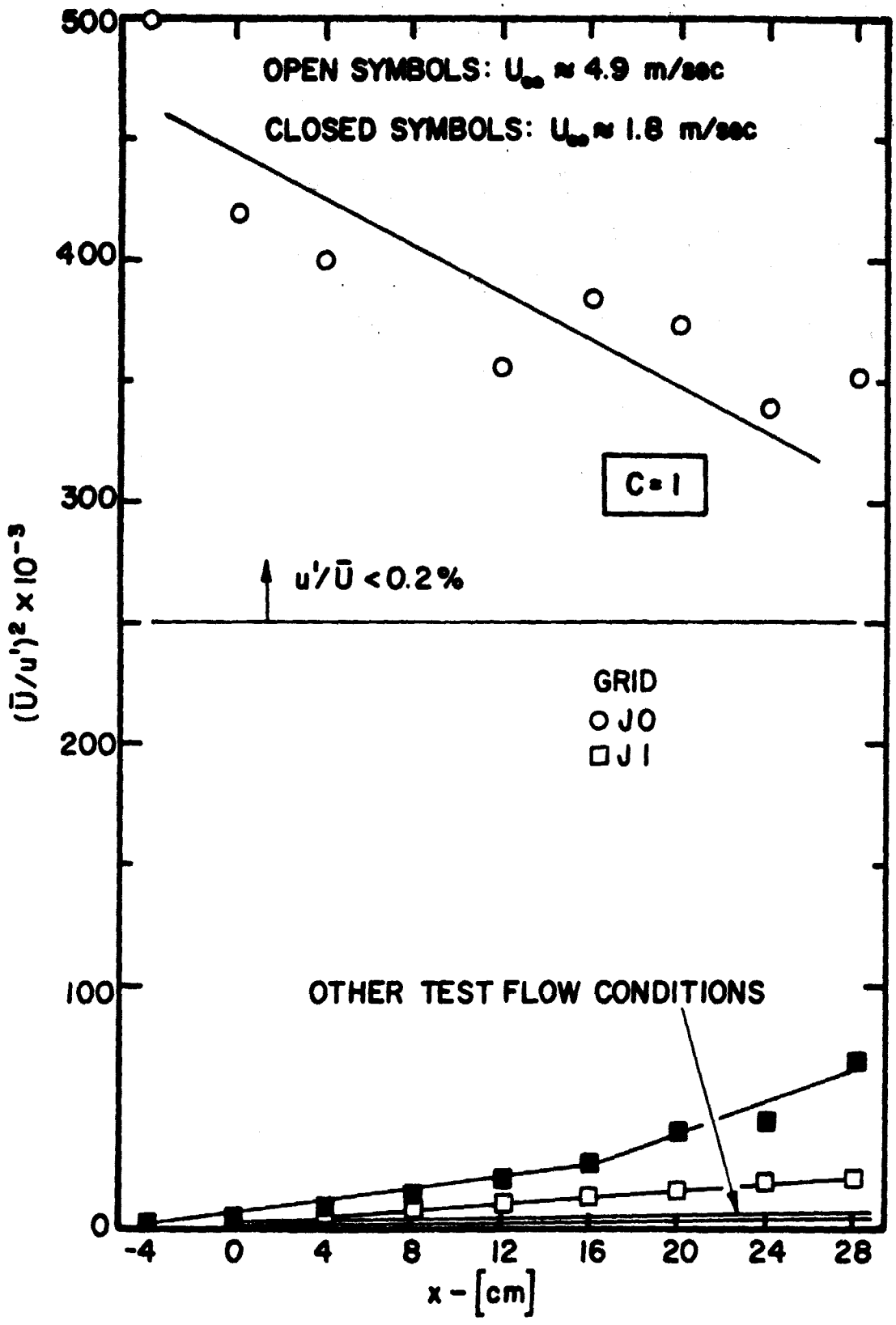

Figure 27. Turbulence-Energy Decay of Streamwise Component of Test Flow Conditions

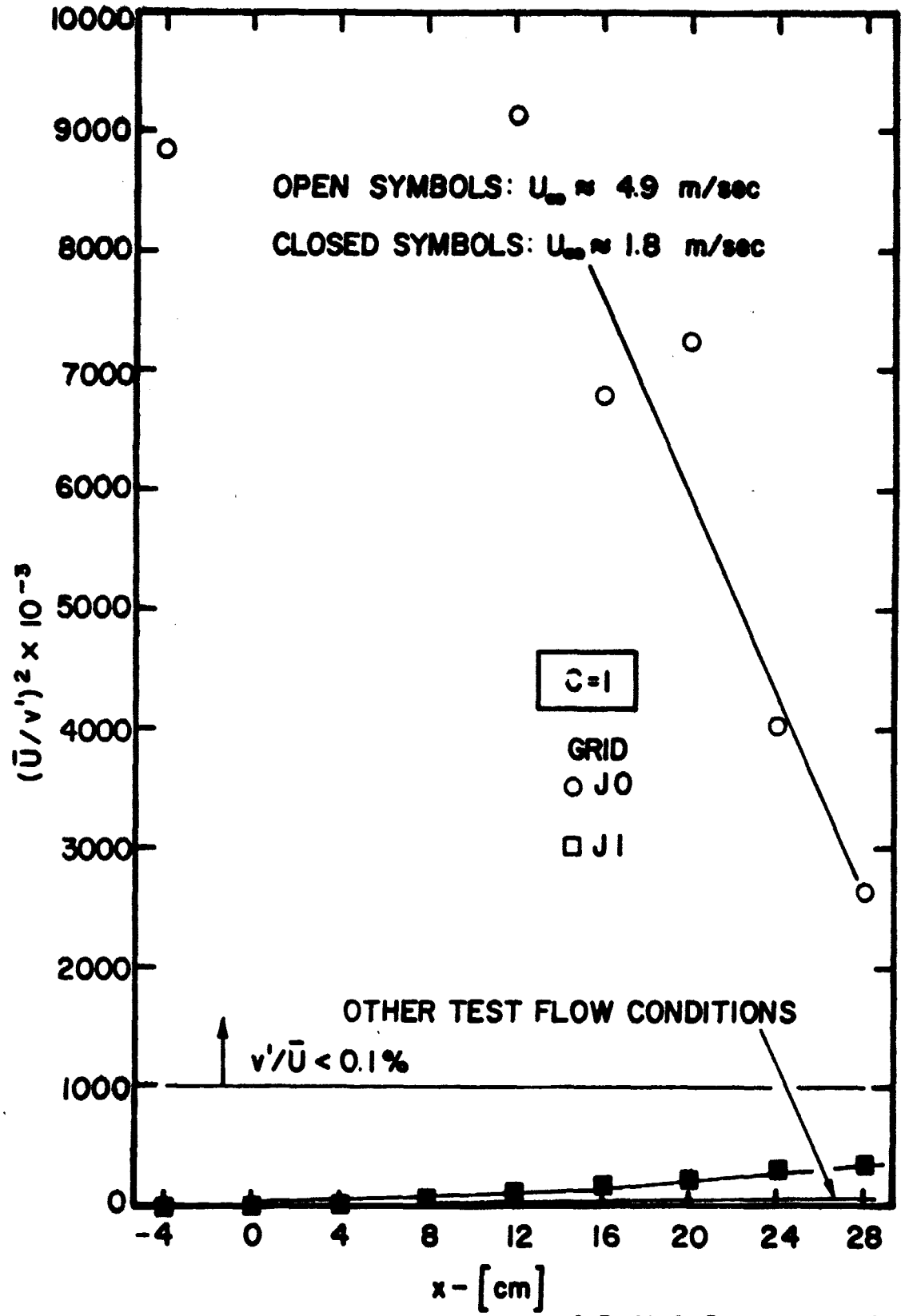

Figure 28. Turbulence-Energy Decay of Radial Component of Test Flow Conditions

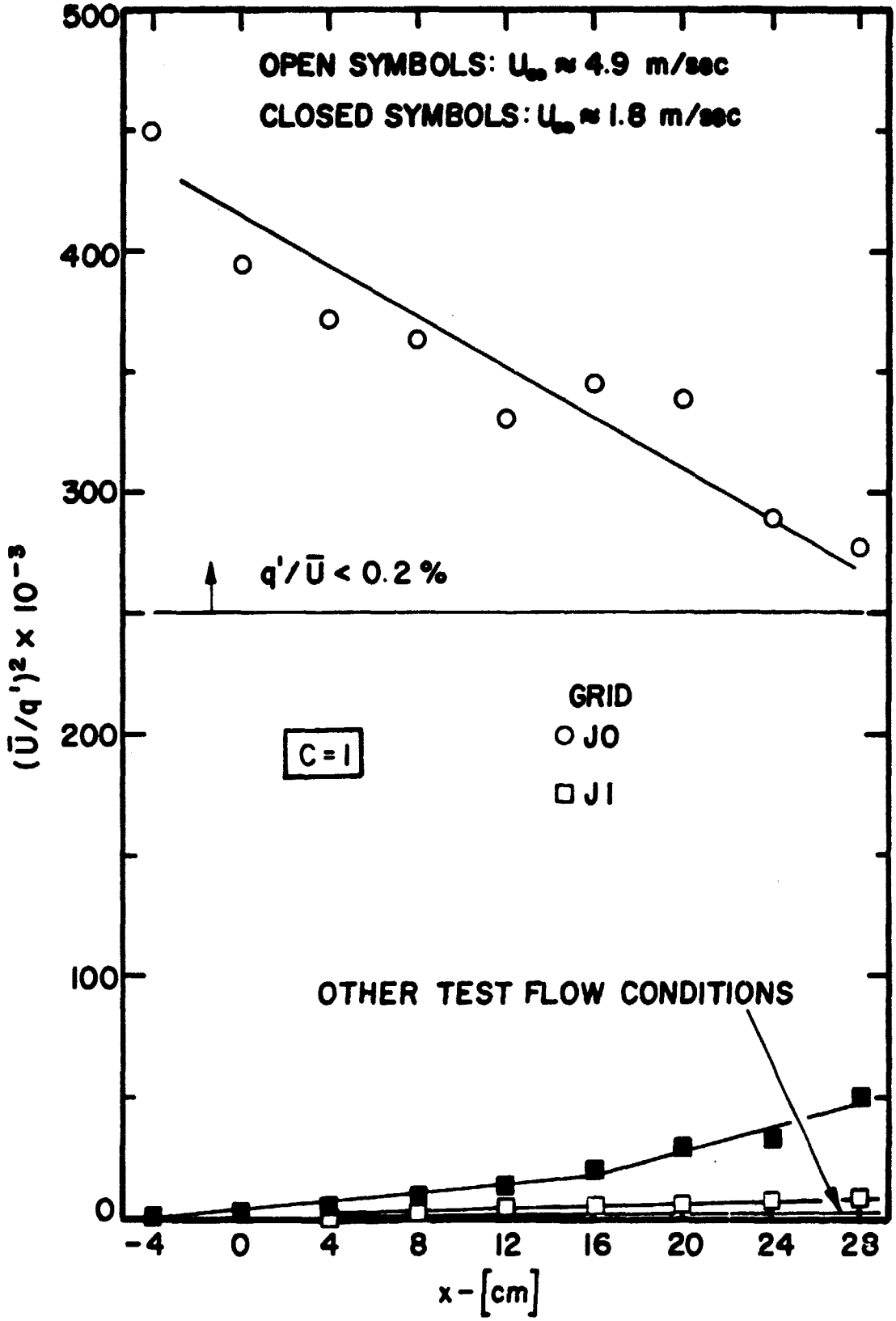

Figure 29. Total Turbulence-Energy Decay of Test Flow Conditions

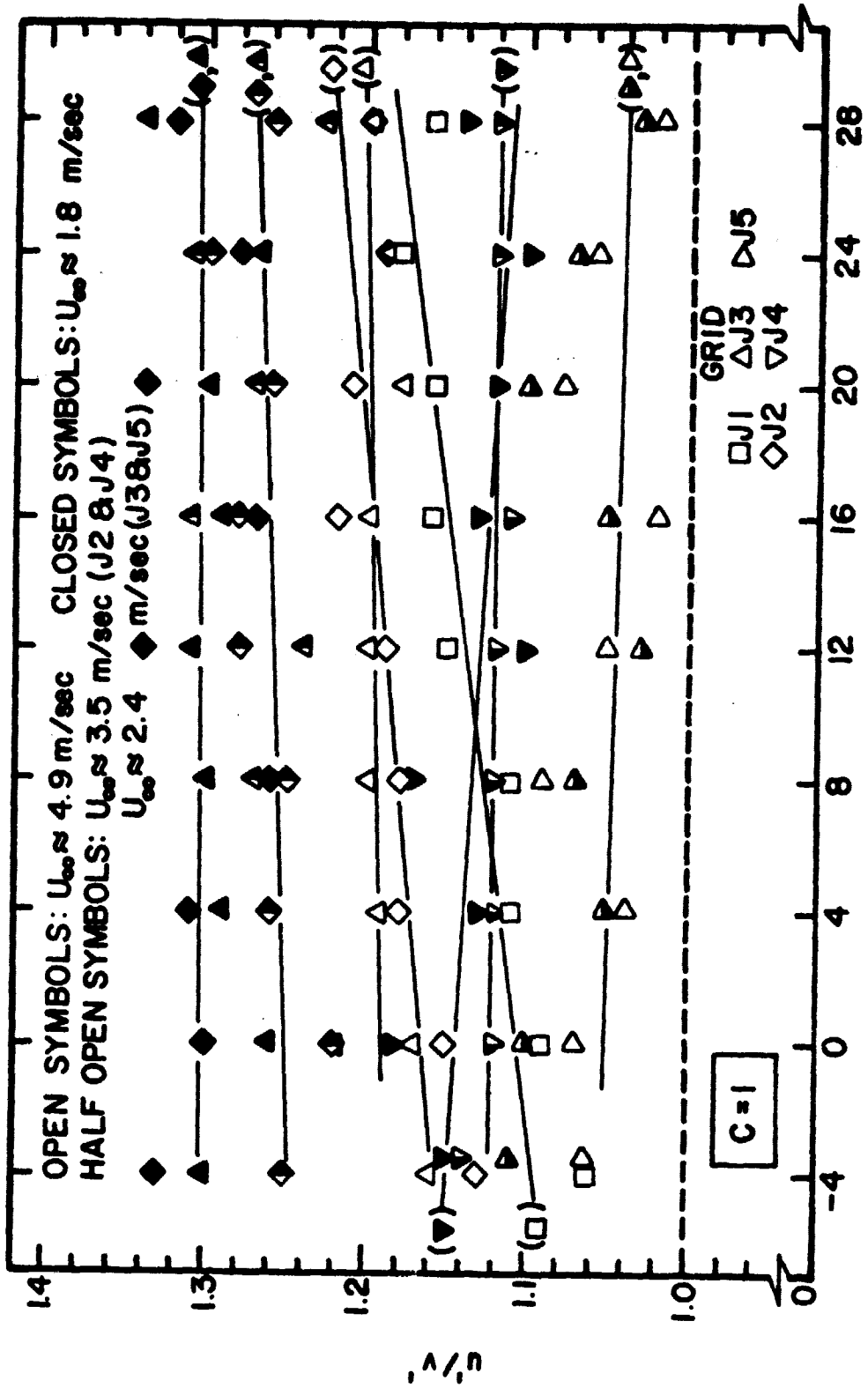

Figure 30. Development of Isotropy of Test Flow Conditions

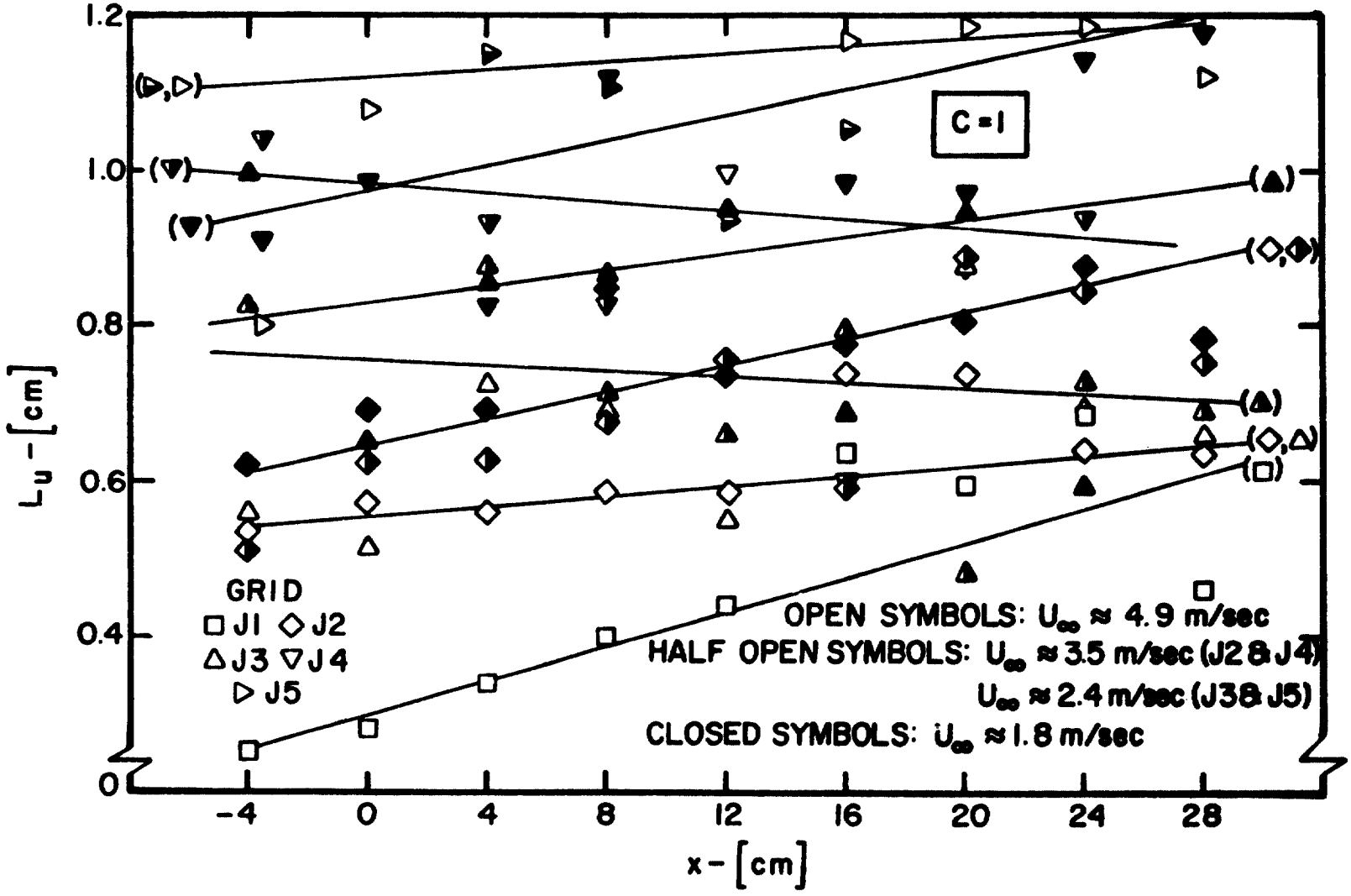

Figure 31. Development of Longitudinal Integral Length-Scales of Test Flow Conditions

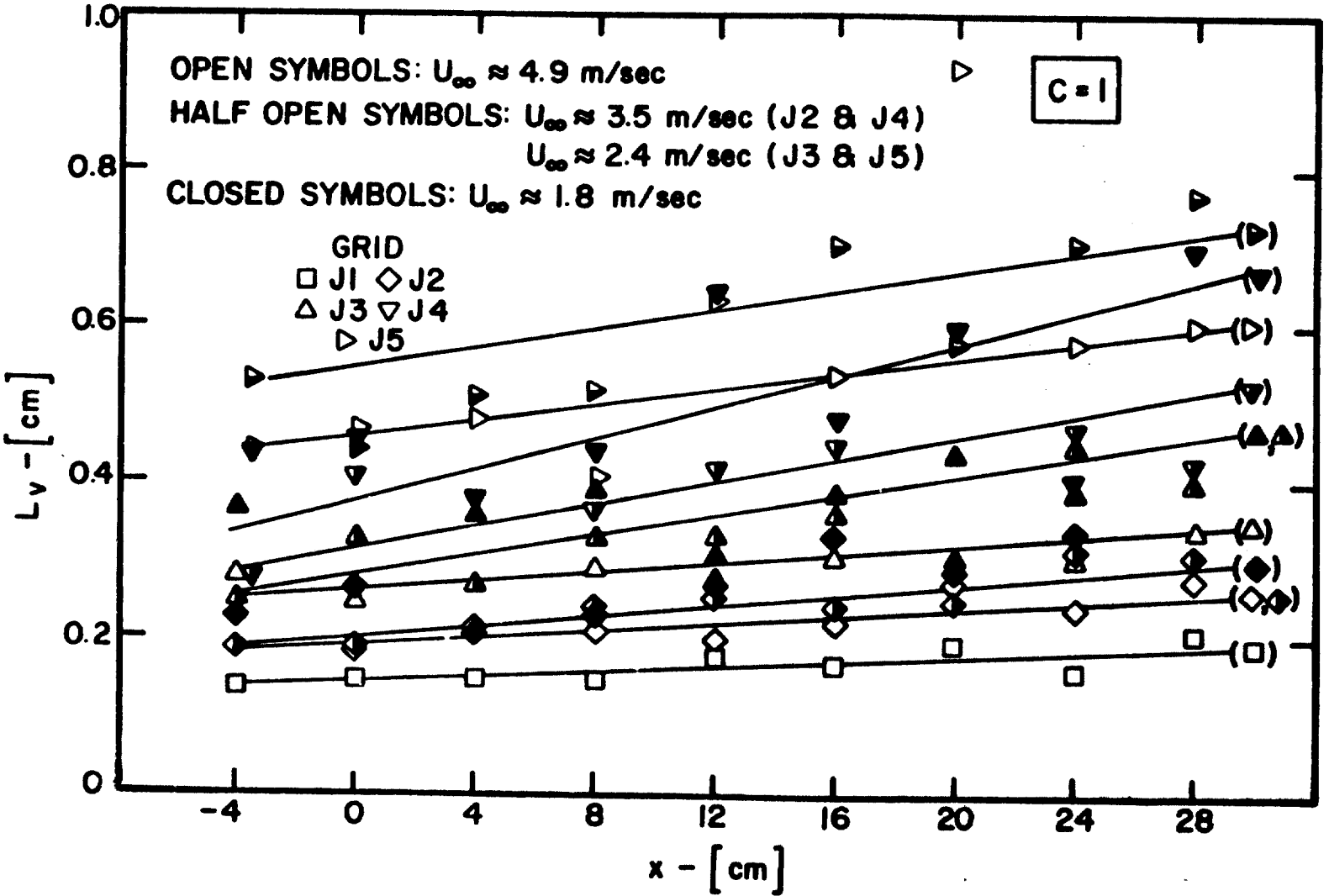

Figure 32. Development of Lateral Integral Length-Scales of Test Flow Conditions

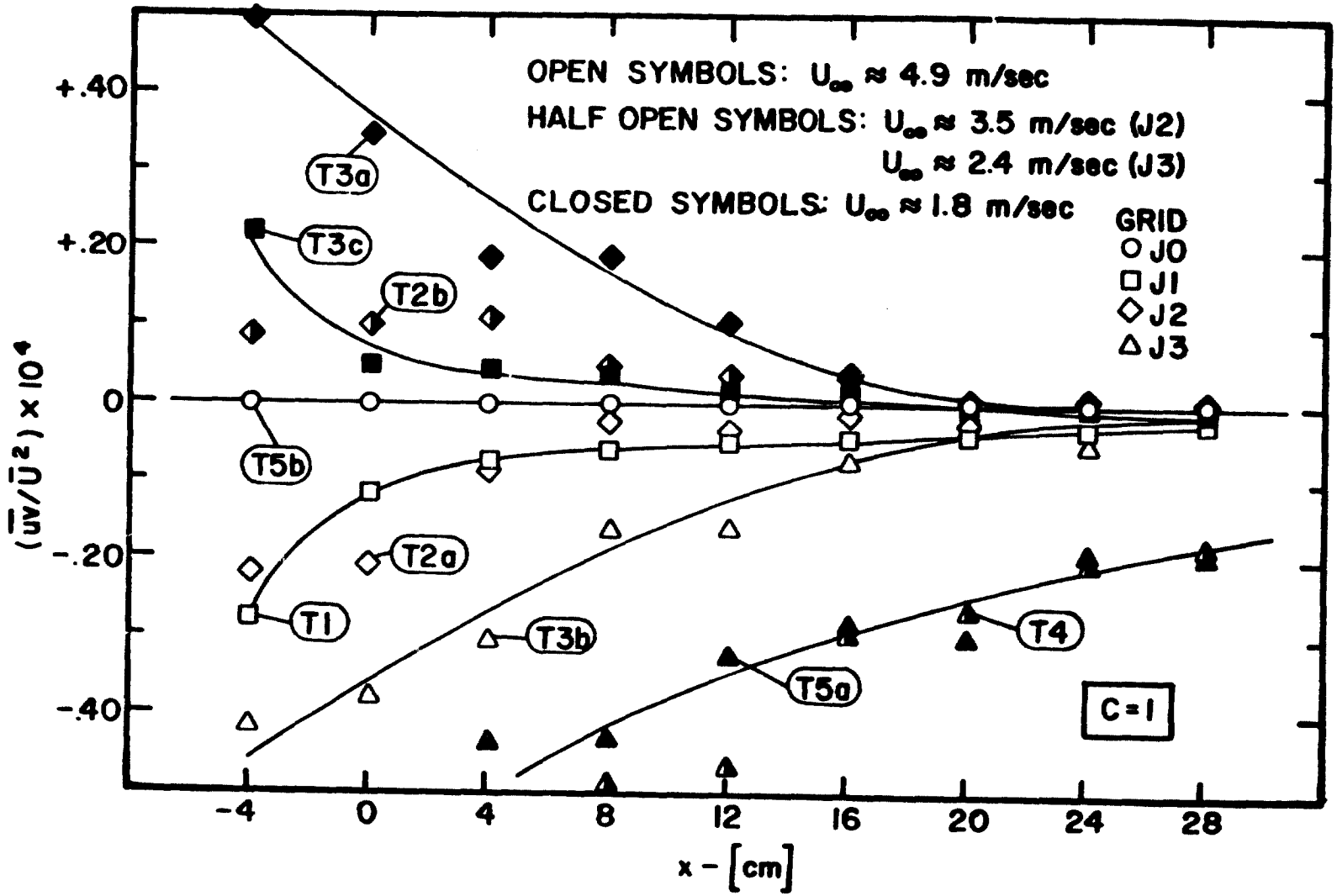

Figure 33. Development of Reynolds Stresses of Some Test Flow Conditions

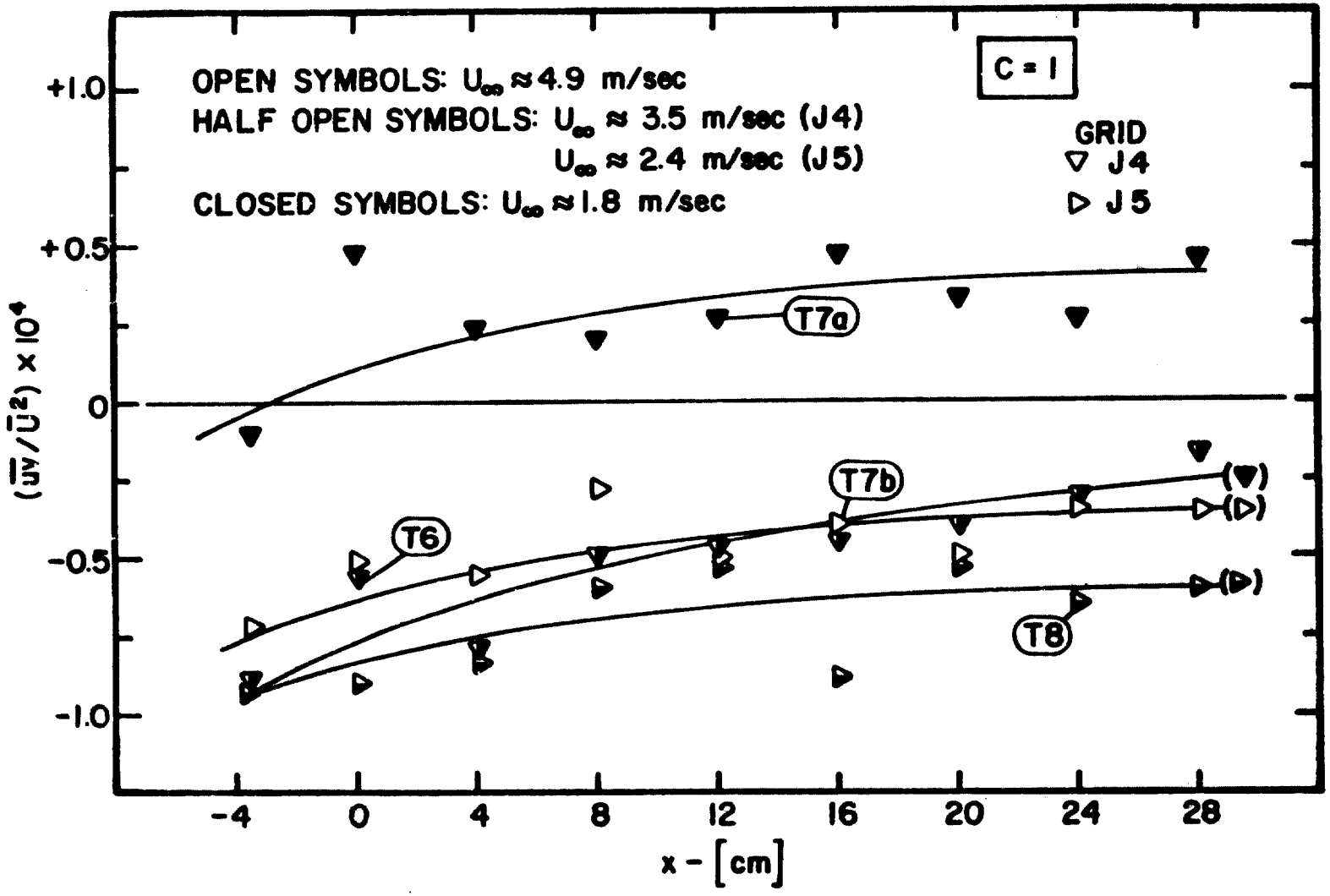

Figure 34. Development of Reynolds Stresses of Additional Test Flow Conditions

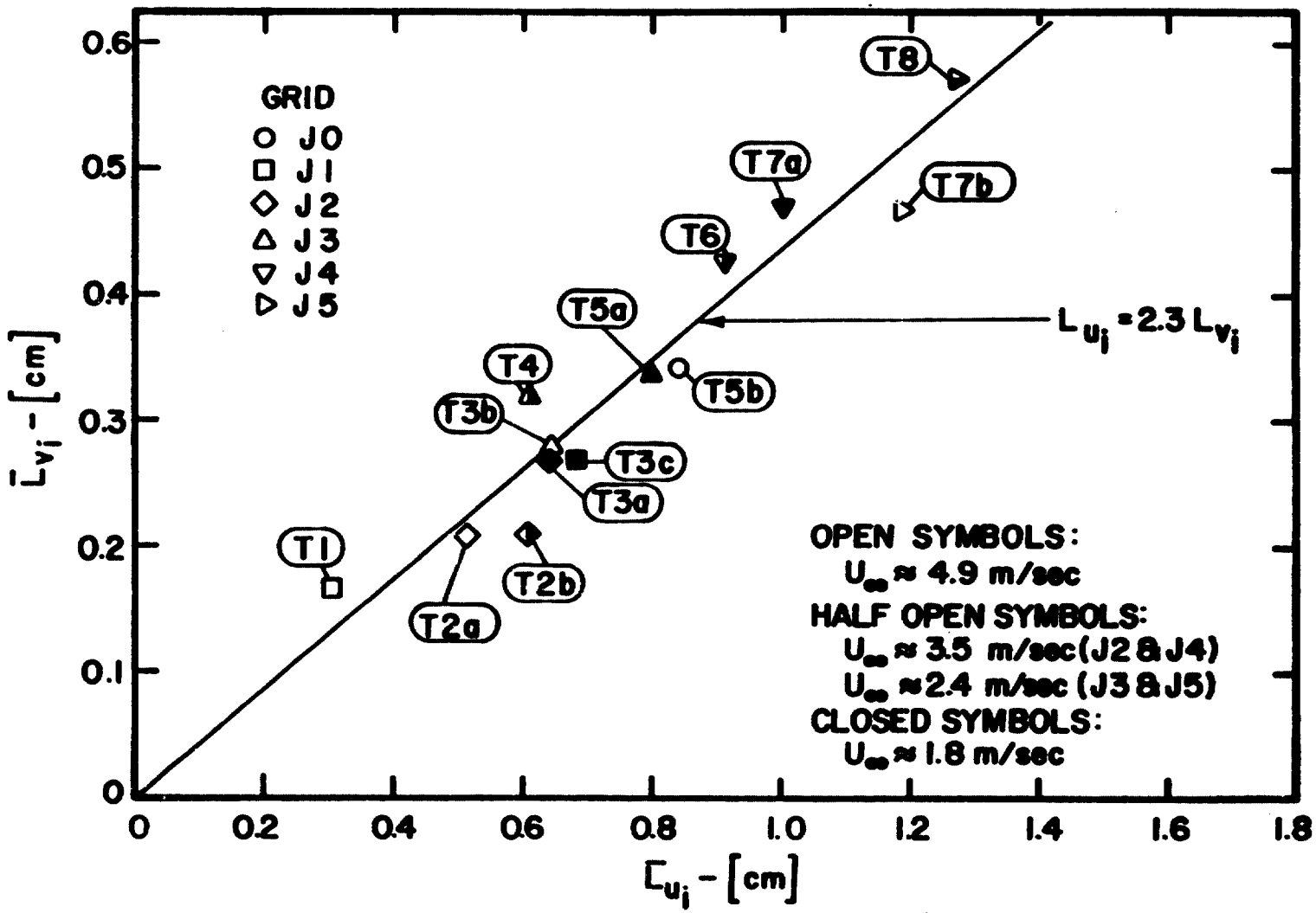

Figure 35. Lateral versus Longitudinal Integral Length Scales of Test Flow Conditions

TEST-FLOW CONDITION	GRID	U_∞ [m/s]	SYMBOL	R_M	$(u'/\bar{U})_1$ %	$(v'/\bar{U})_1$ %	$(q'/\bar{U})_1$ %
T1	J1	4.9	□	760	1.48	1.34	2.41
T2a	J2	4.9	◇	1930	1.99	1.73	3.16
T2b	J2	3.5	◈	1300	2.05	1.71	3.17
T3a	J2	1.8	◆	775	2.29	1.86	3.49
T3b	J3	4.9	△	3890	2.40	2.09	3.81
T3c	J1	1.8	■	270←	1.41←	0.94←	1.95←
T4	J3	2.4	▲	1950	2.41	2.01	3.72
T5a	J3	1.8	▲	1550	2.40	1.96	3.66
T5b	J0	4.9	○	227	<0.2	<0.1	<0.2
T6	J4	3.5	▼	3850	2.69	2.49	4.44
T7a	J4	1.8	▼	2100	2.64	2.39	4.29
T7b	J5	4.9	▷	→8130	→3.01	→2.84	→5.02
T8	J5	2.4	▶	4060	2.90	2.77	4.87

→ LARGEST VALUE
← SMALLEST VALUE

Figure 36. Summary of Some Statistics for Test Flow Conditions

TEST-FLOW CONDITION	$\bar{L}_{u_i}$ [cm]	$\bar{L}_{v_i}$ [cm]	$R_{\lambda i}$	$\frac{\partial}{\partial(\bar{x}/M)}\left(\frac{\bar{U}^2}{u'^2}\right)$	$\bar{x}_o/M$
T1	0.308 ←	0.167 ←	7.2	144.5	16
T2a	0.516	0.208	14	92.5	11
T2b	0.607	0.209	12	84.1	13
T3a	0.645	0.269	10	75.4	15
T3b	0.643	0.276	24	68.3 ←	11
T3c	0.686	0.268	2.3 ←	→491.5	32
T4	0.610	0.321	16	73.4	11
T5a	0.800	0.337	14	74.0	12
T5b	~0.84	~0.34	—	—	—
T6	0.913	0.466	22	77.0	11
T7a	1.003	0.468	16	83.7	13
T7b	1.187	0.425	→31	82.7	11
T8	→1.27	→0.570	22	85.8	11

→ LARGEST VALUE

← SMALLEST VALUE

Figure 37. Summary of Additional Statistics for Test Flow Conditions

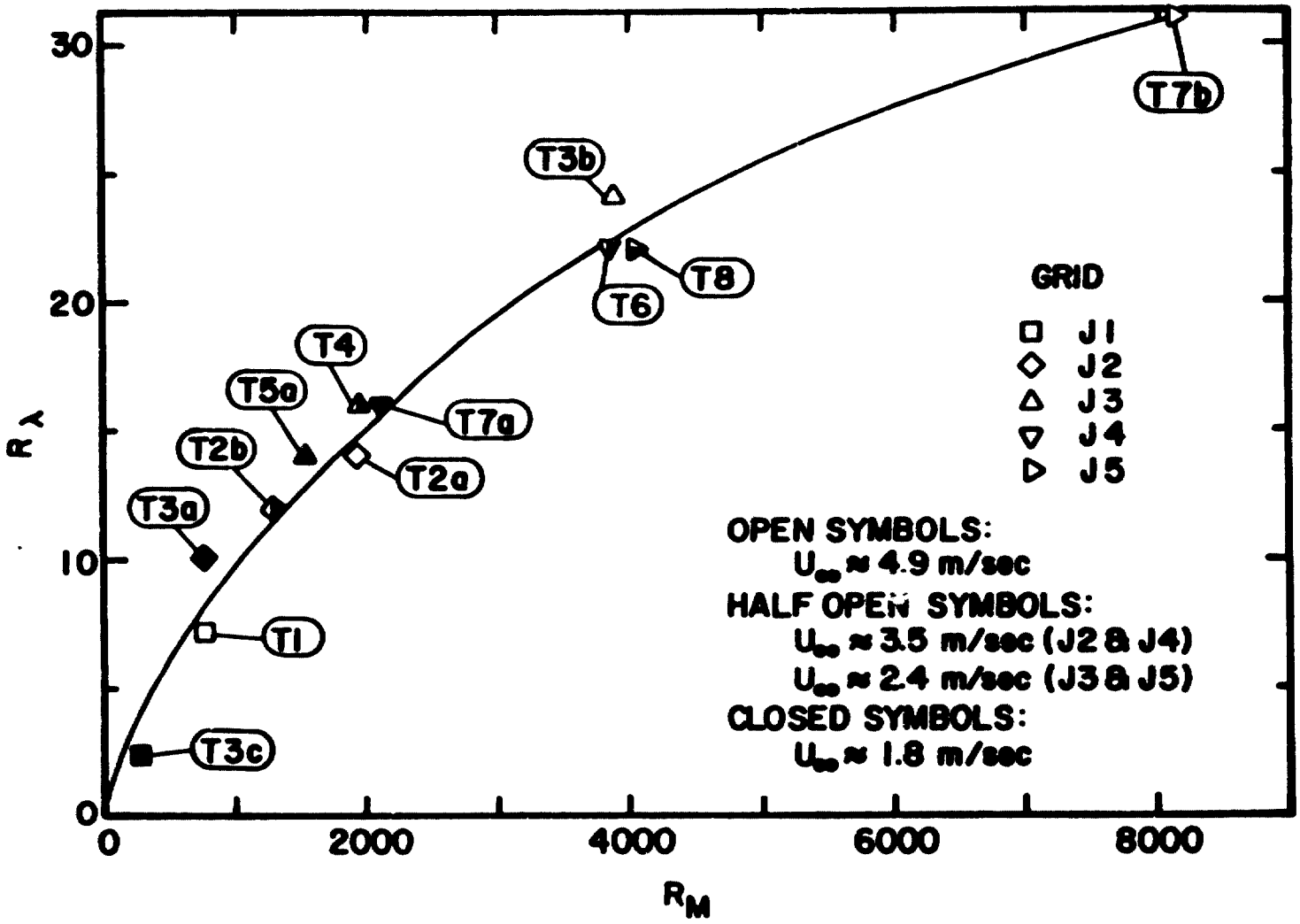

Figure 38. Turbulence versus Mesh Reynolds Number of Test Flow Conditions

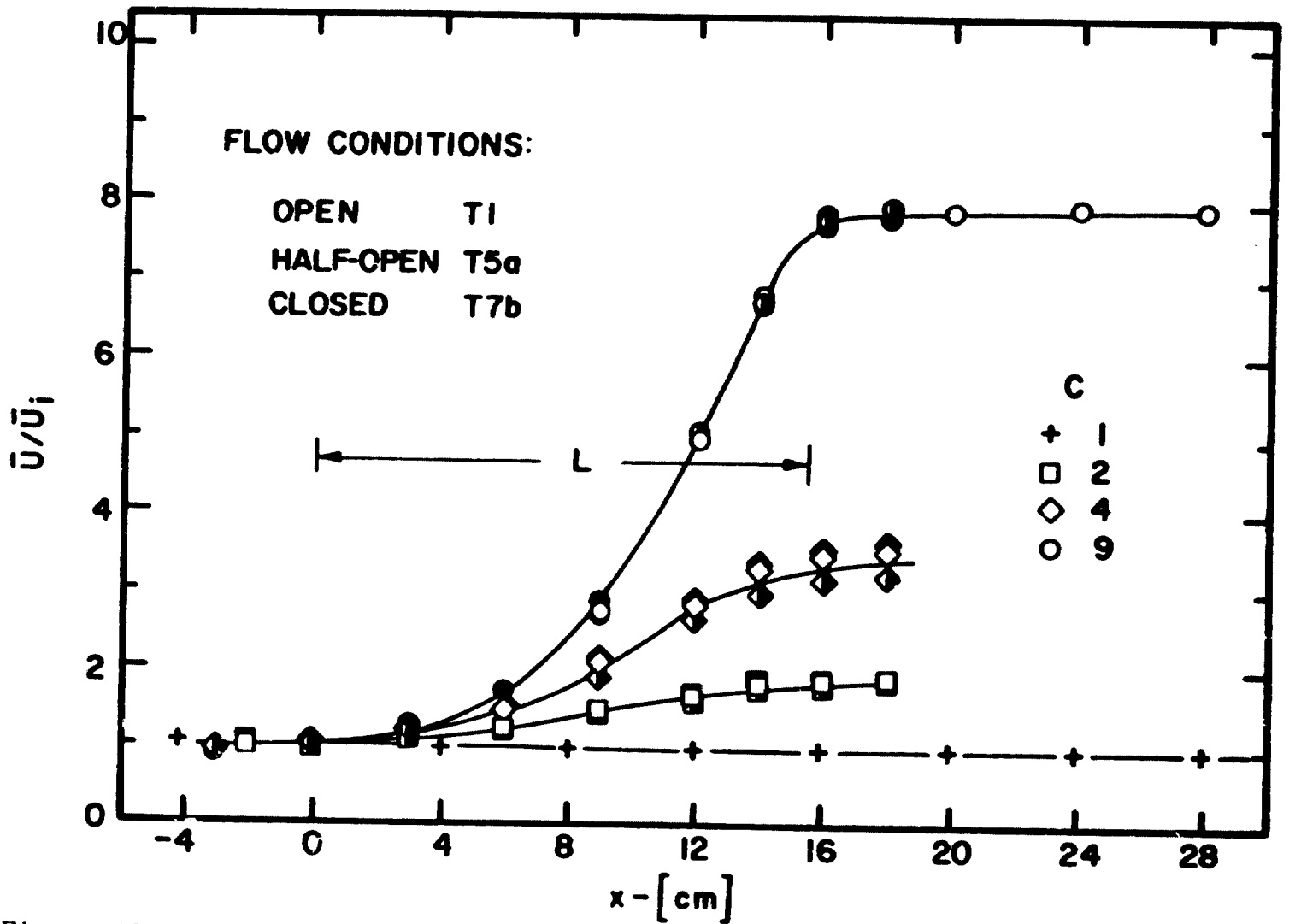

Figure 39. Normalized Streamwise Mean Velocity through Various Contractions in Flow Conditions T1, T5a and T7b

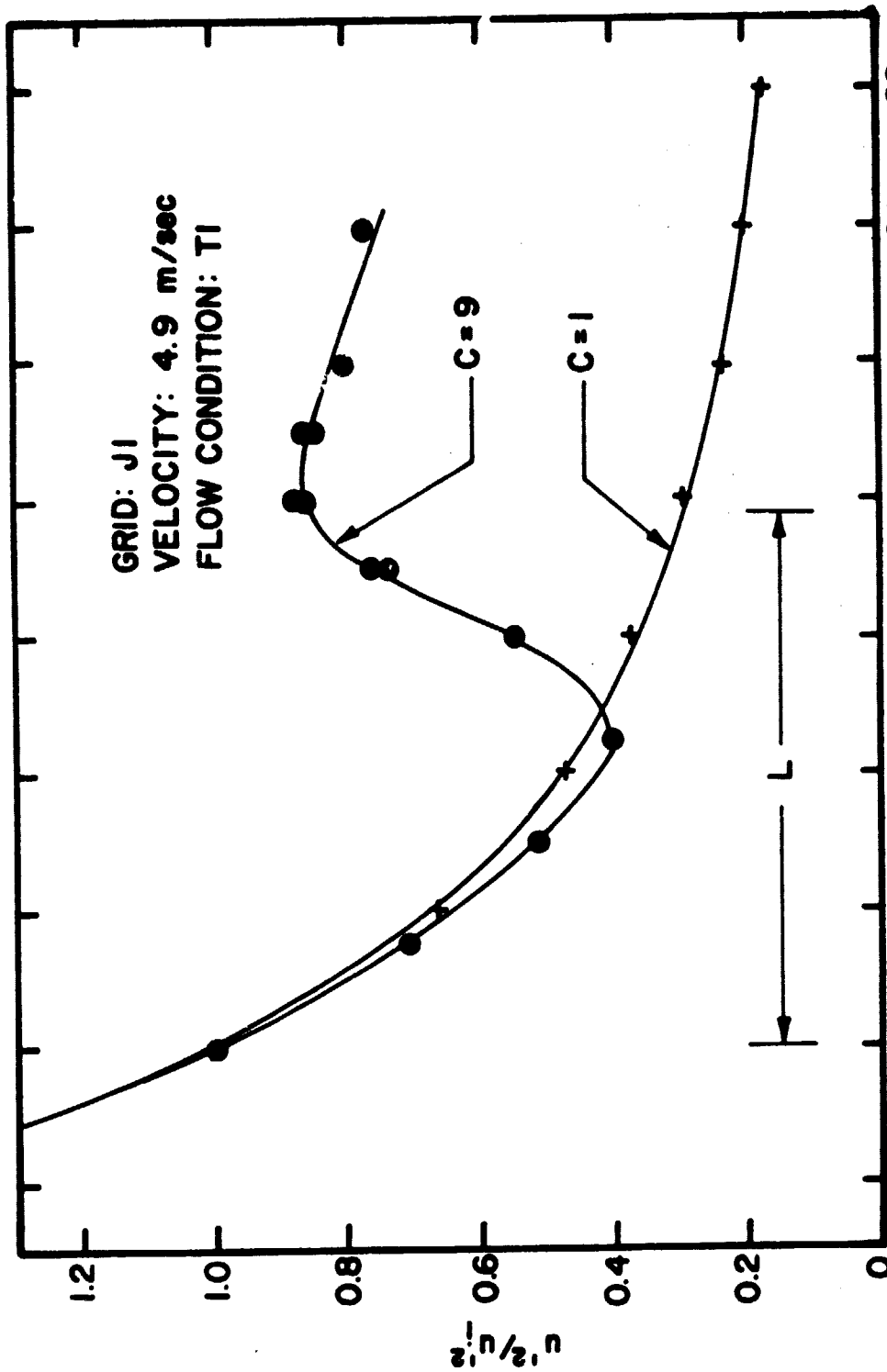

Figure 40. Normalized Streamwise Turbulence Energy through and Downstream of a Contraction in Flow Condition T1

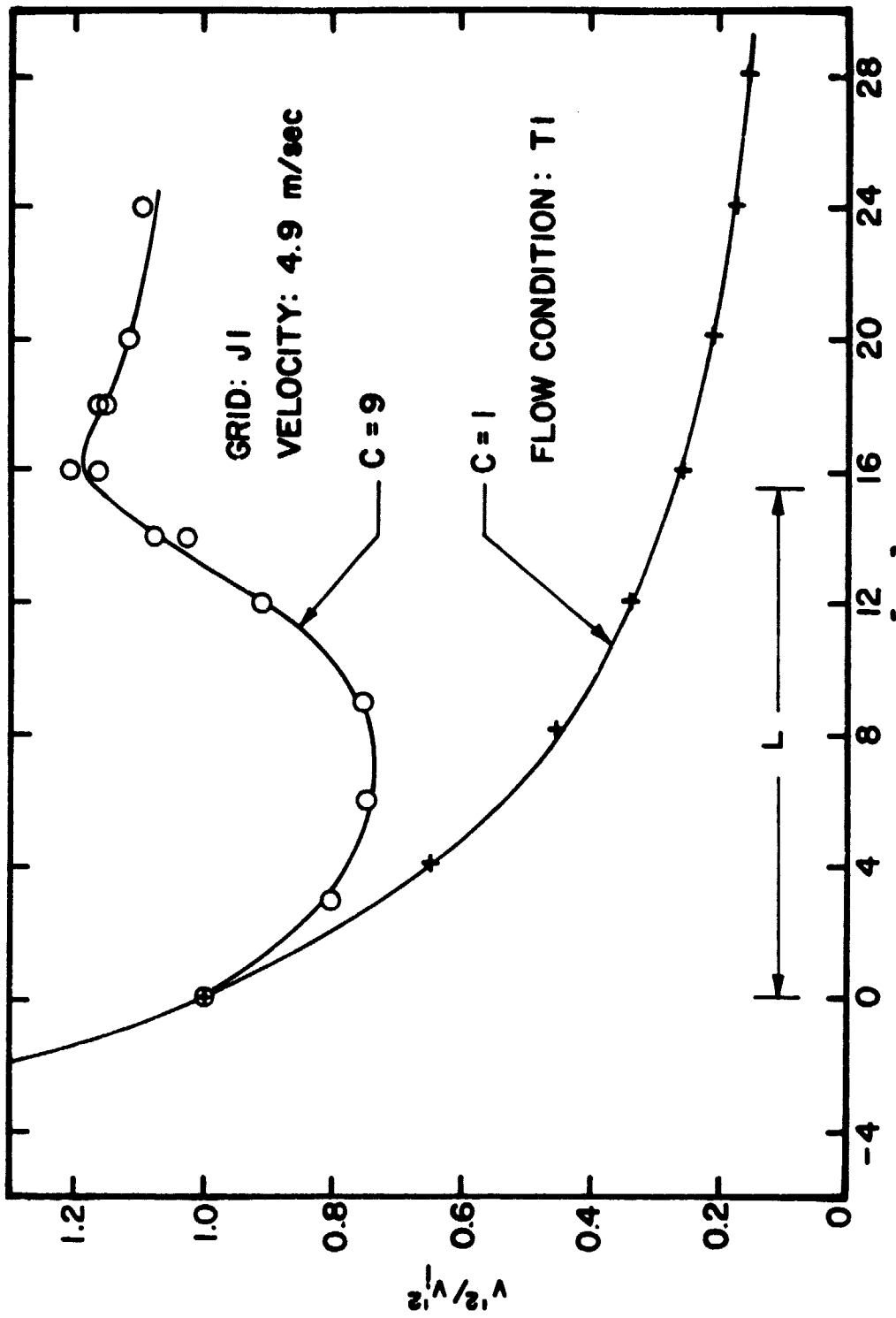

Figure 41. Normalized Radial Turbulence Energy through and Downstream of a Contraction in Flow Condition T1

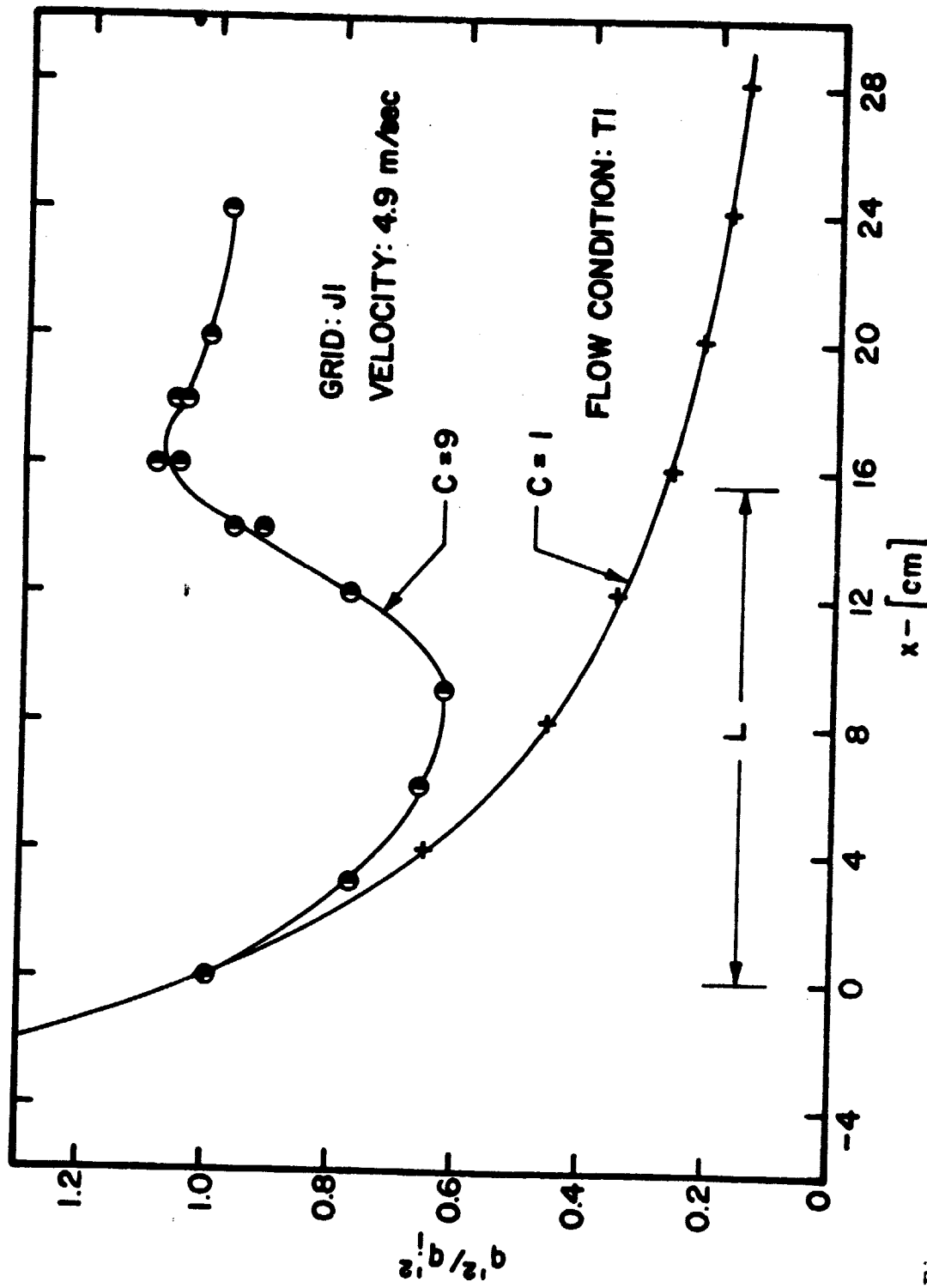

Figure 42. Normalized Total Turbulence Energy through and Downstream of a Contraction in Flow Condition T1

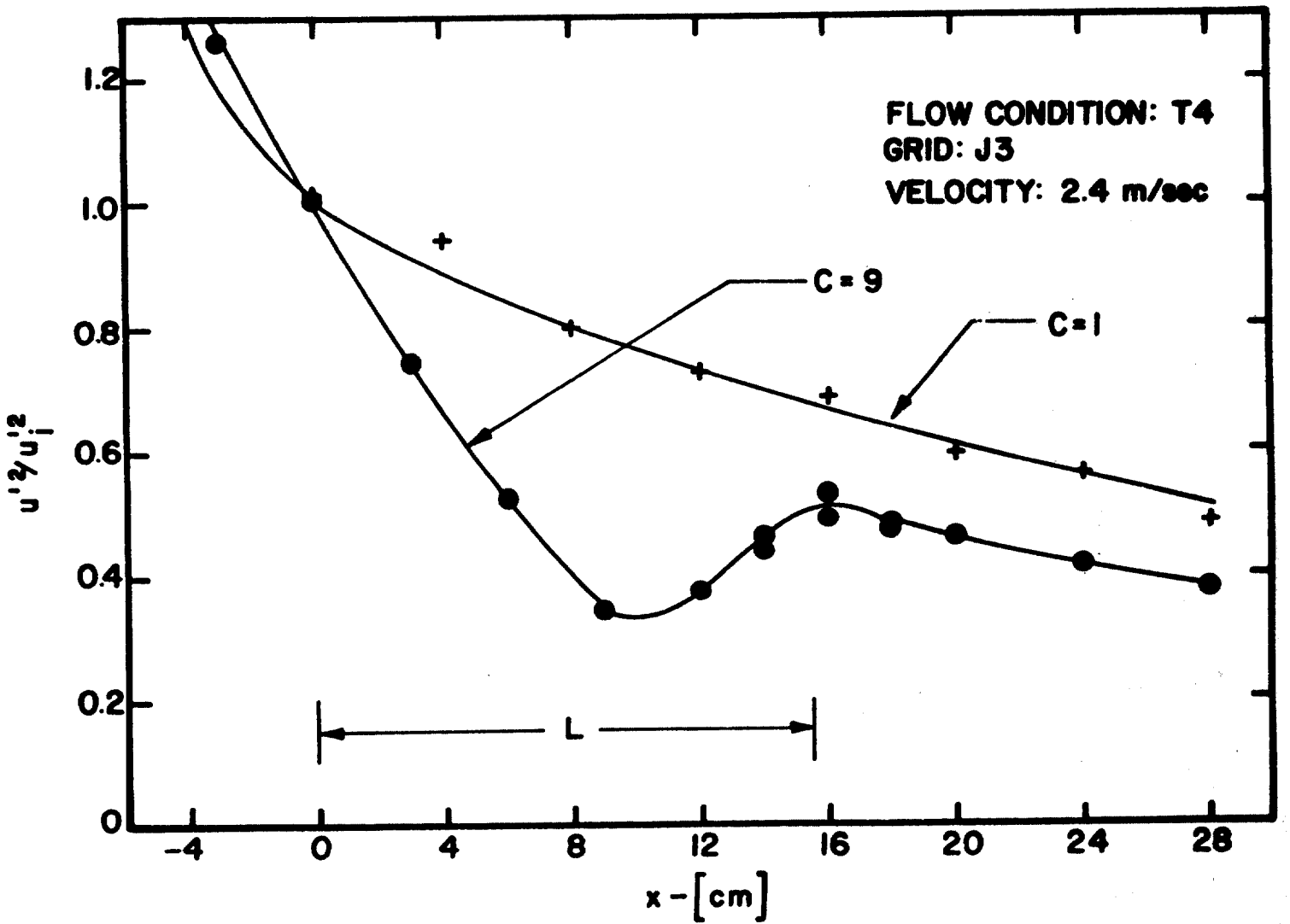

Figure 43. Normalized Streamwise Turbulence Energy through and Downstream of a Contraction in Flow Condition T4

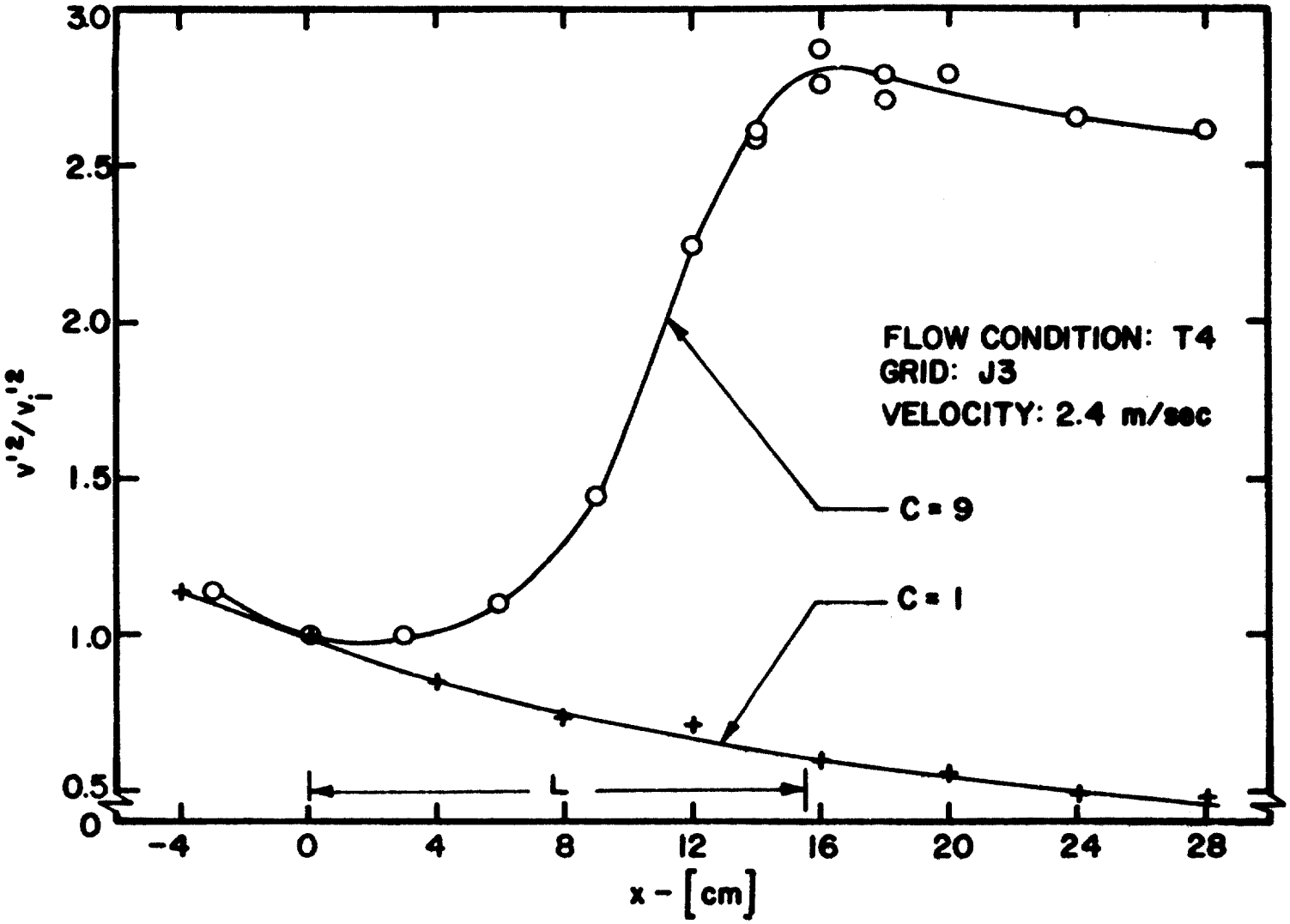

Figure 44. Normalized Radial Turbulence Energy through and Downstream of a Contraction in Flow Condition T4

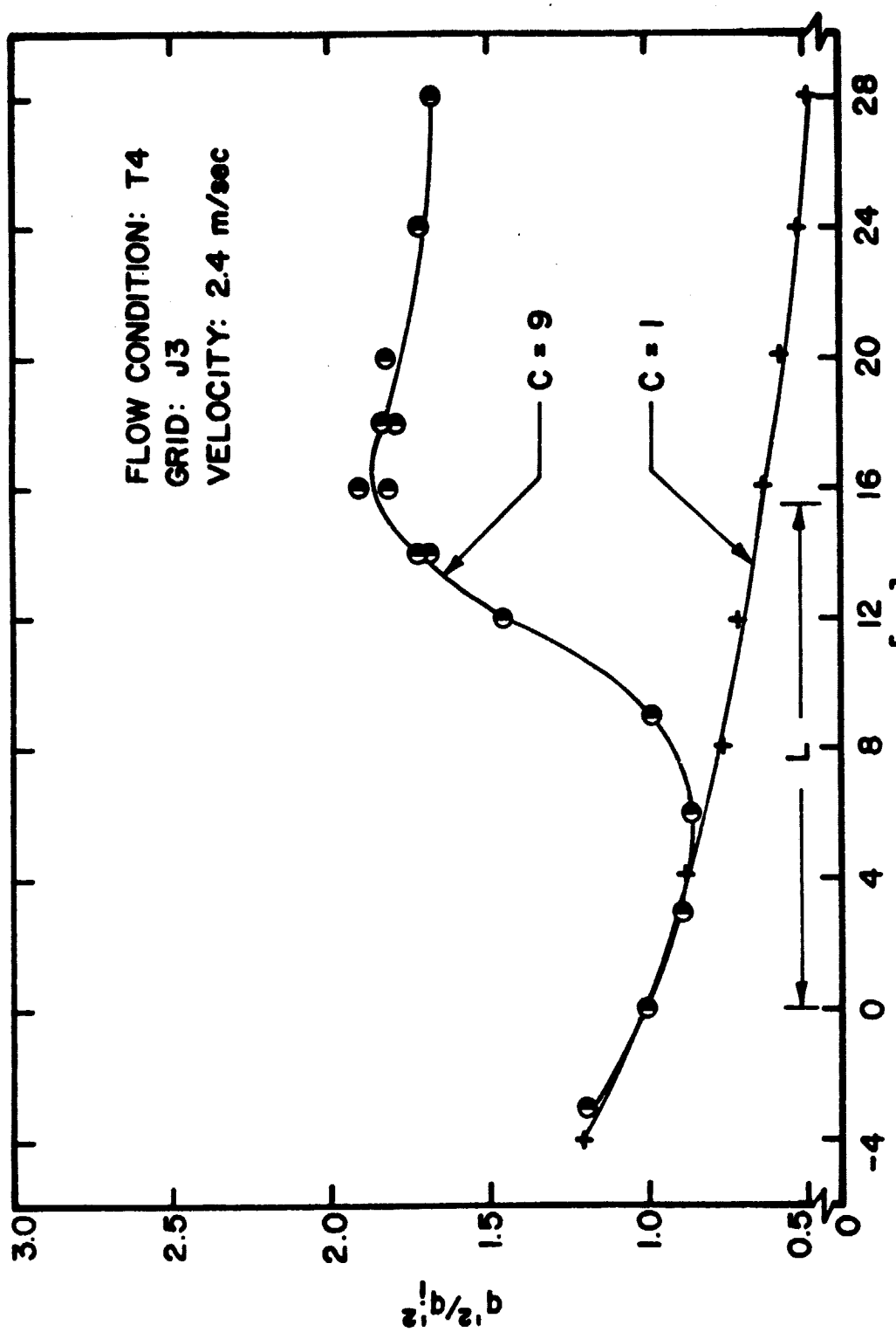

Figure 45. Normalized Total Turbulence Energy through and Downstream of a Contraction in Flow Condition T4

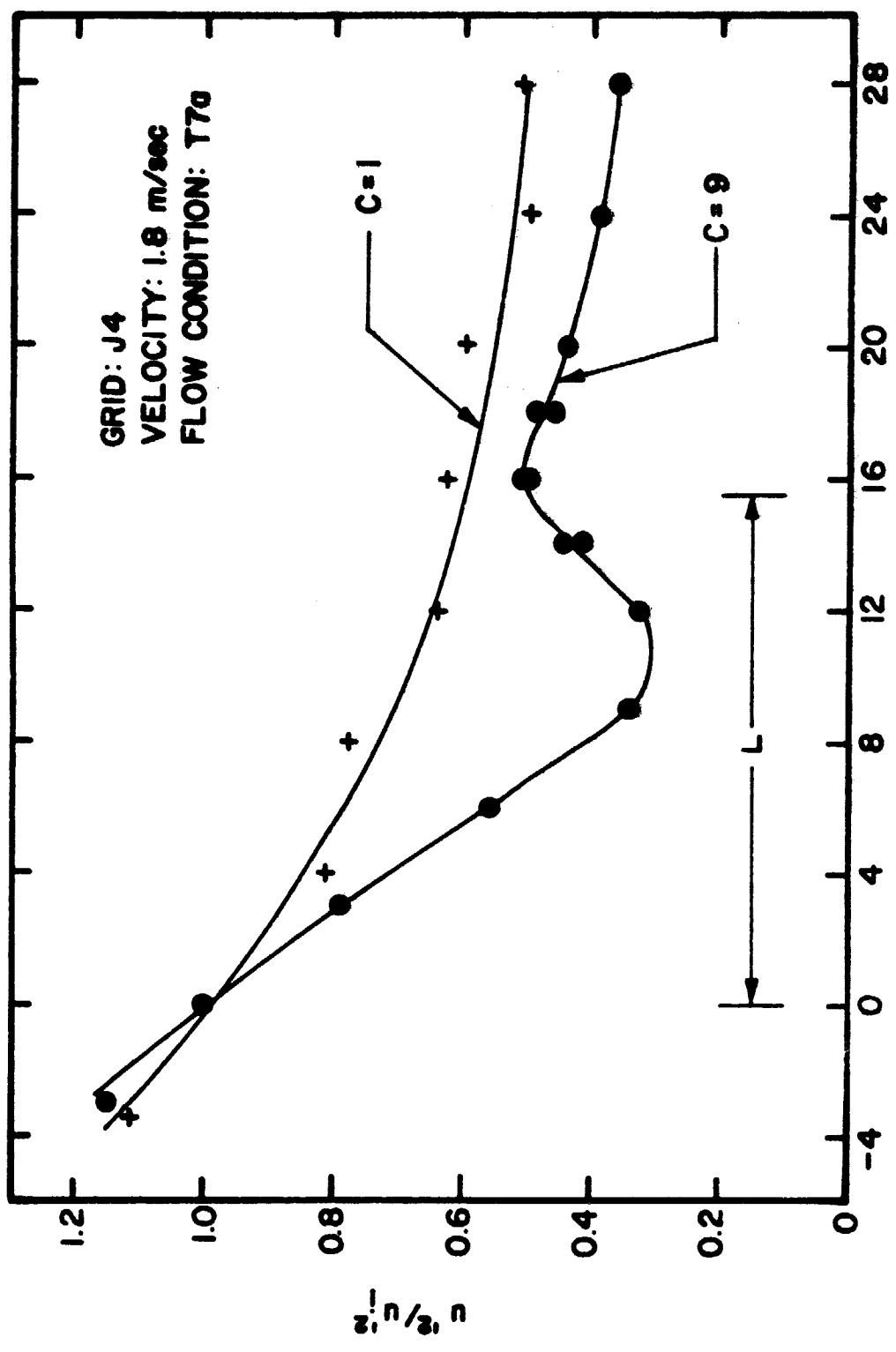

Figure 46. Normalized Streamwise Turbulence Energy through and Downstream of a Contraction in Flow Condition T7a

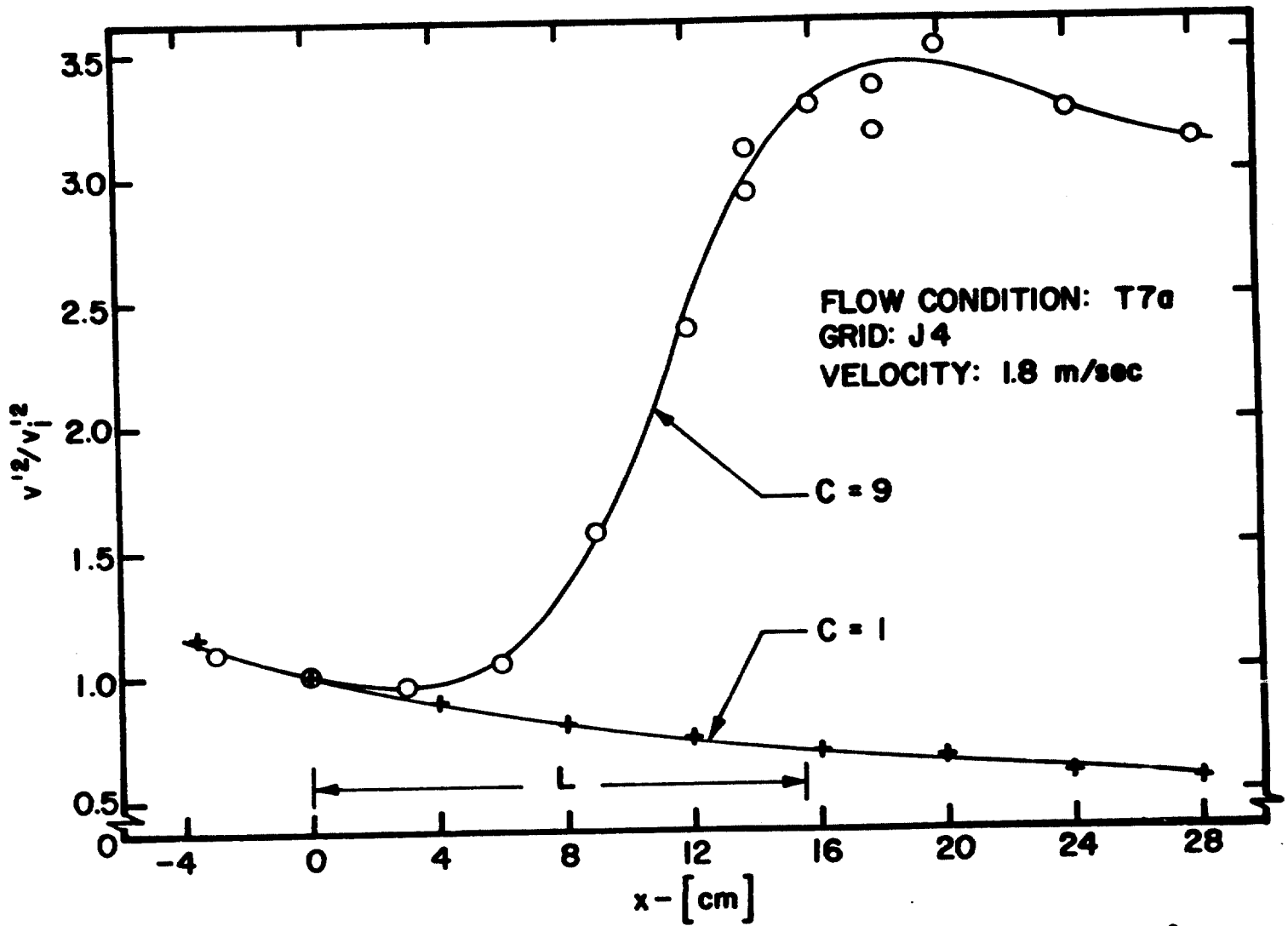

Figure 47. Normalized Radial Turbulence Energy through and Downstream of a Contraction in Flow Condition T7a

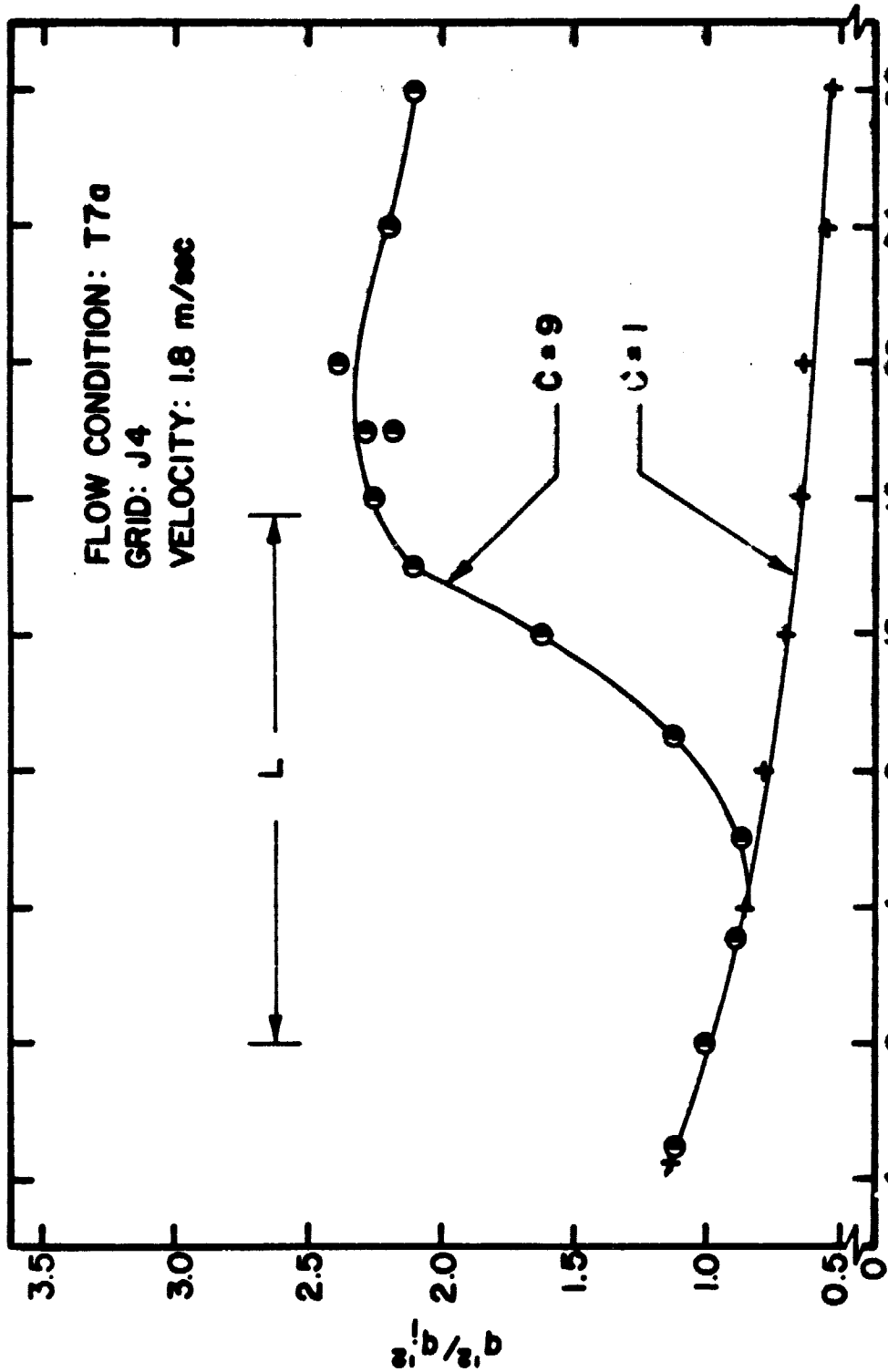

Figure 48. Normalized Total Turbulence Energy through and Downstream of a Contraction in Flow Condition T7a

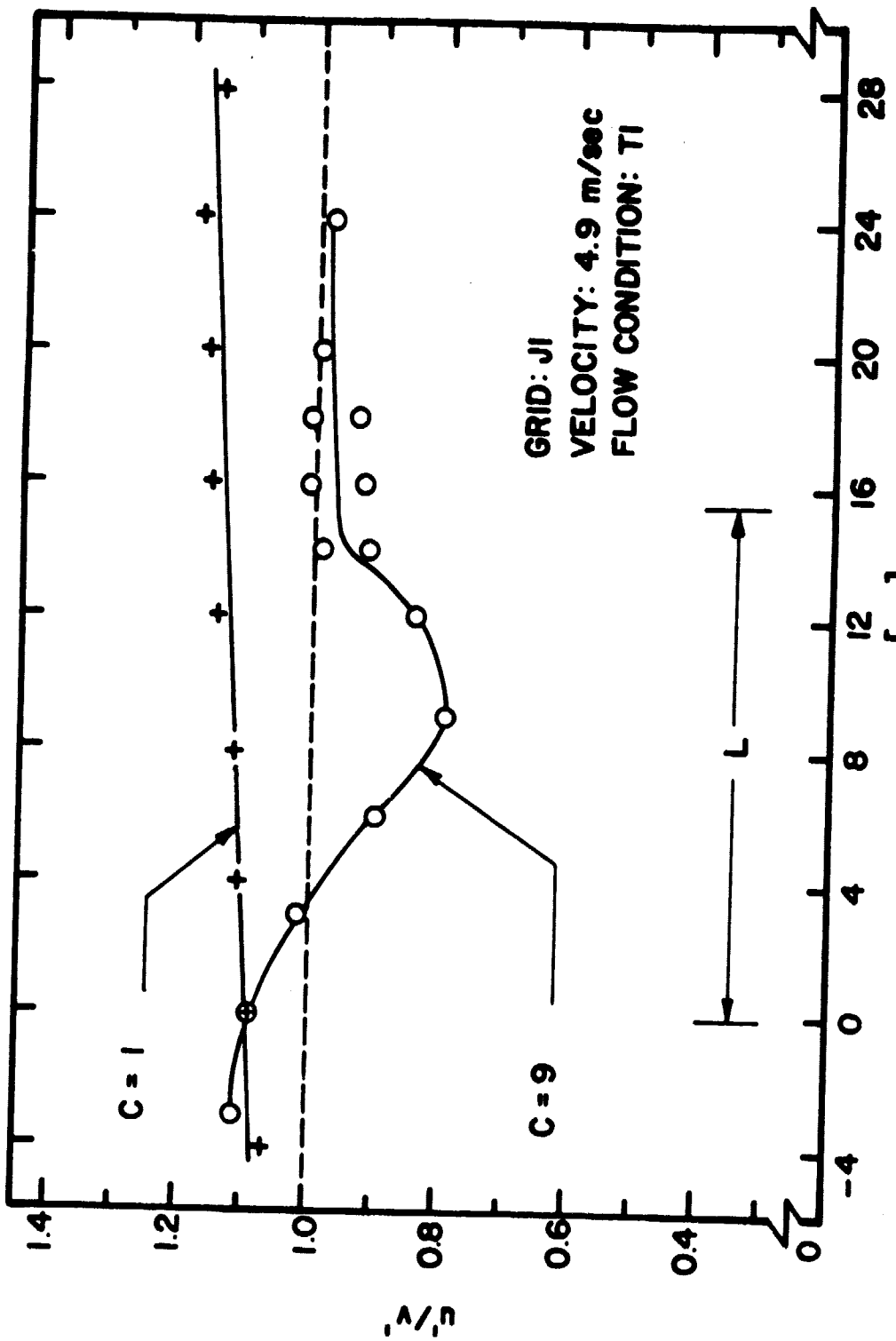

Figure 49. Isotropy through and Downstream of a Contraction in Flow Condition T1

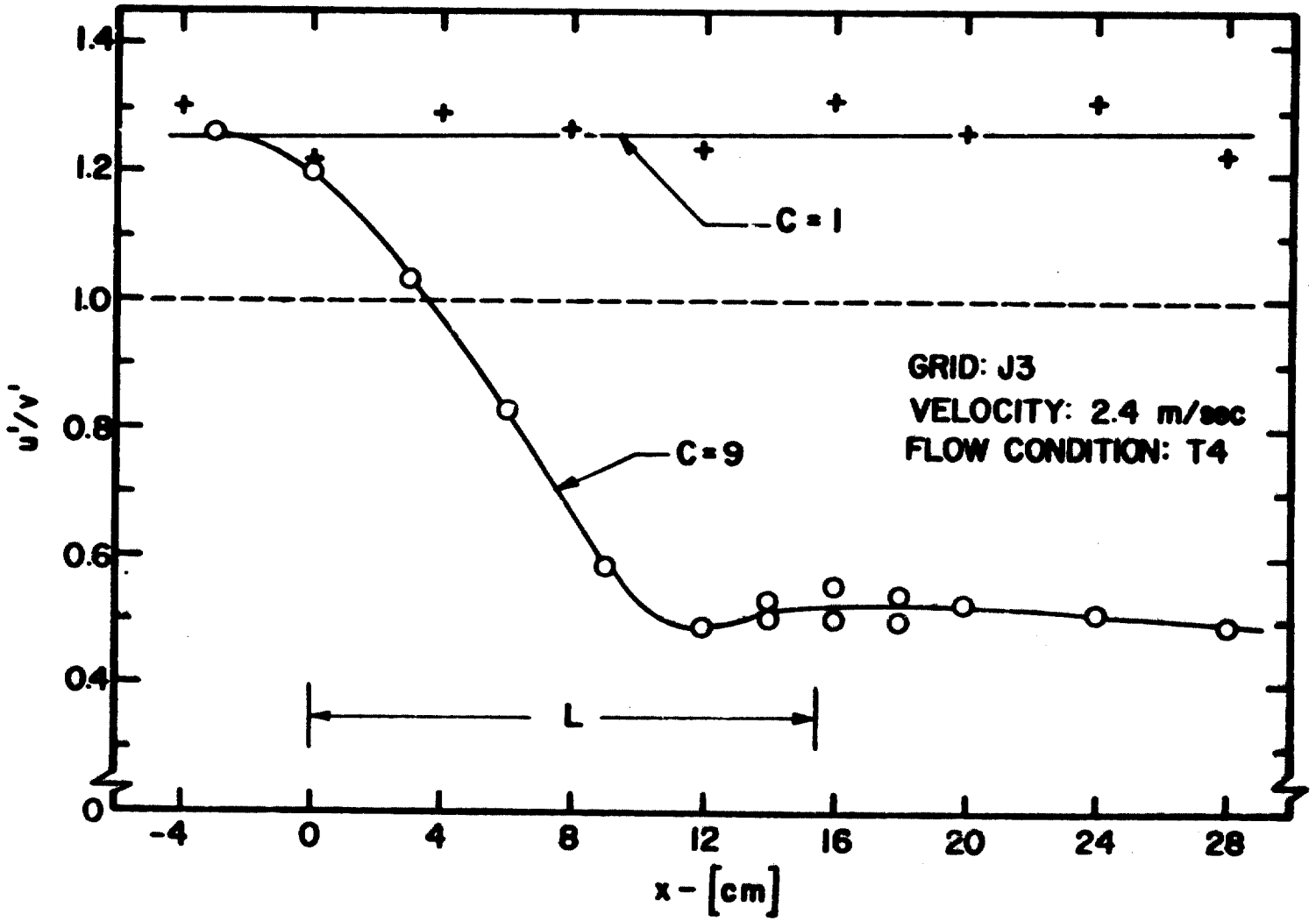

Figure 50. Isotropy through and Downstream of a Contraction in Flow Condition T4

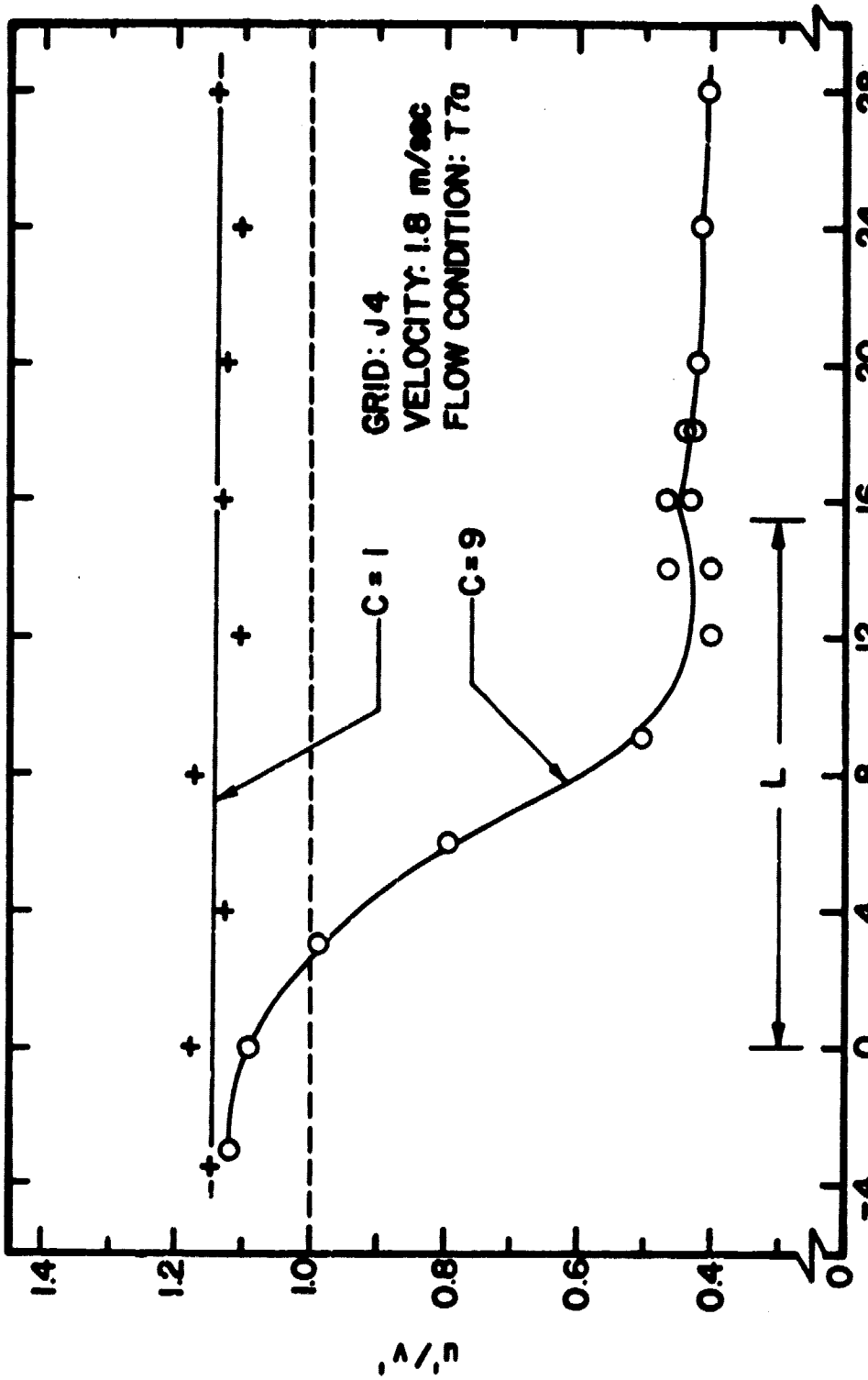

Figure 51. Isotropy through and Downstream of a Contraction in Flow Condition T7a

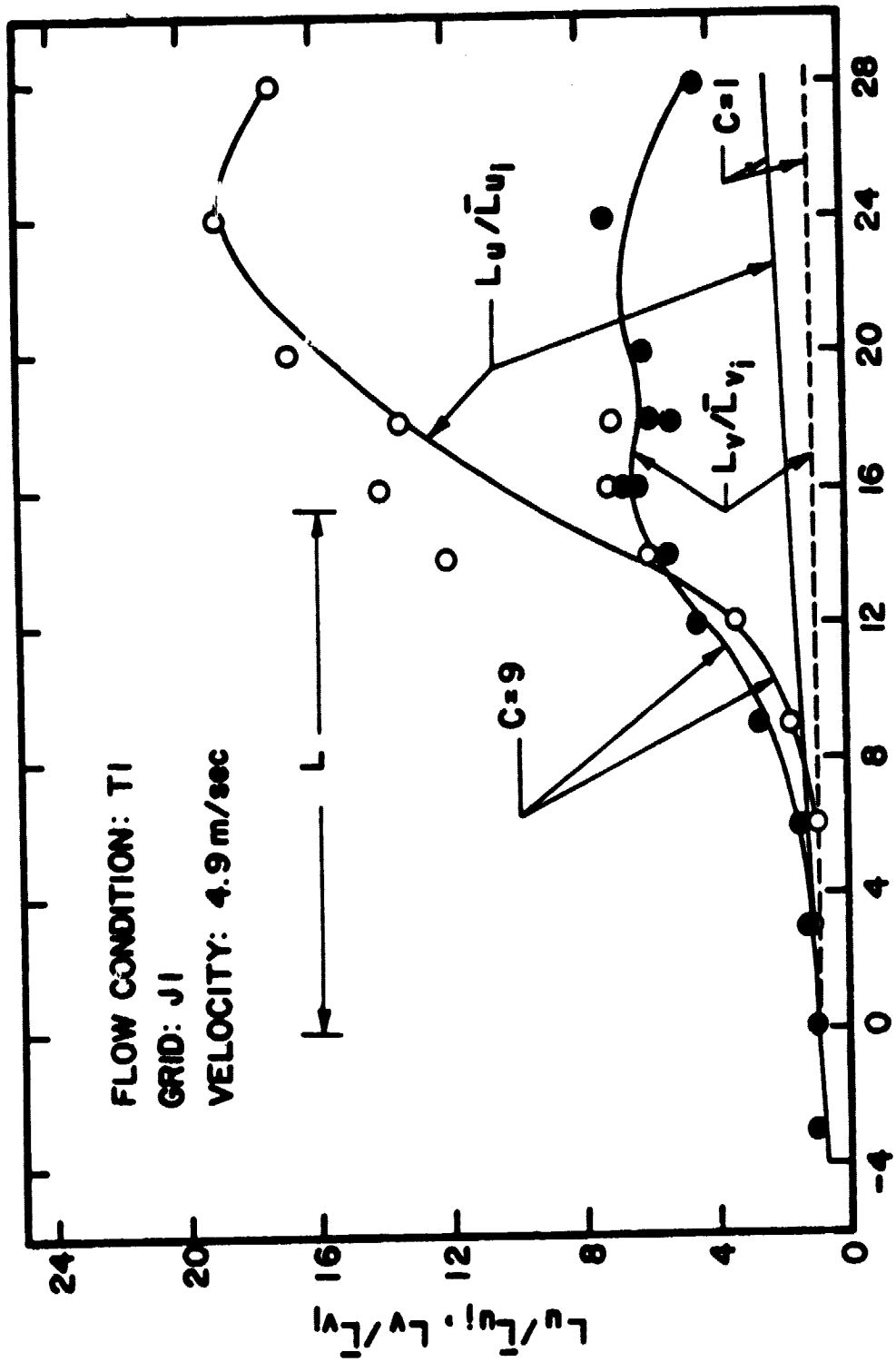

Figure 52. Normalized Length Scales through and Downstream of a Contraction in Flow Condition T1

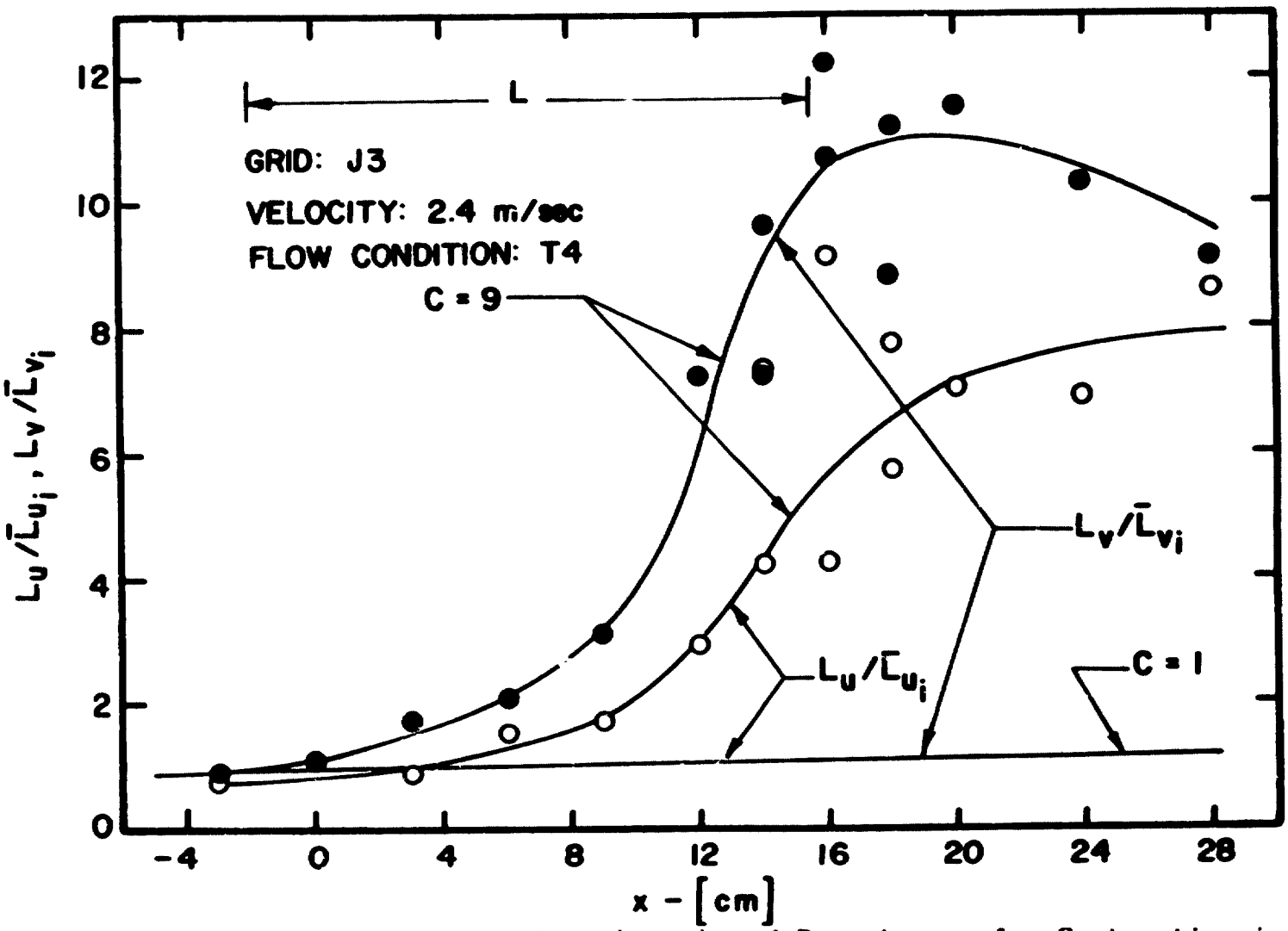

Figure 53. Normalized Length Scales through and Downstream of a Contraction in Flow Condition T4

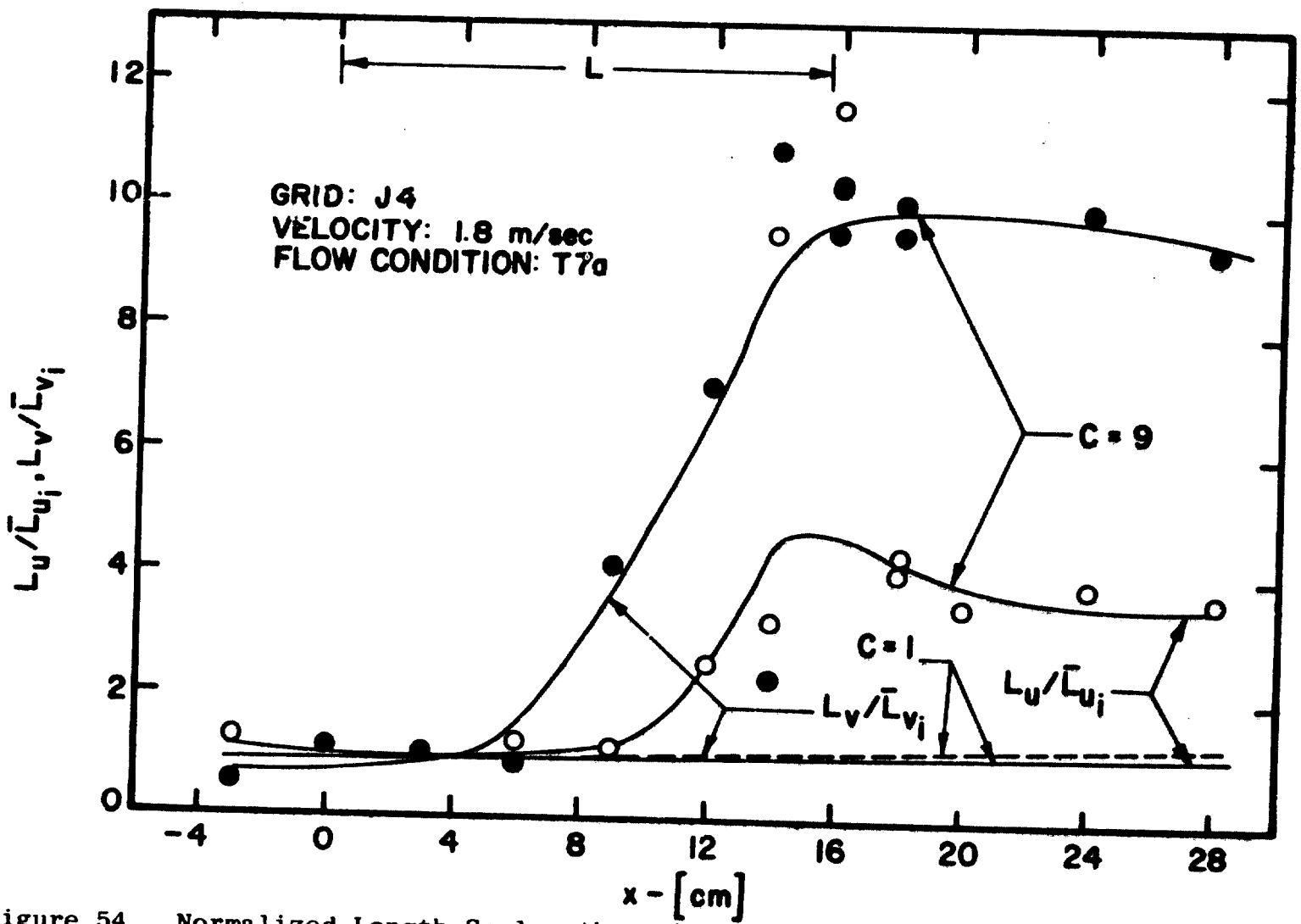

Figure 54. Normalized Length Scales through and Downstream of a Contraction in Flow Condition T7a

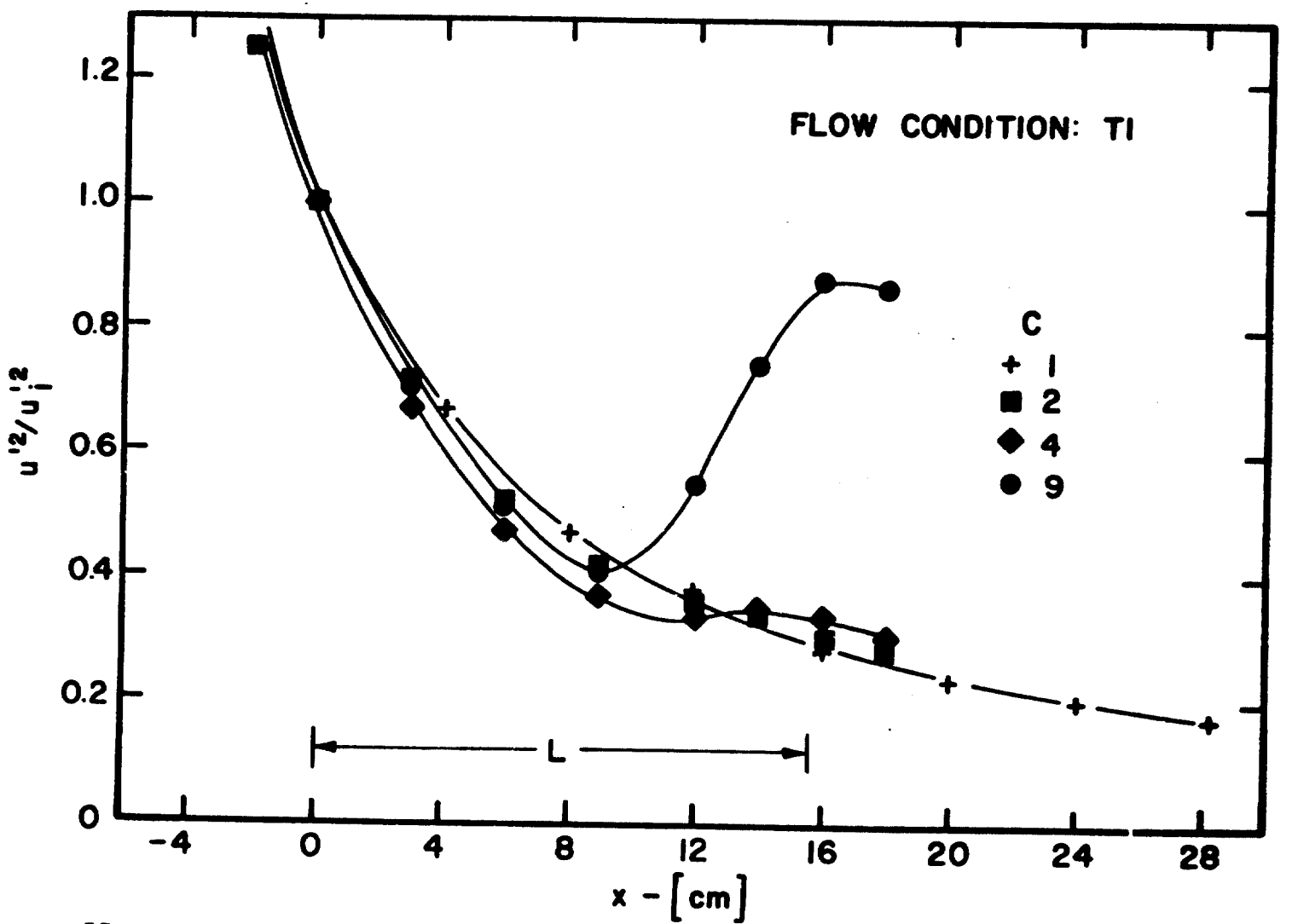

Figure 55. Normalized Streamwise Turbulence Energy through Moderate Contractions in Flow Condition T1

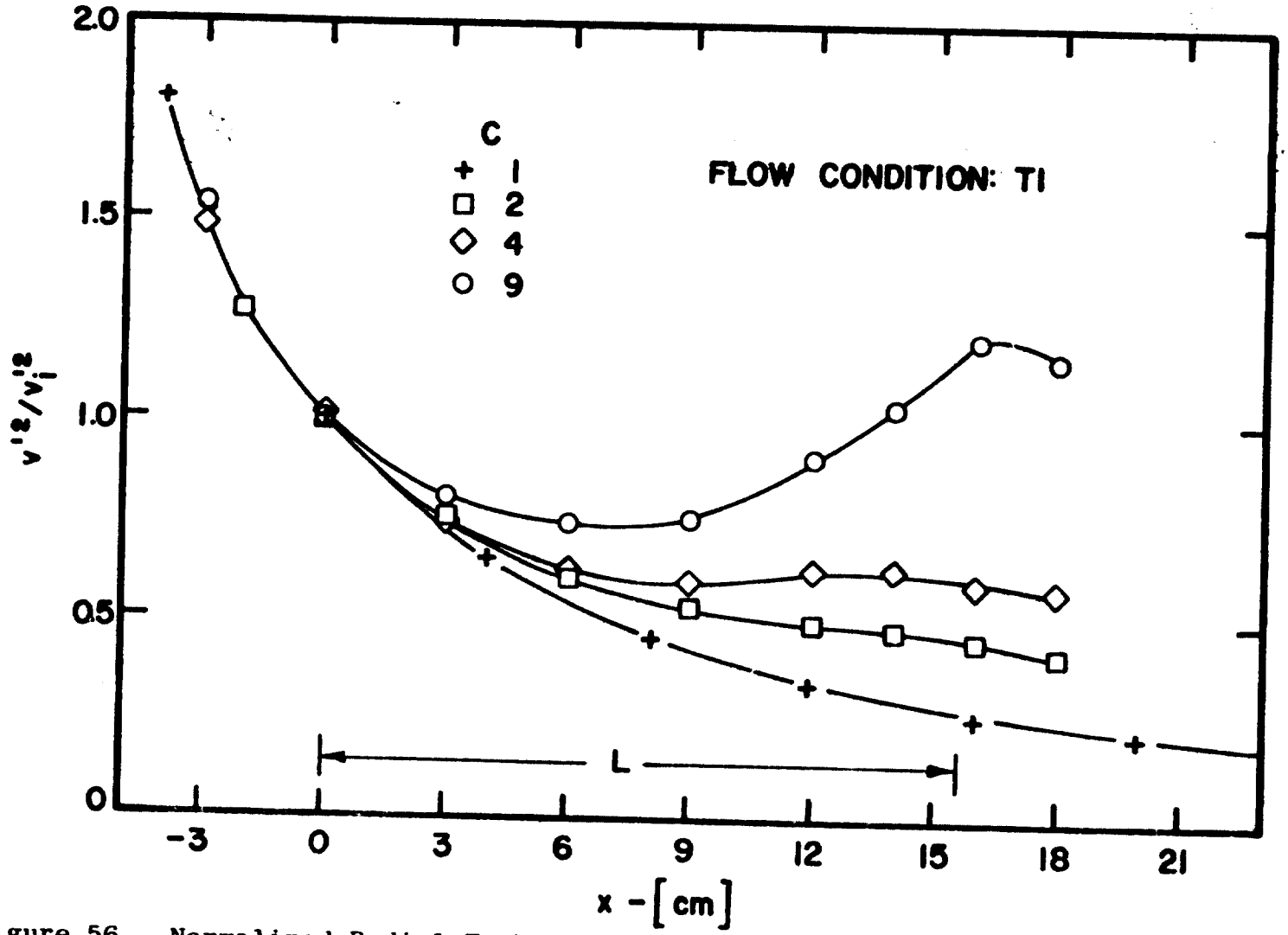

Figure 56. Normalized Radial Turbulence Energy through Moderate Contractions in Flow Condition T1

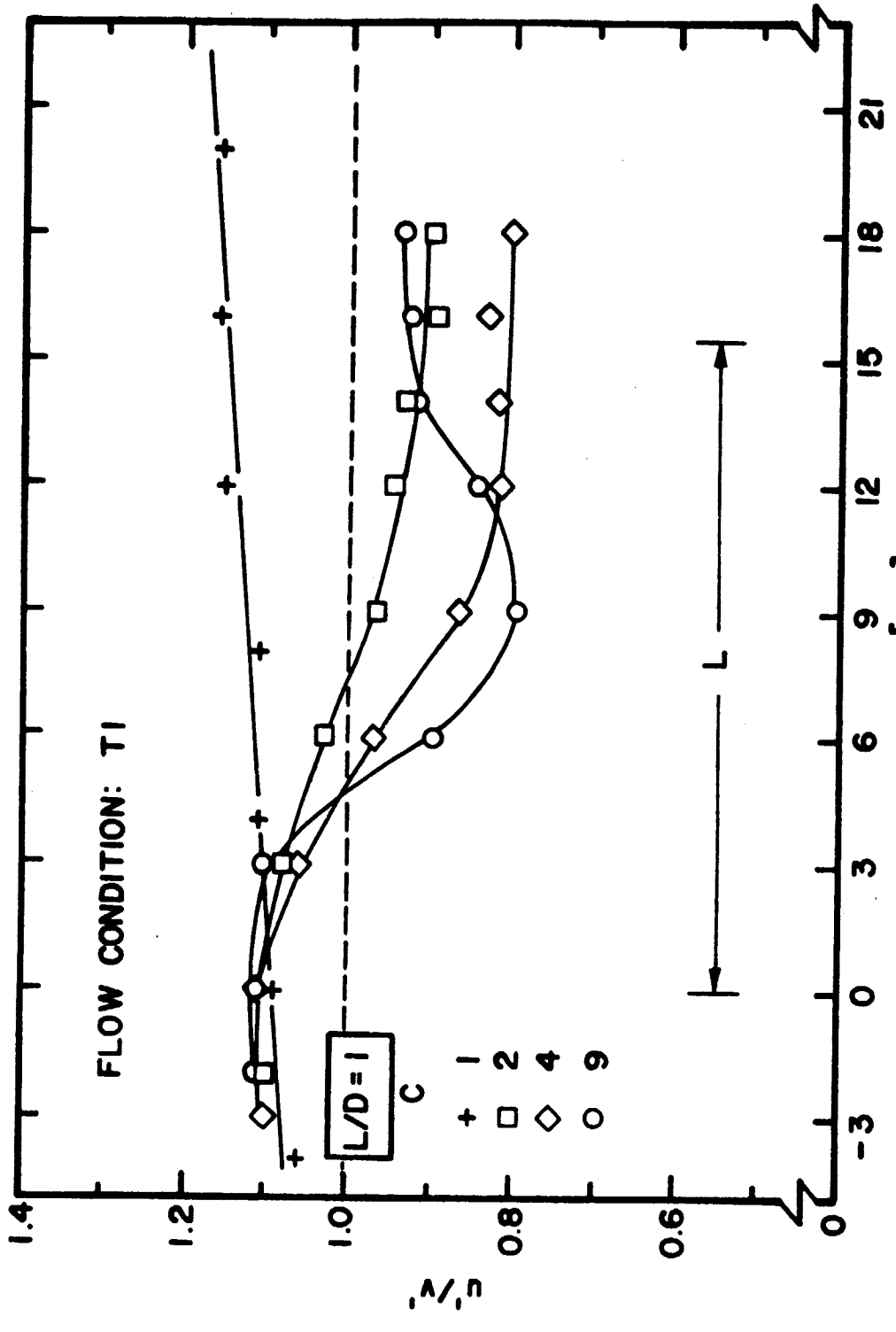

Figure 57. Isotropy through Moderate Contractions in Flow Condition T1

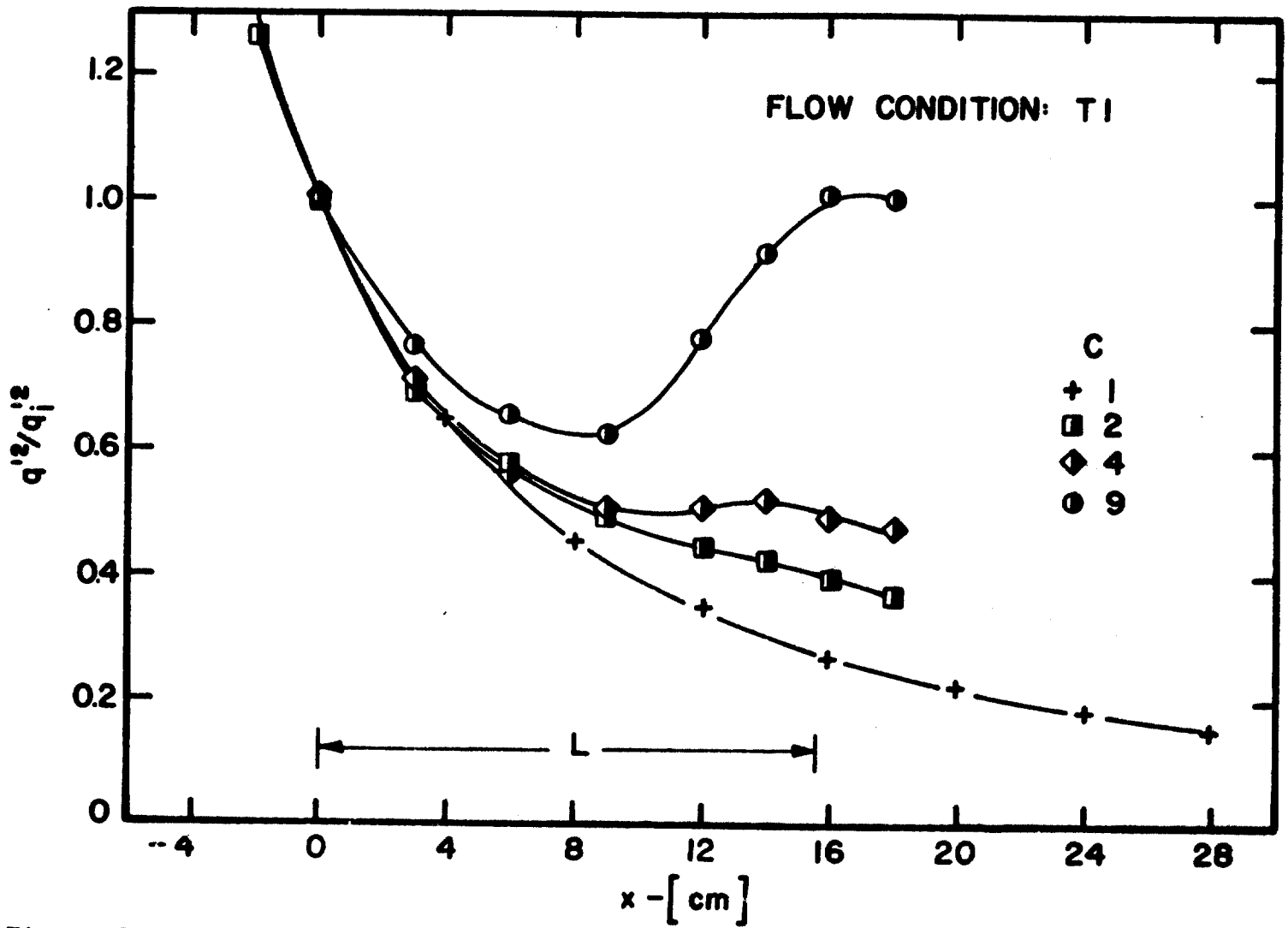

Figure 58. Normalized Total Turbulence Energy through Moderate Contractions in Flow Condition T1

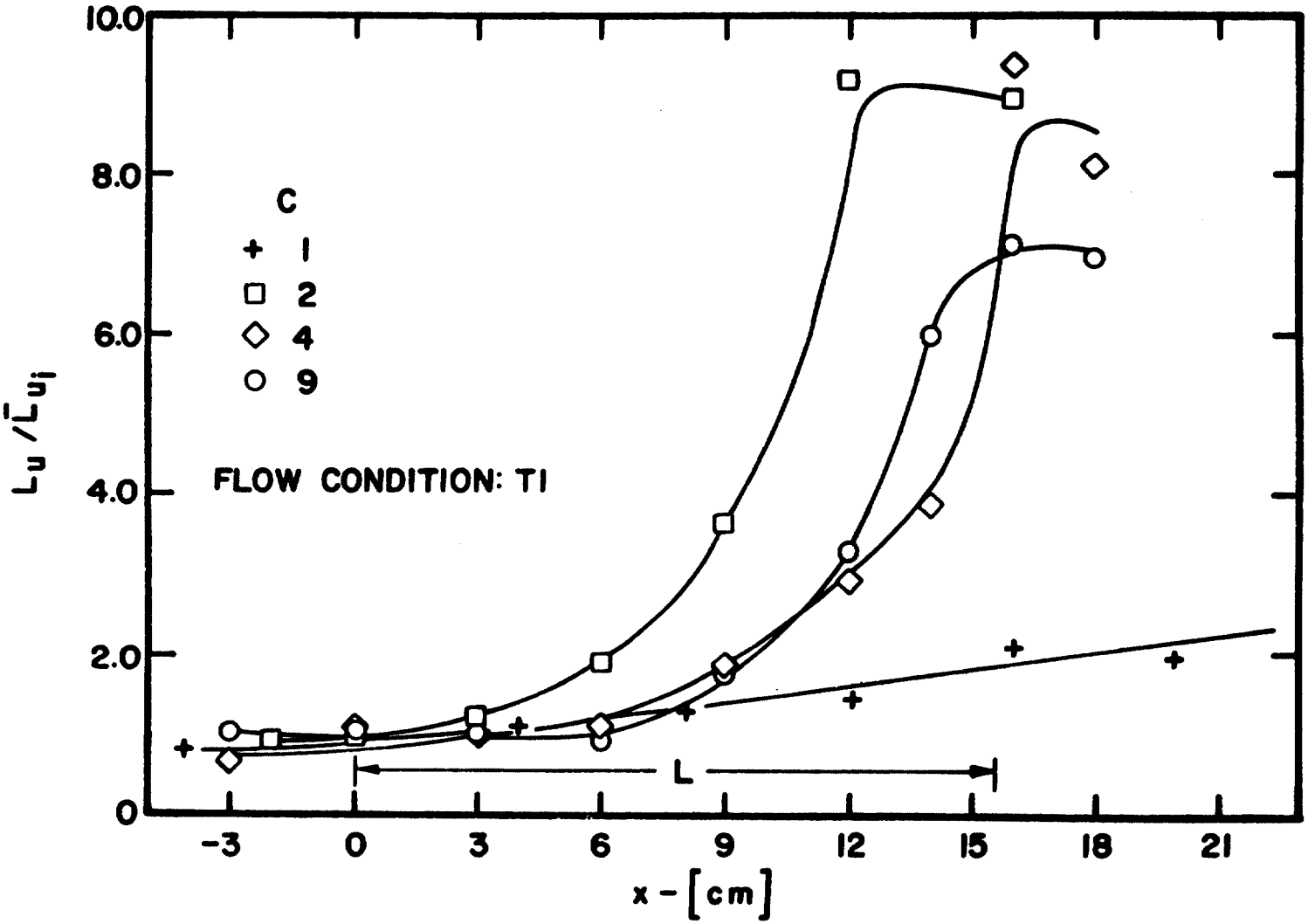

Figure 59. Normalized Longitudinal Length Scales through Moderate Contractions in Flow Condition T1

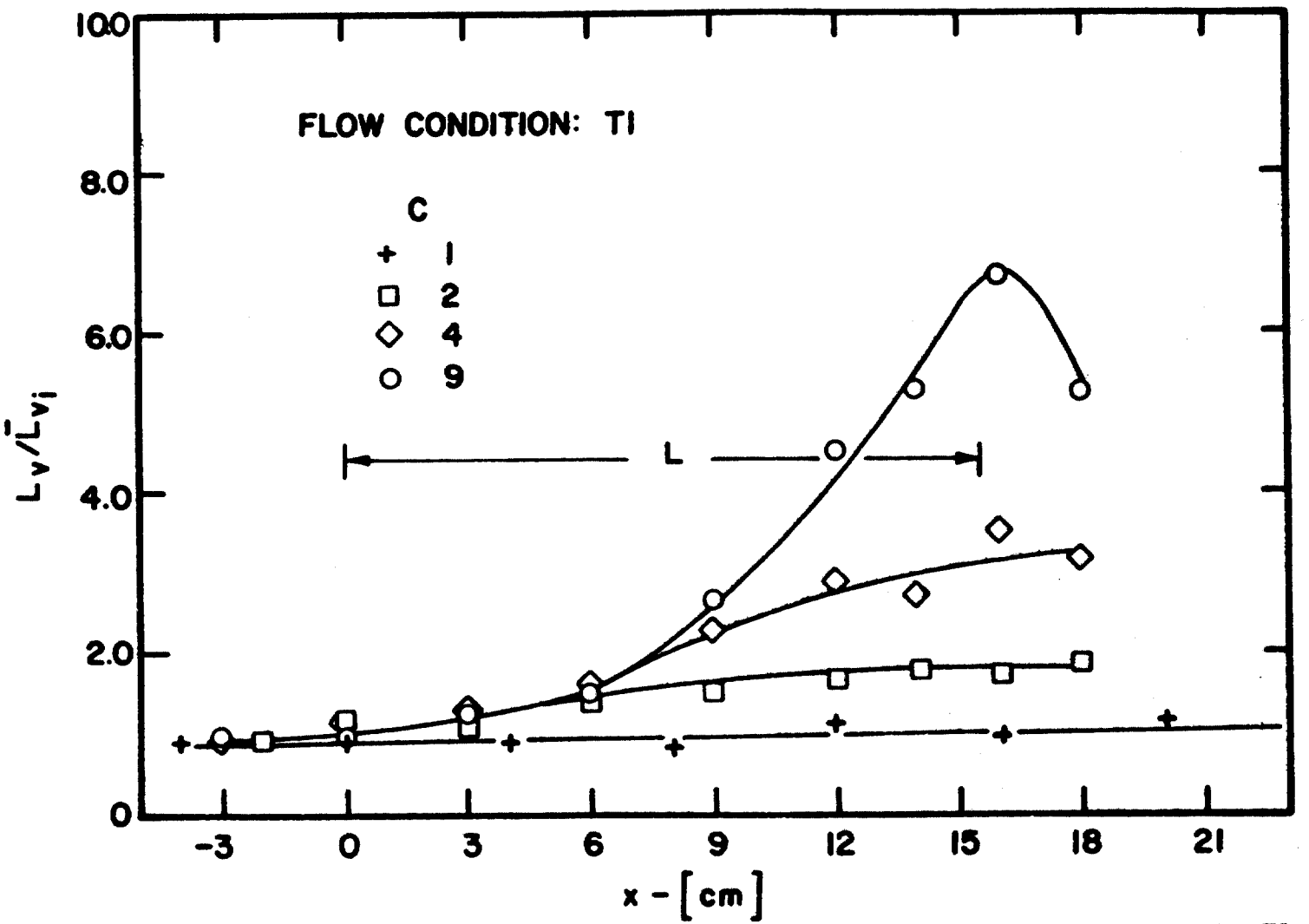

Figure 60. Normalized Lateral Length Scales through Moderate Contractions in Flow Condition T1

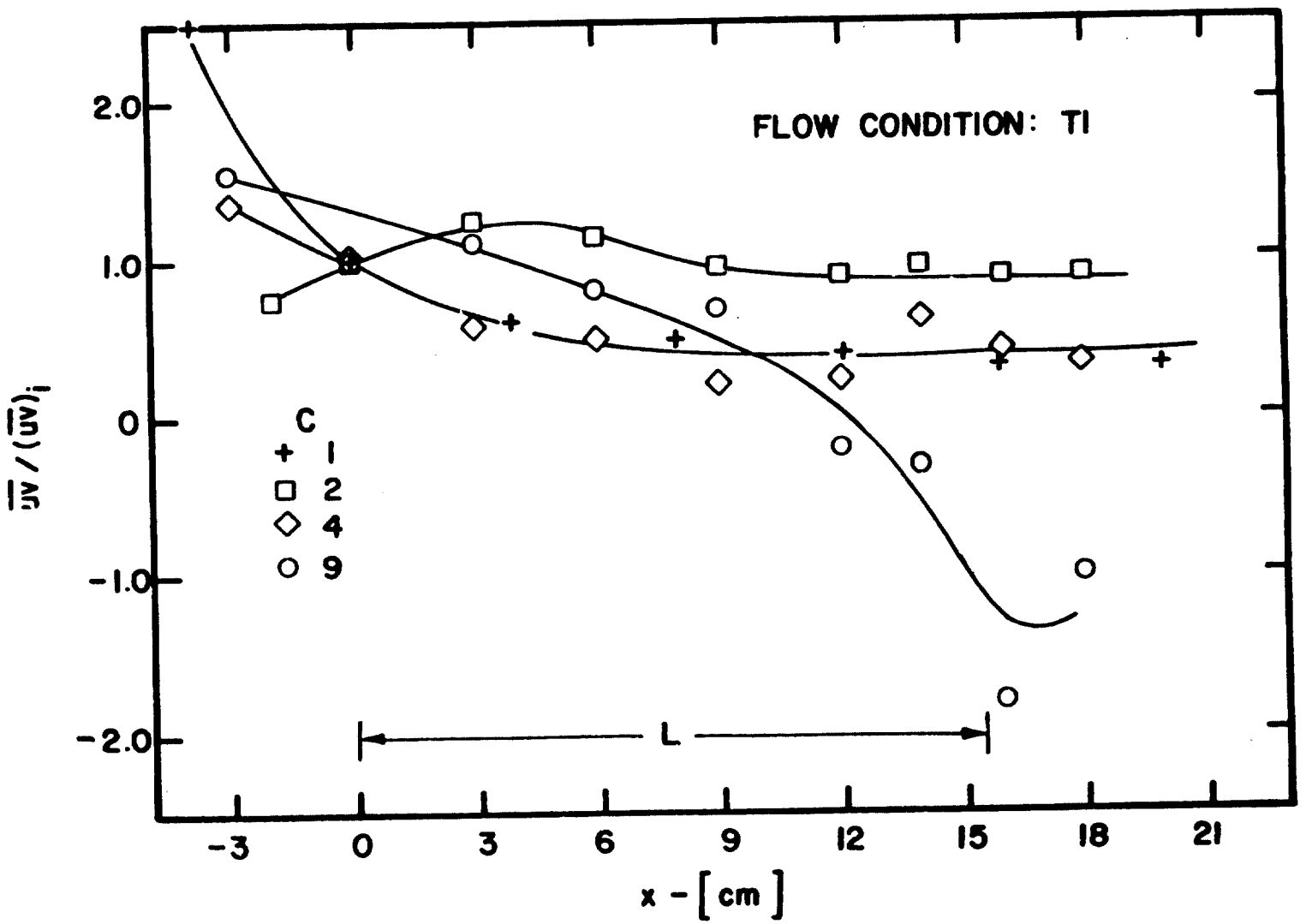

Figure 61. Normalized Reynolds Stresses through Moderate Contractions in Flow Condition TI

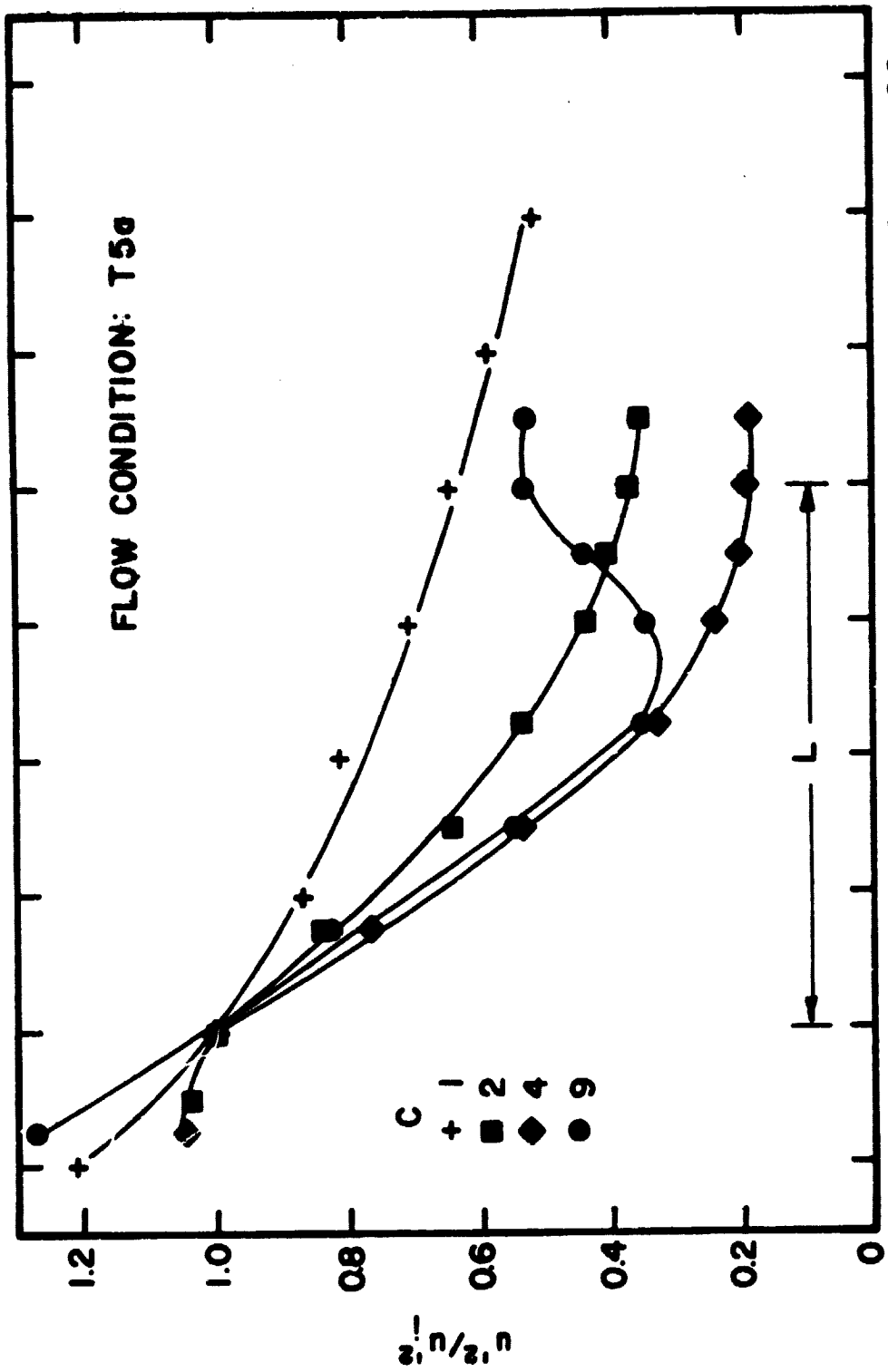

Figure 62. Normalized Streamwise Turbulence Energy through Moderate Contractions in Flow Condition T5a

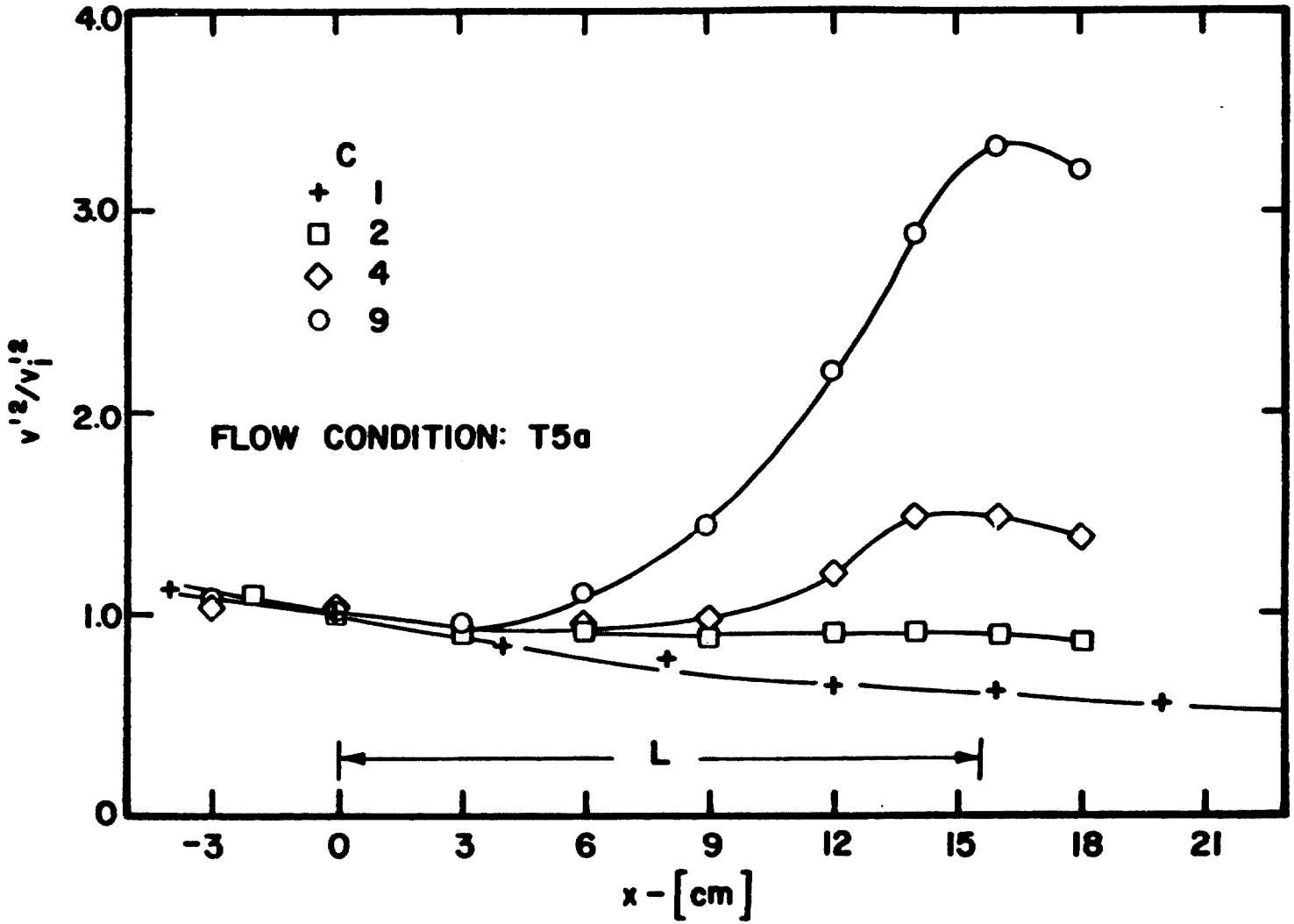

Figure 63. Normalized Radial Turbulence Energy through Moderate Contractions in Flow Condition T5a

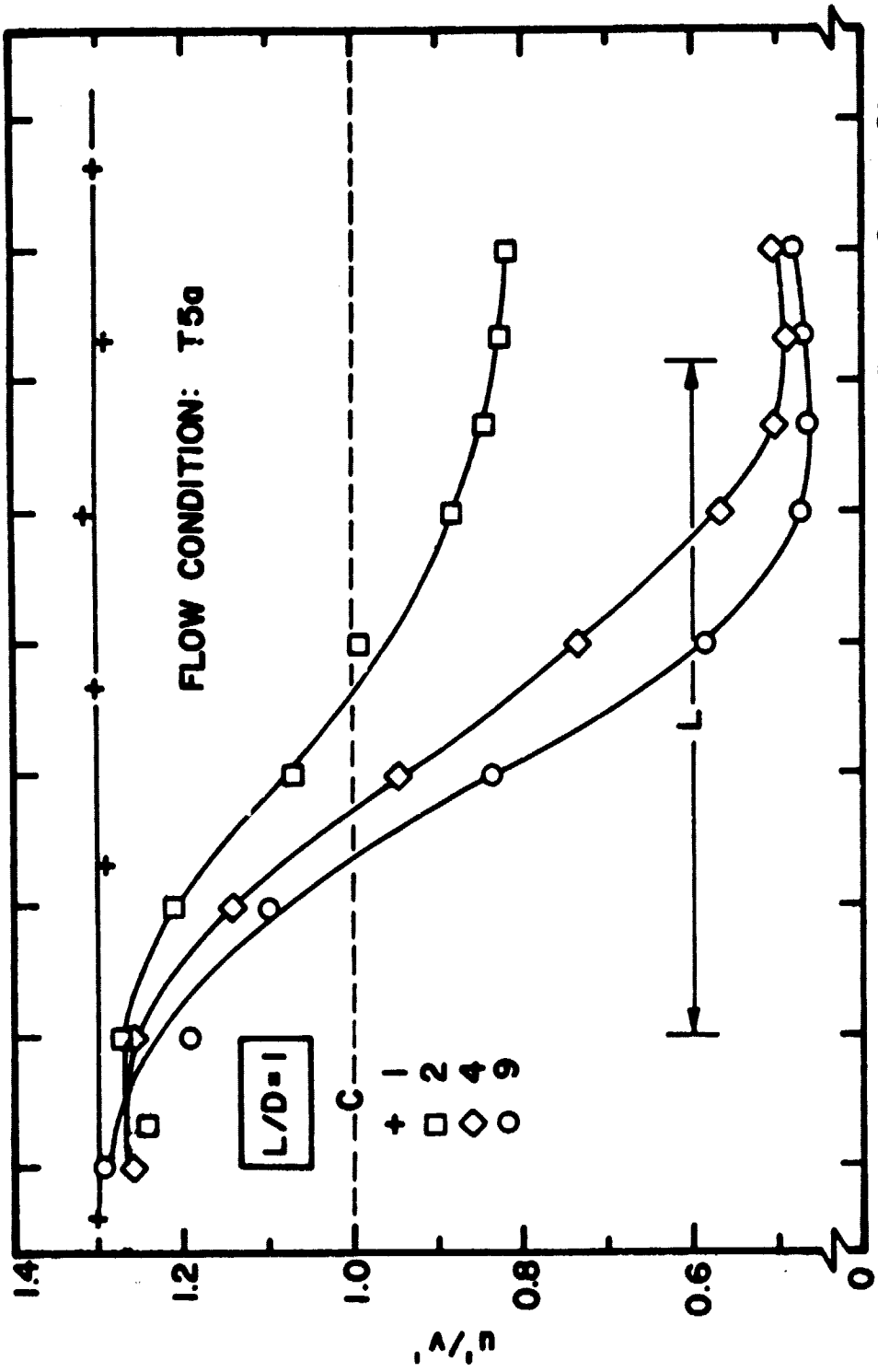

Figure 64. Isotropy through Moderate Contractions in Flow Condition T5a

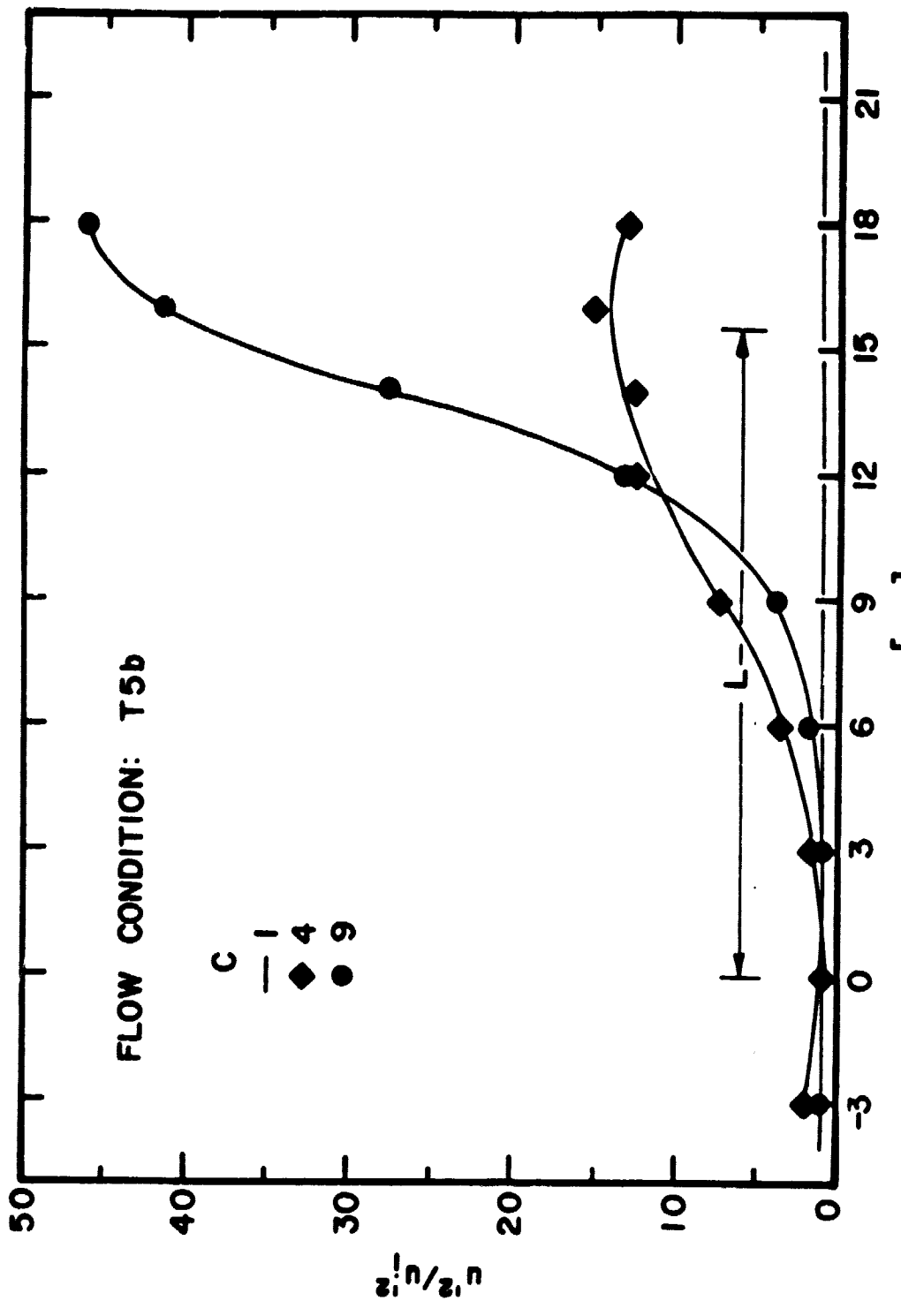

Figure 65. Normalized Streamwise Turbulence Energy through Moderate Contractions in Flow Condition T5b

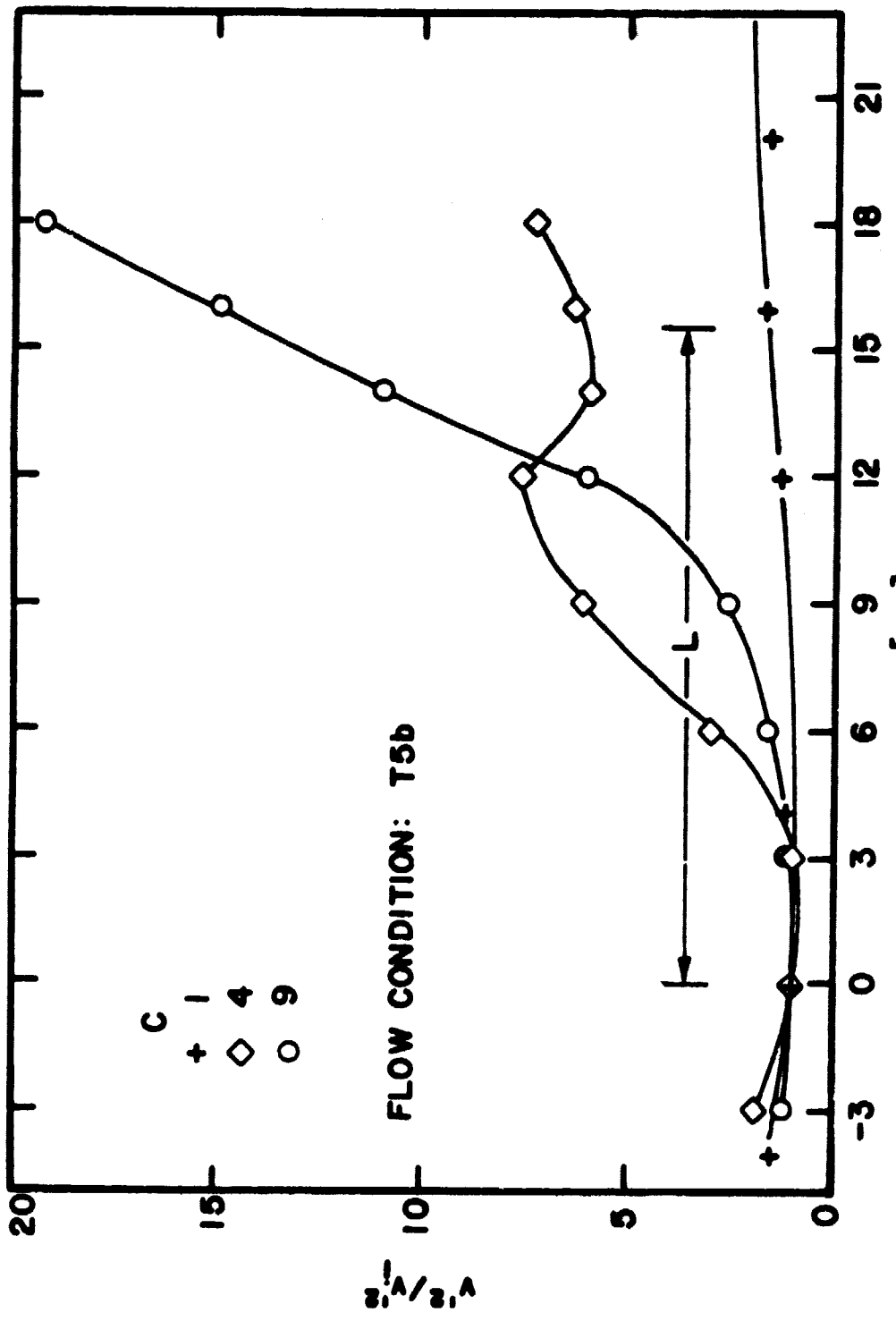

Figure 66. Normalized Radial Turbulence Energy through Moderate Contractions in Flow Condition T5b

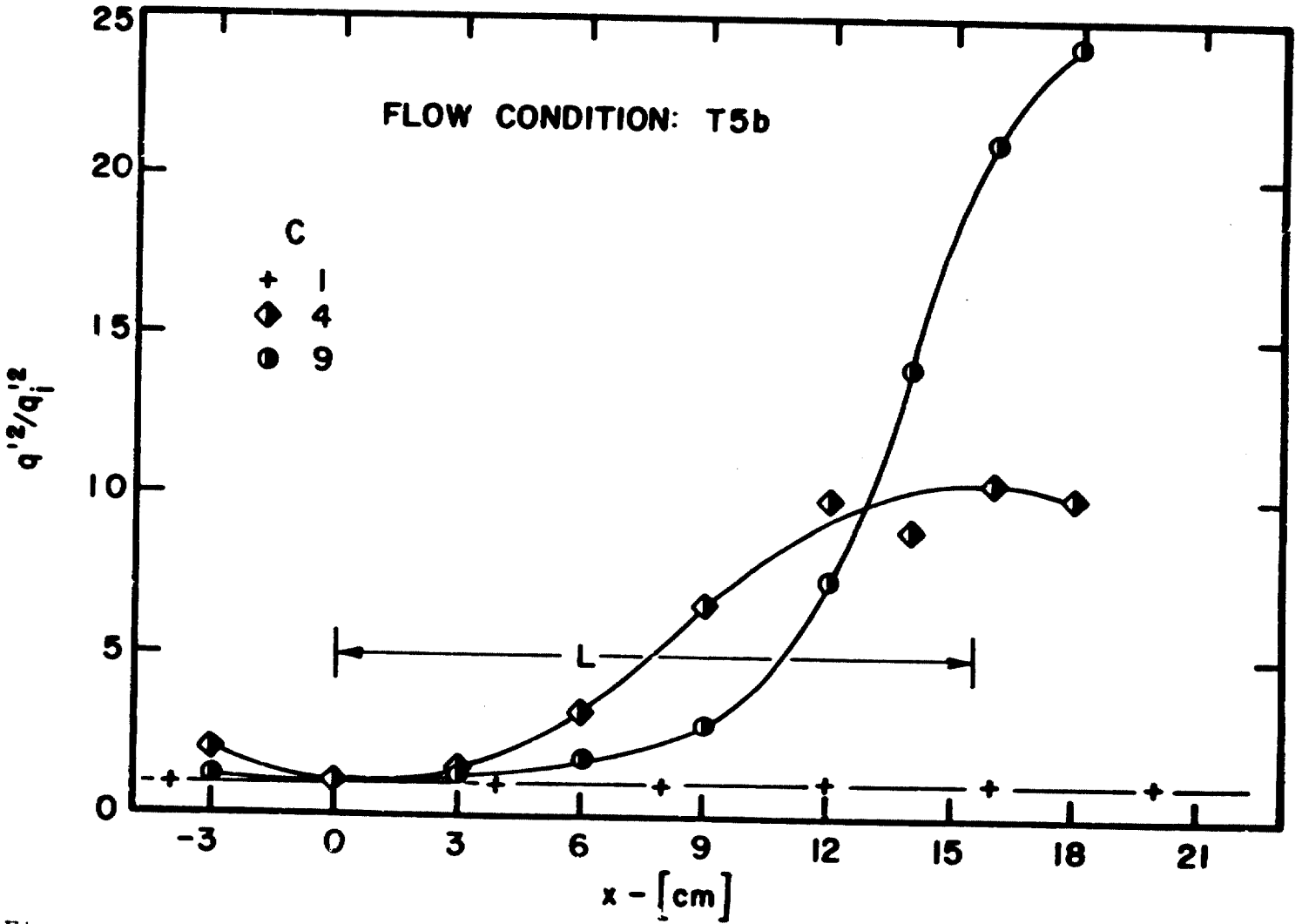

Figure 67. Normalized Total Turbulence Energy through Moderate Contractions in Flow Condition T5b

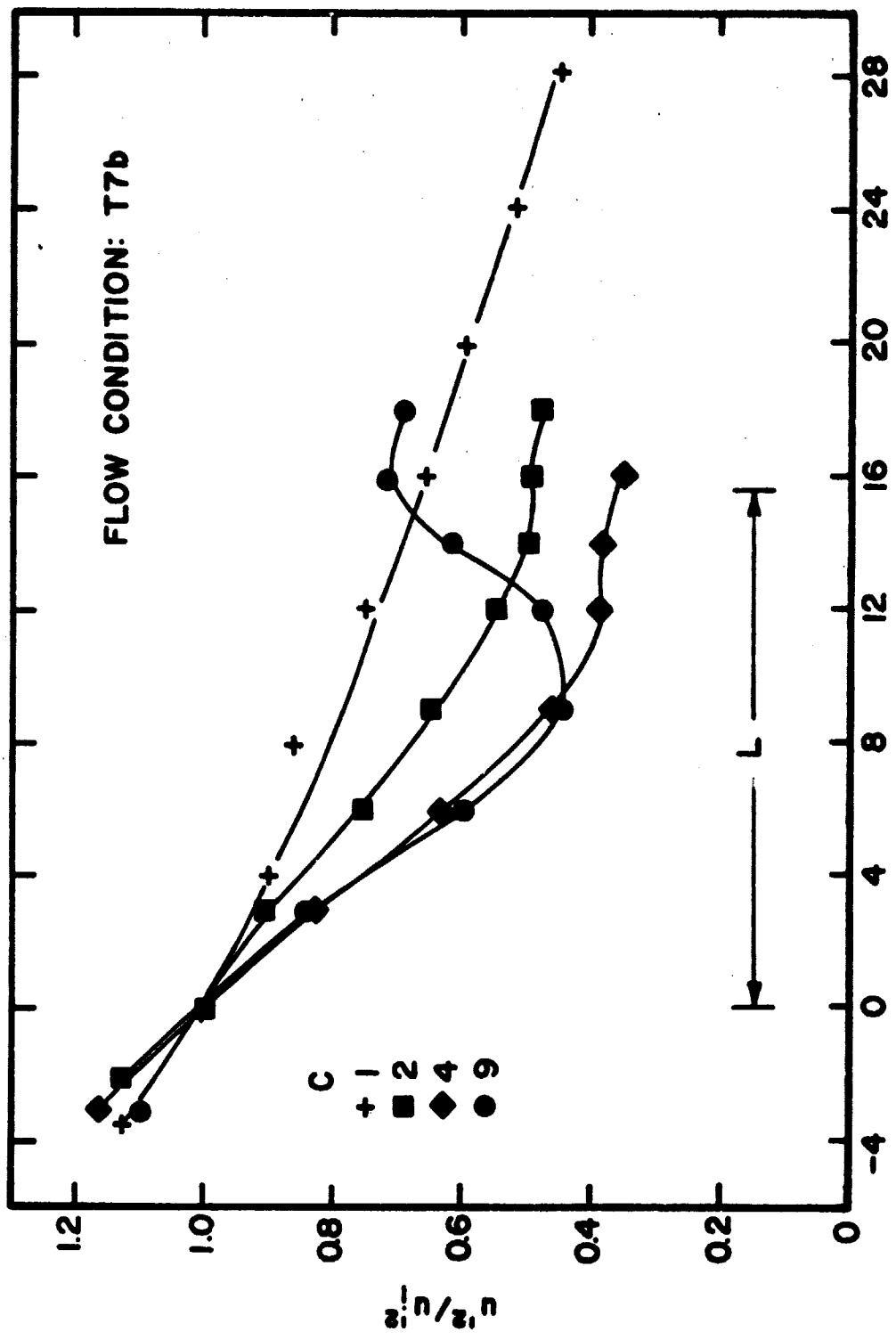

Figure 68. Normalized Streamwise Turbulence Energy through Moderate Contractions in Flow Condition T7b

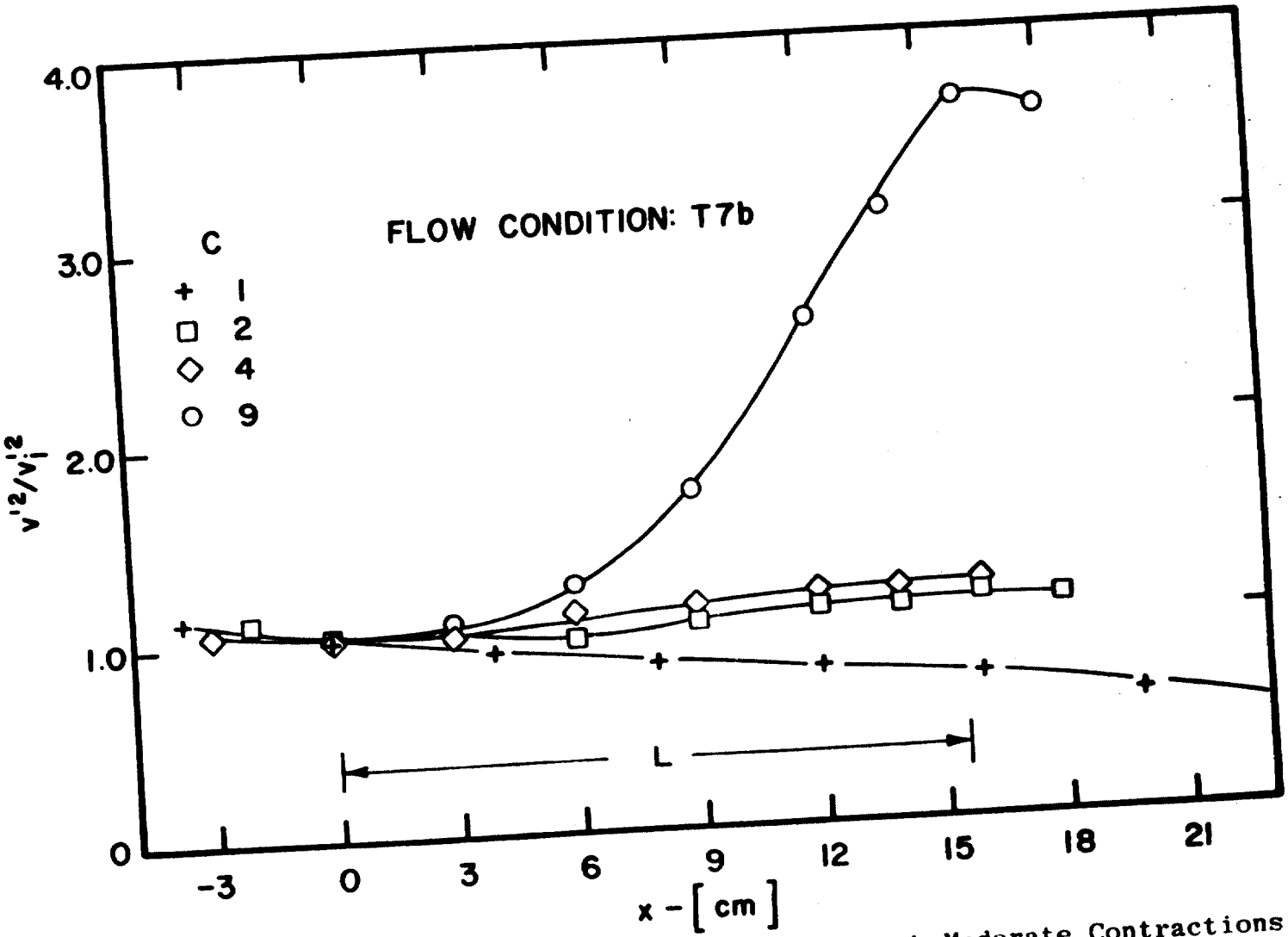

Figure 69. Normalized Radial Turbulence Energy through Moderate Contractions in Flow Condition T7b

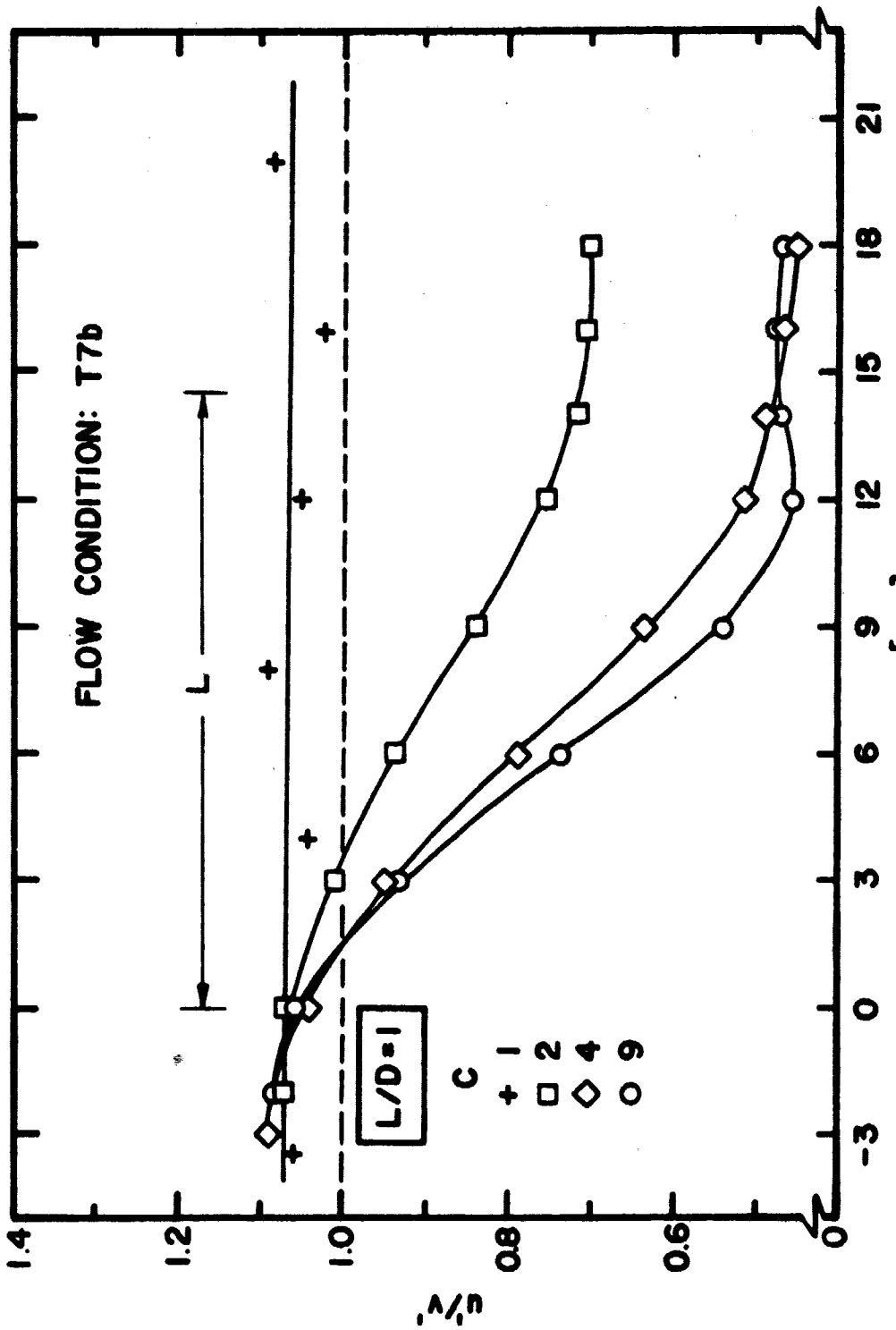

Figure 70. Isotropy through Moderate Contractions in Flow Condition T7b

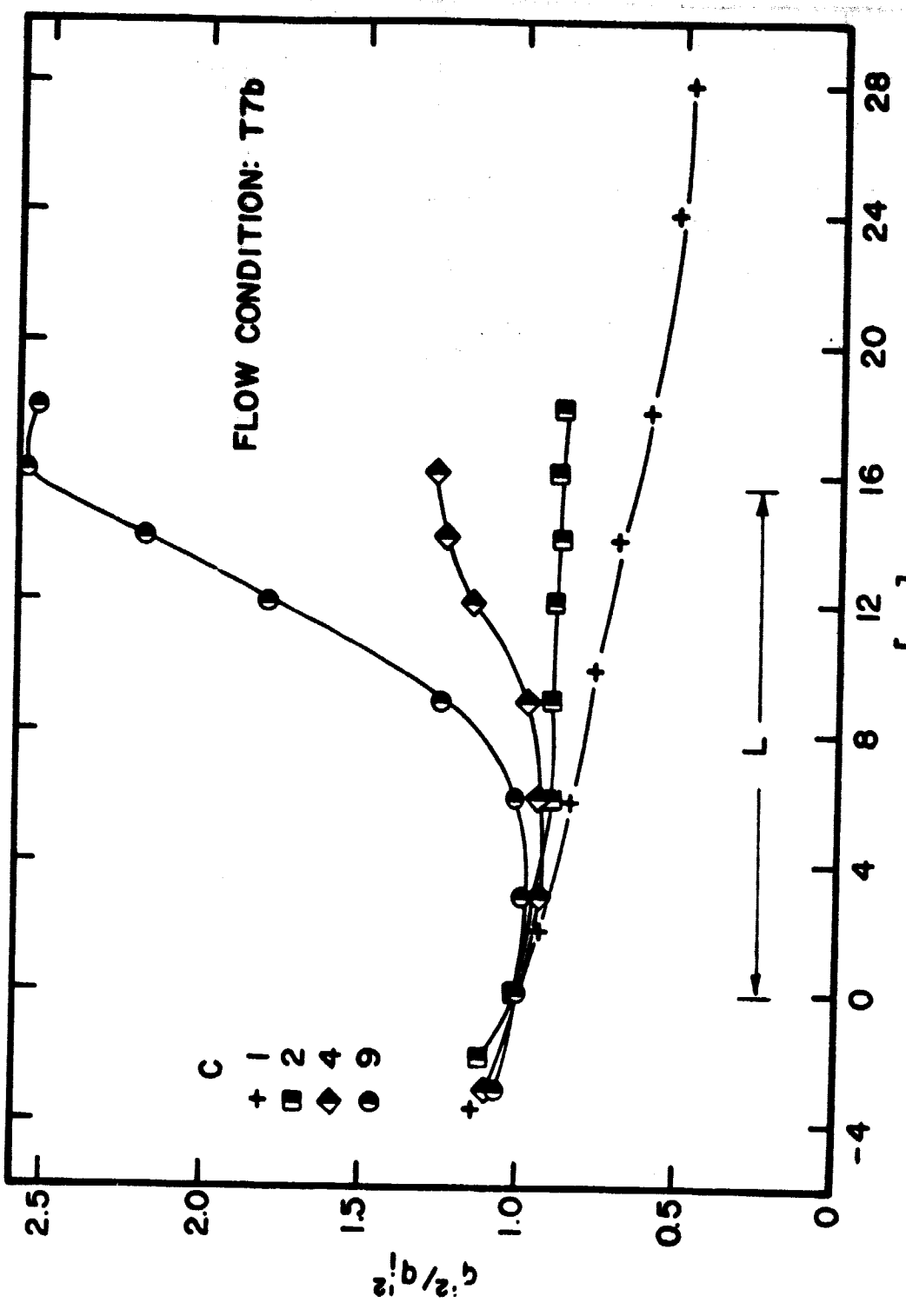

Figure 71. Normalized Total Turbulence Energy through Moderate Contractions in Flow Condition T7b

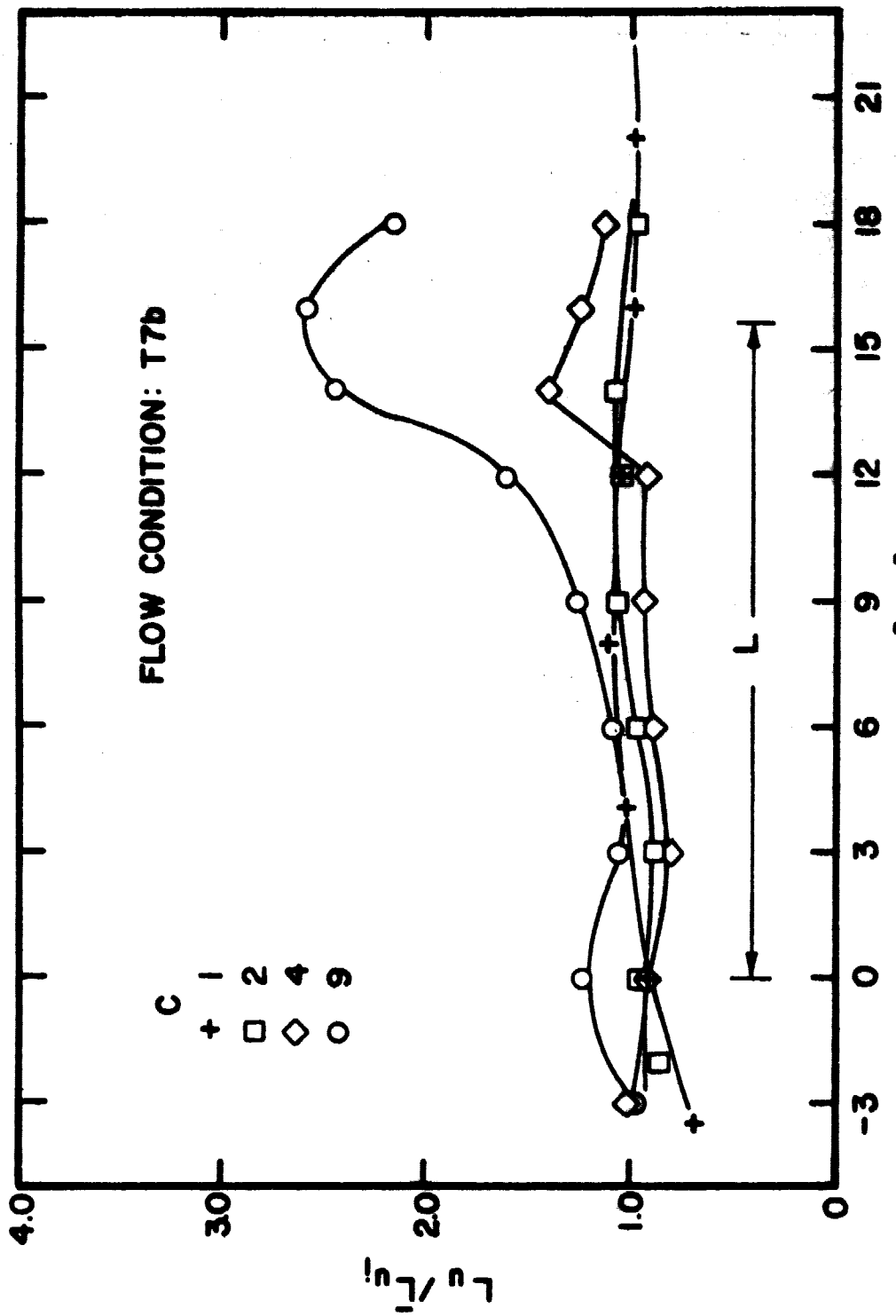

Figure 72. Normalized Longitudinal Length Scales through Moderate Contractions in Flow Condition T7b

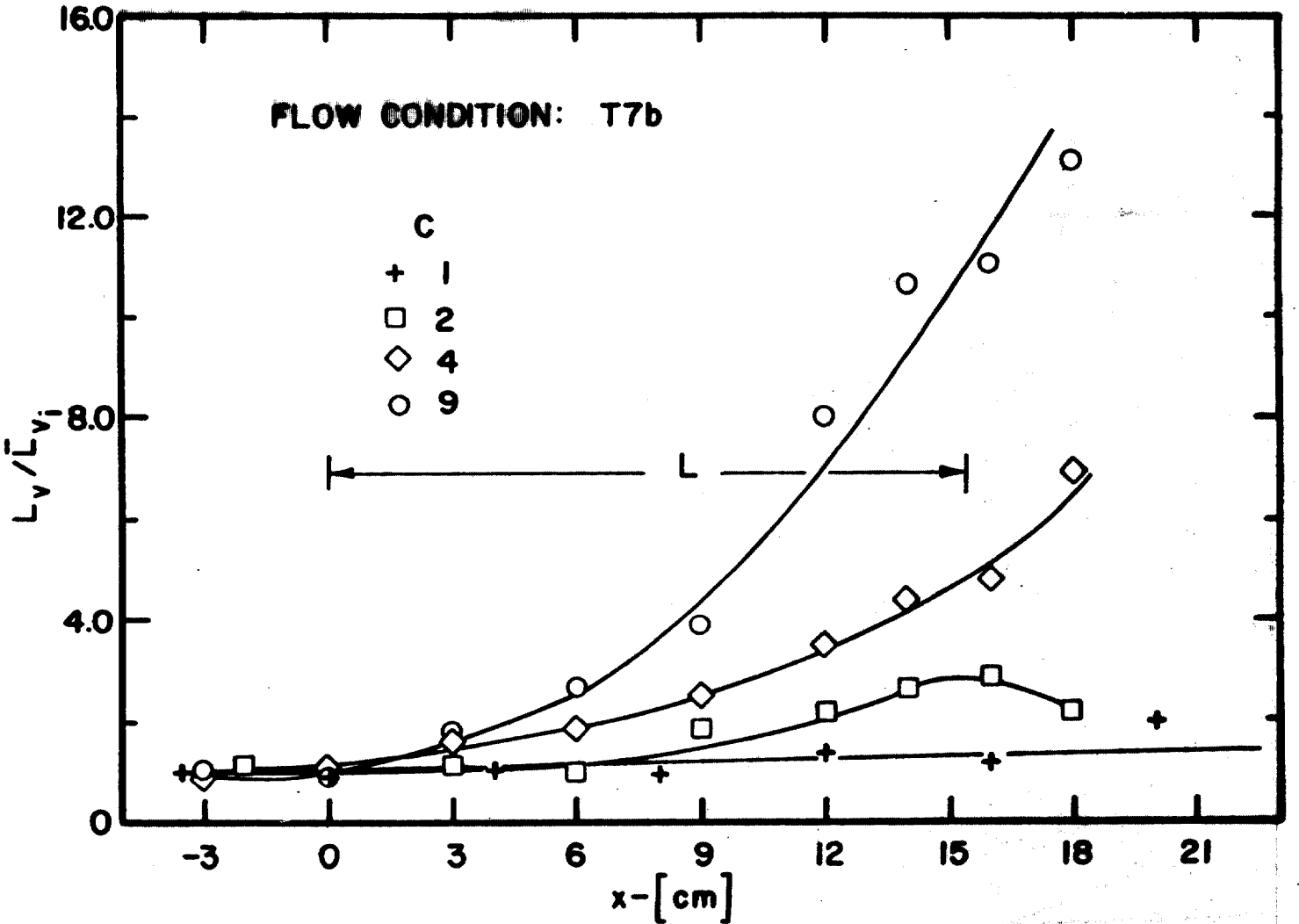

Figure 73. Normalized Lateral Length Scales through Moderate Contractions in Flow Condition T7b

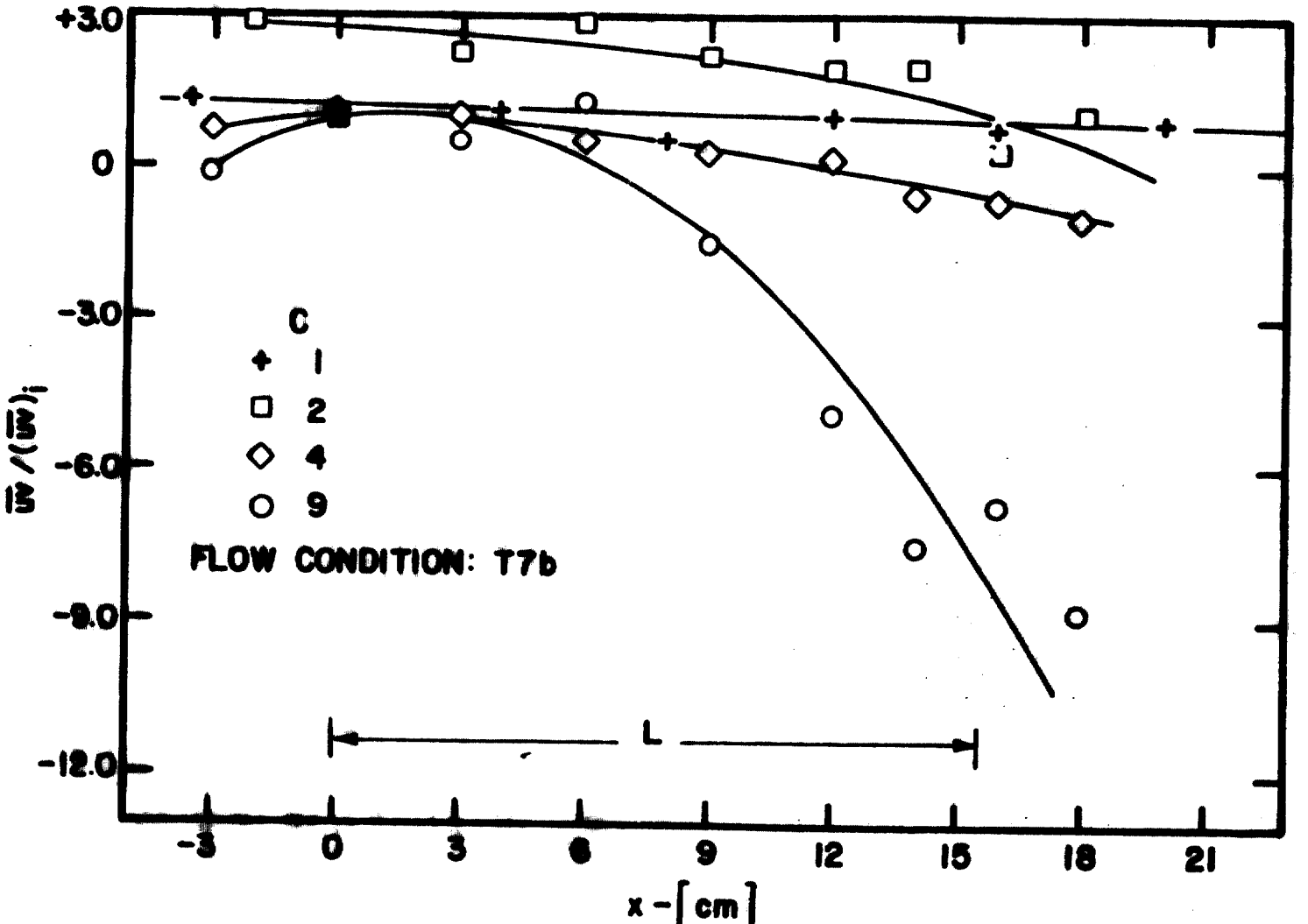

Figure 74. Normalized Reynolds Stresses through Moderate Contractions in Flow Condition T7b

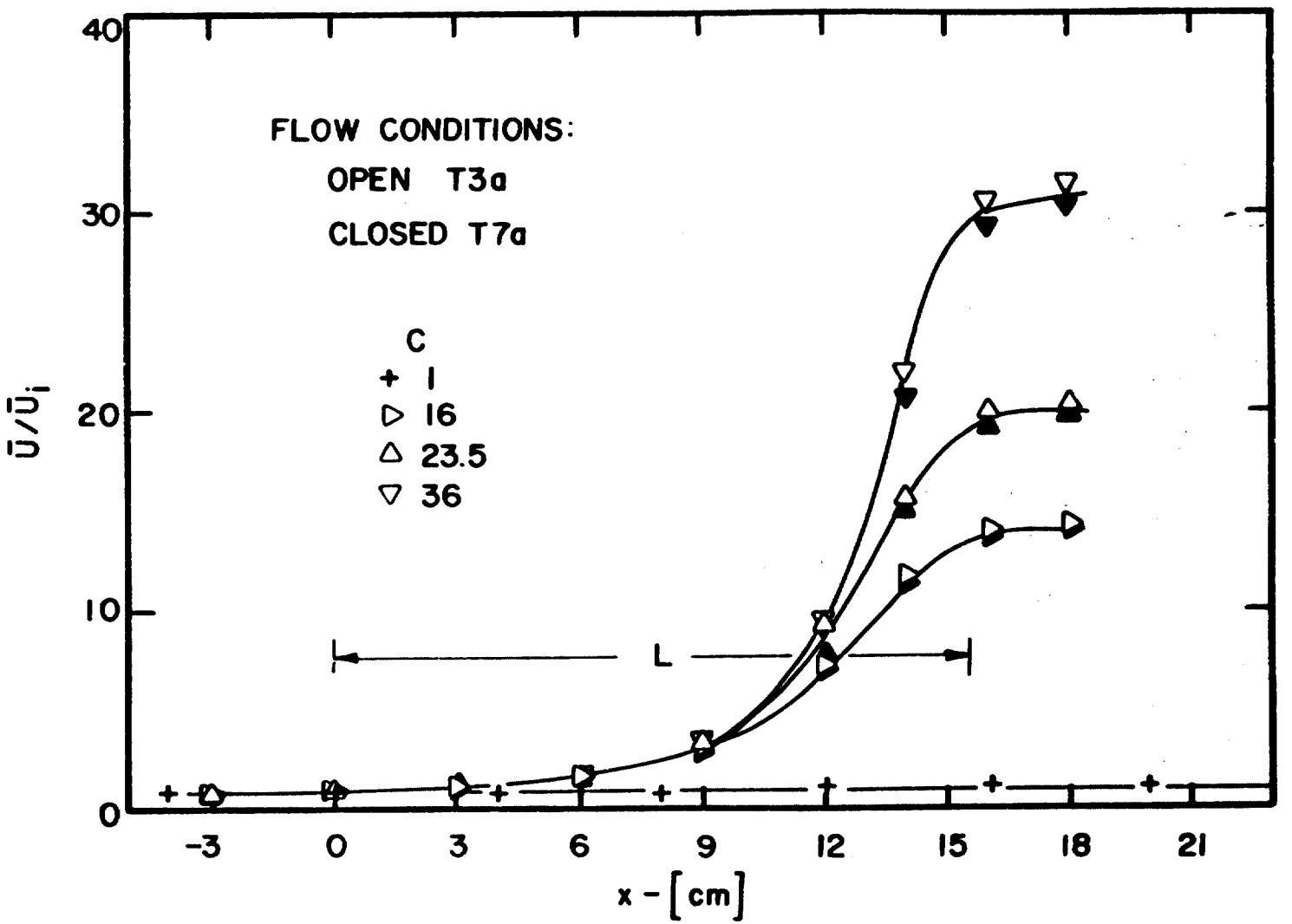

Figure 75. Normalized Streamwise Mean Velocity through High Contractions in Flow Conditions T3a and T7a

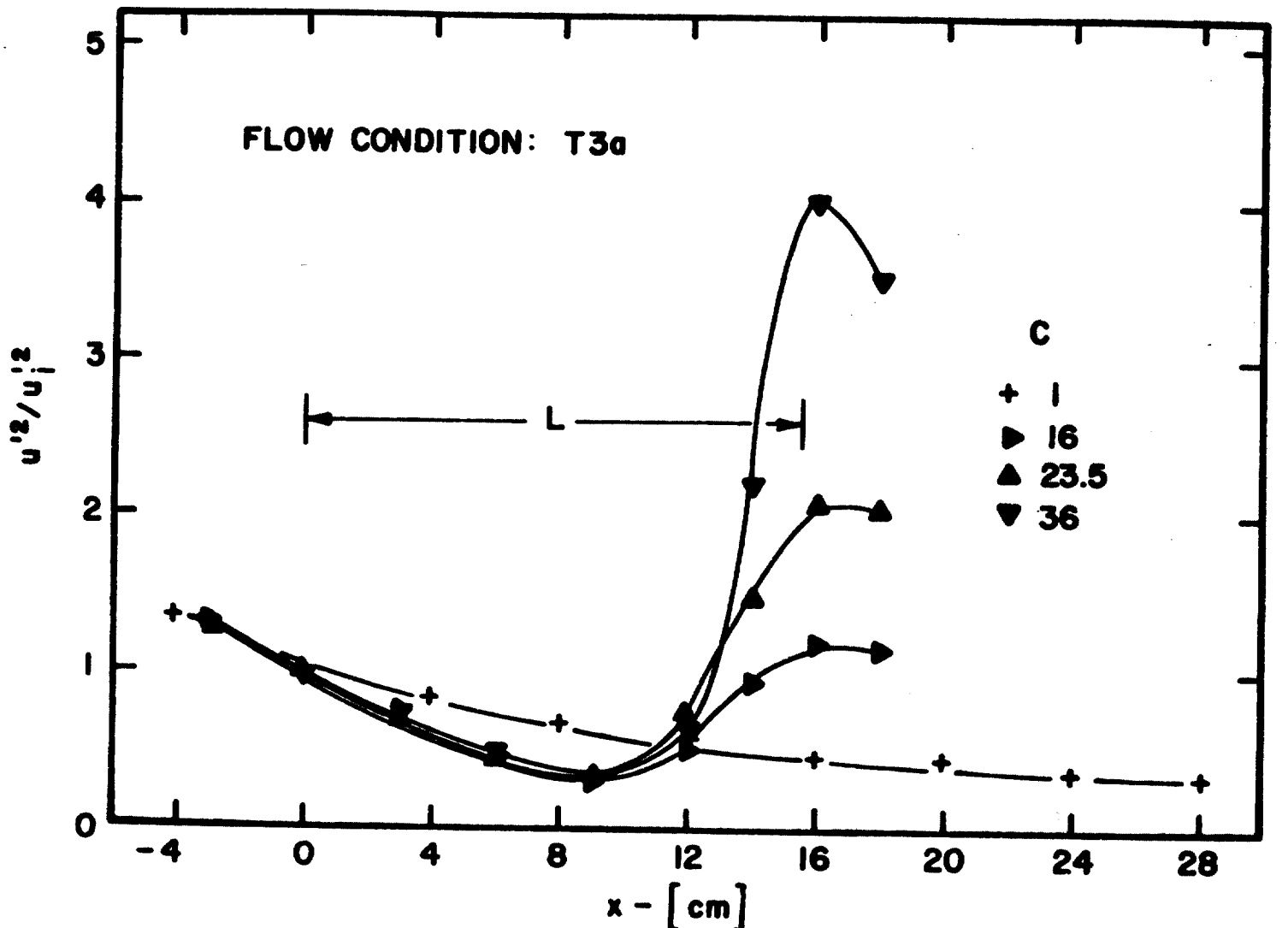

Figure 76. Normalized Streamwise Turbulence Energy through High Contractions in Flow Condition T3a

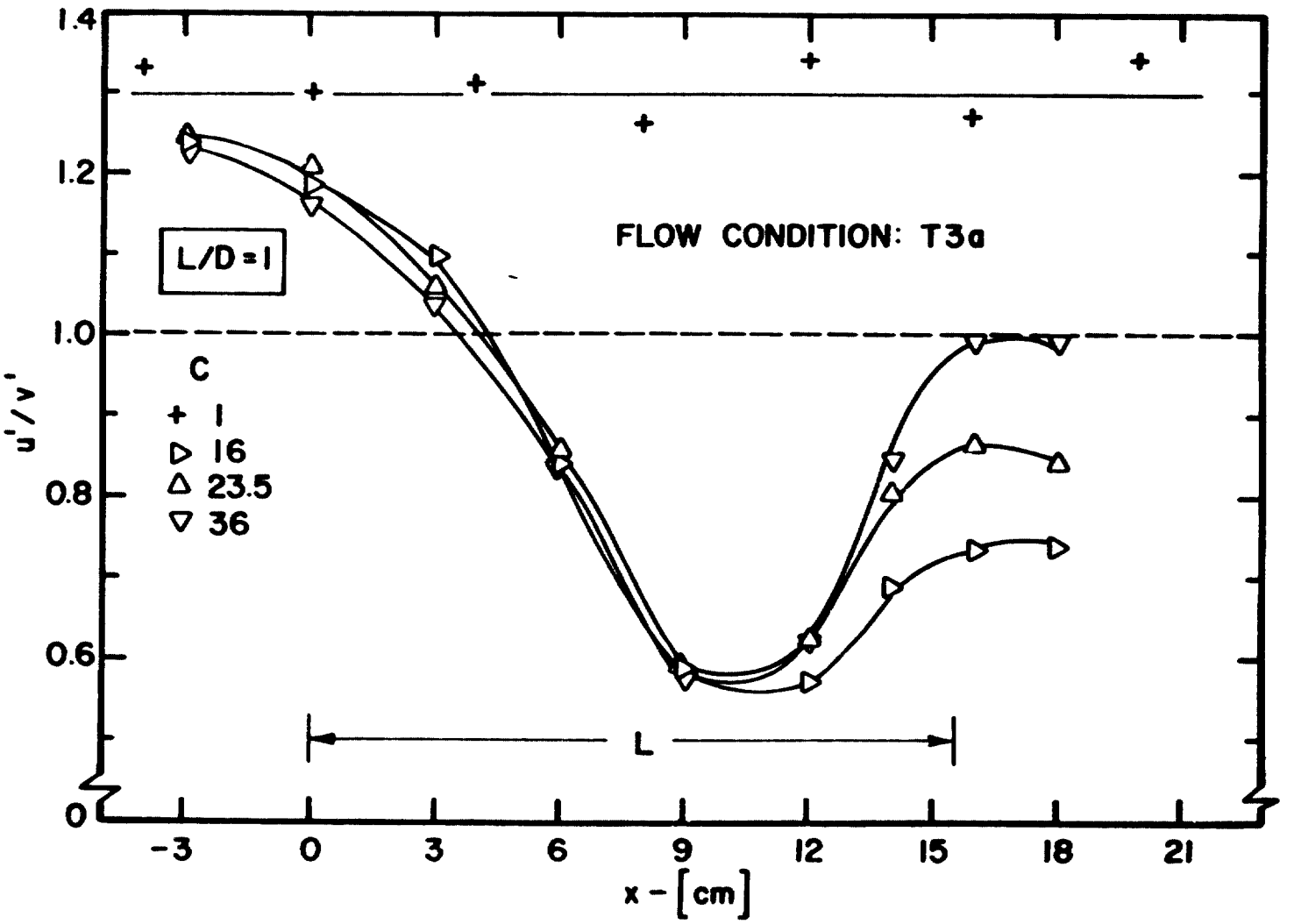

Figure 77. Isotropy through High Contractions in Flow Condition T3a

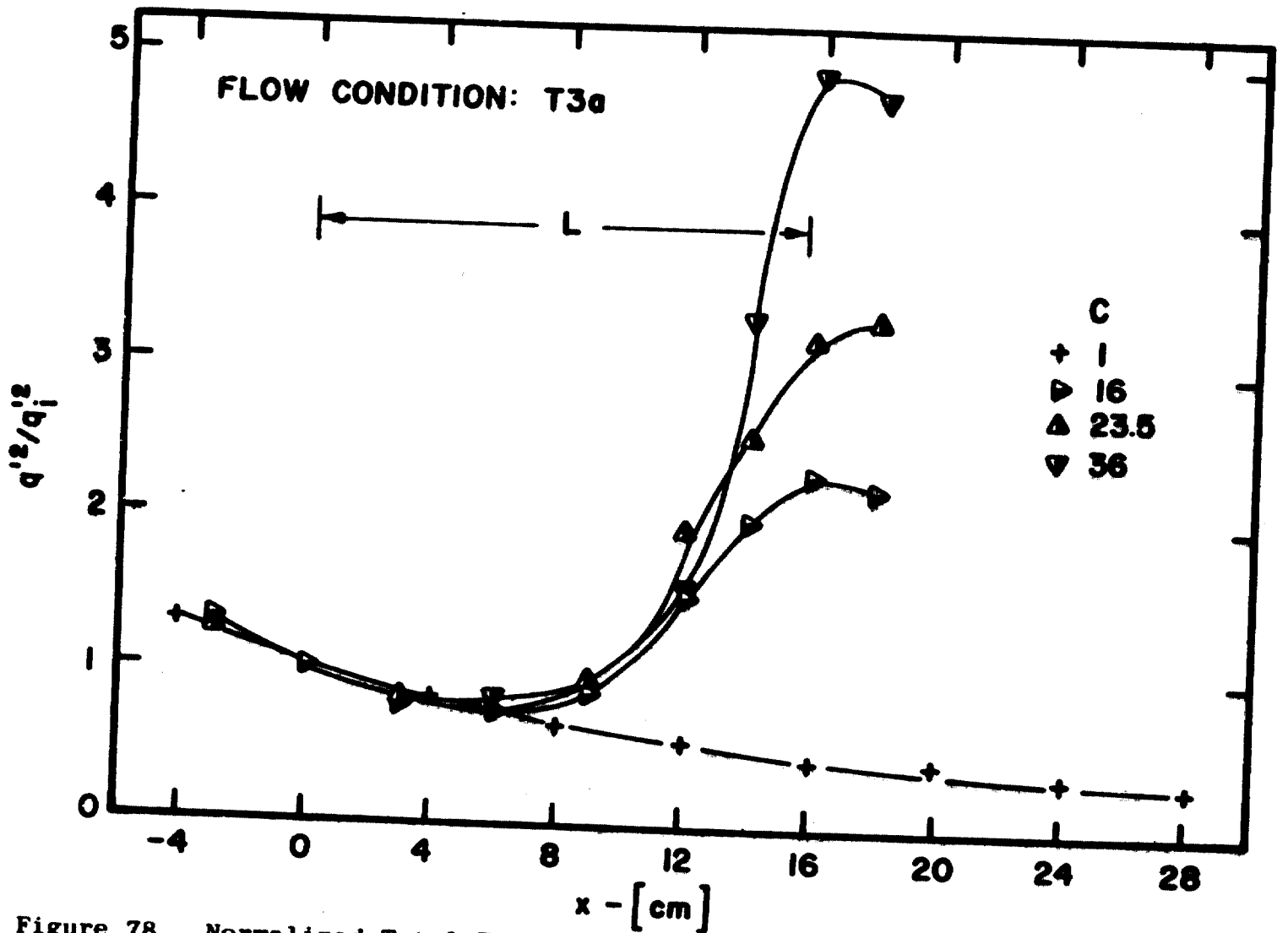

Figure 78. Normalized Total Turbulence Energy through High Contractions in Flow Condition T3a

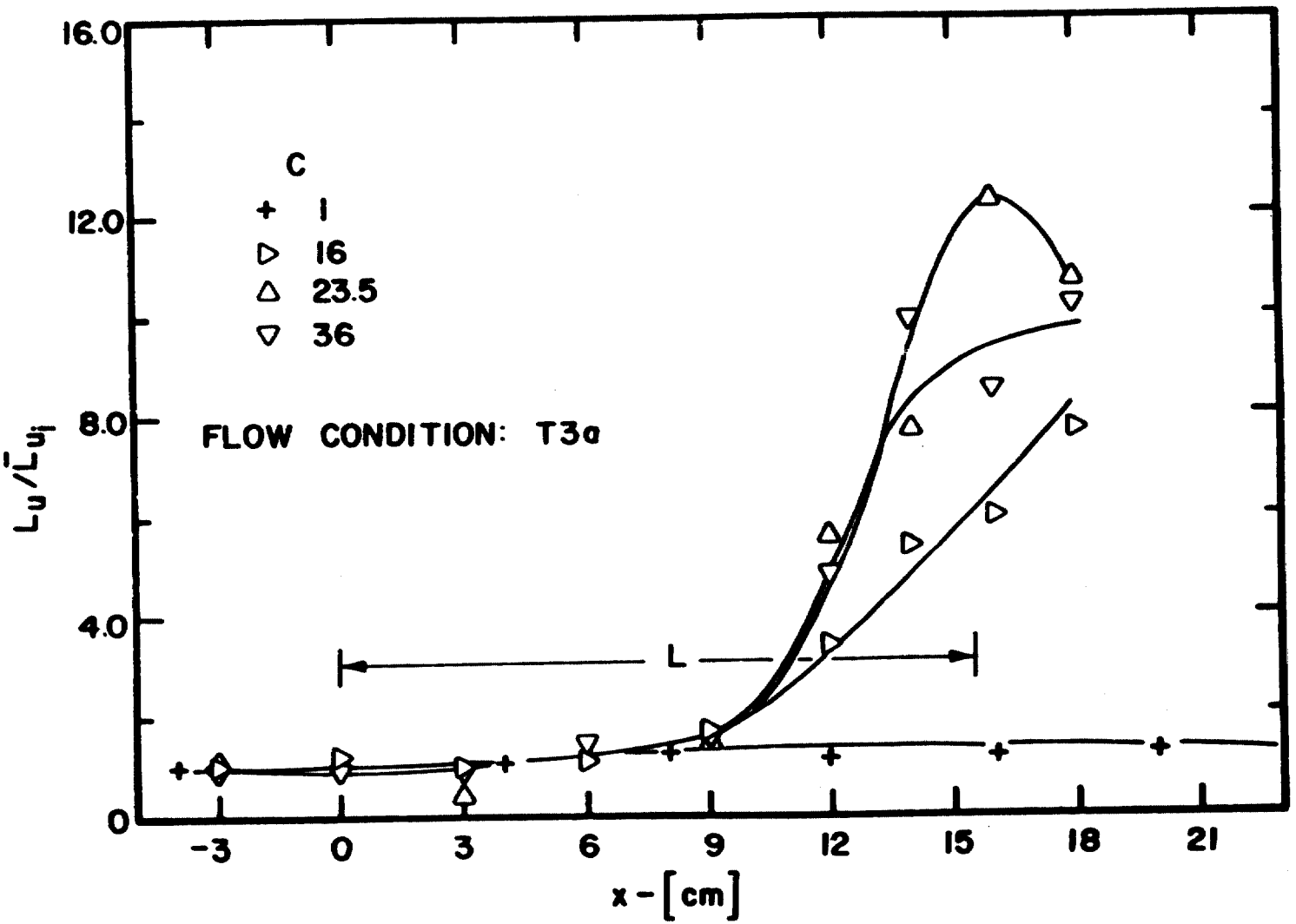

Figure 79. Normalized Longitudinal Length Scales through High Contractions in Flow Condition T3a

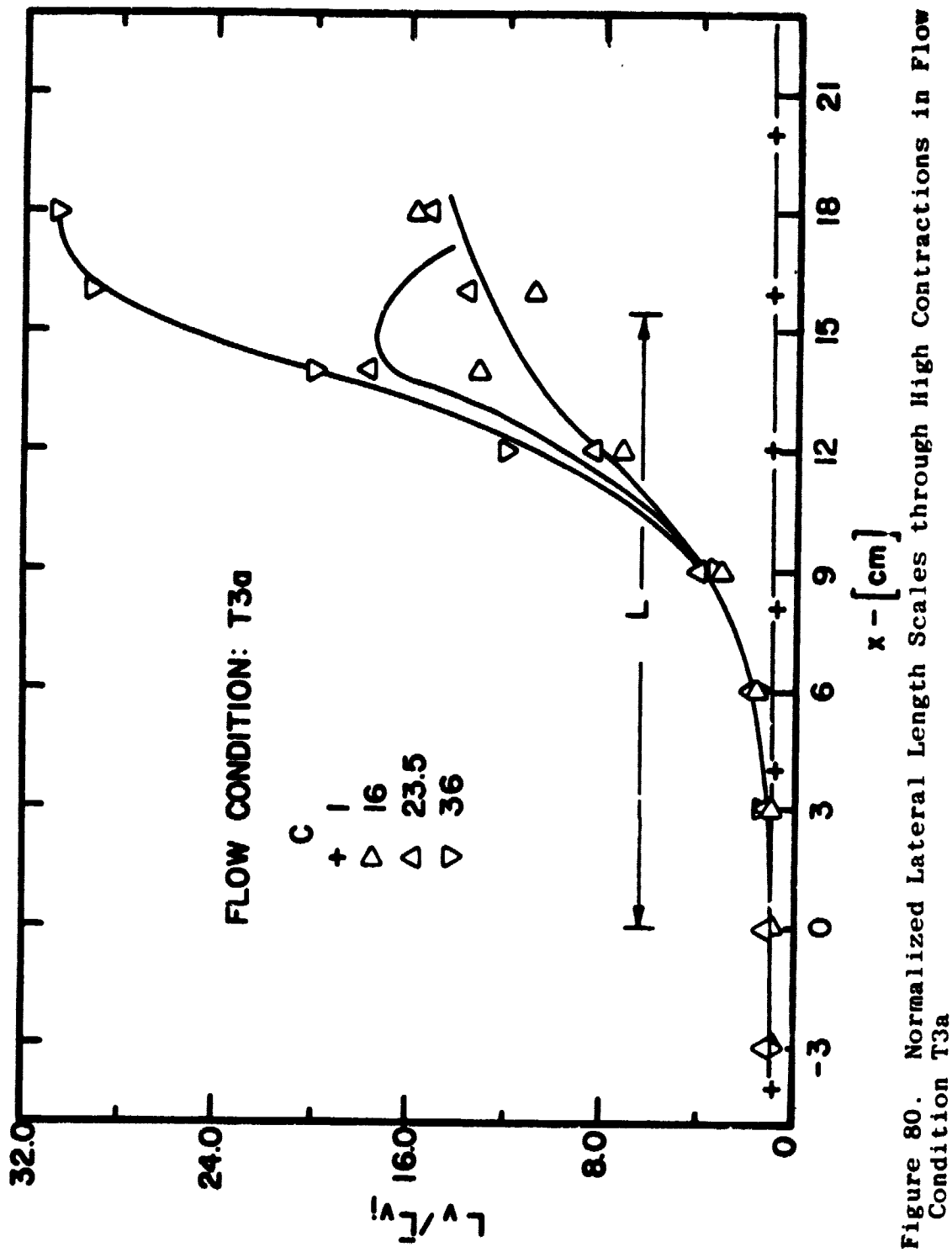

Figure 80. Normalized Lateral Length Scales through High Contractions in Flow Condition T3a

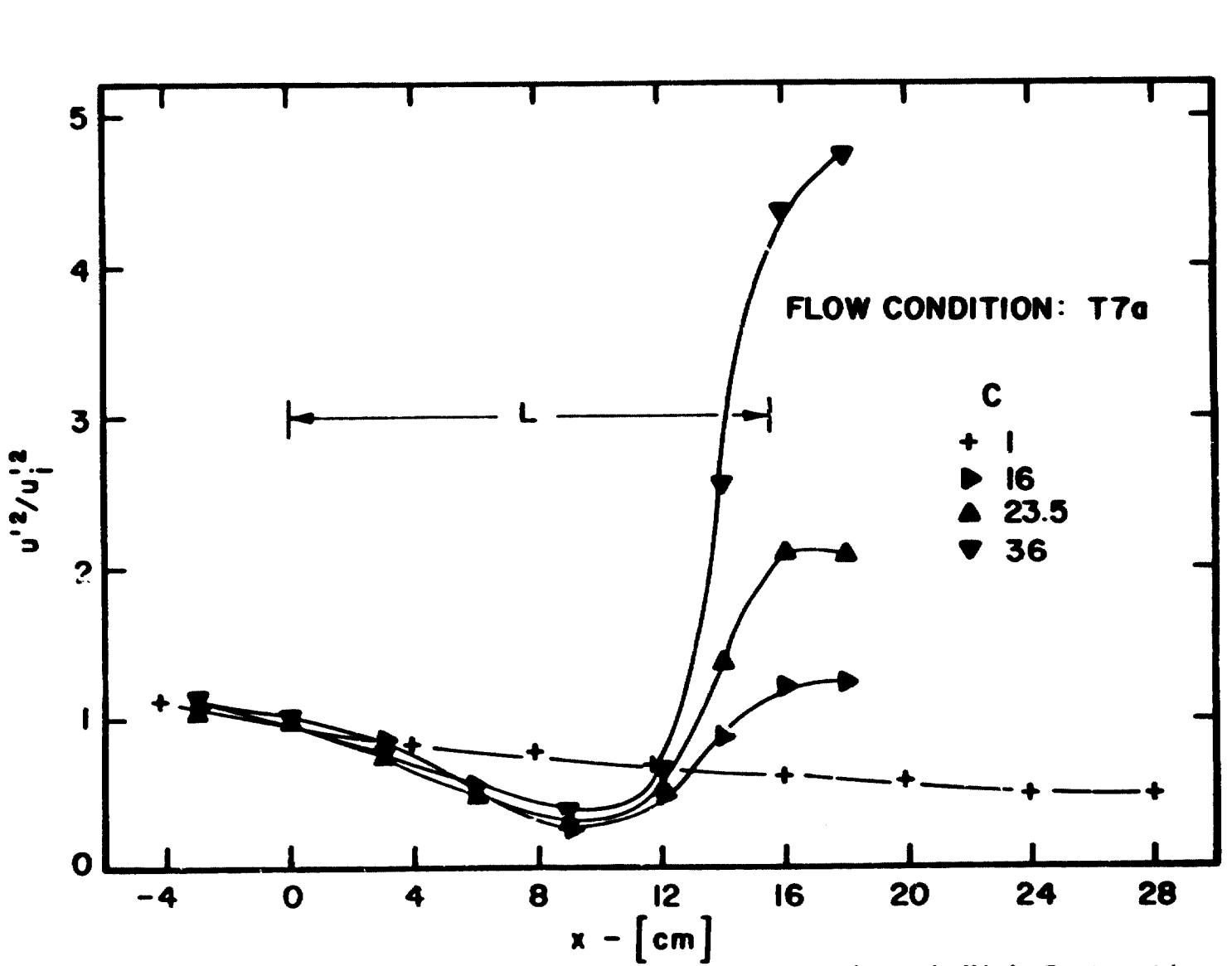

Figure 81. Normalized Streamwise Turbulence Energy through High Contractions in Flow Condition T7a

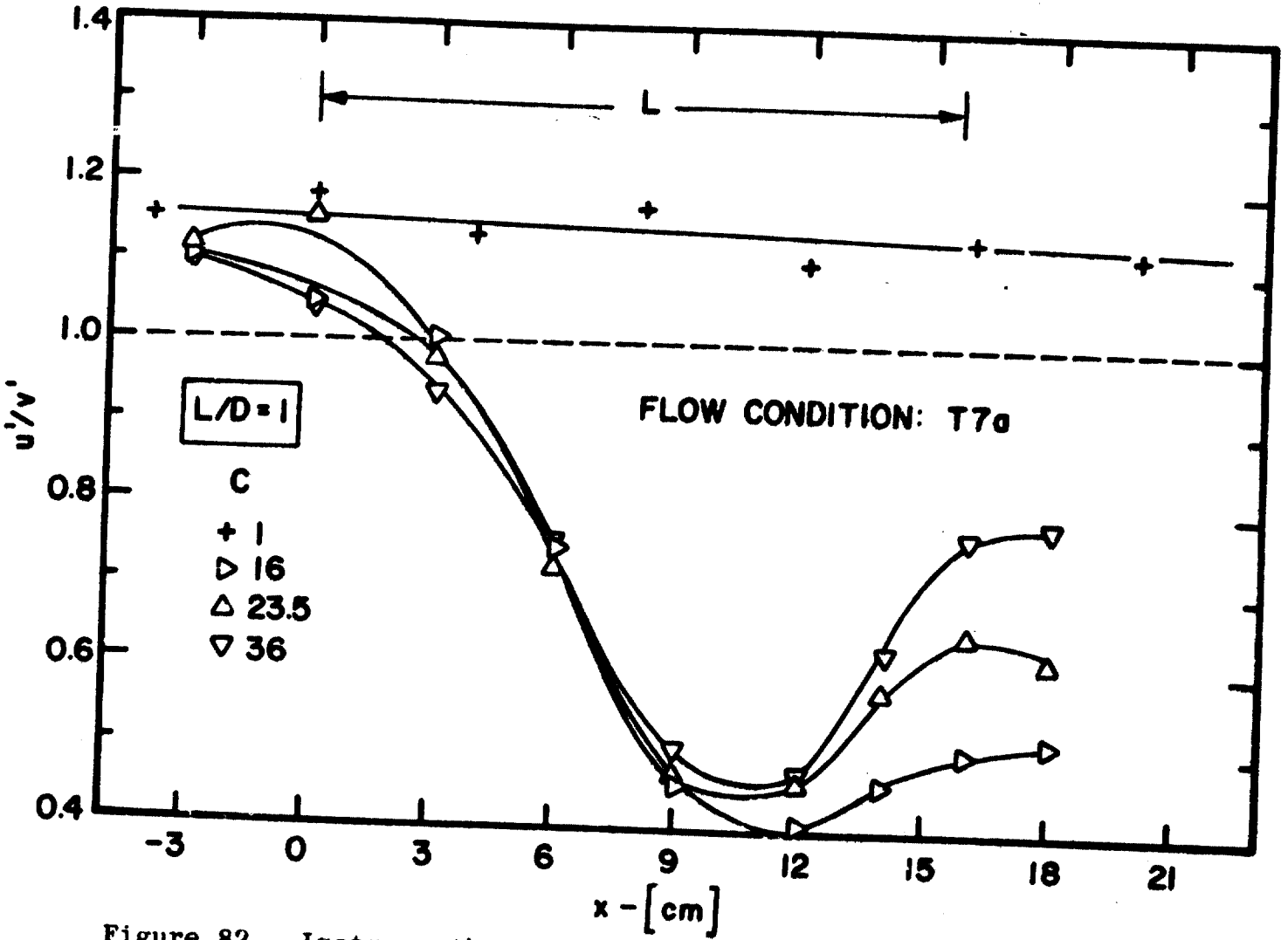

Figure 82. Isotropy through High Contractions in Flow Condition T7a

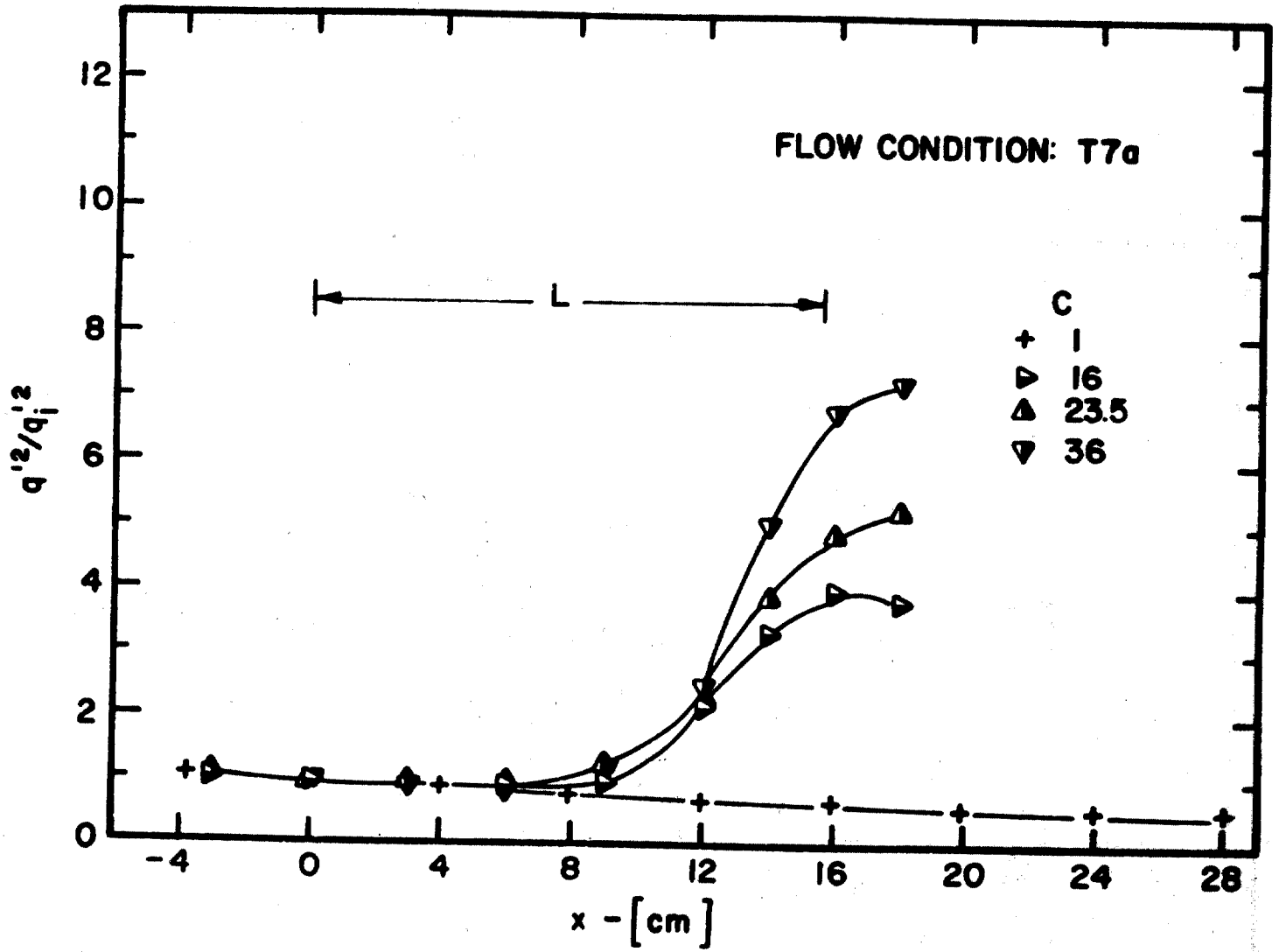

Figure 83. Normalized Total Turbulence Energy through High Contractions in Flow Condition T7a

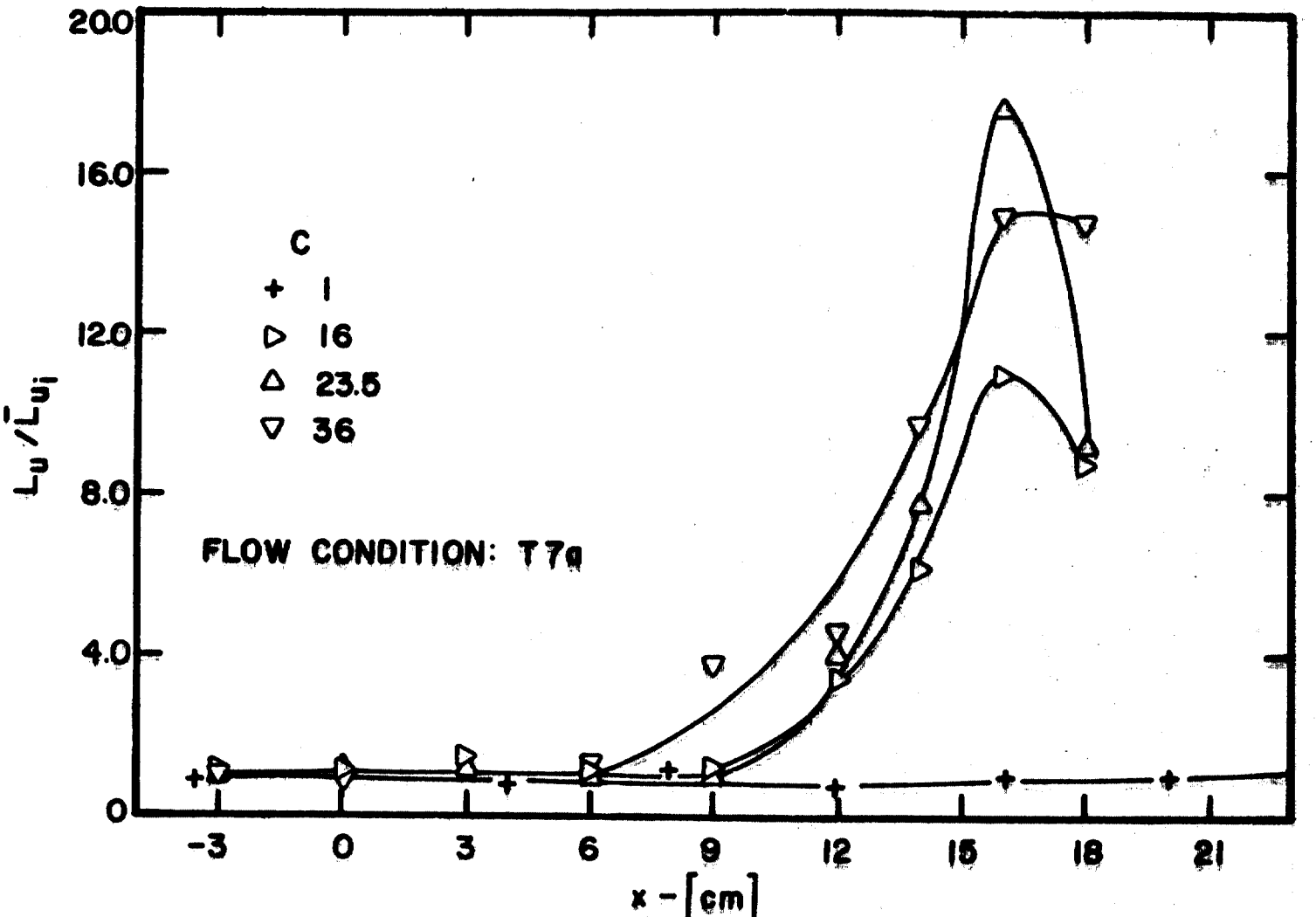

Figure 84. Normalized Longitudinal Length Scales through High Contractions in Flow Condition T7a

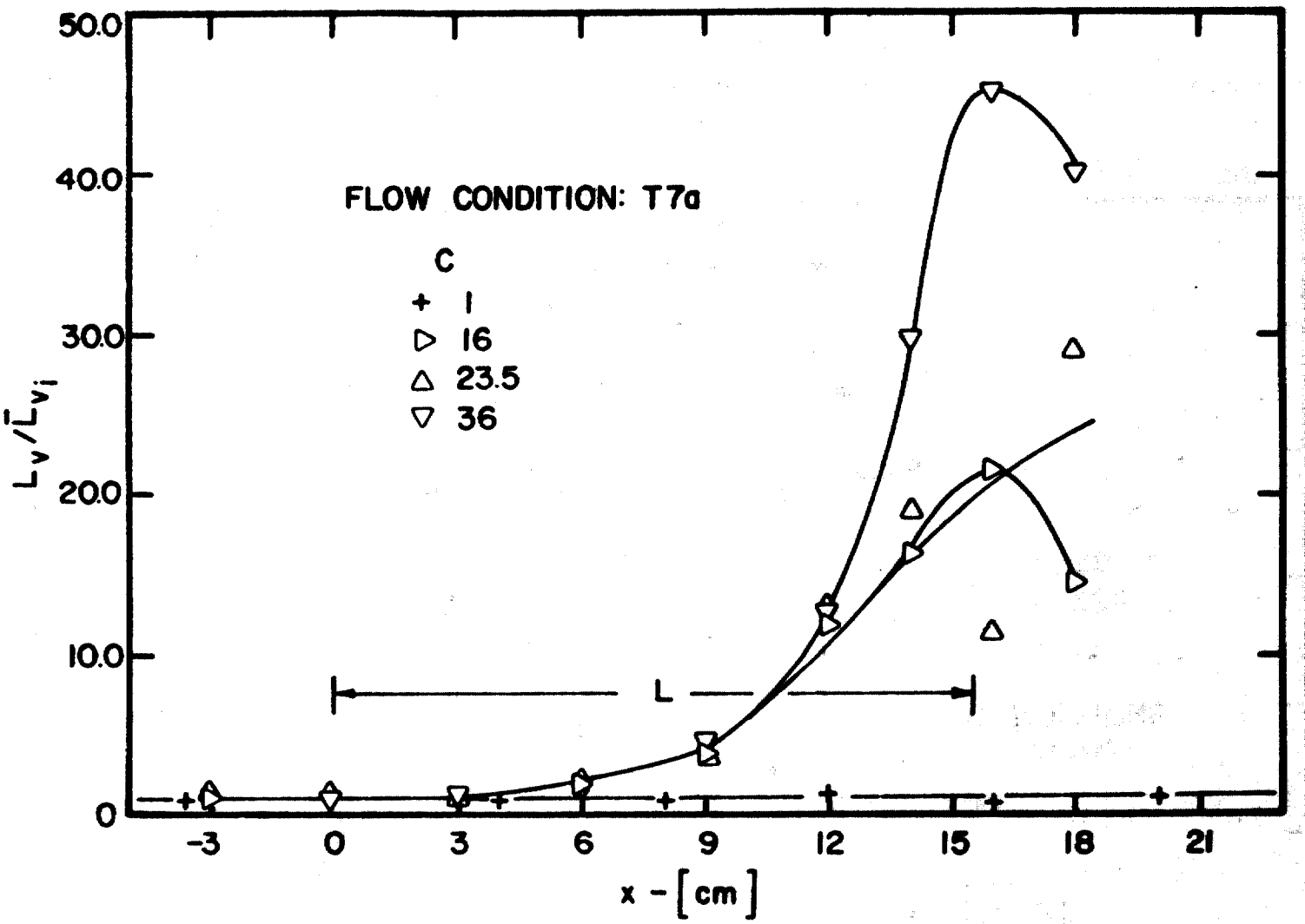

Figure 85. Normalized Lateral Length Scales through High Contractions in Flow Condition T7a

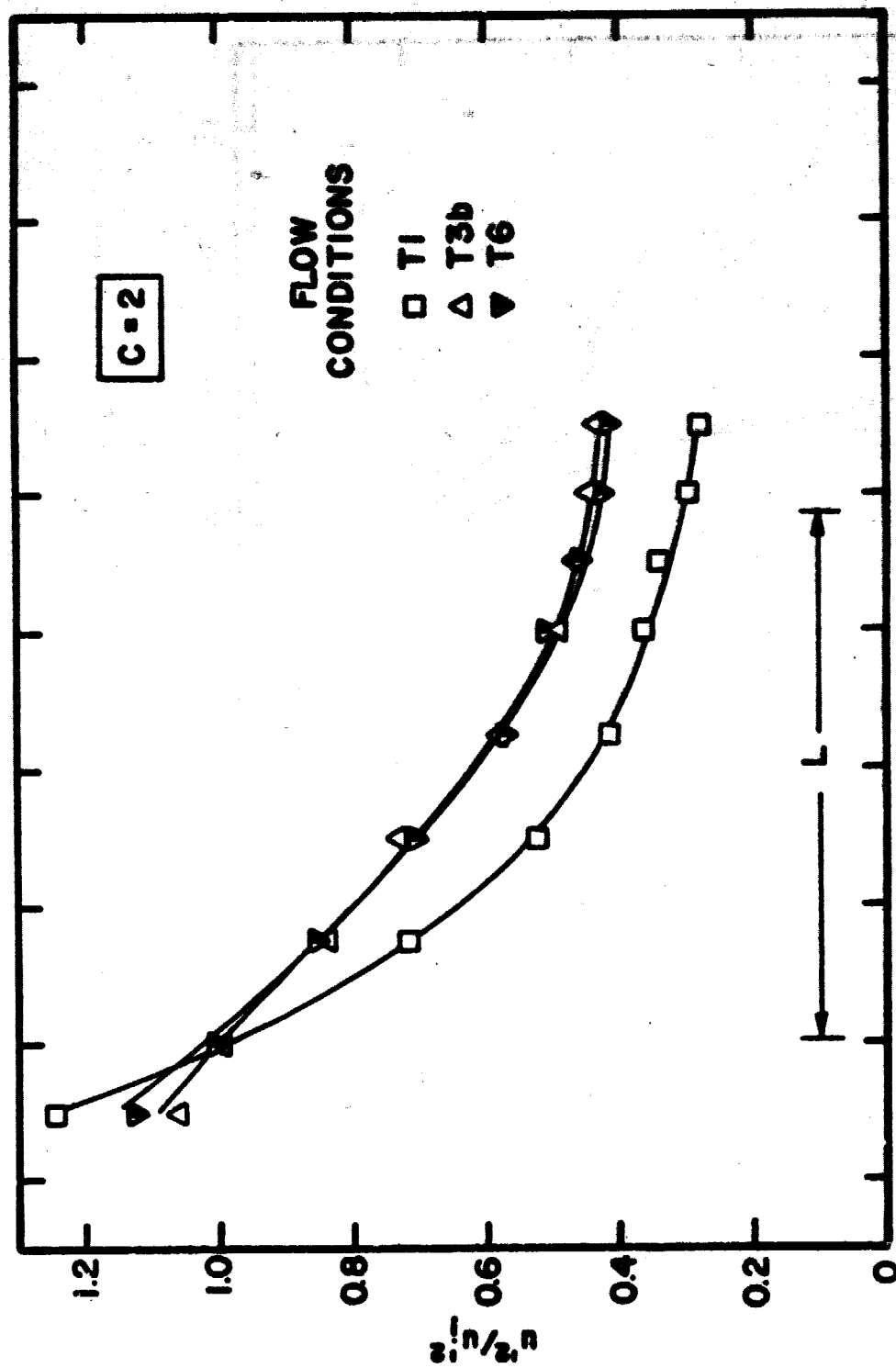

Figure 86. Normalized Streamwise Turbulence Energy through a Mild Contraction in Flow Conditions T1, T3b and T6

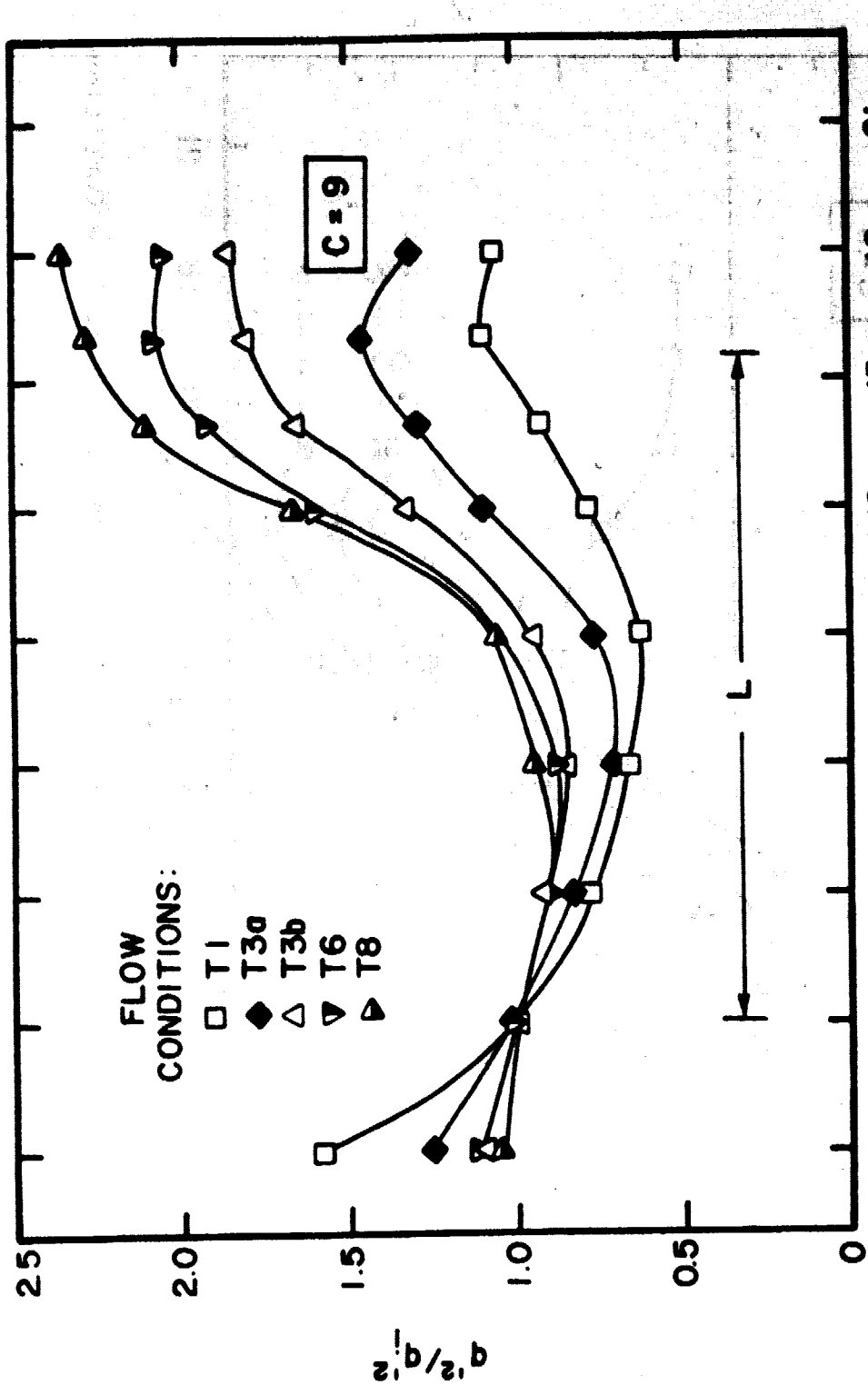

Figure 89. Normalized Total Turbulence Energy through a Moderate Contraction in Several Flow Conditions

271-272

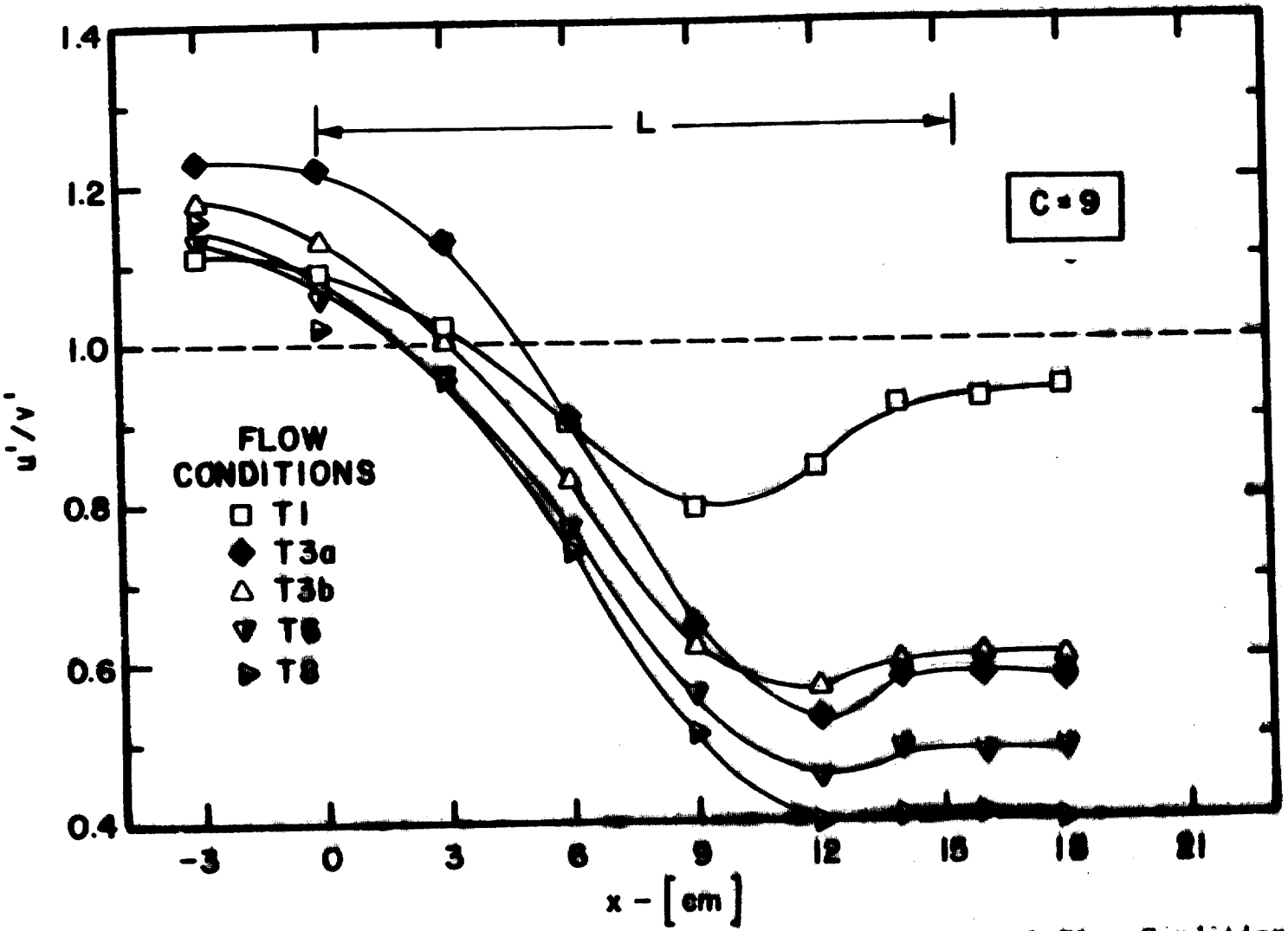

Figure 90. Isotropy through a Moderate Contraction in Several Flow Conditions

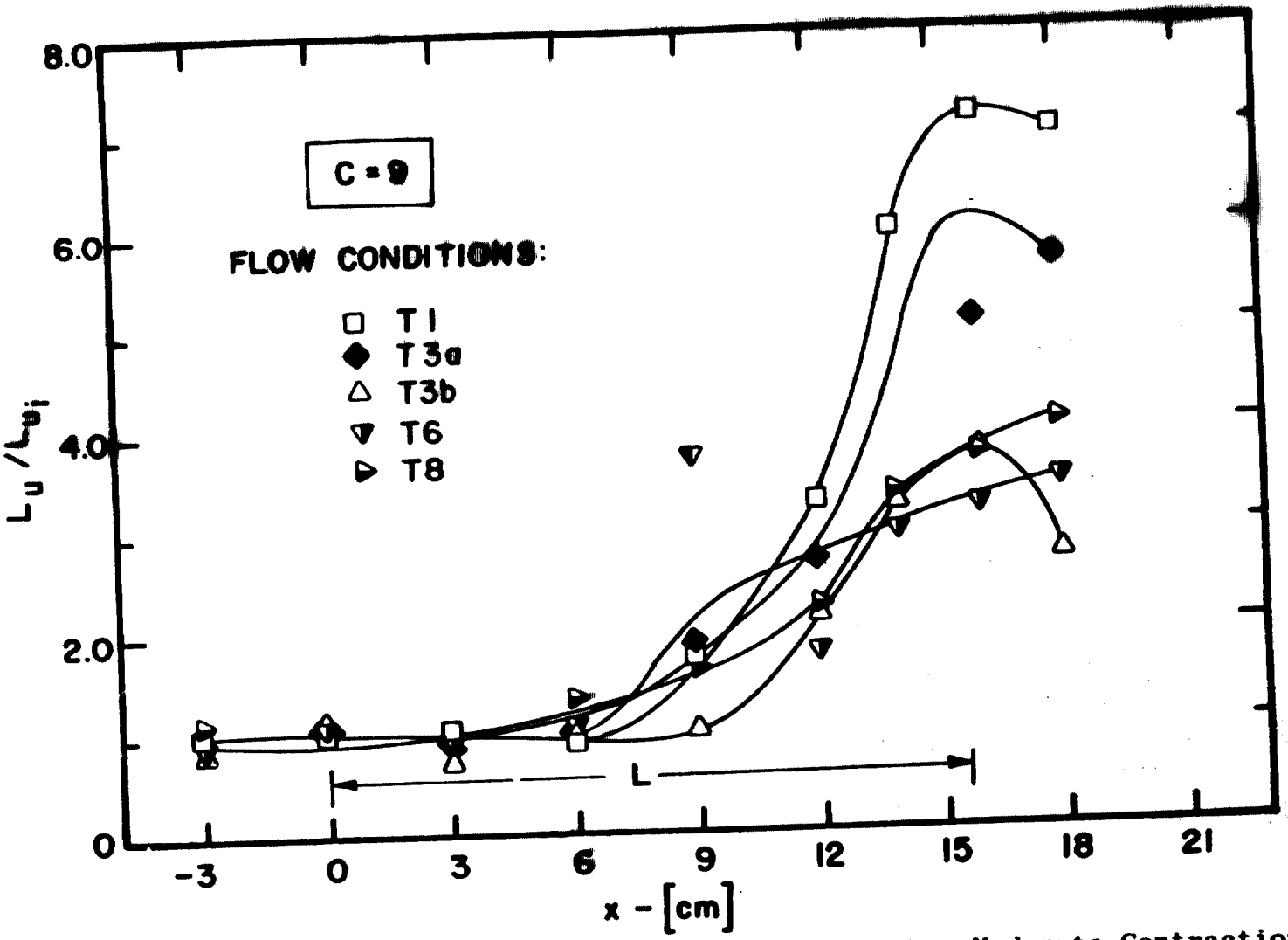

Figure 91. Normalized Longitudinal Length Scales through a Moderate Contraction in Several Flow Conditions

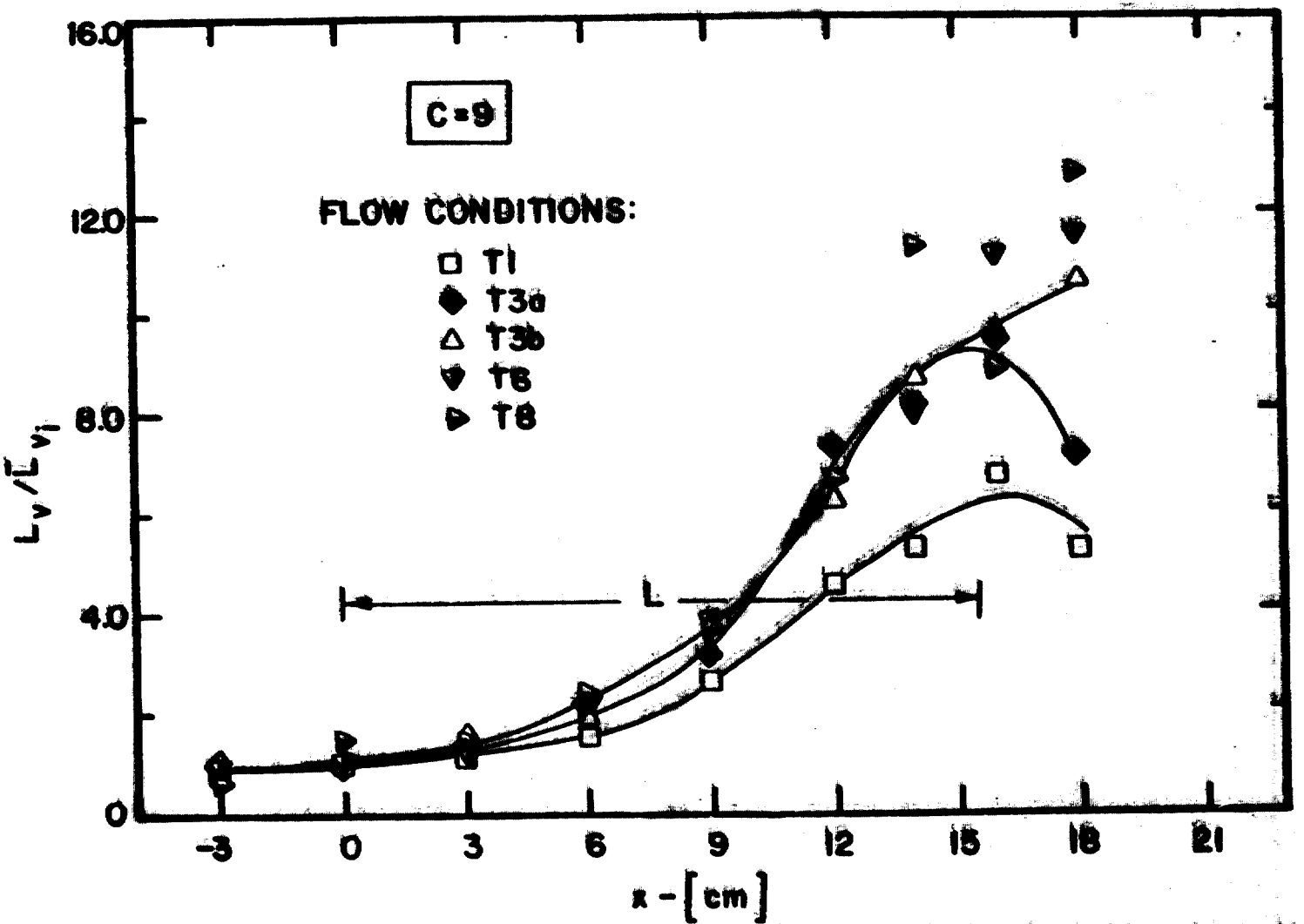

Figure 92. Normalized Lateral Length Scales through a Moderate Contraction in Several Flow Conditions

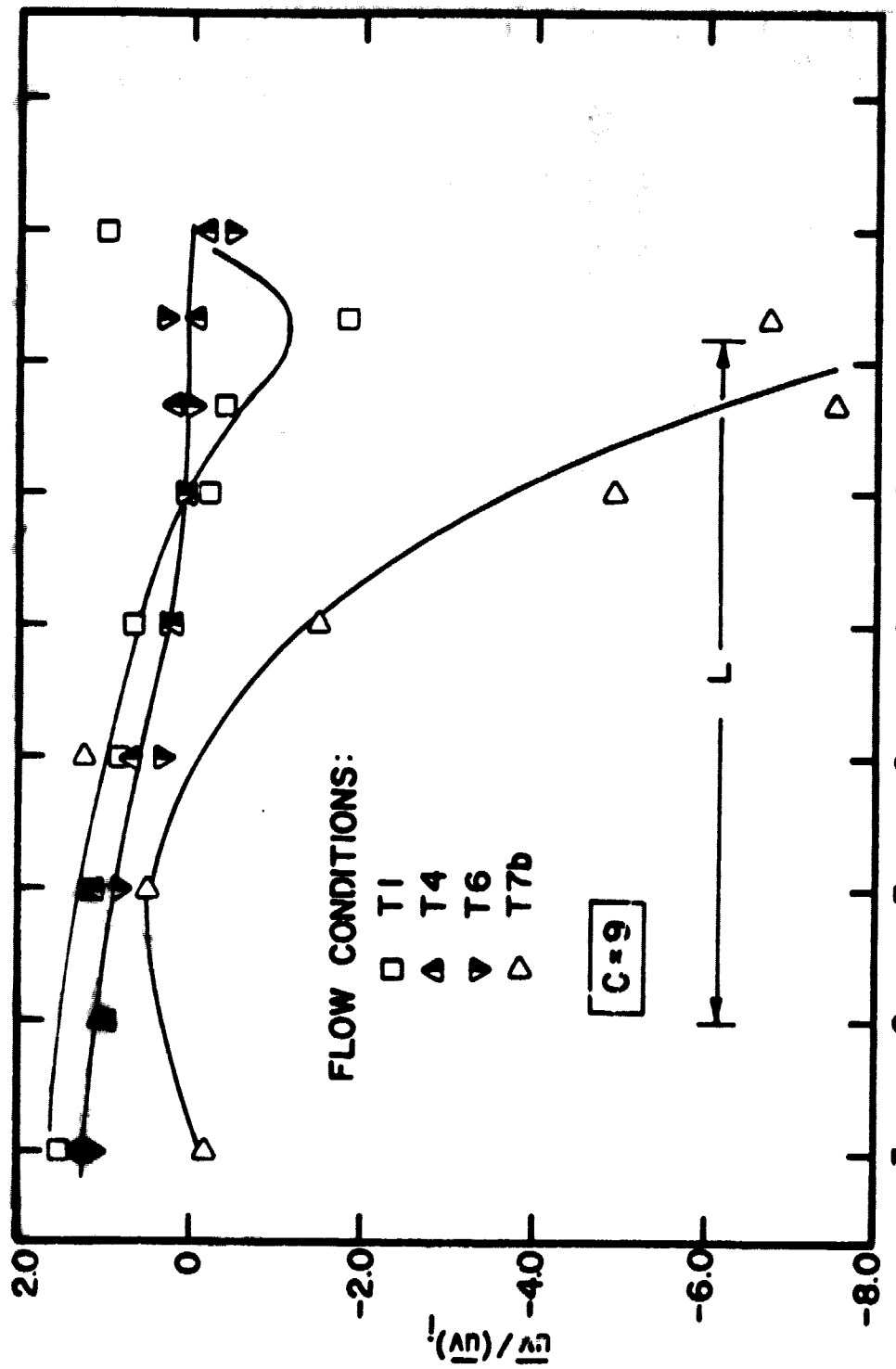

Figure 93. Normalized Reynolds Stresses through a Moderate Contraction in Several Flow Conditions

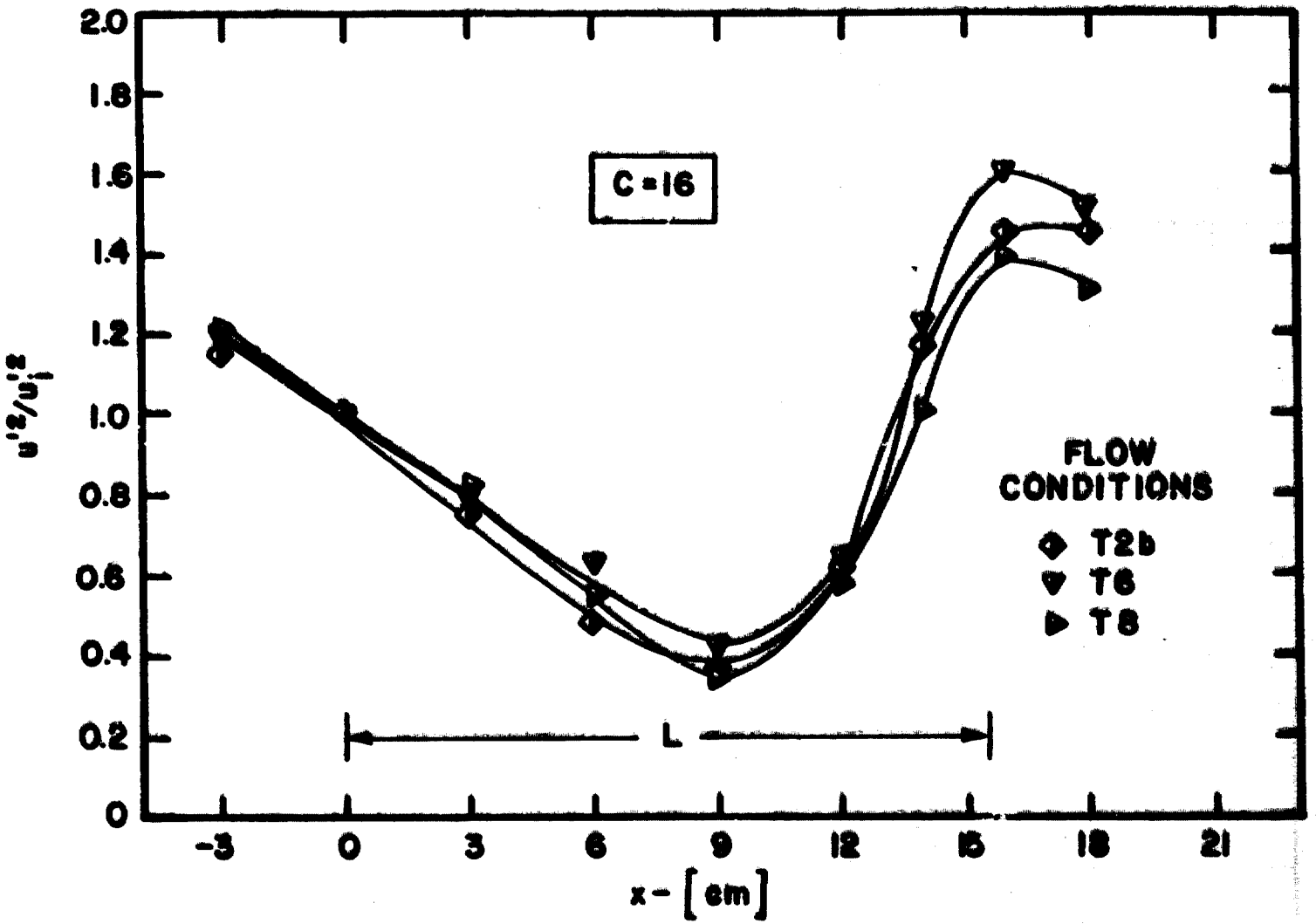

Figure 94. Normalized Streamwise Turbulence Energy through a High Contraction in Several Flow Conditions

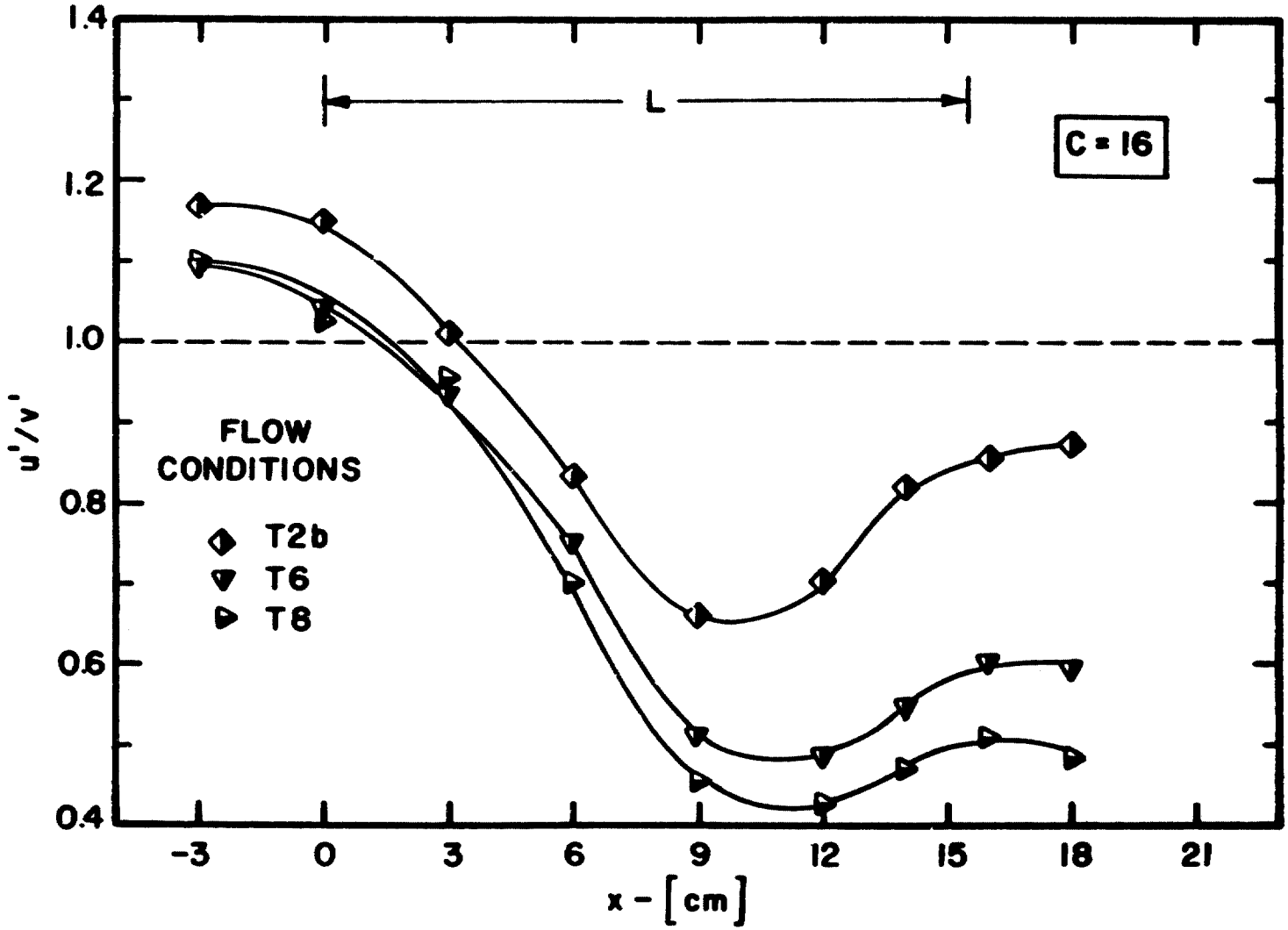

Figure 95. Isotropy through a High Contraction in Several Flow Conditions

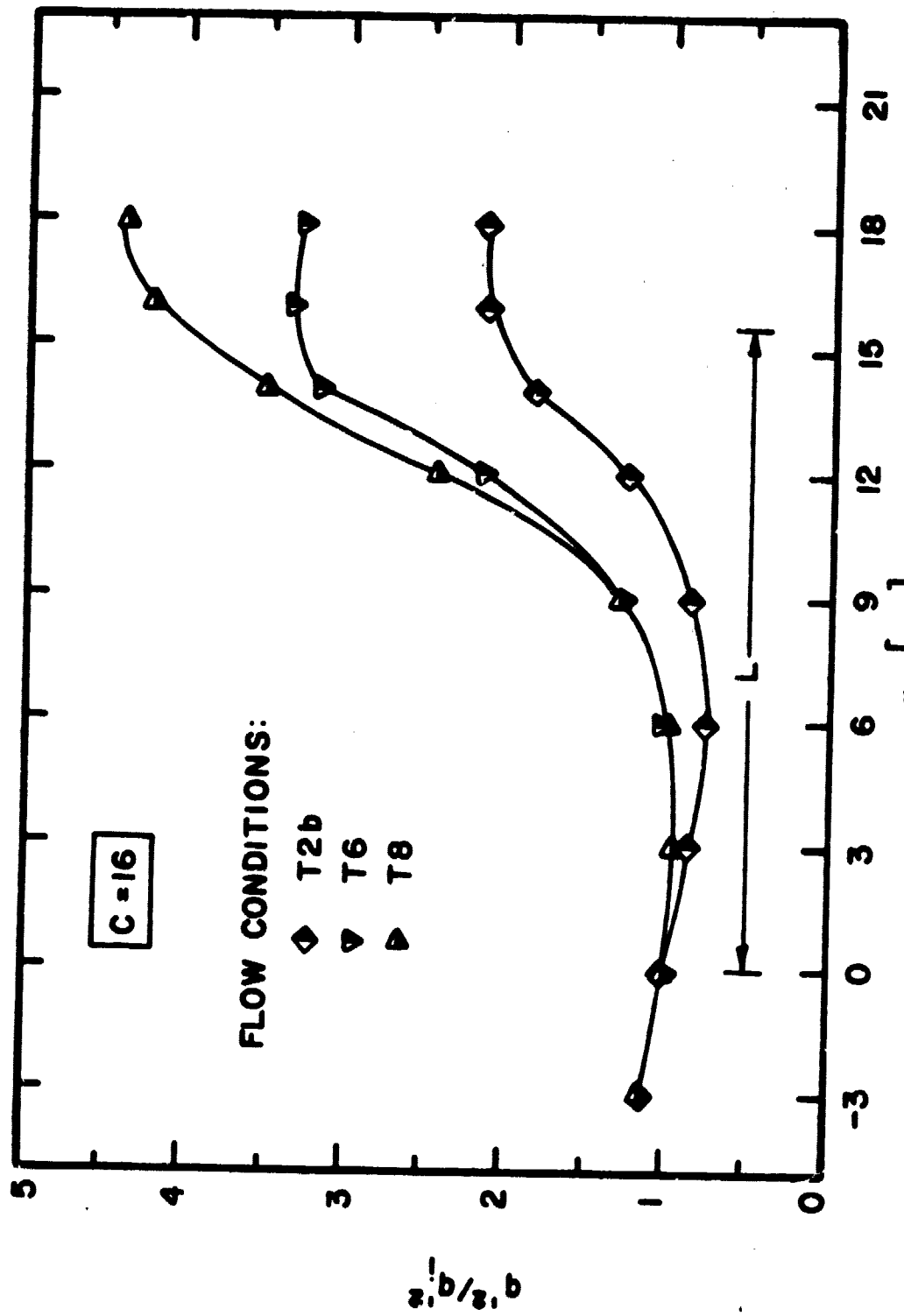

Figure 96. Normalized Total Turbulence Energy through a High Contraction in Several Flow Conditions

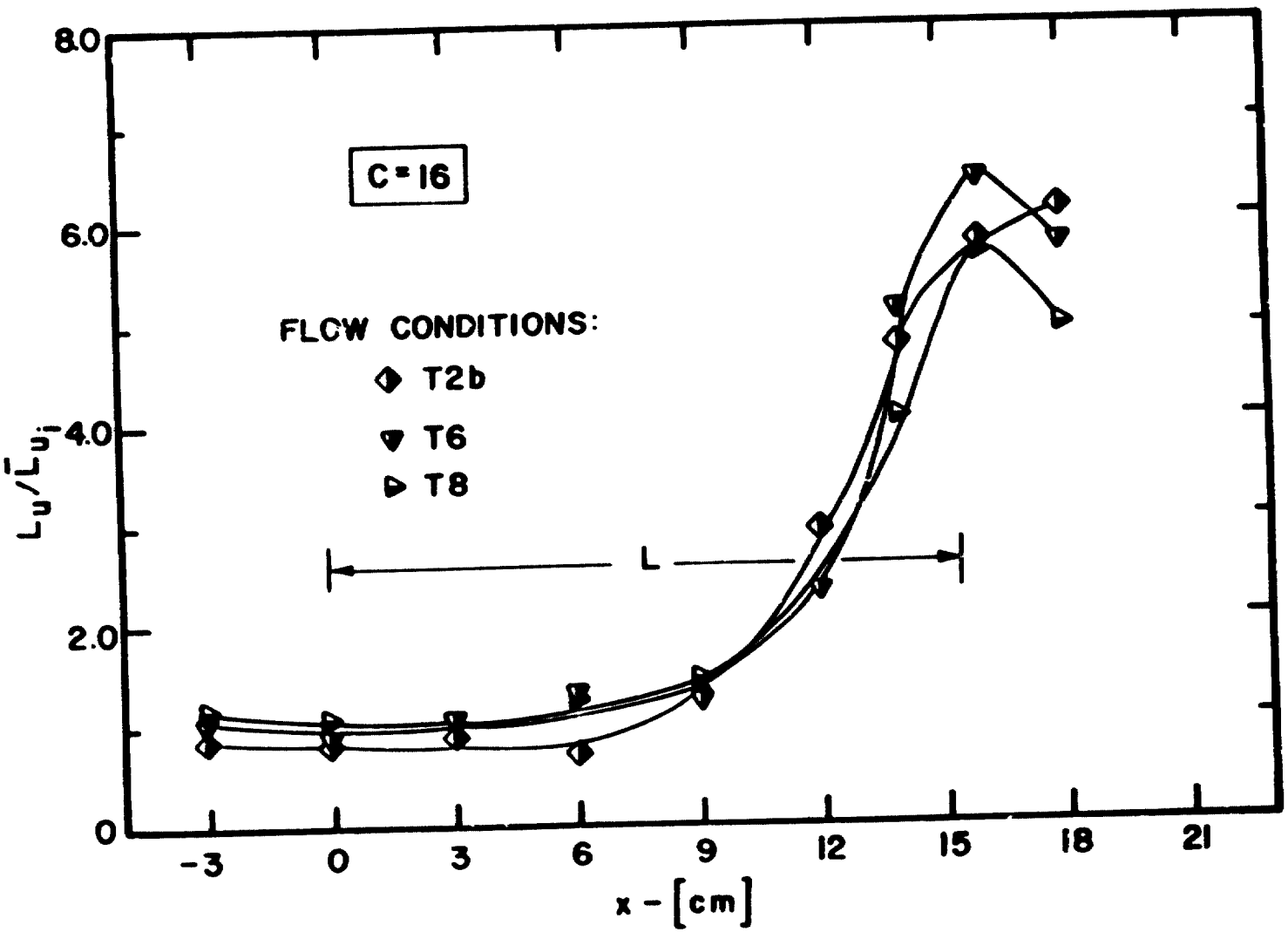

Figure 97. Normalized Longitudinal Length Scales through a High Contraction in Several Flow Conditions

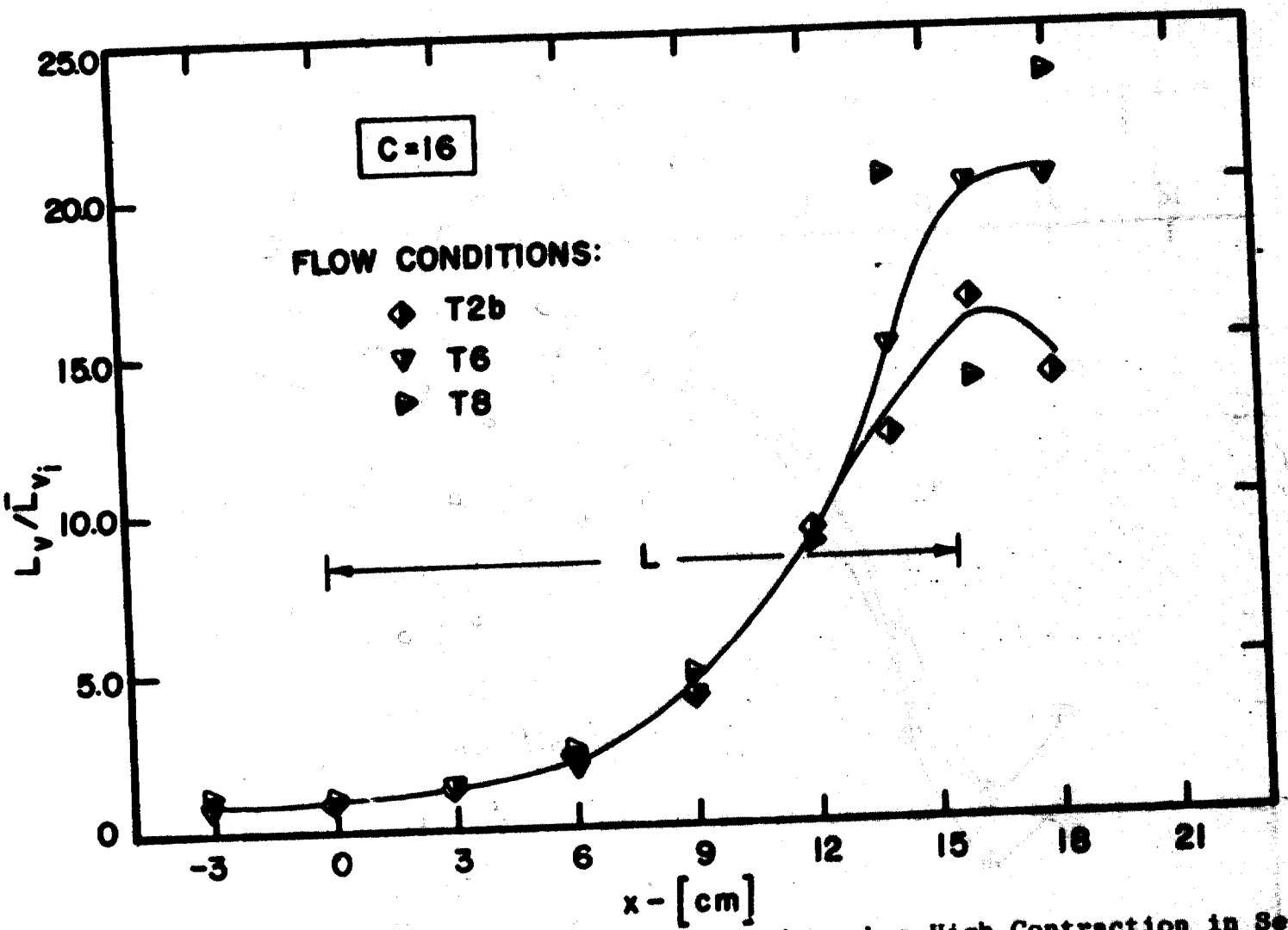

Figure 98. Normalized Lateral Length Scales through a High Contraction in Several Flow Conditions

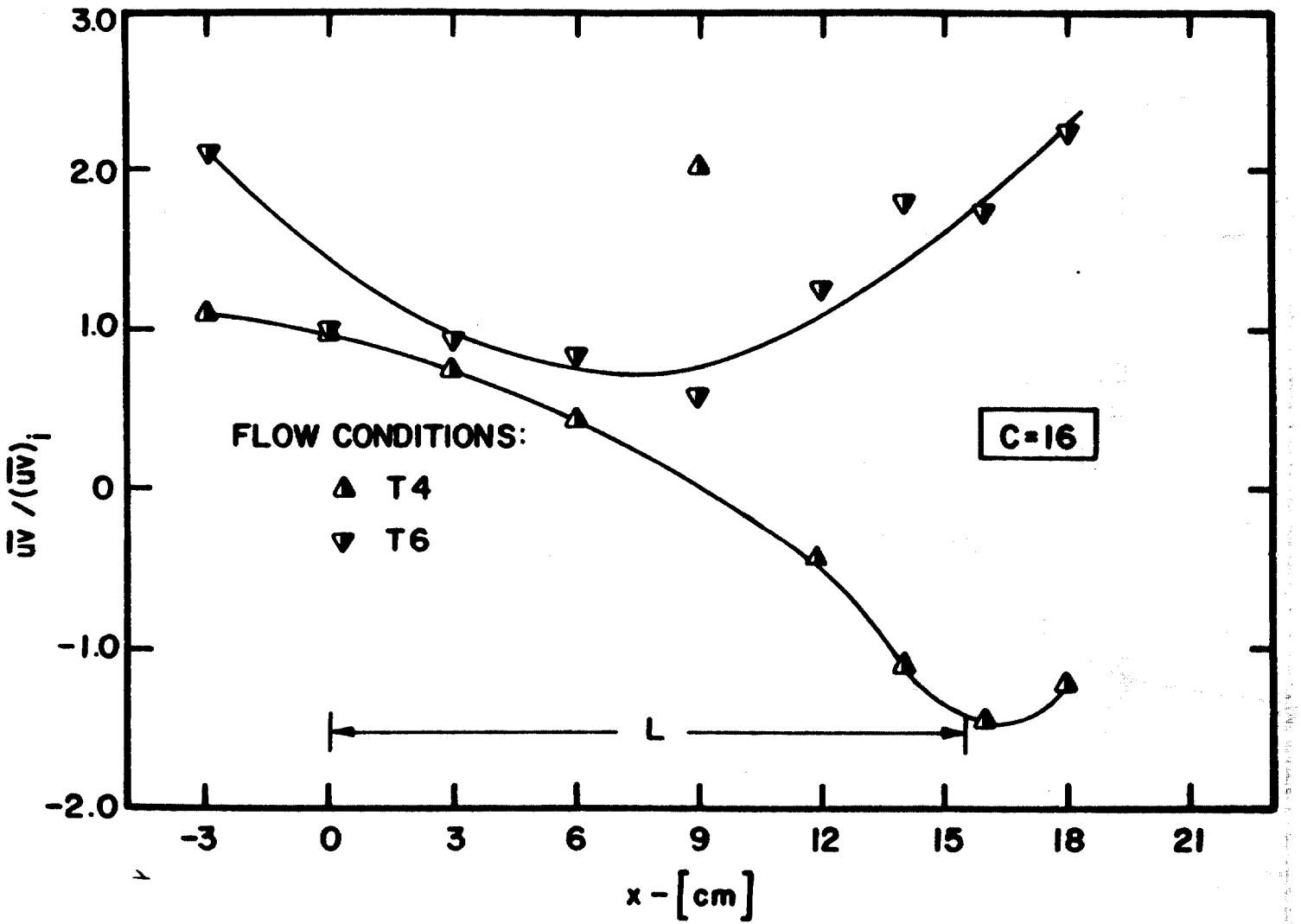

Figure 99. Normalized Reynolds Stresses through a High Contraction in Flow Conditions T4 and T6

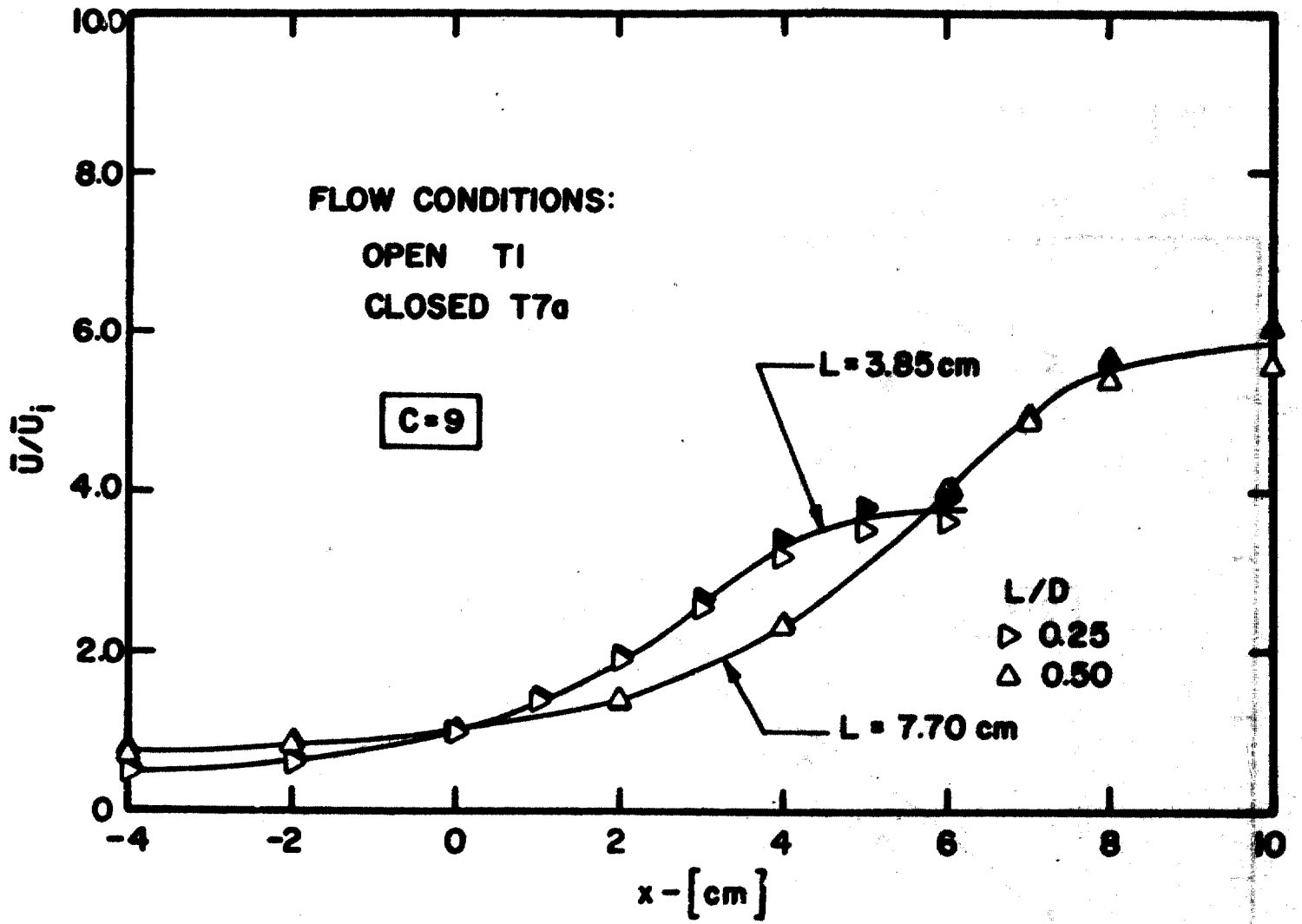

Figure 100. Normalized Streamwise Mean Velocity through Short Contractions in Flow Conditions T1 and T7a

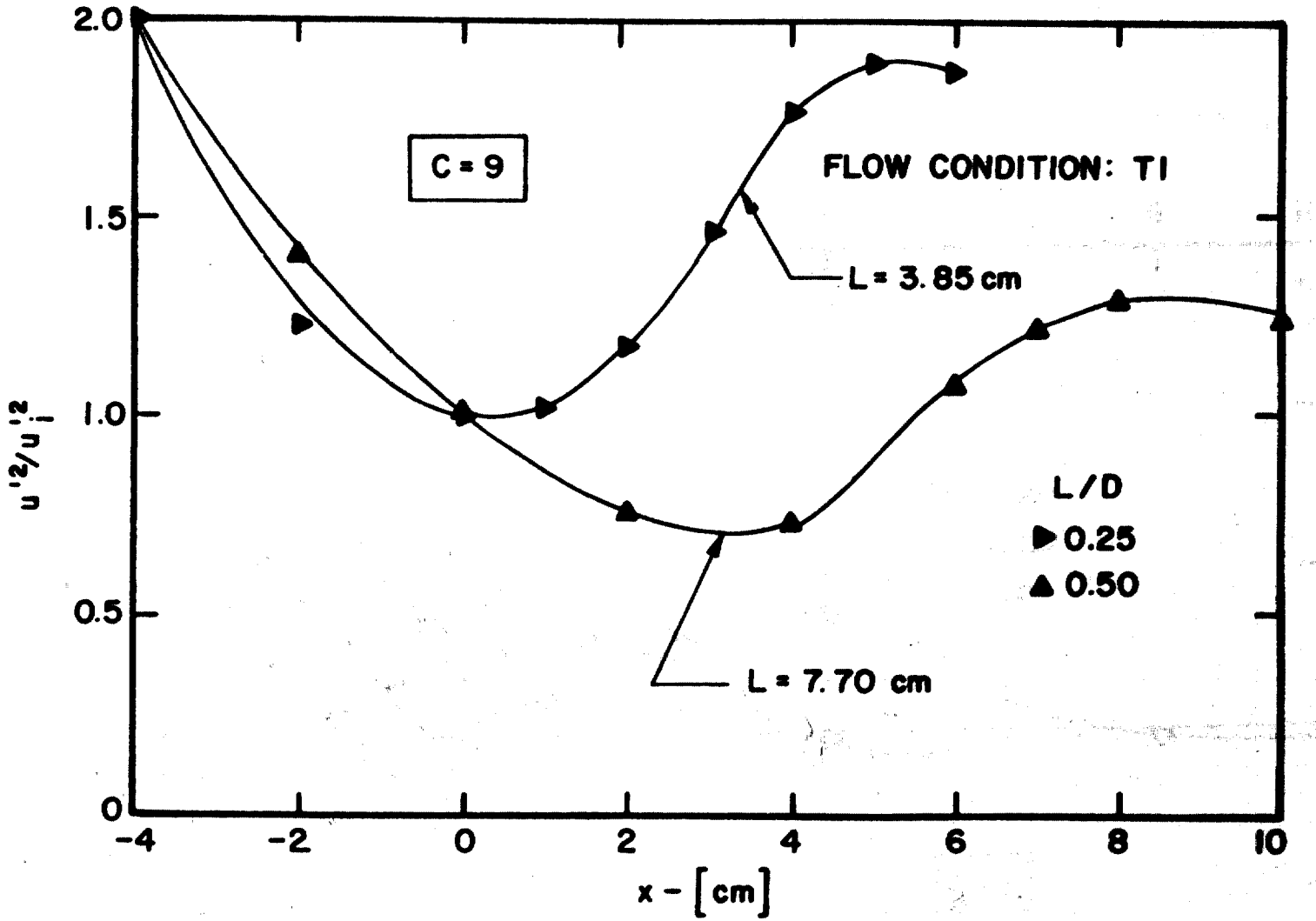

Figure 101. Normalized Streamwise Turbulence Energy through Short Contractions in Flow Condition TI

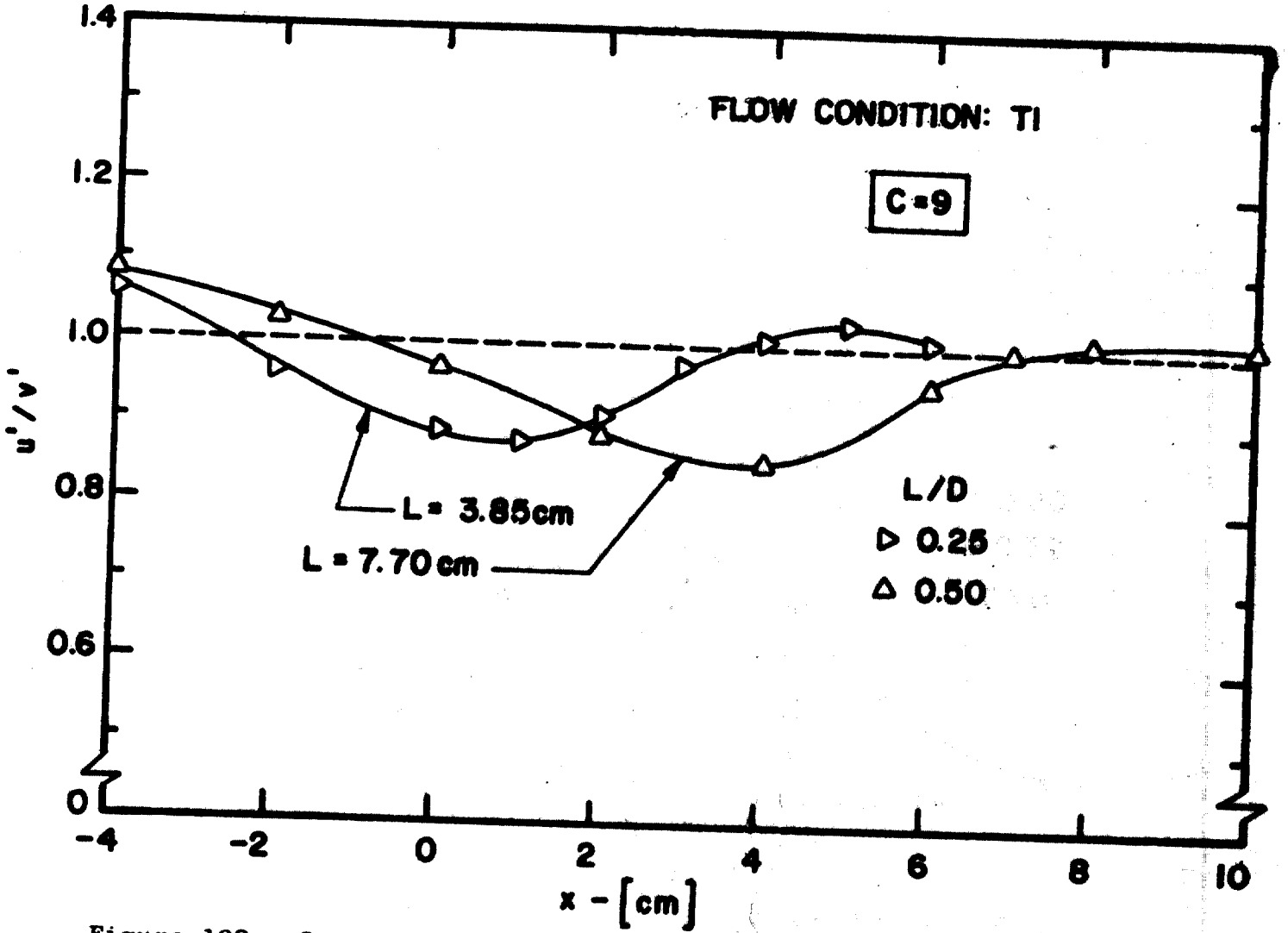

Figure 102. Isotropy through Short Contractions in Flow Condition T1

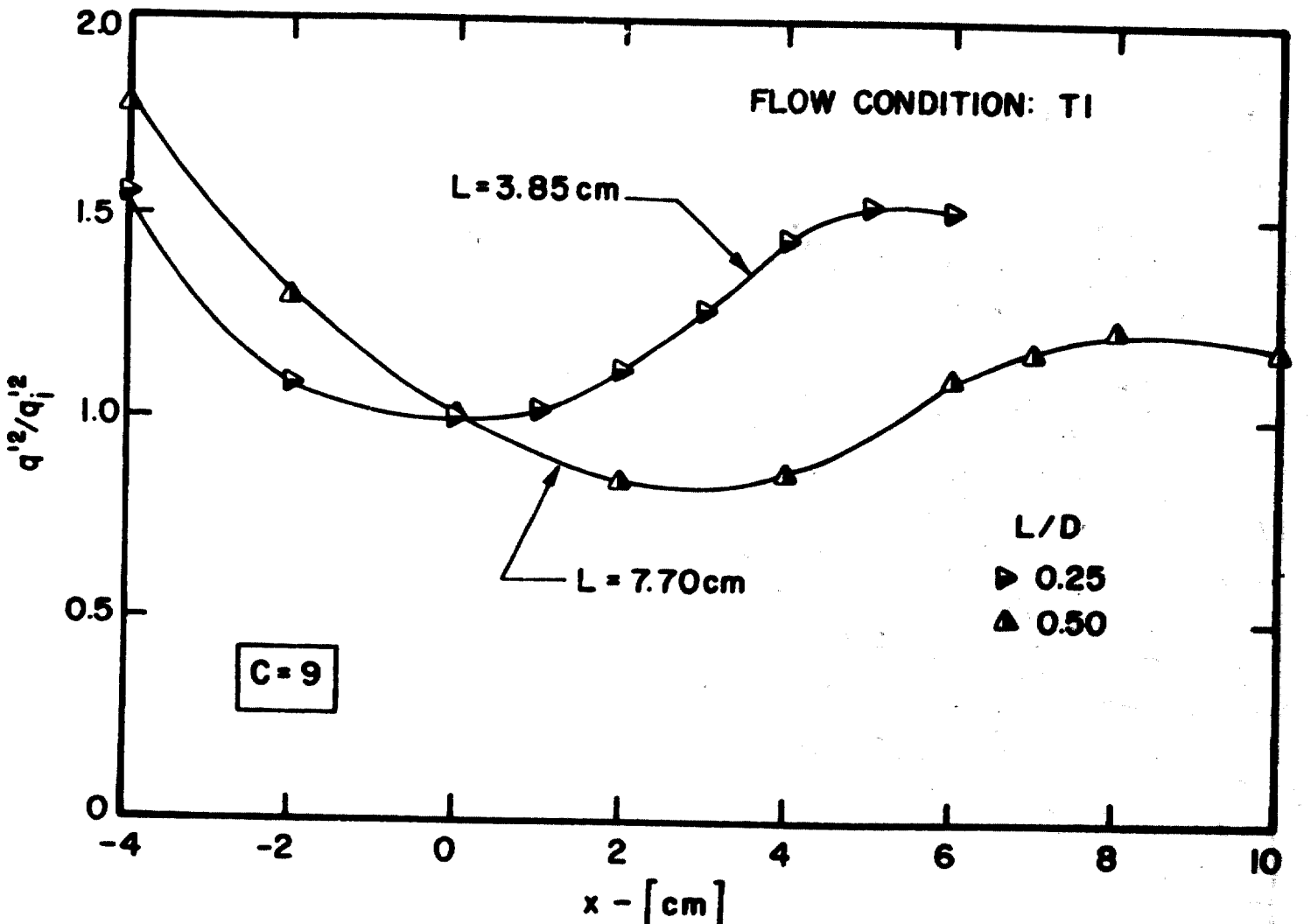

Figure 103. Normalized Total Turbulence Energy through Short Contractions in Flow Condition TI

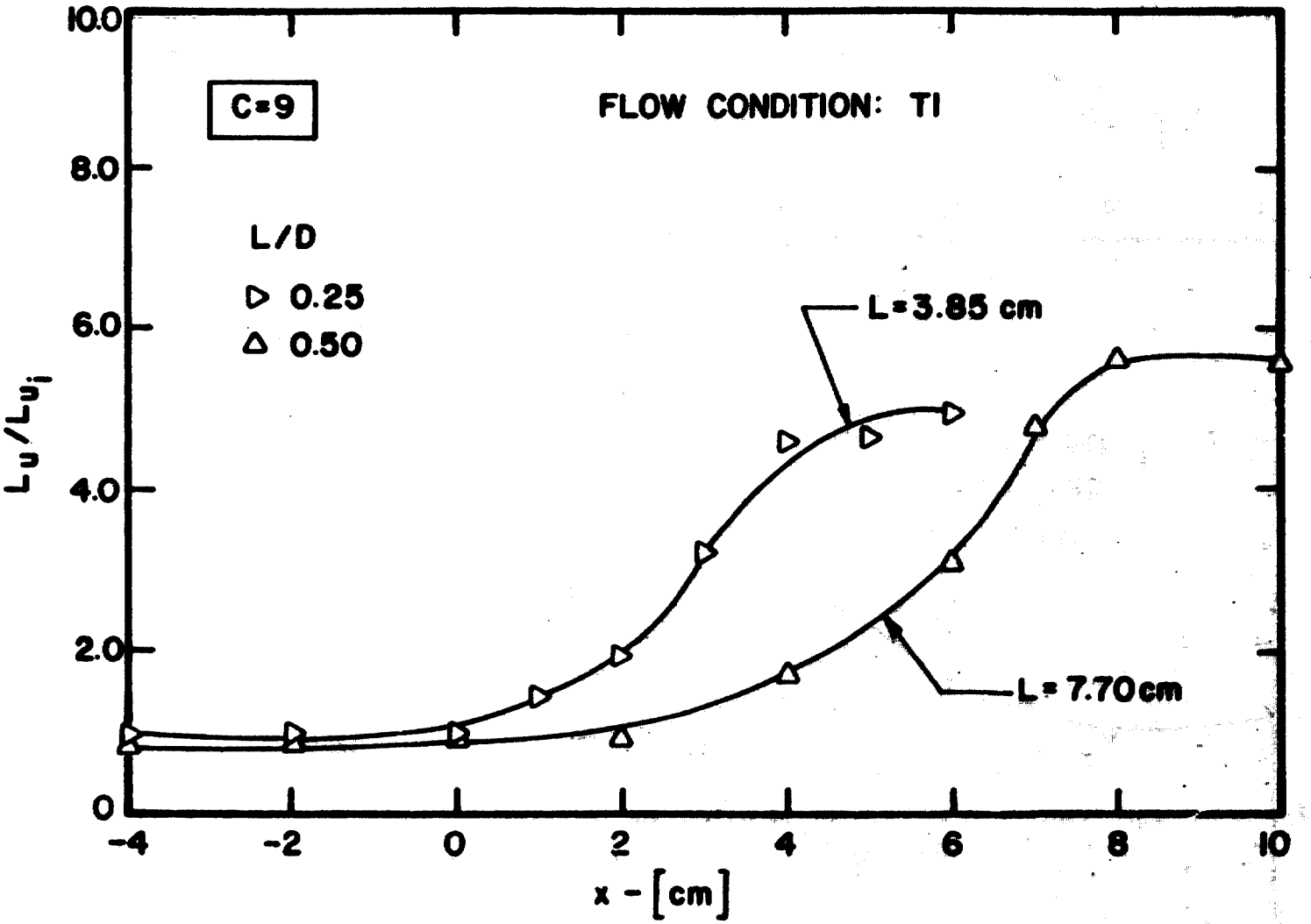

Figure 104. Normalized Longitudinal Length Scales through Short Contractions in Flow Condition T1

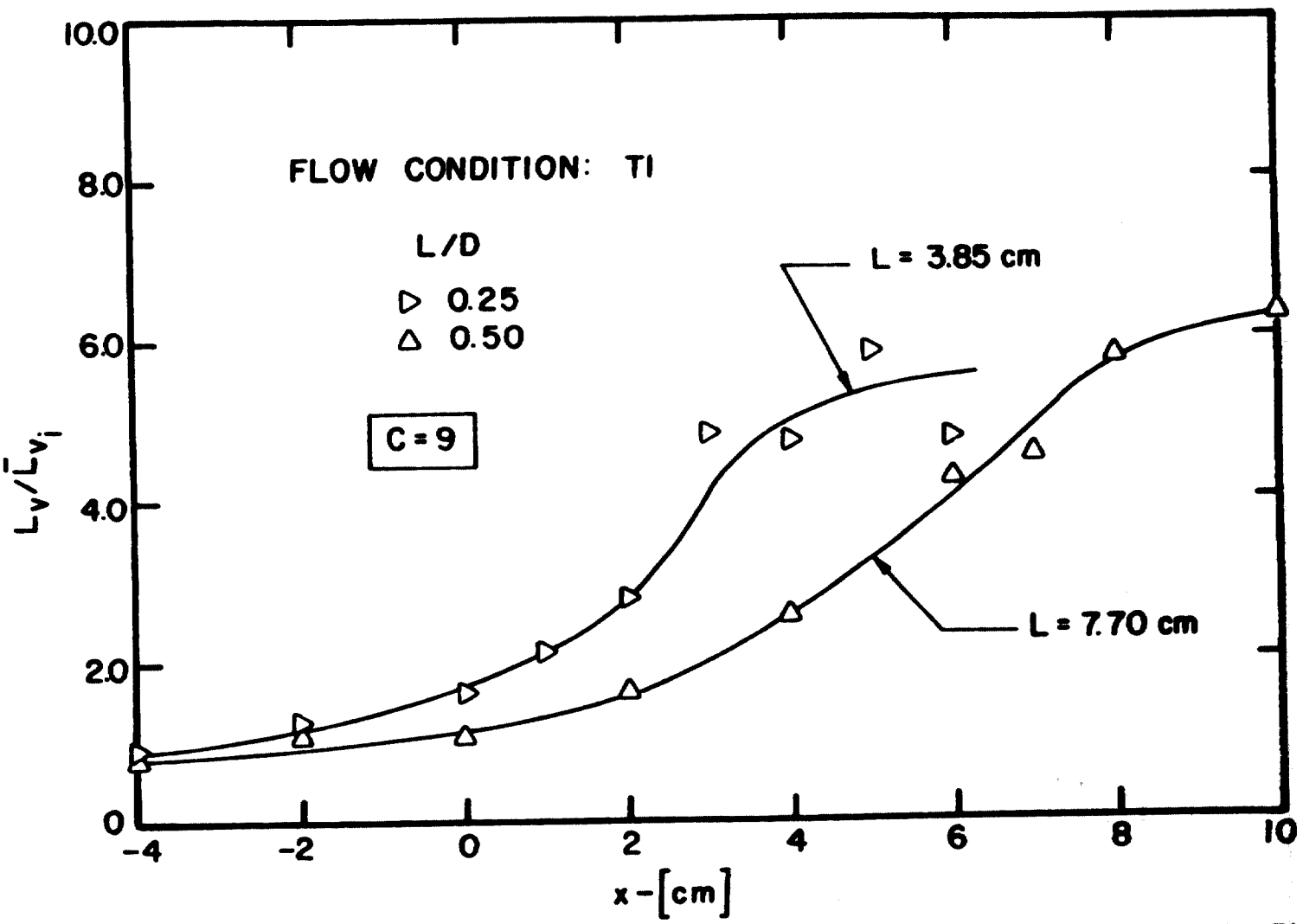

Figure 105. Normalized Lateral Length Scales through Short Contractions in Flow Condition TI

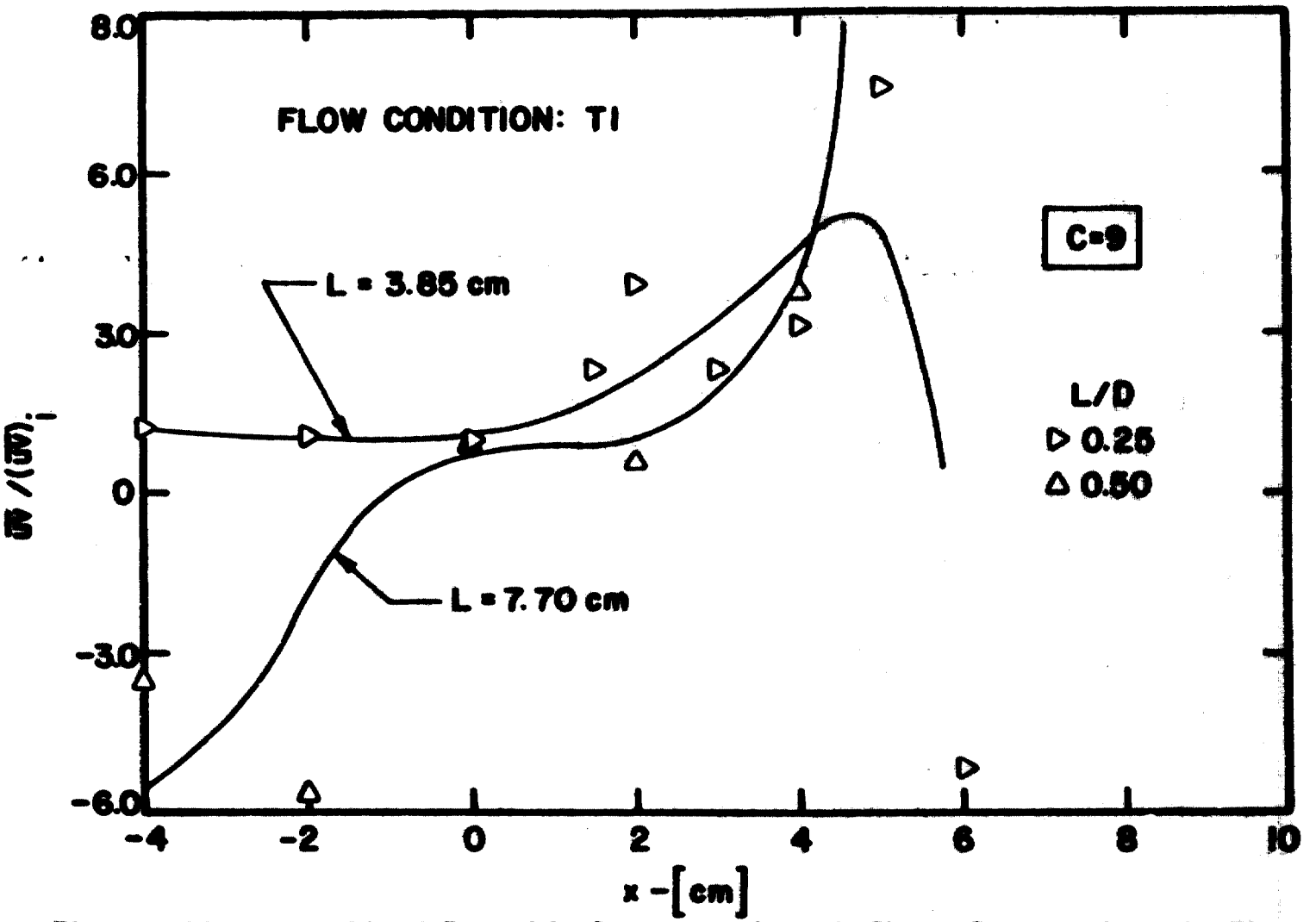

Figure 106. Normalized Reynolds Stresses through Short Contractions in Flow Condition T1

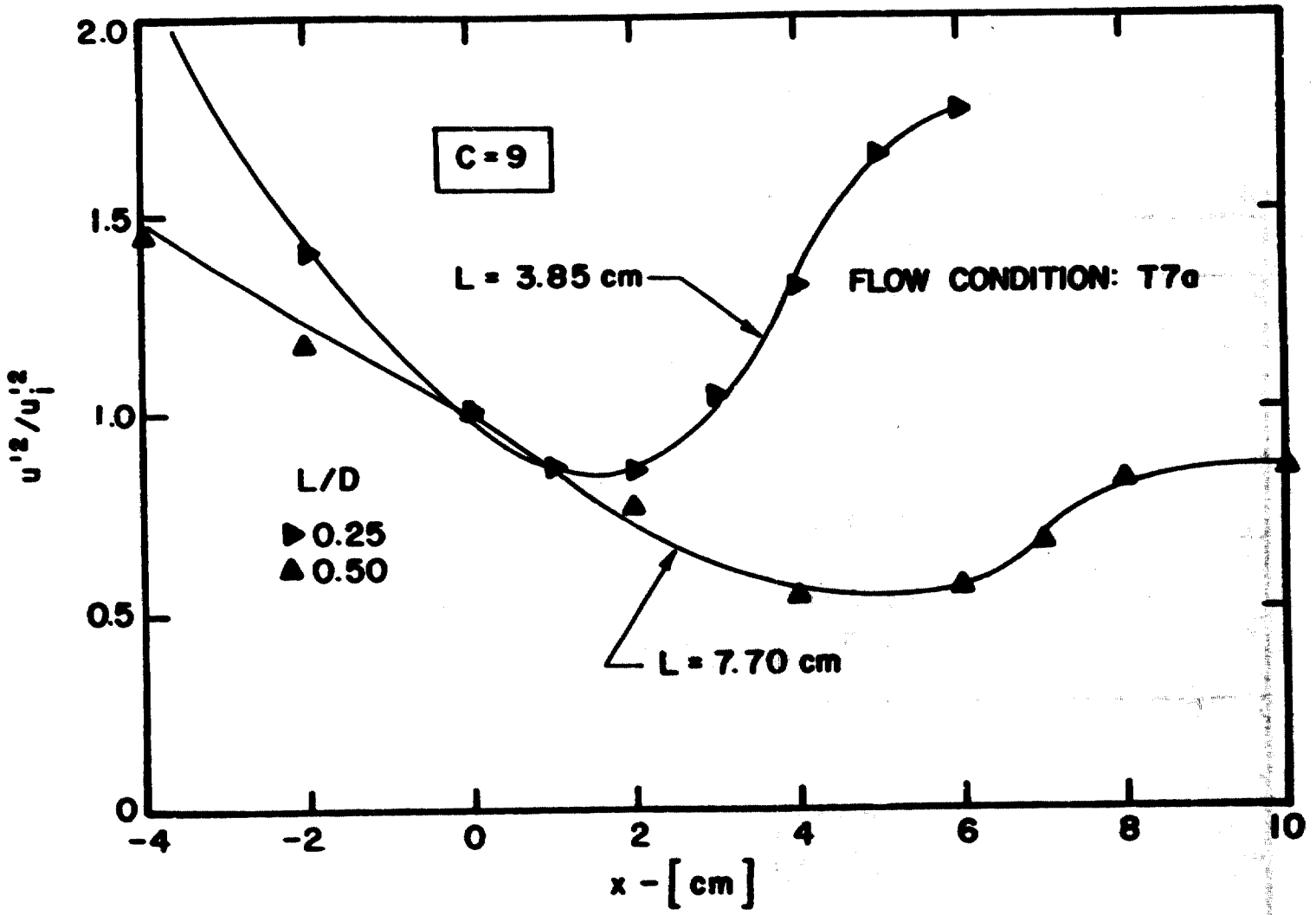

Figure 107. Normalized Streamwise Turbulence Energy through Short Contractions in Flow Condition T7a

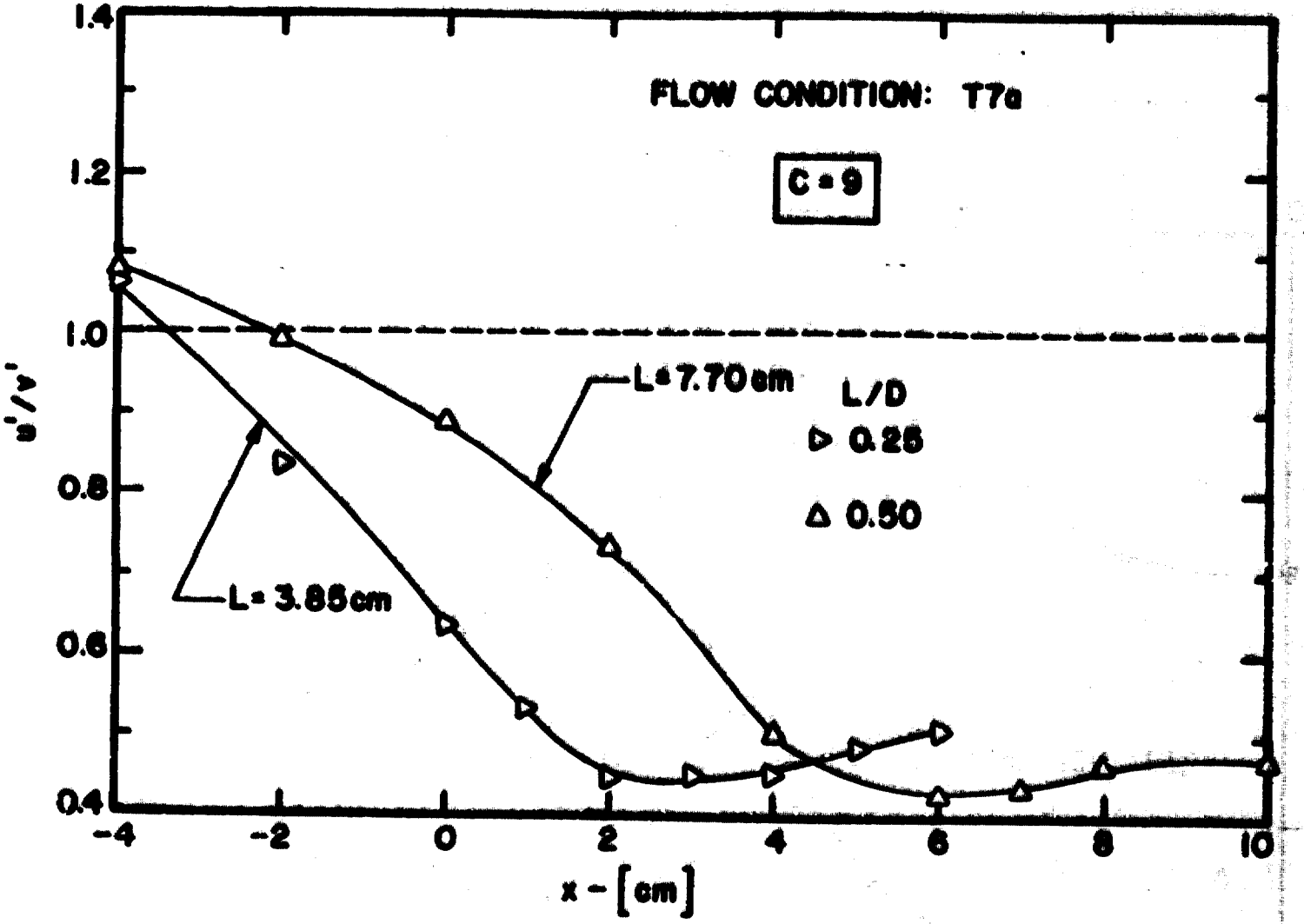

Figure 108. Isotropy through Short Contractions in Flow Condition T7a

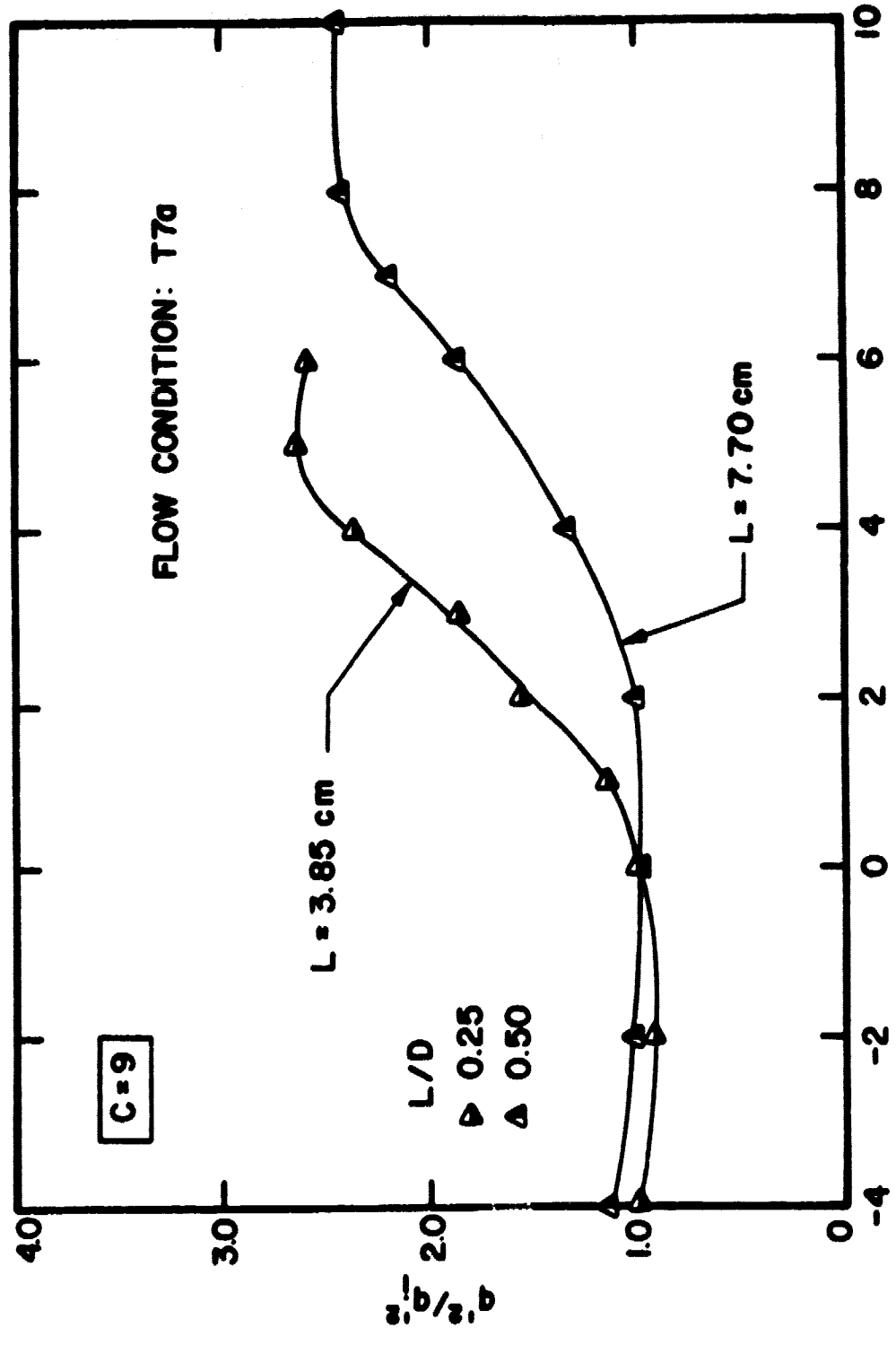

Figure 109. Normalized Total Turbulence Energy through Short Contractions in Flow Condition T7a

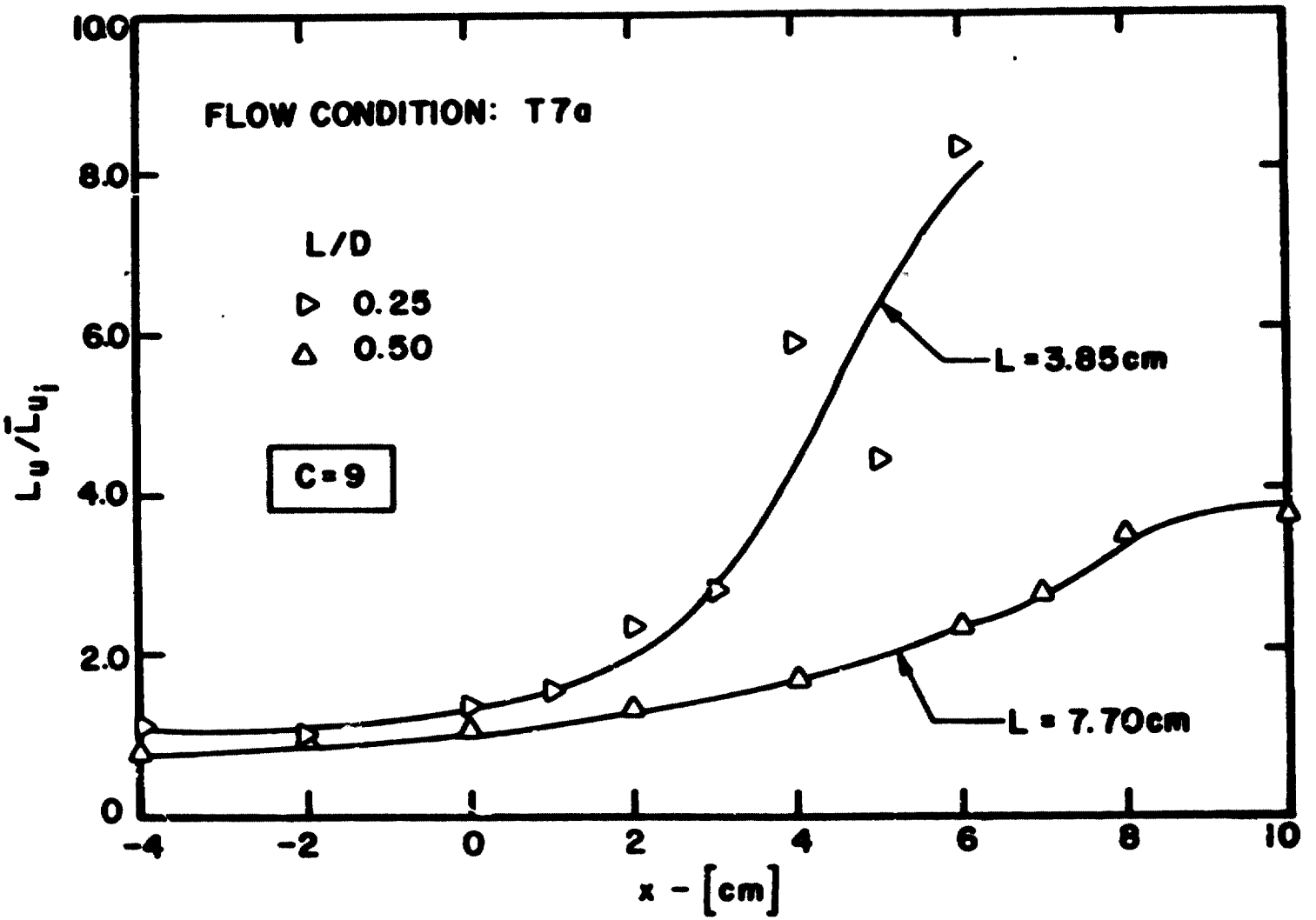

Figure 110. Normalized Longitudinal Length Scales through Snort Contractions in Flow Condition T7a

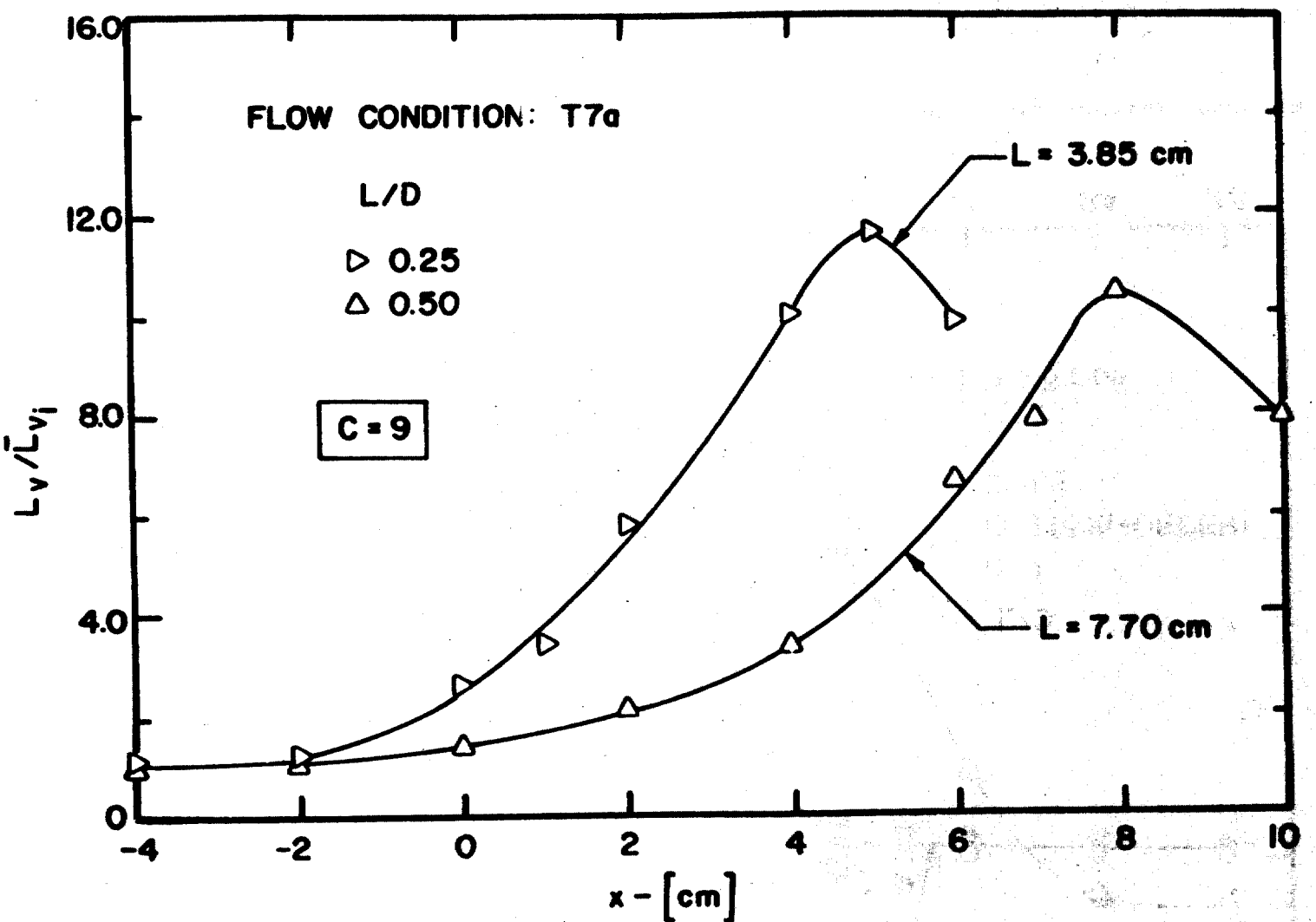

Figure 111. Normalized Lateral Length Scales through Short Contractions in Flow Condition T7a

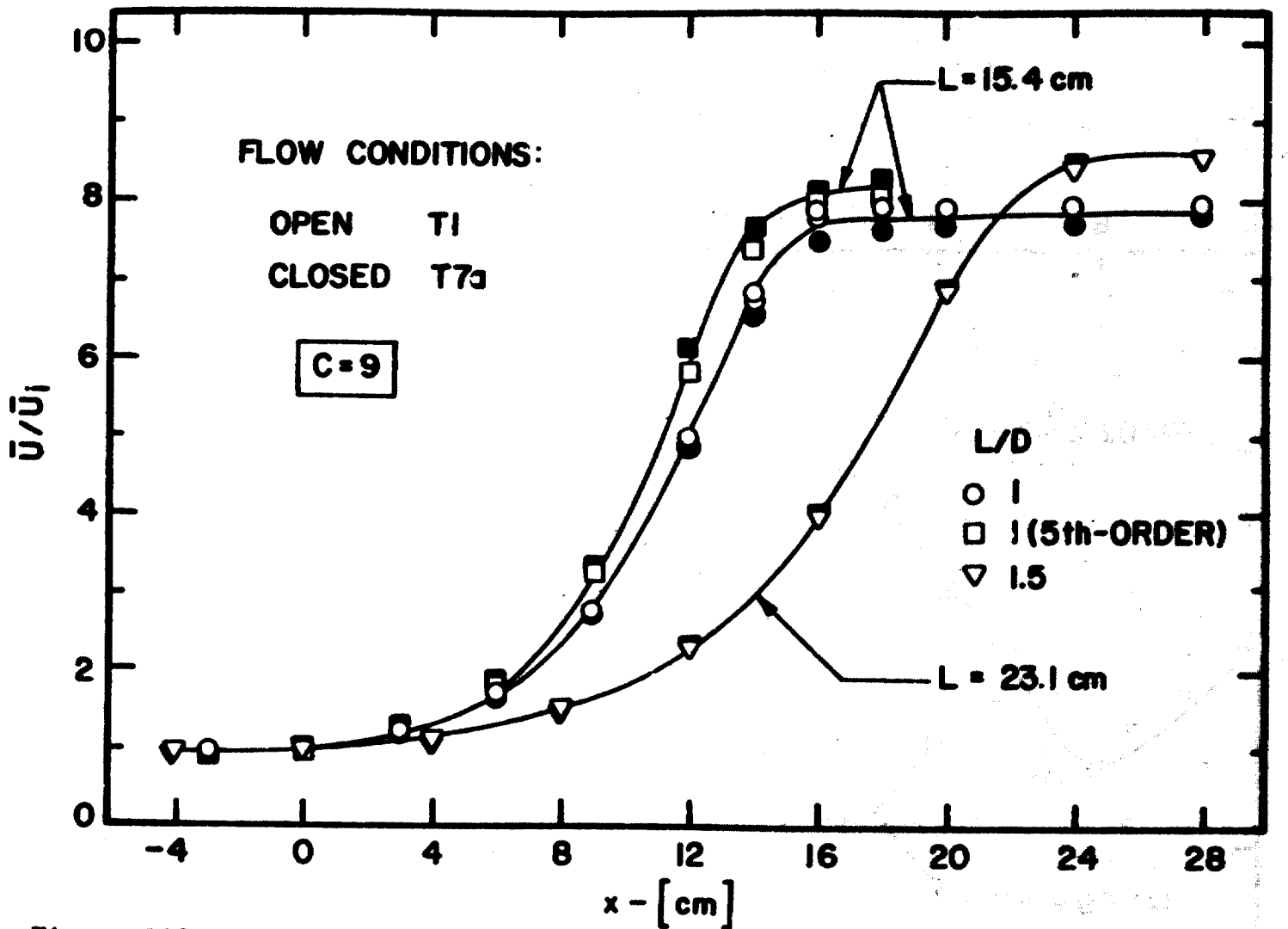

Figure 112. Normalized Streamwise Mean Velocity through Long Contractions in Flow Conditions T1 and T7a

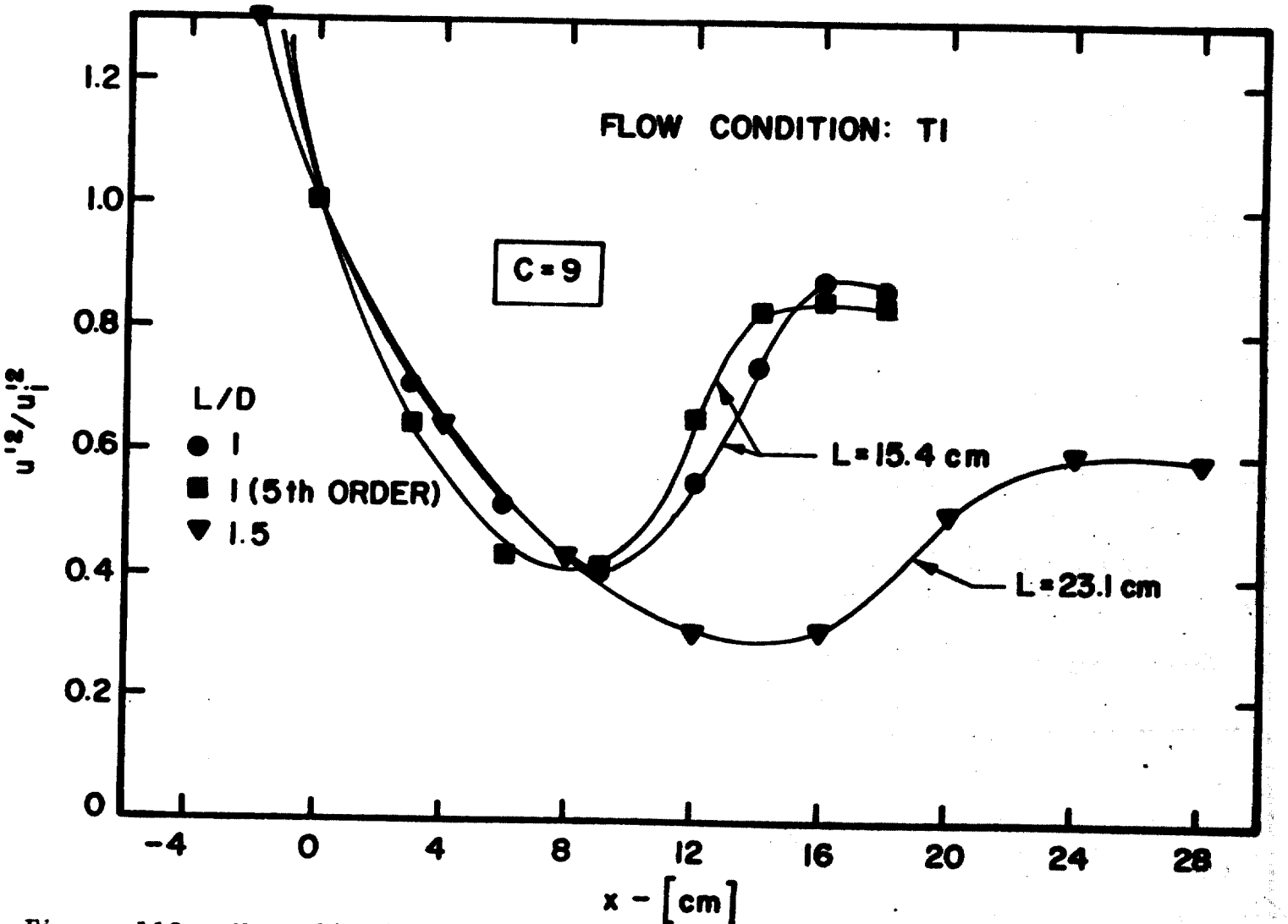

Figure 113. Normalized Streamwise Turbulence Energy through Long Contractions in Flow Condition T1

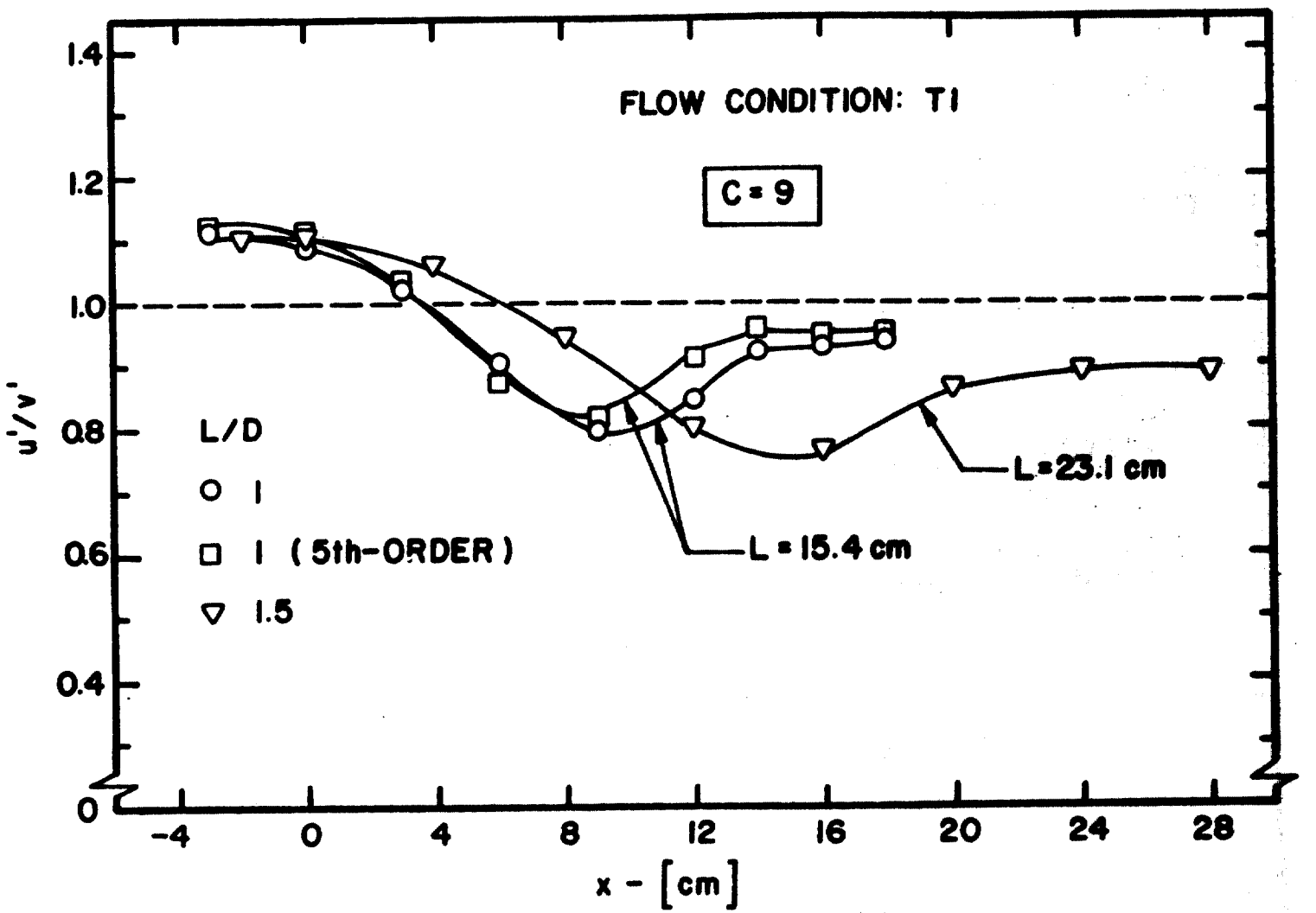

Figure 114. Isotropy through Long Contractions in Flow Condition T1

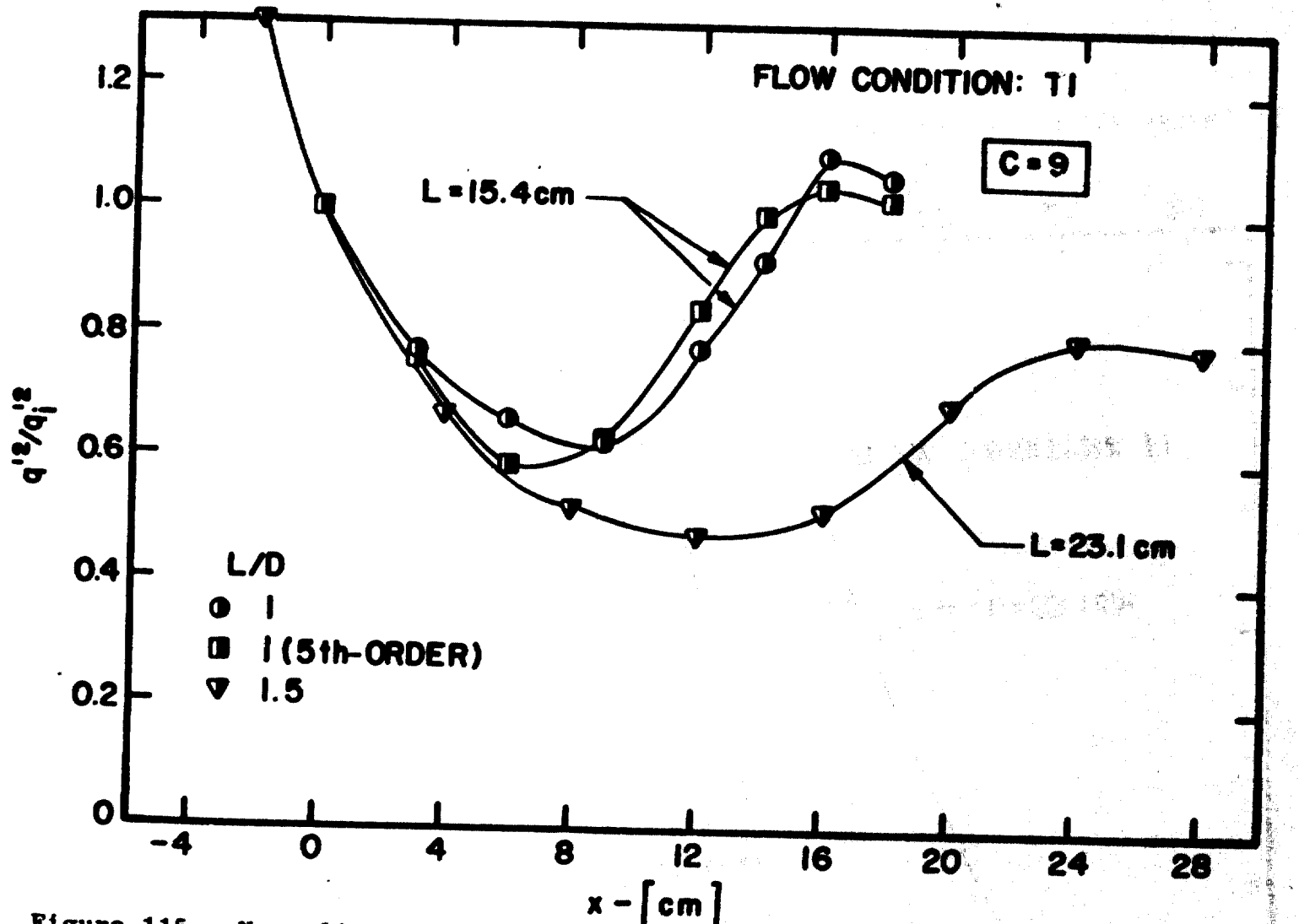

Figure 115. Normalized Total Turbulence Energy through Long Contractions in Flow Condition T1

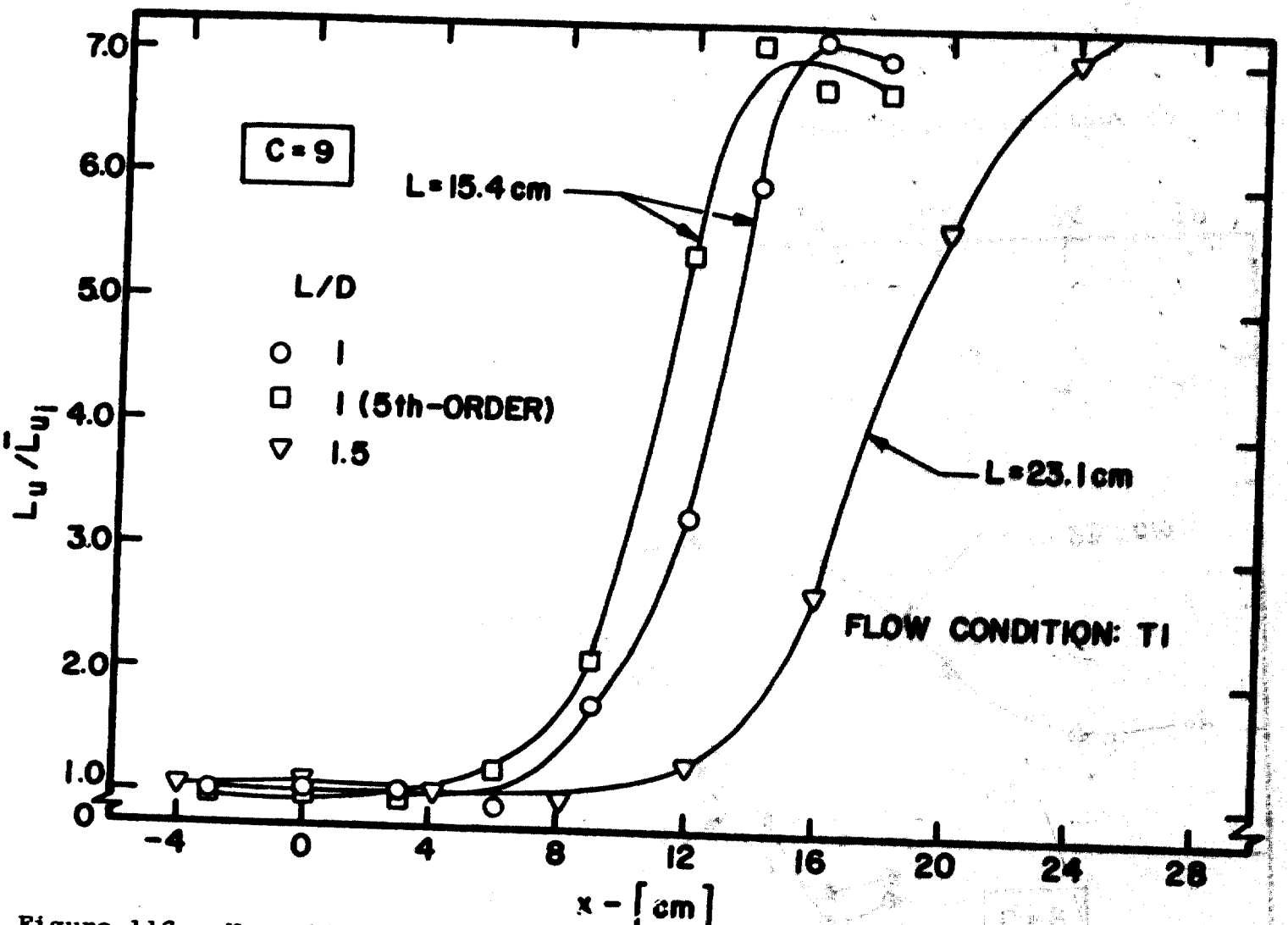

Figure 116. Normalized Longitudinal Length Scales through Long Contractions in Flow Condition T1

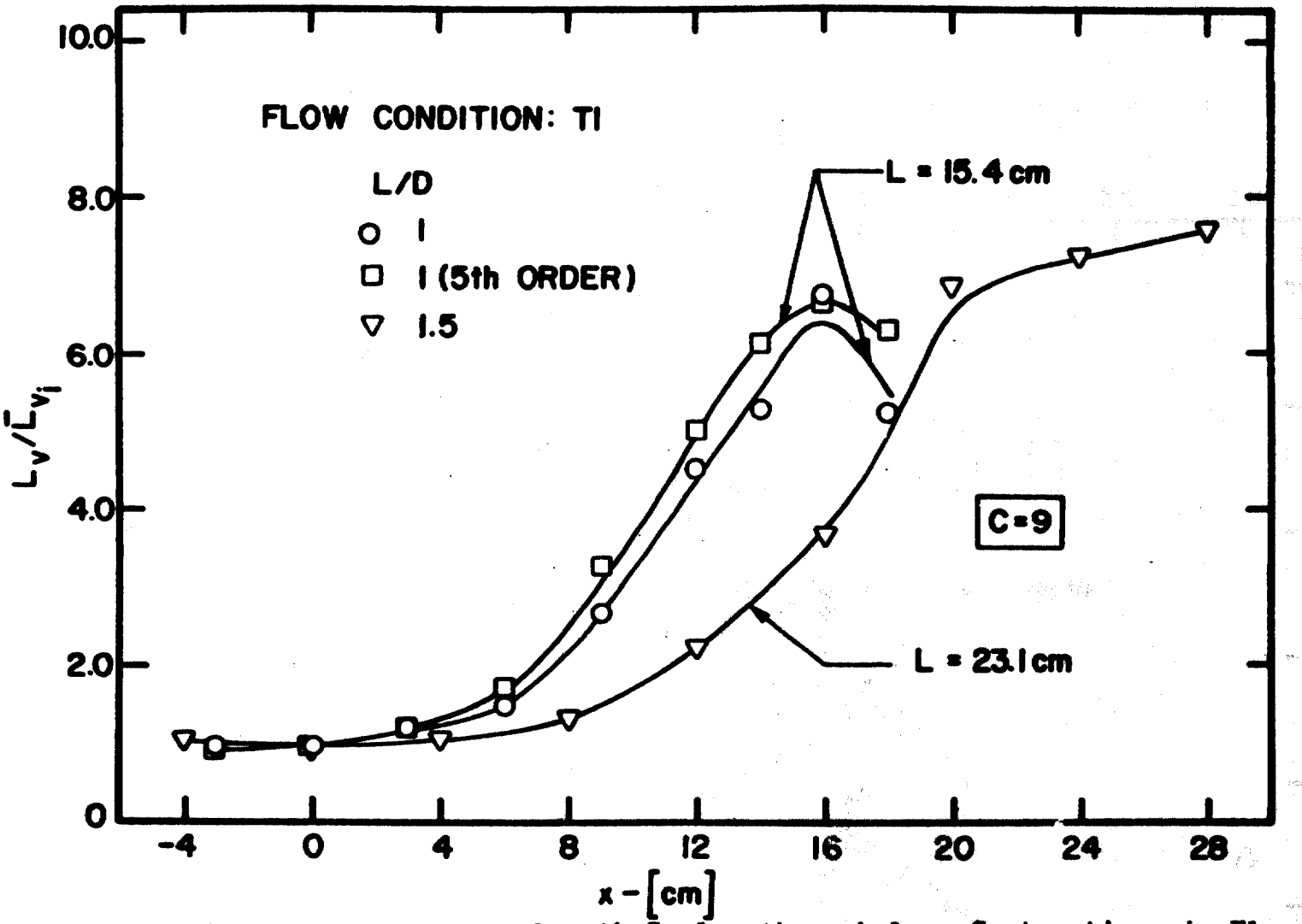

Figure 117. Normalized Lateral Length Scales through Long Contractions in Flow Condition T1

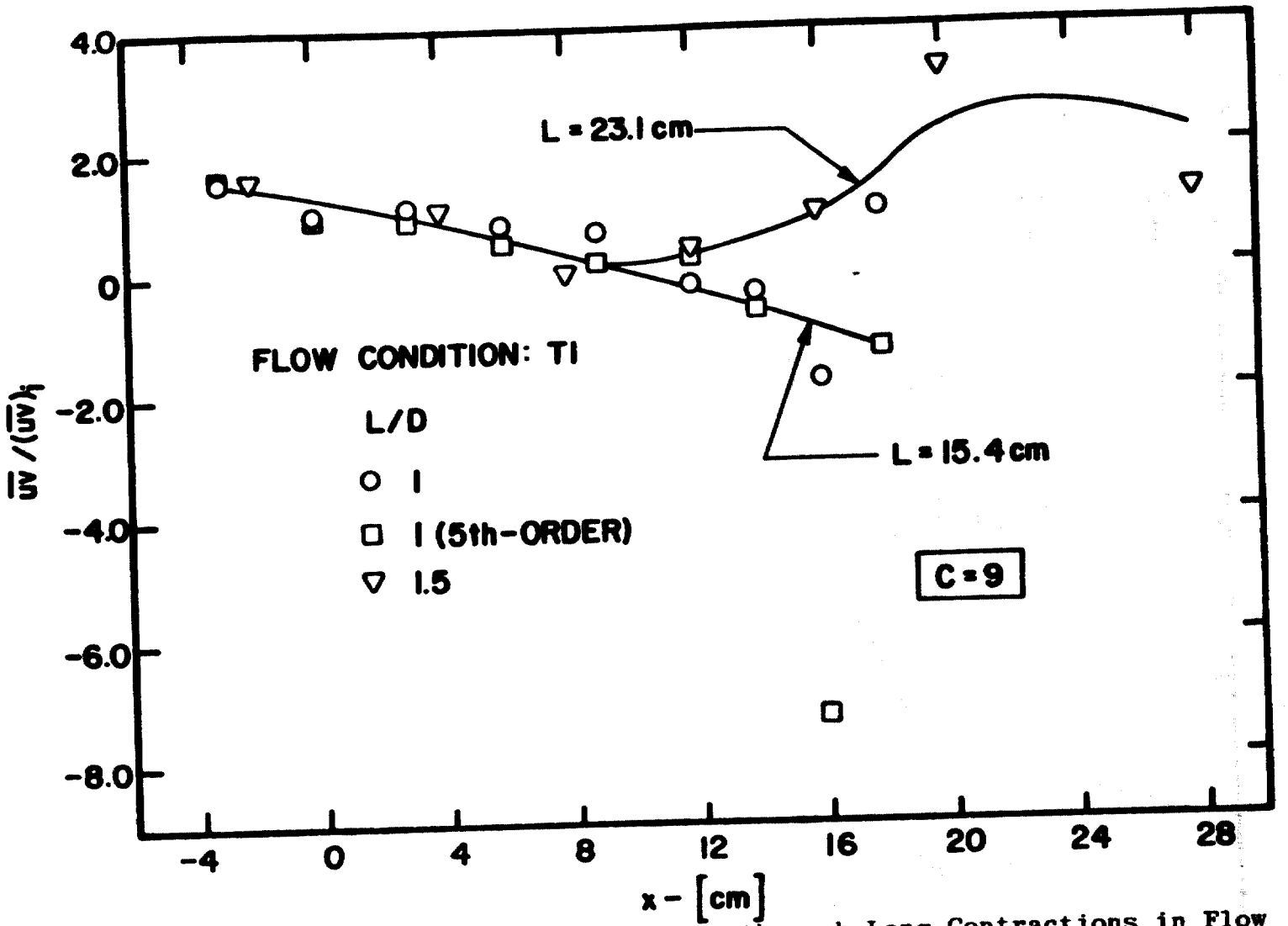

Figure 118. Normalized Reynolds Stresses through Long Contractions in Flow Condition T1

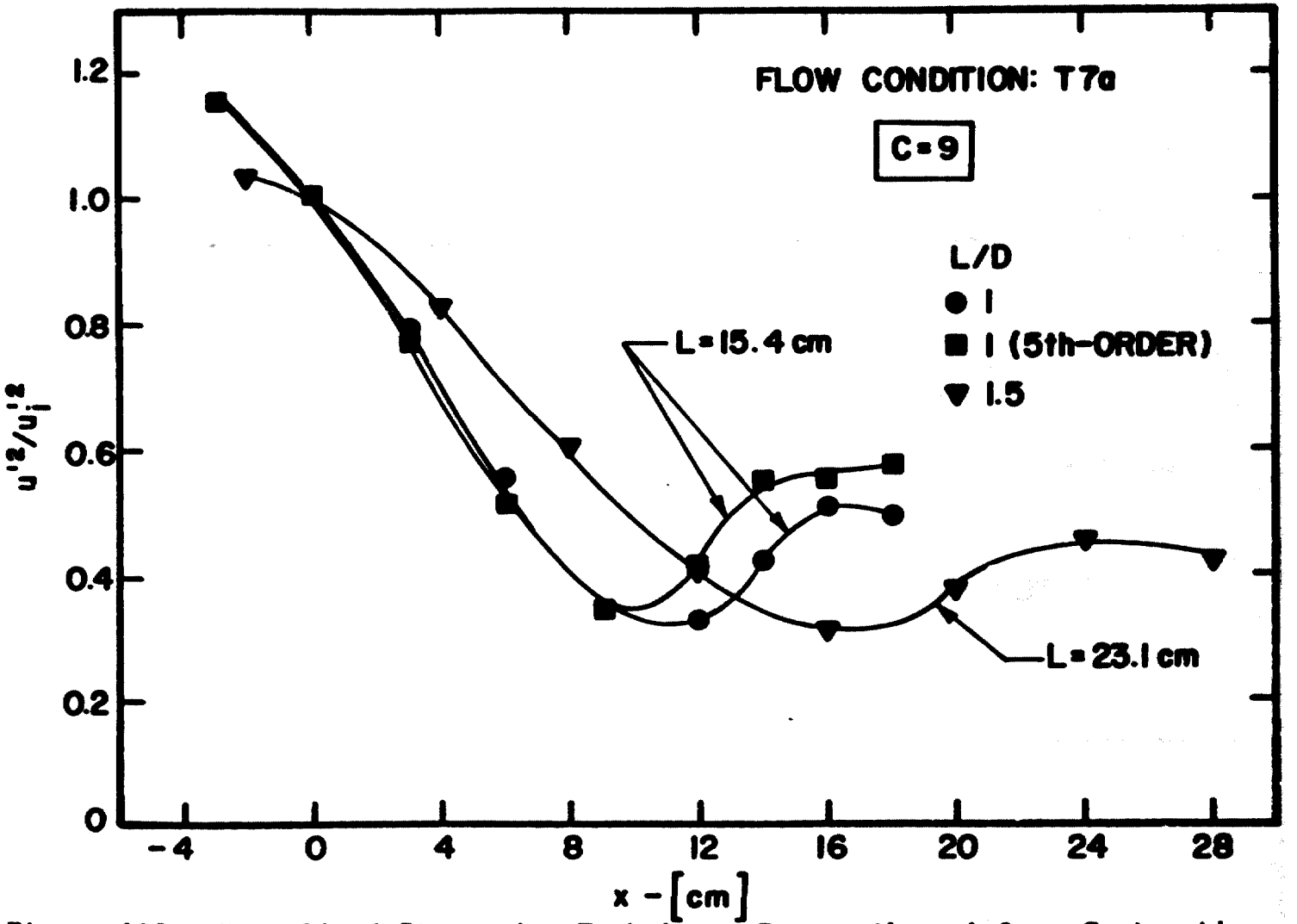

Figure 119. Normalized Streamwise Turbulence Energy through Long Contractions in Flow Condition T7a

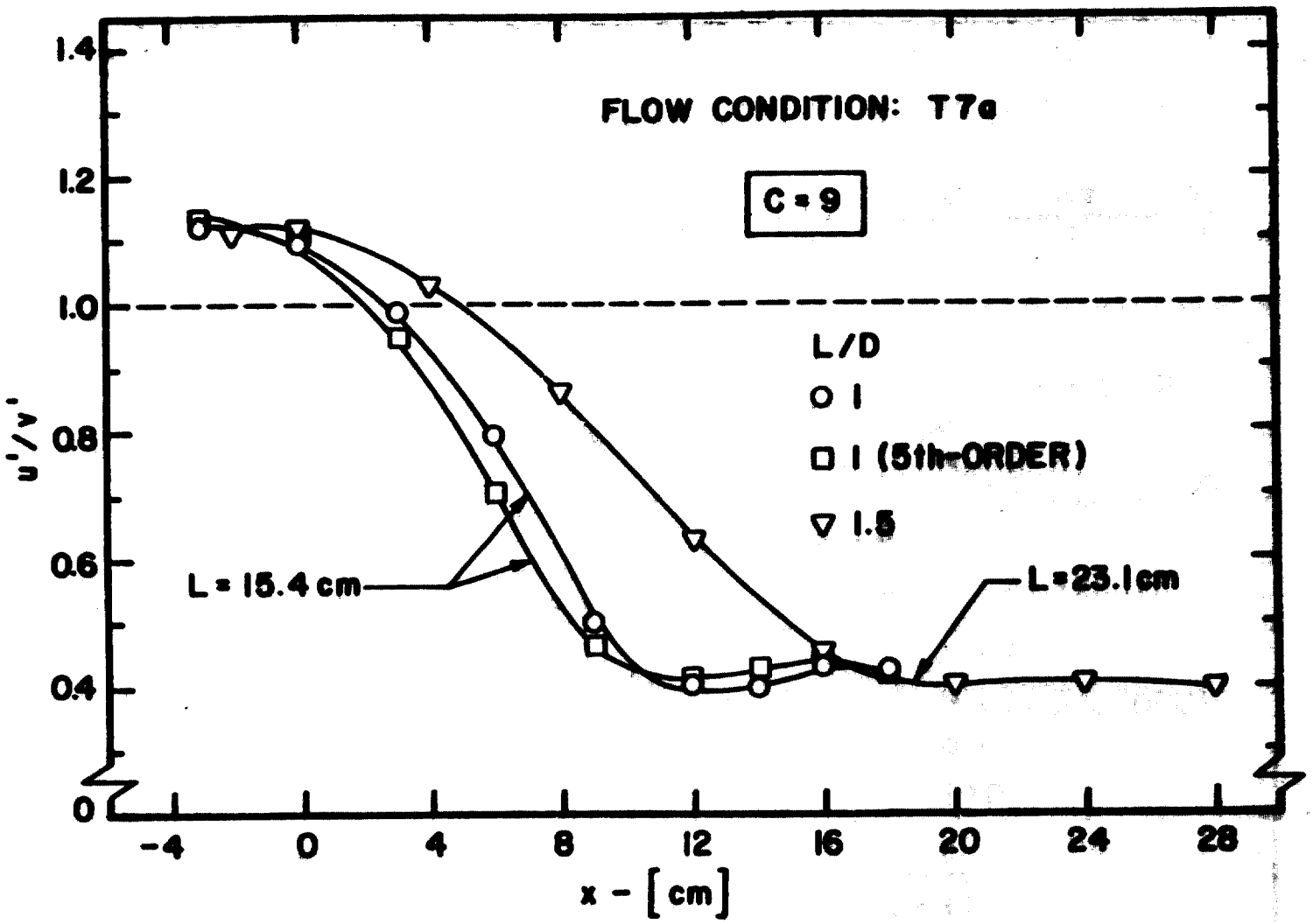

Figure 120. Isotropy through Long Contractions in Flow Condition T7a

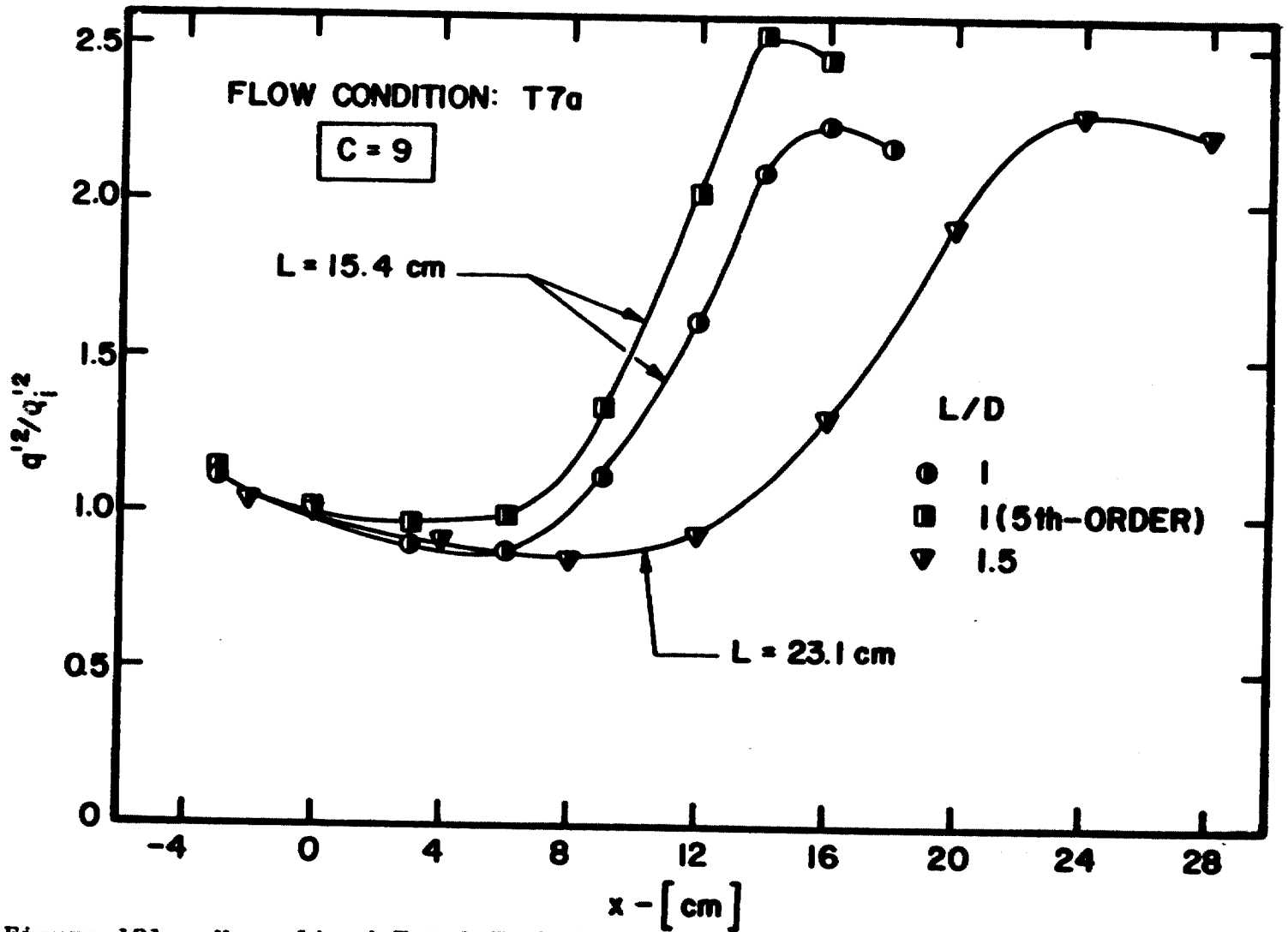

Figure 121. Normalized Total Turbulence Energy through Long Contractions in Flow Condition T7a

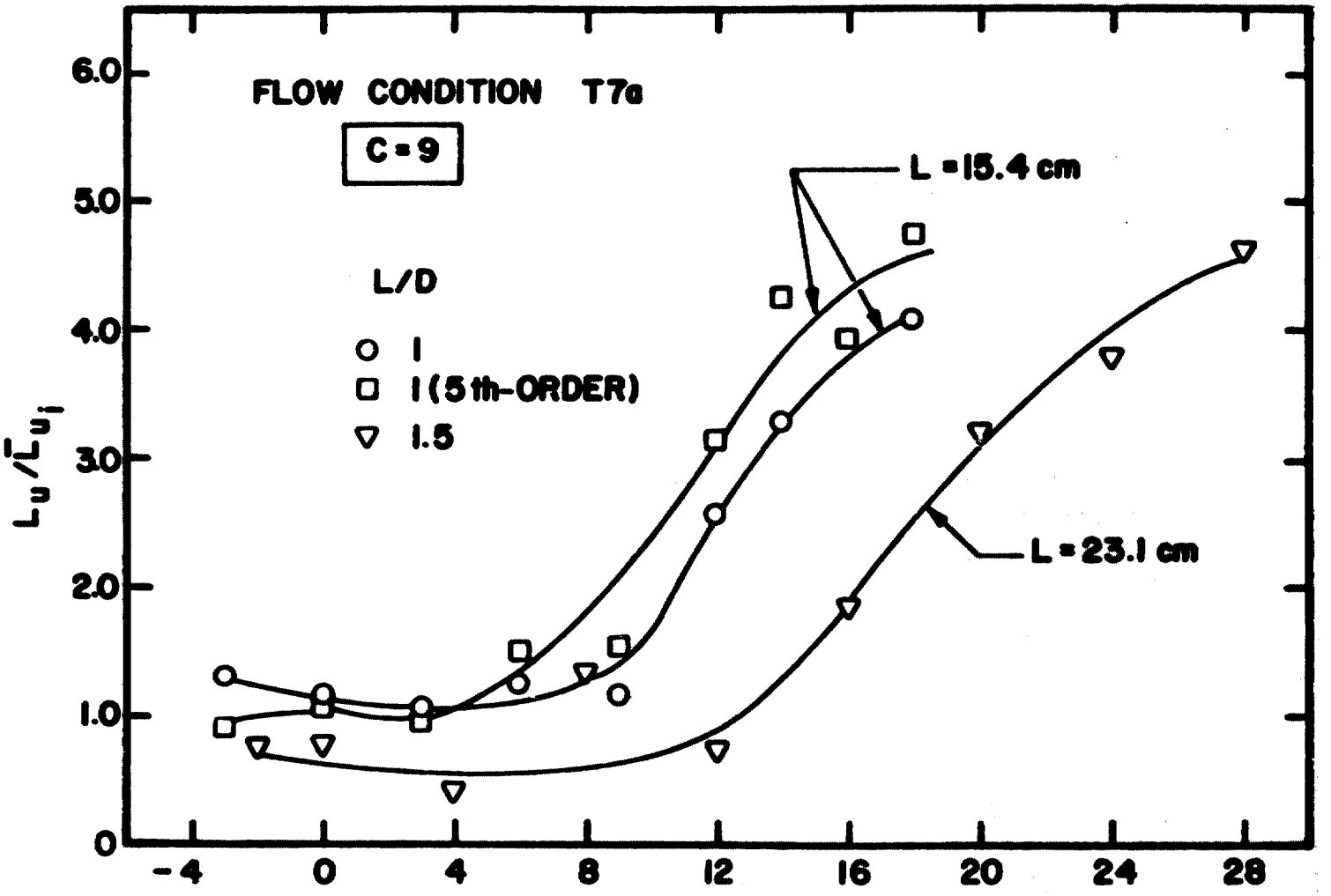

Fig. 122. Normalized Longitudinal Length Scales through Long Contractions in Flow Condition T7a

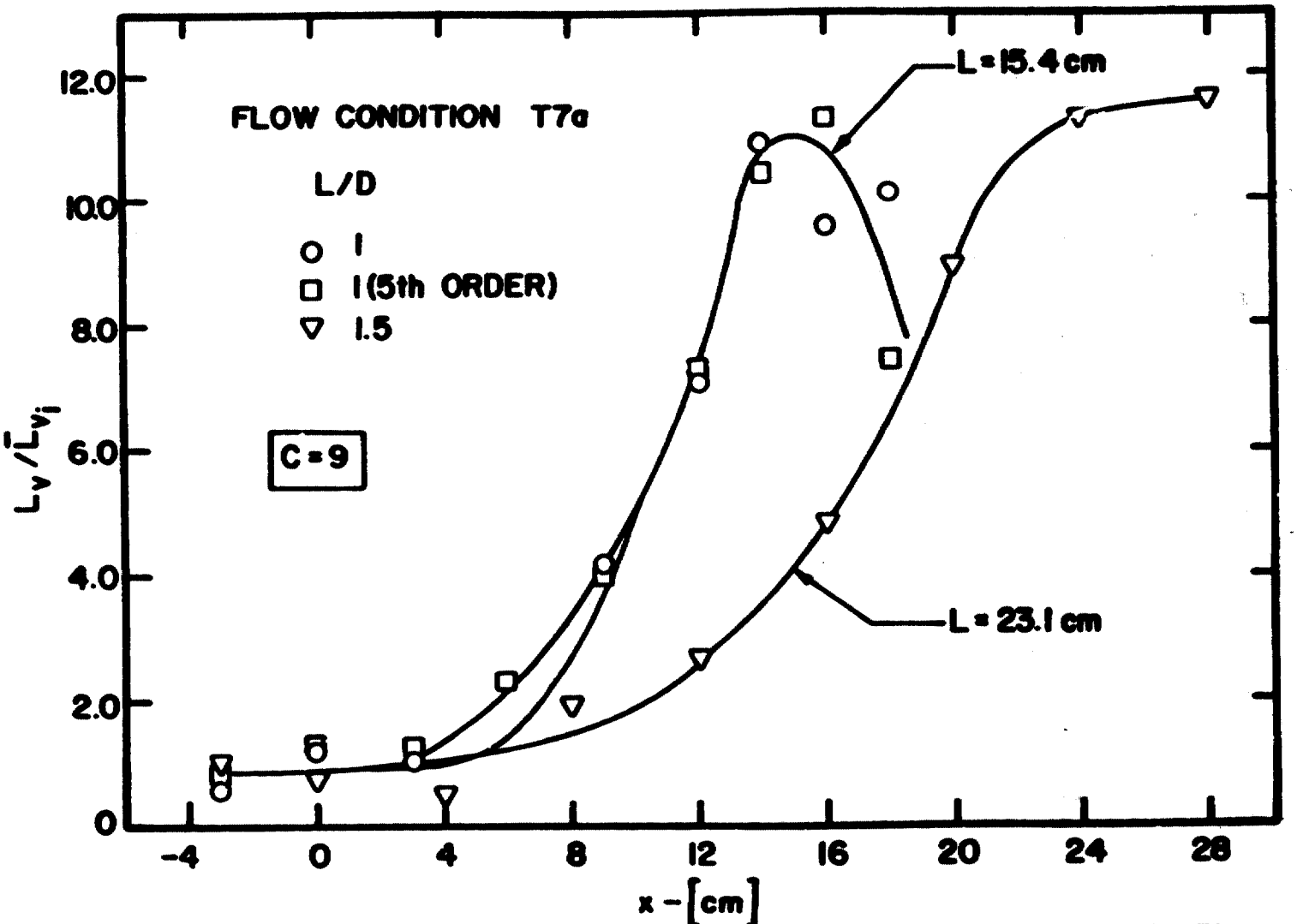

Figure 123. Normalized Lateral Length Scales through Long Contractions in Flow Condition T7a

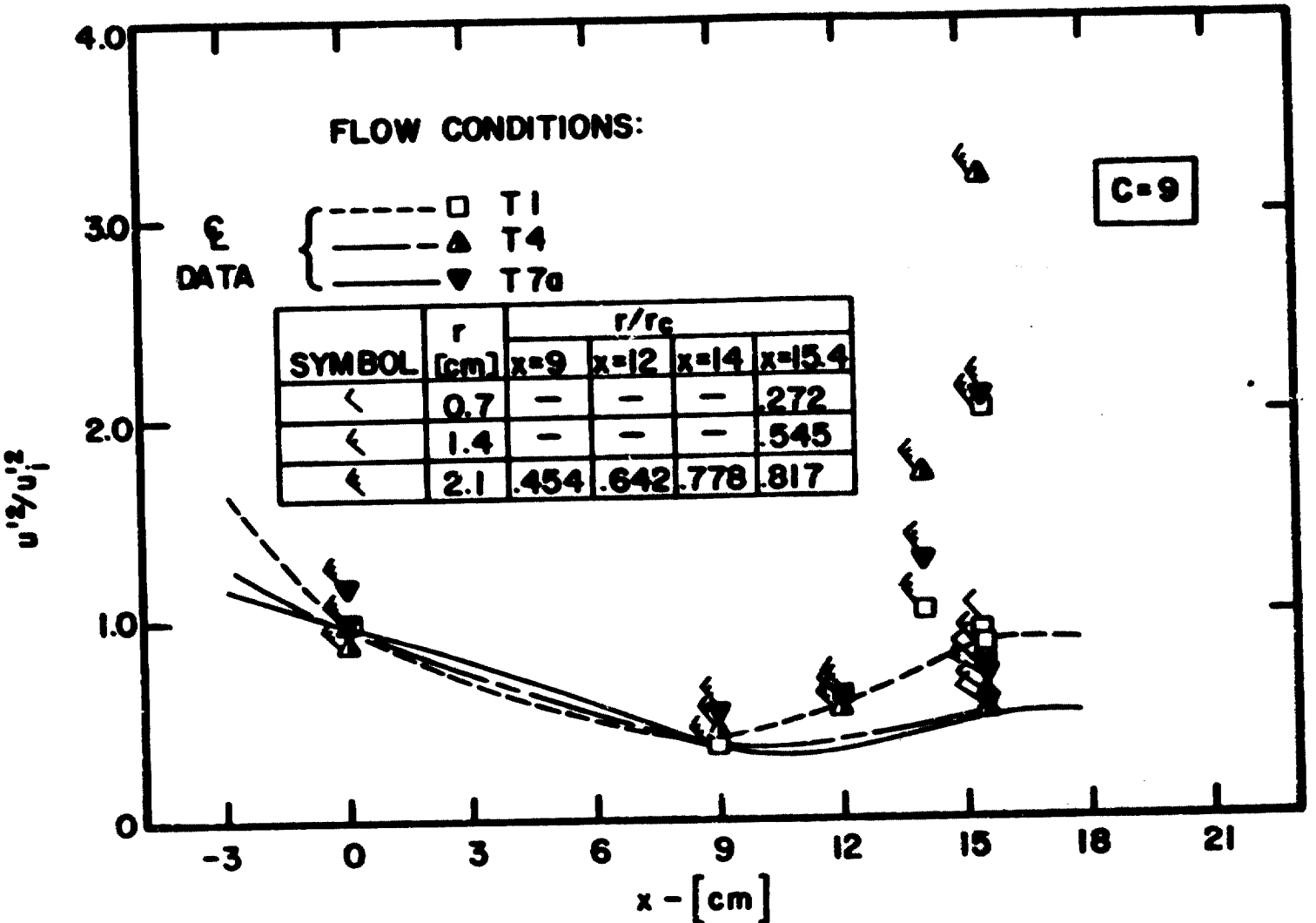

Figure 124. Normalized Streamwise Turbulence Energy Both On- and Off-Axis, in Flow Conditions T1, T4 and T7a

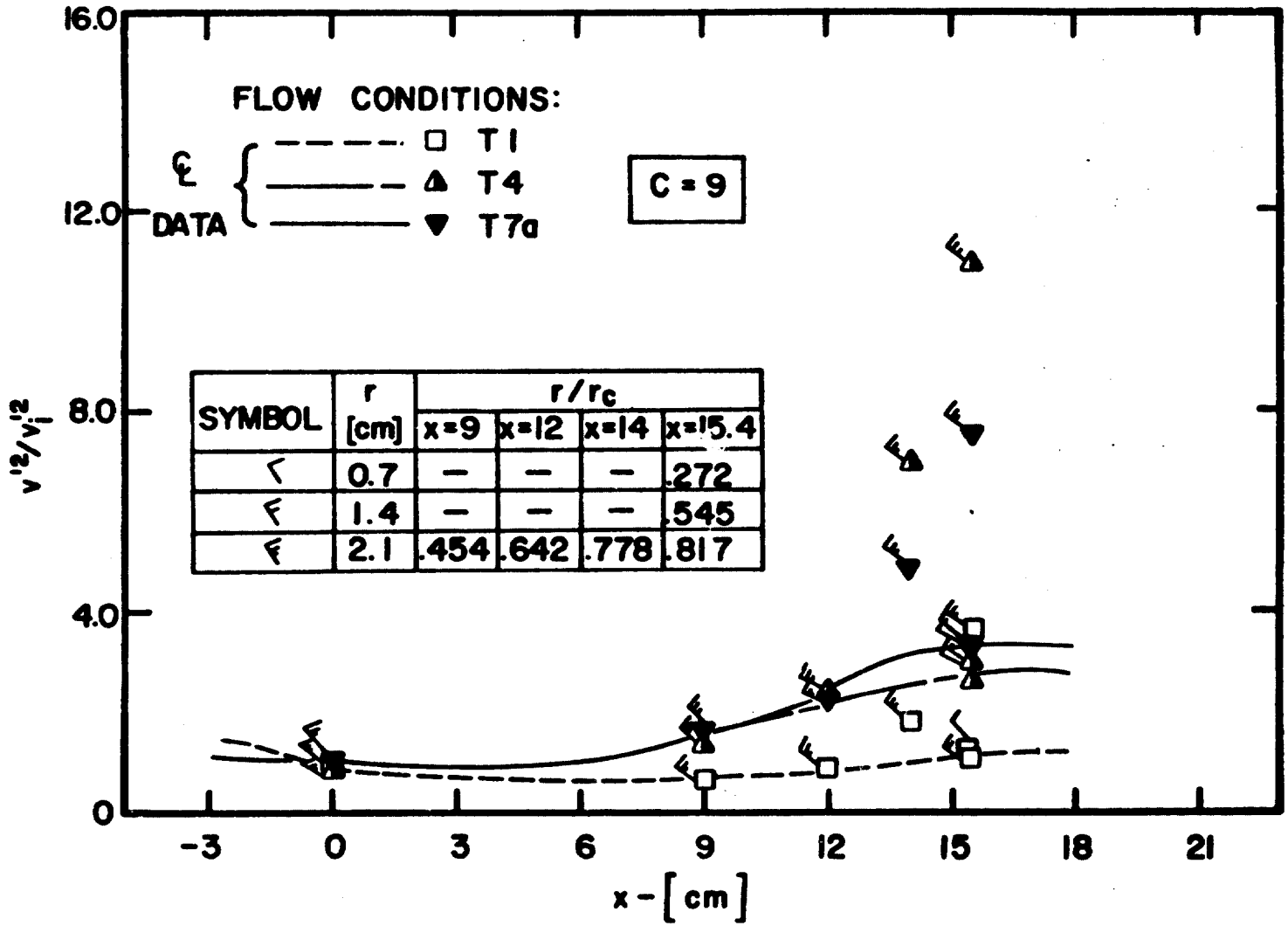

Figure 125. Normalized Radial Turbulence Energy, Both On- and Off-Axis, in Flow Conditions T1, T4 and T7a

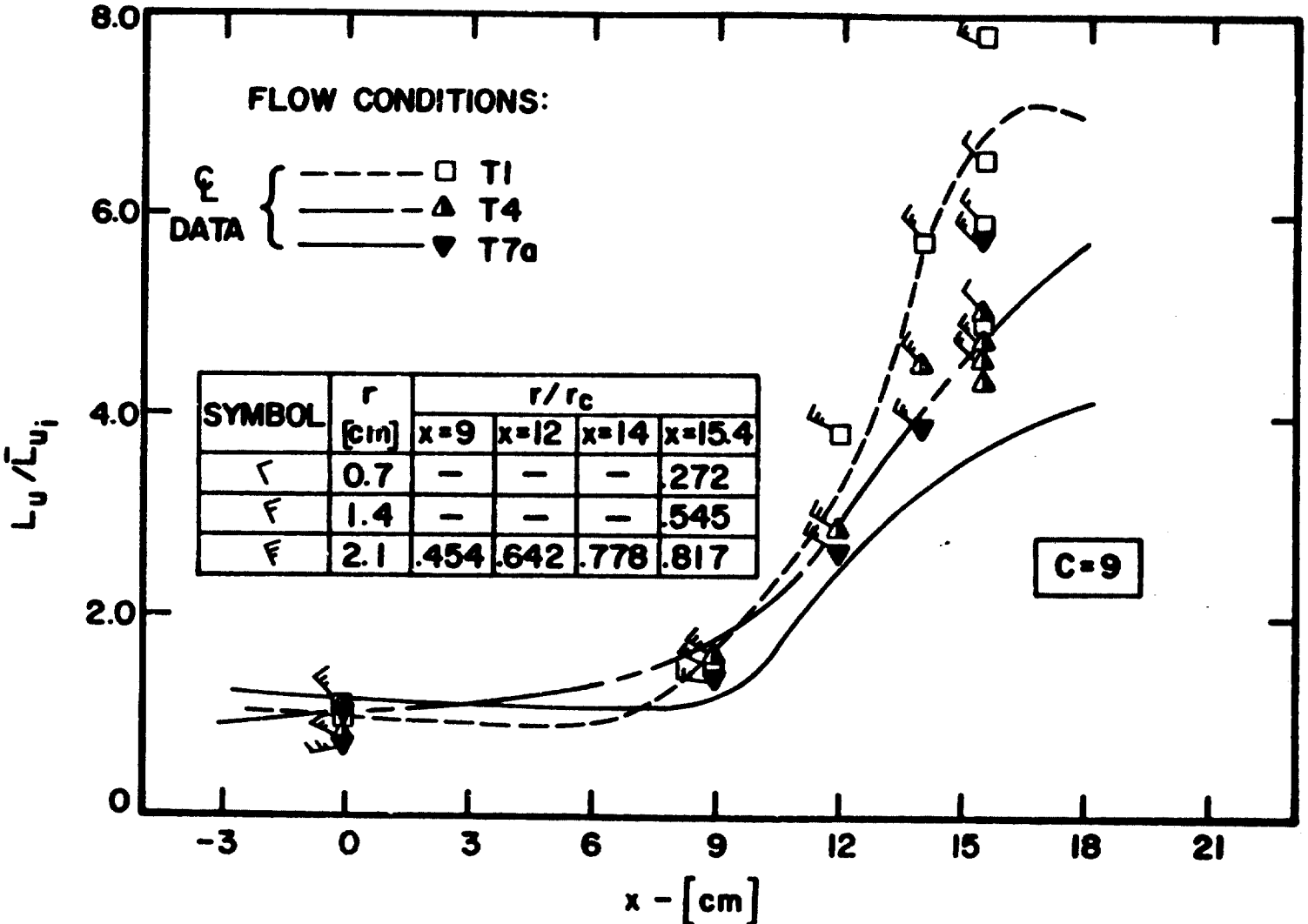

Figure 126. Normalized Longitudinal Length Scales, Both On- and Off-Axis, in Flow Conditions T1, T4 and T7a

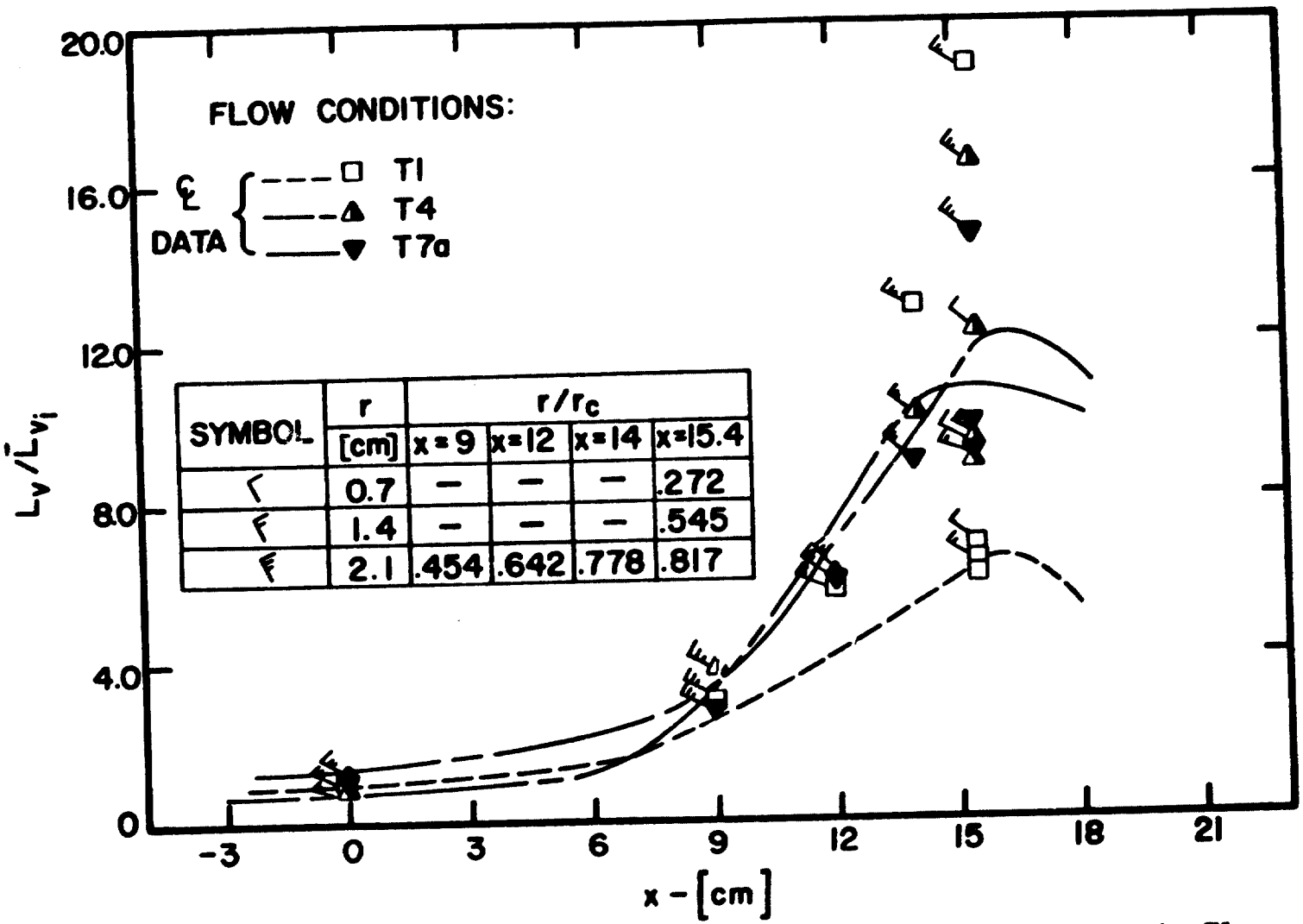

Figure 127. Normalized Lateral Length Scales, Both On- and Off-Axis, in Flow Conditions T1, T4 and T7a

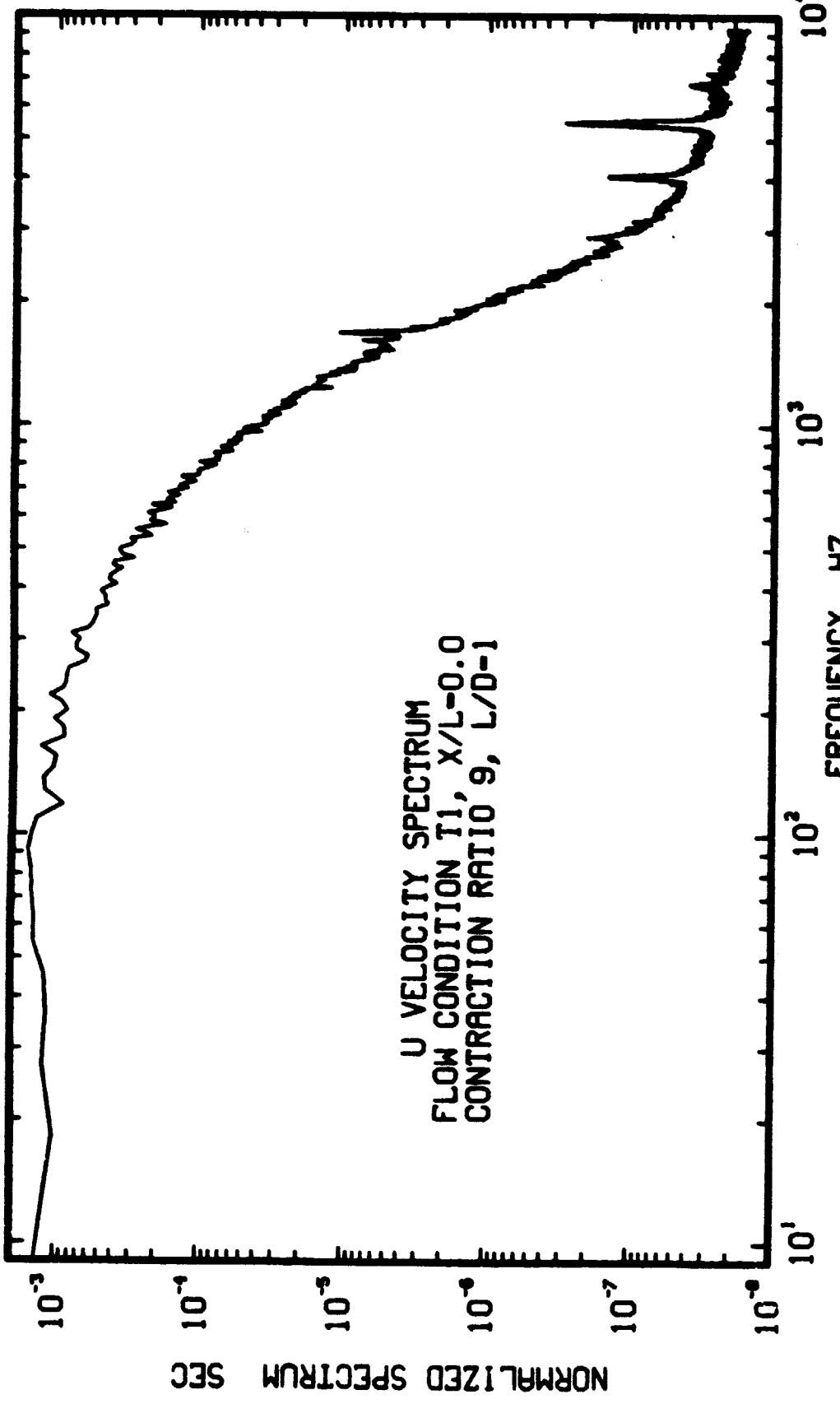

Figure 128. Normalized Streamwise-Velocity Spectrum at Inlet of a Moderate Contraction in Flow Condition T1

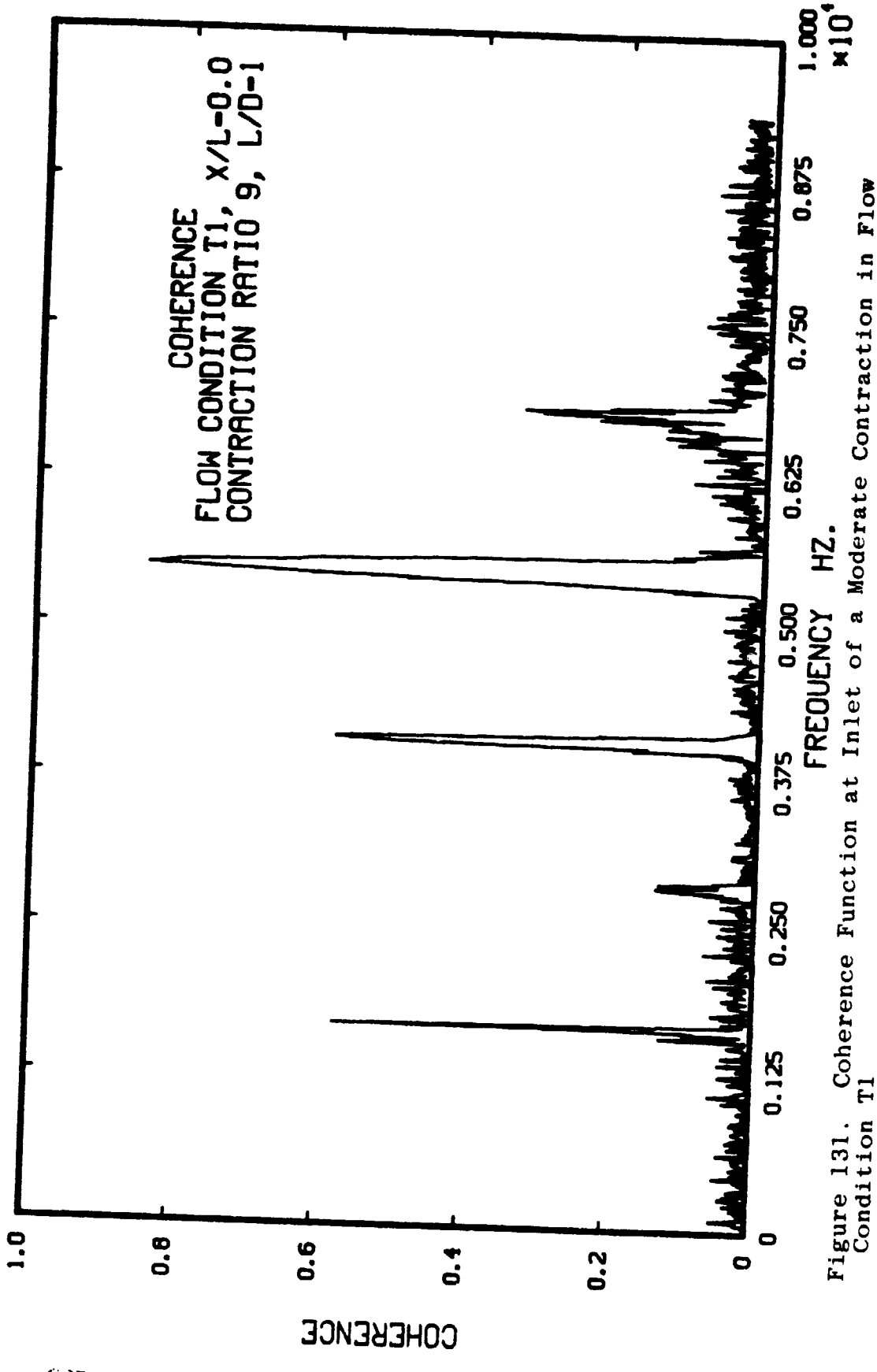

Figure 131. Coherence Function at Inlet of a Moderate Contraction in Flow Condition T1

213 - 314

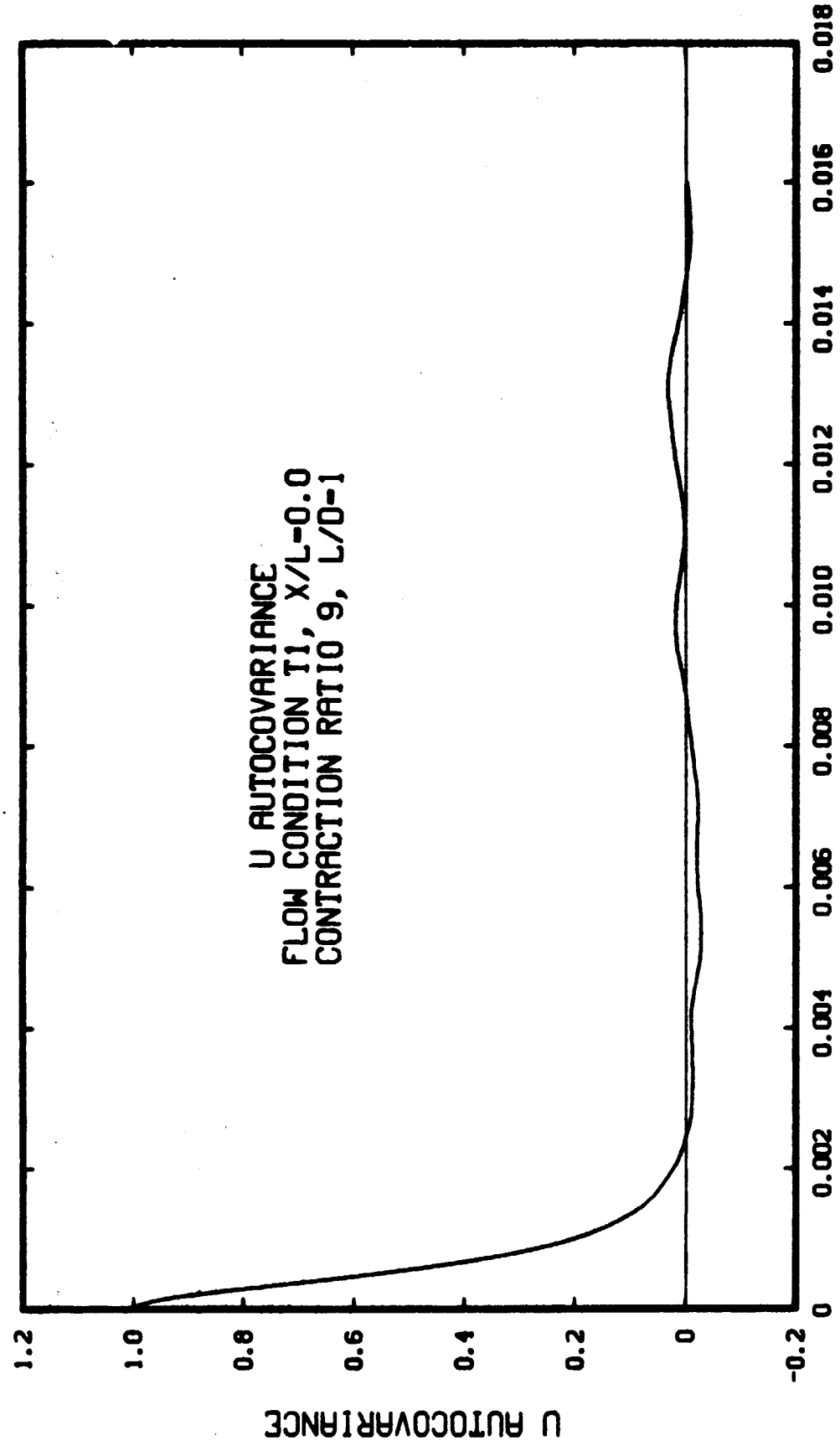

Figure 132. Streamwise-Velocity Autocovariance Function at Inlet of a Moderate Contraction in Flow Condition T1

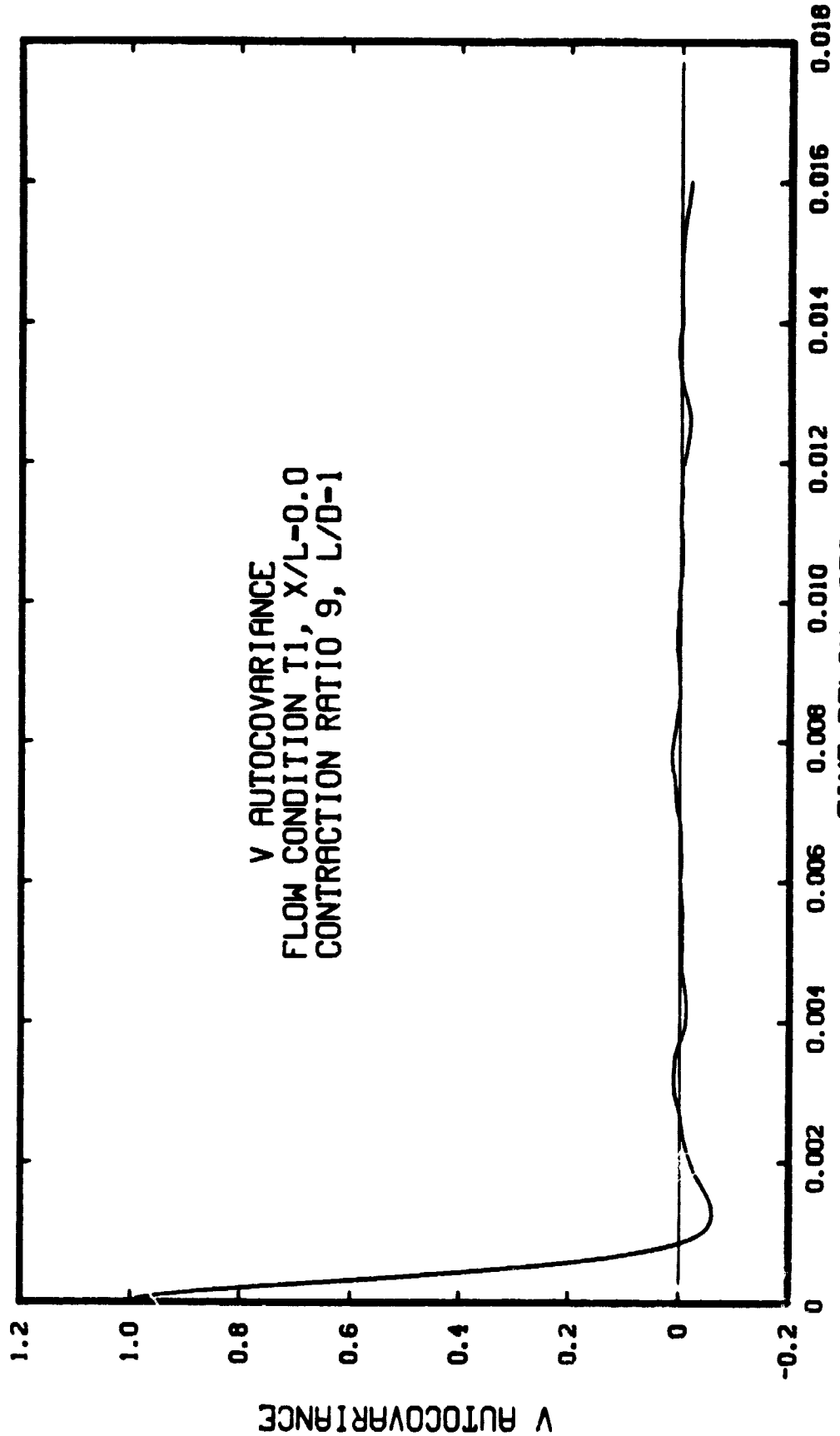

Figure 133. Radial-Velocity Autocovariance Function at Inlet of a Moderate Contraction in Flow Condition T1

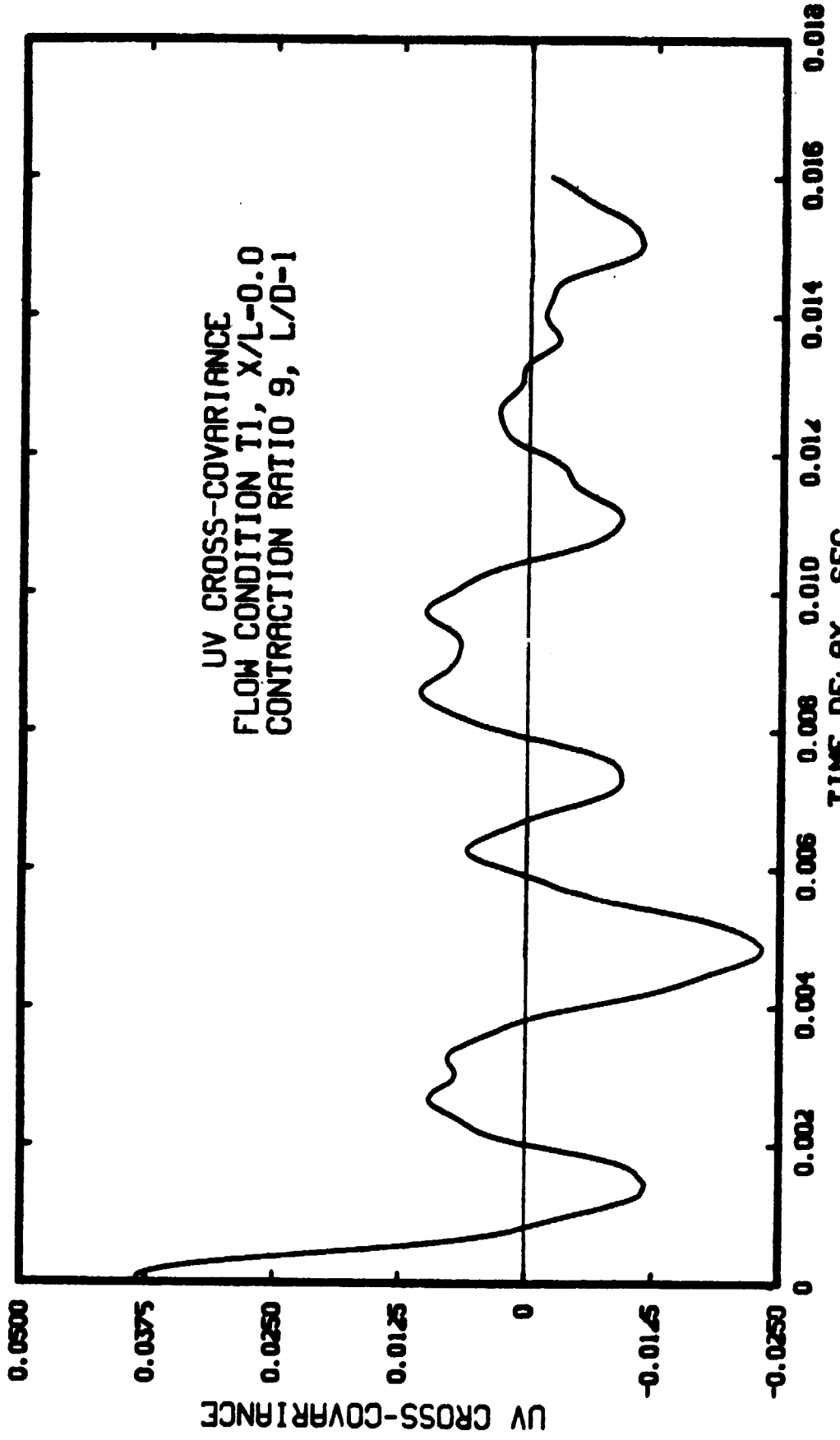

Figure 134. Streamwise-Radial Velocity Cross-Covariance Function at Inlet of a Moderate Contraction in Flow Condition T1

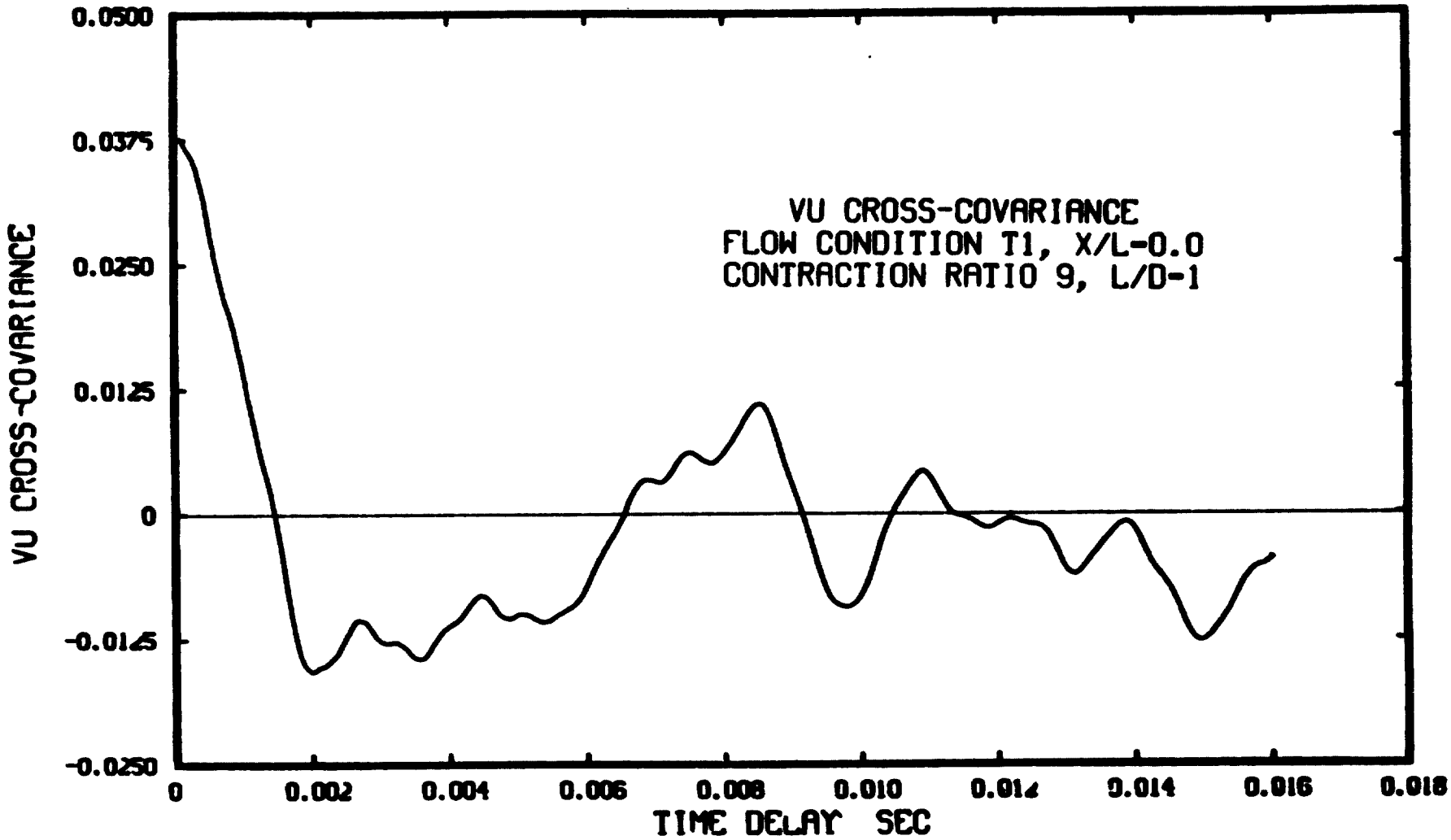

Figure 135. Radial-Streamwise Velocity Cross-Covariance Function at Inlet of a Moderate Contraction in Flow Condition T1

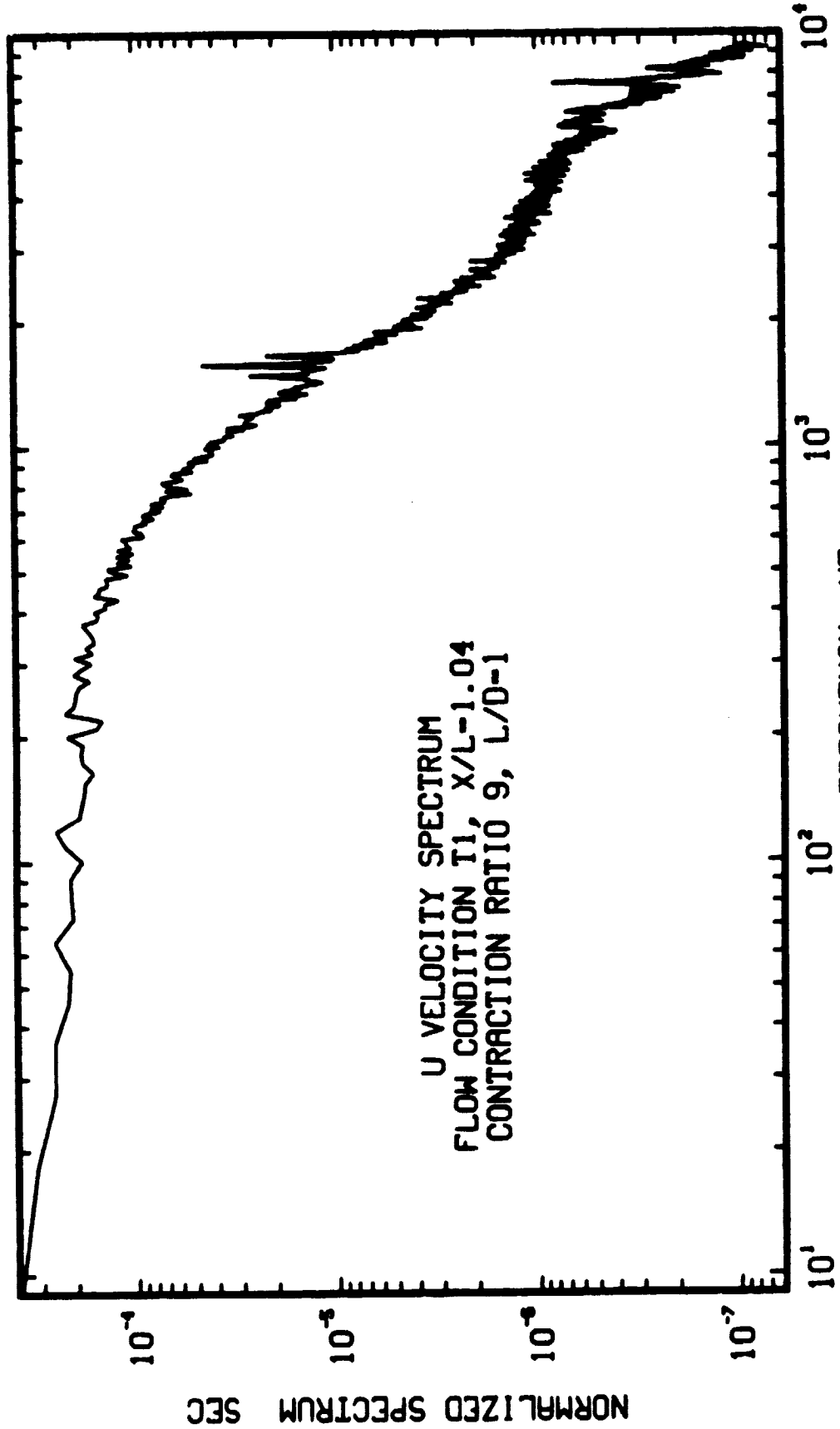

Figure 136. Normalized Streamwise-Velocity Spectrum Near Exit of a Moderate Contraction in Flow Condition T1

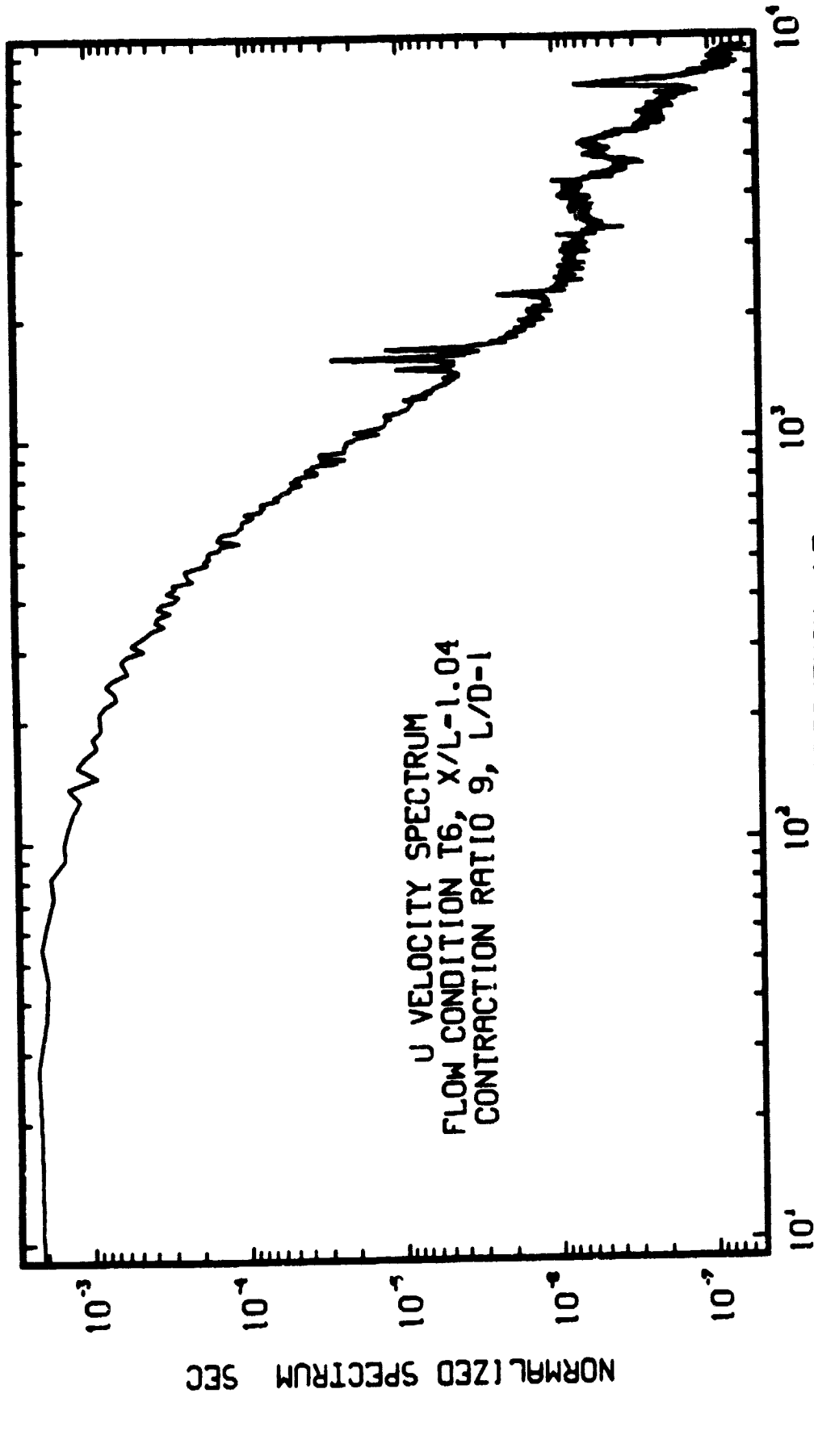

Figure 137. Normalized Streamwise-Velocity Spectrum Near Exit of a Moderate Contraction in Flow Condition T6

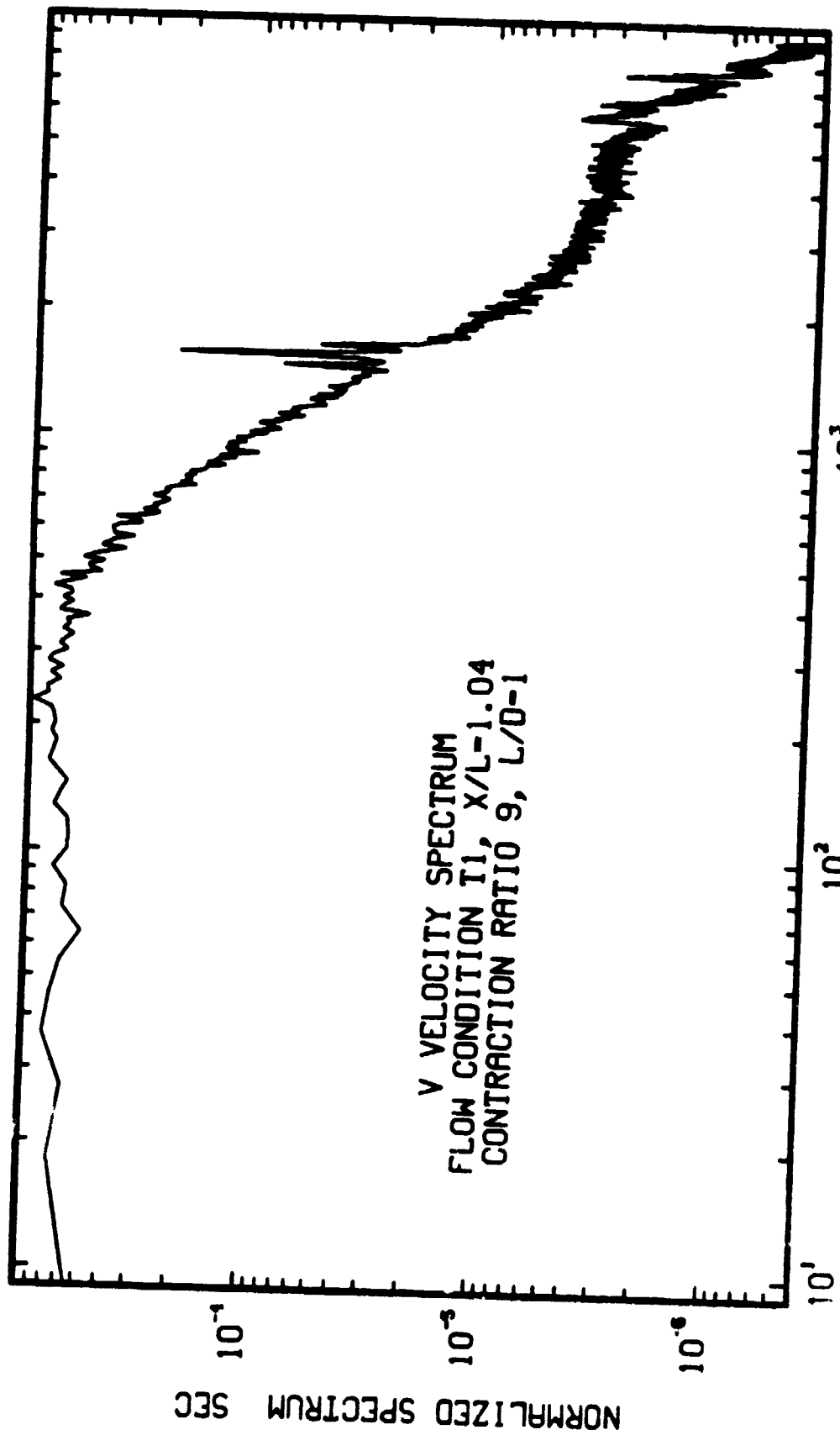

Figure 138. Normalized Radial-Velocity Spectrum Near Exit of a Moderate Contraction in Flow Condition T1

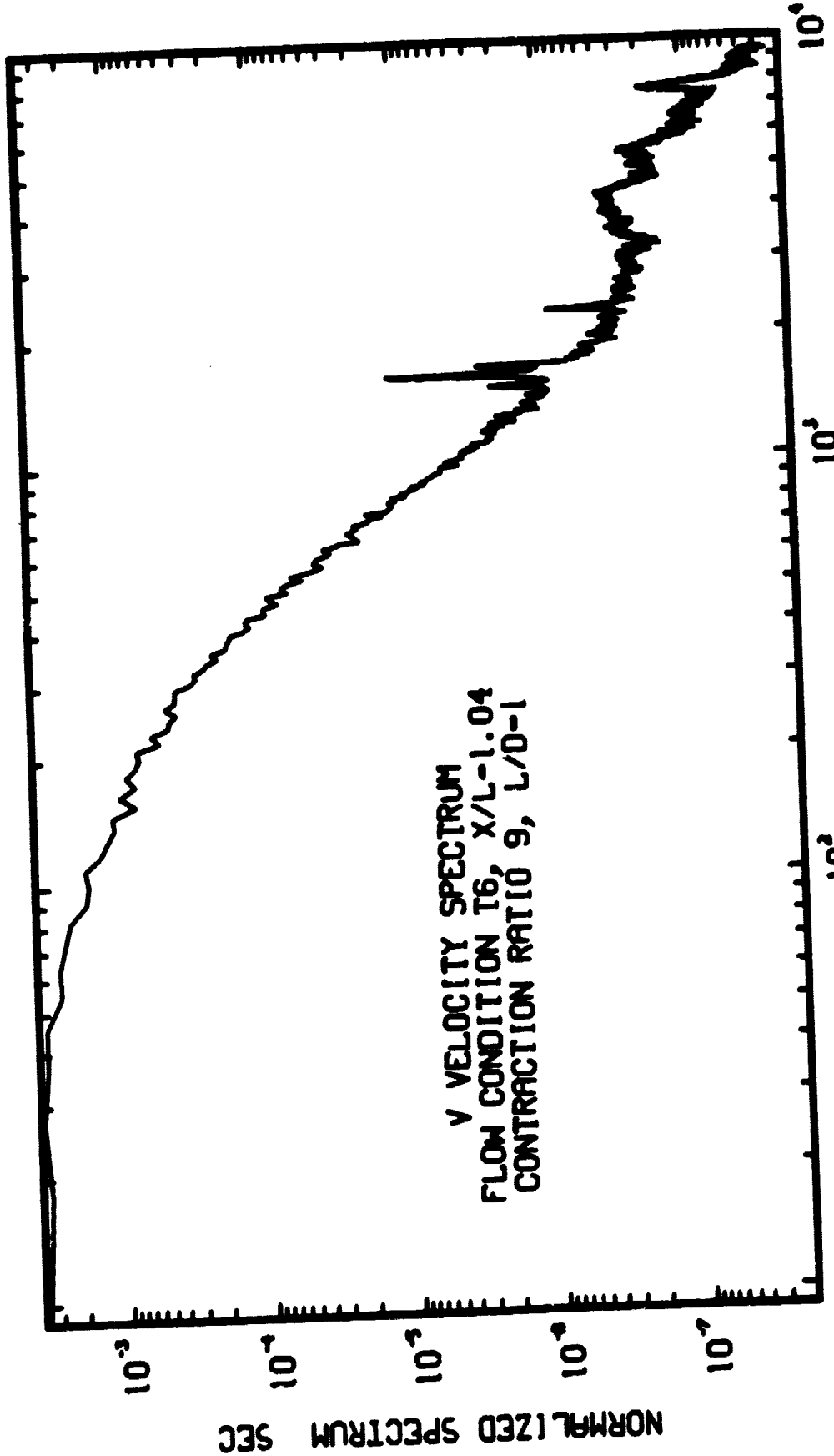

Figure 139. Normalized Radial-Velocity Spectrum Near Exit of a Moderate Contraction in Flow Condition T6

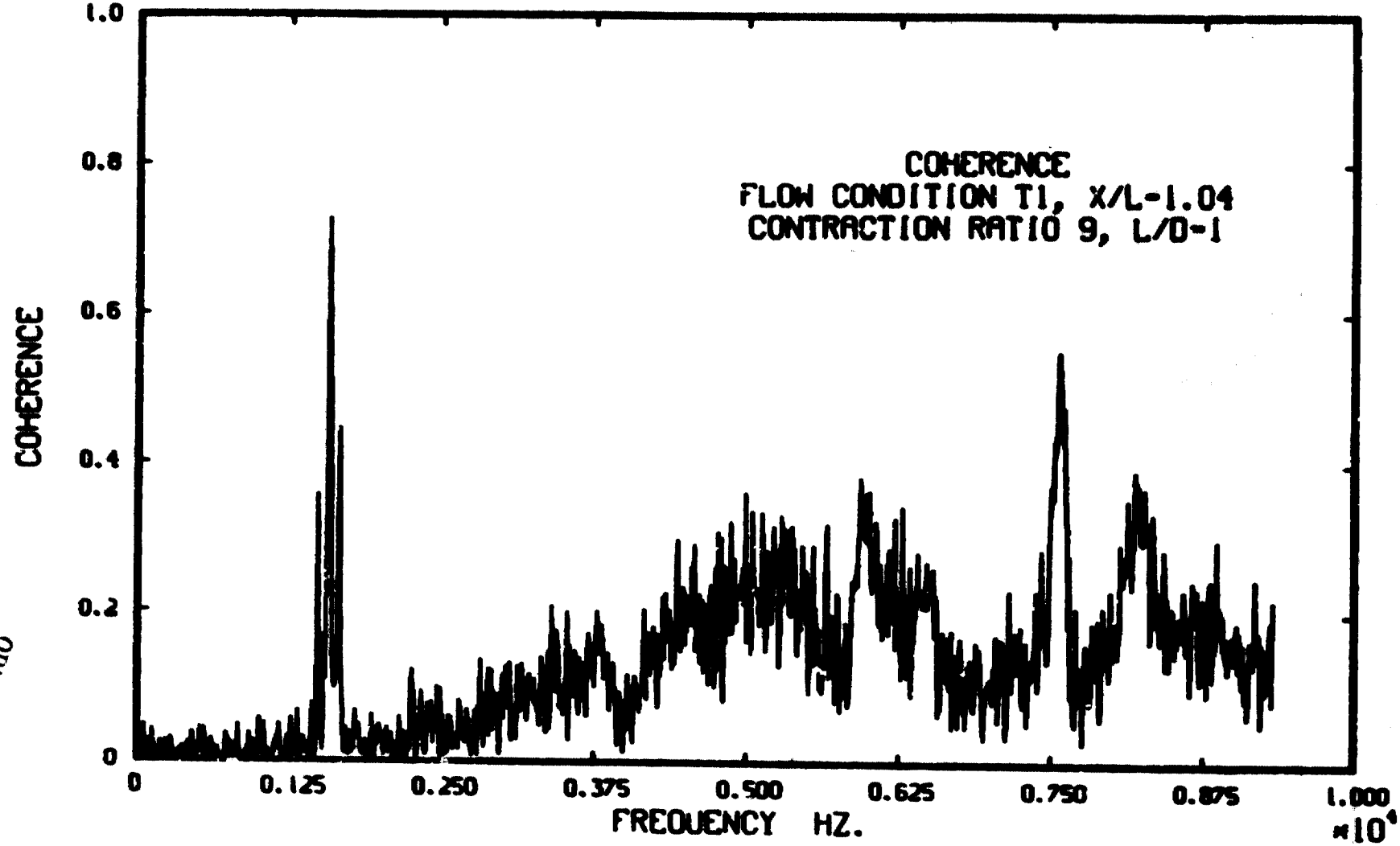

Figure 140. Coherence Function Near Exit of a Moderate Contraction in Flow Condition T1

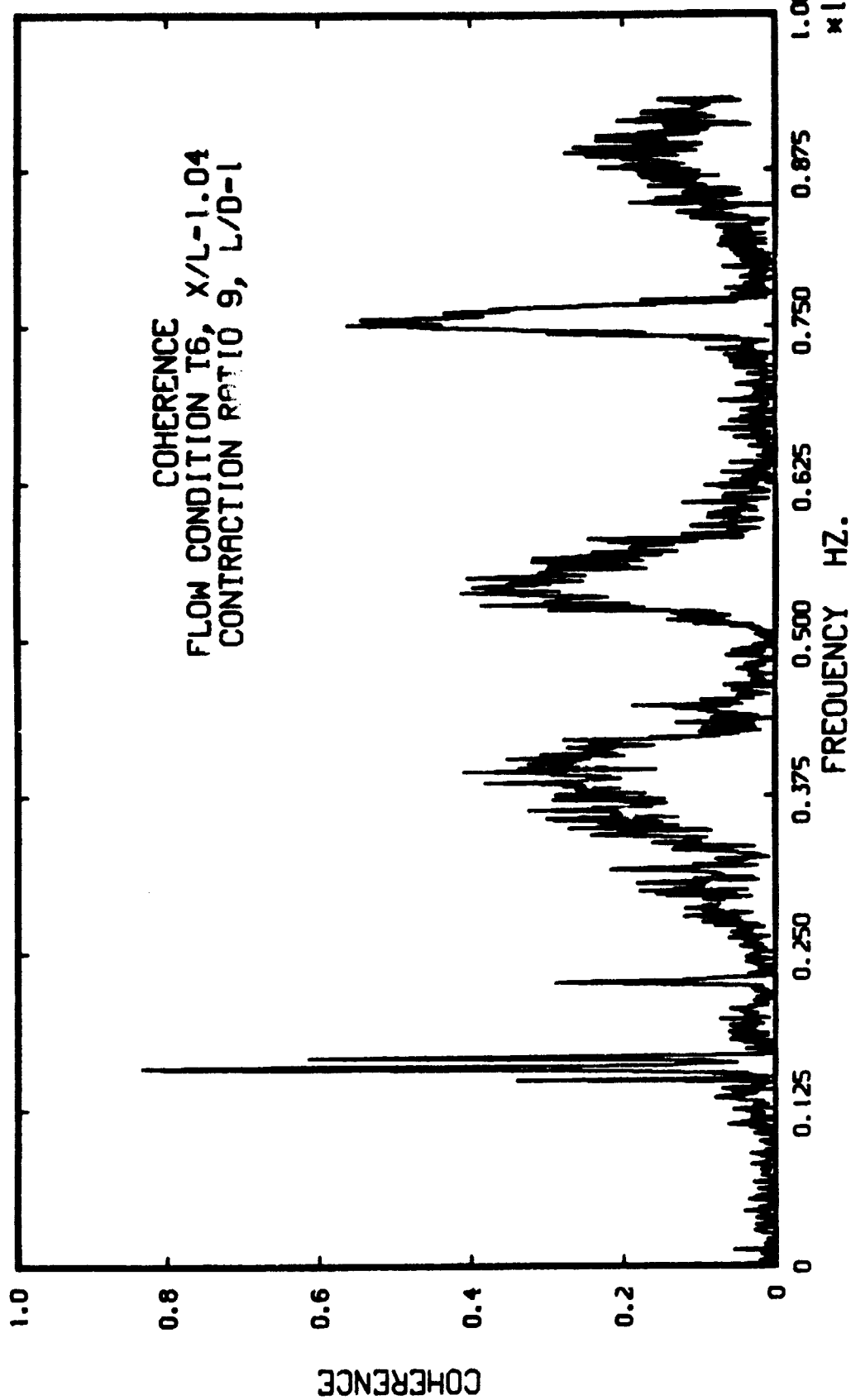

Figure 141. Coherence Function Near Exit of a Moderate Contraction in Flow Condition T6

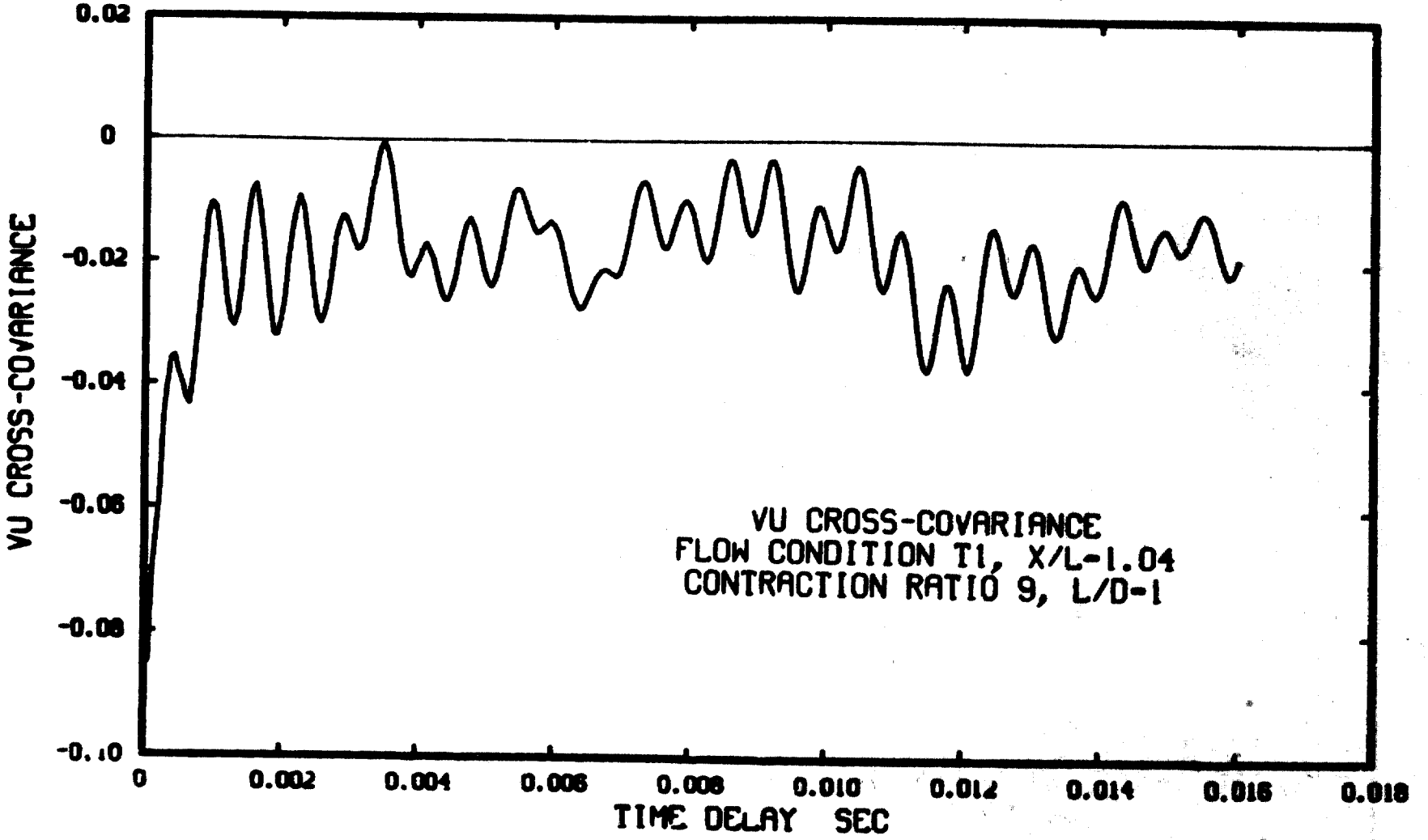

Figure 142. Cross-Covariance Function Near Exit of a Moderate Contraction in Flow Condition T1

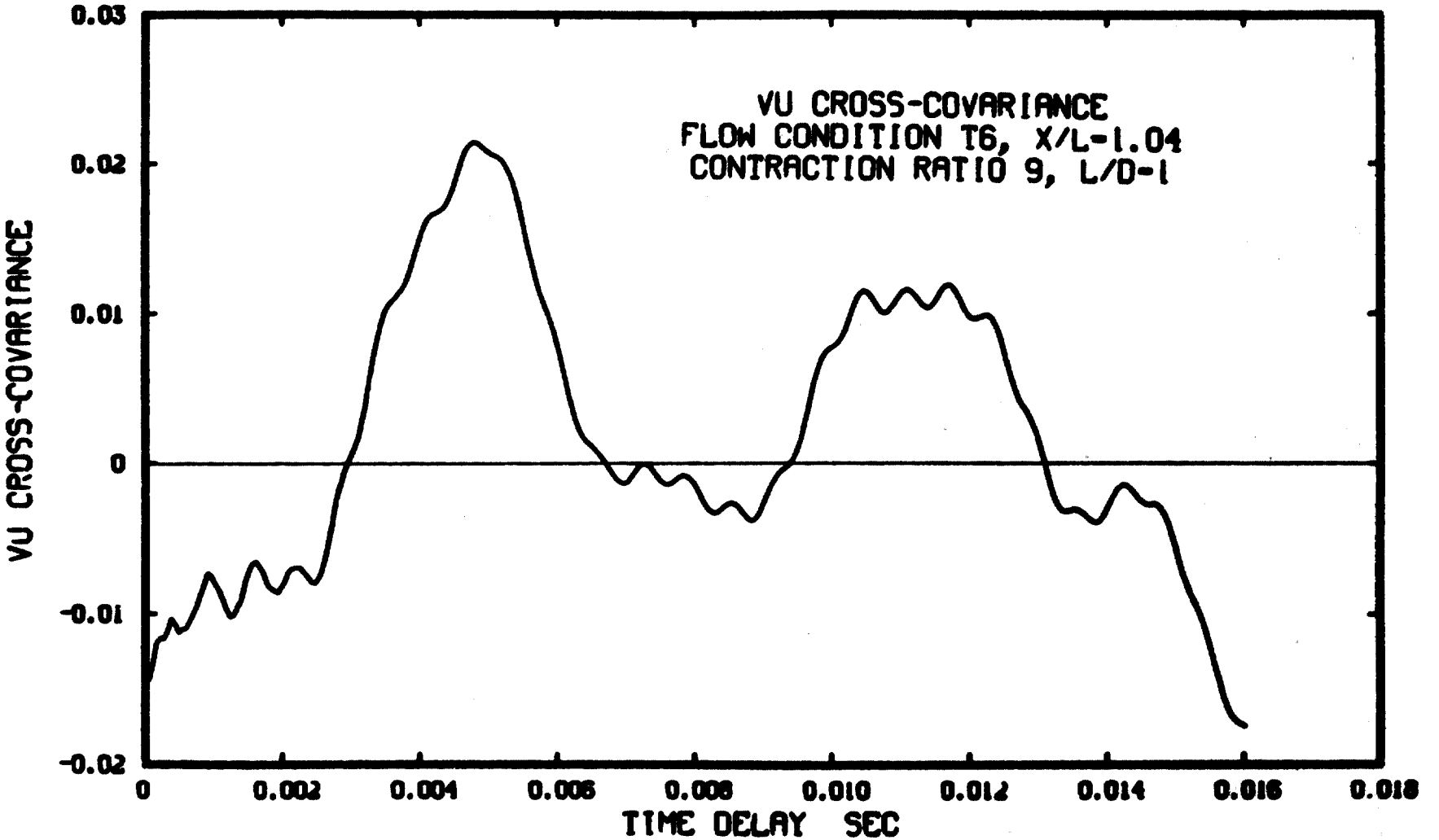

Figure 143. Cross-Covariance Function Near Exit of a Moderate Contraction in Flow Condition T6

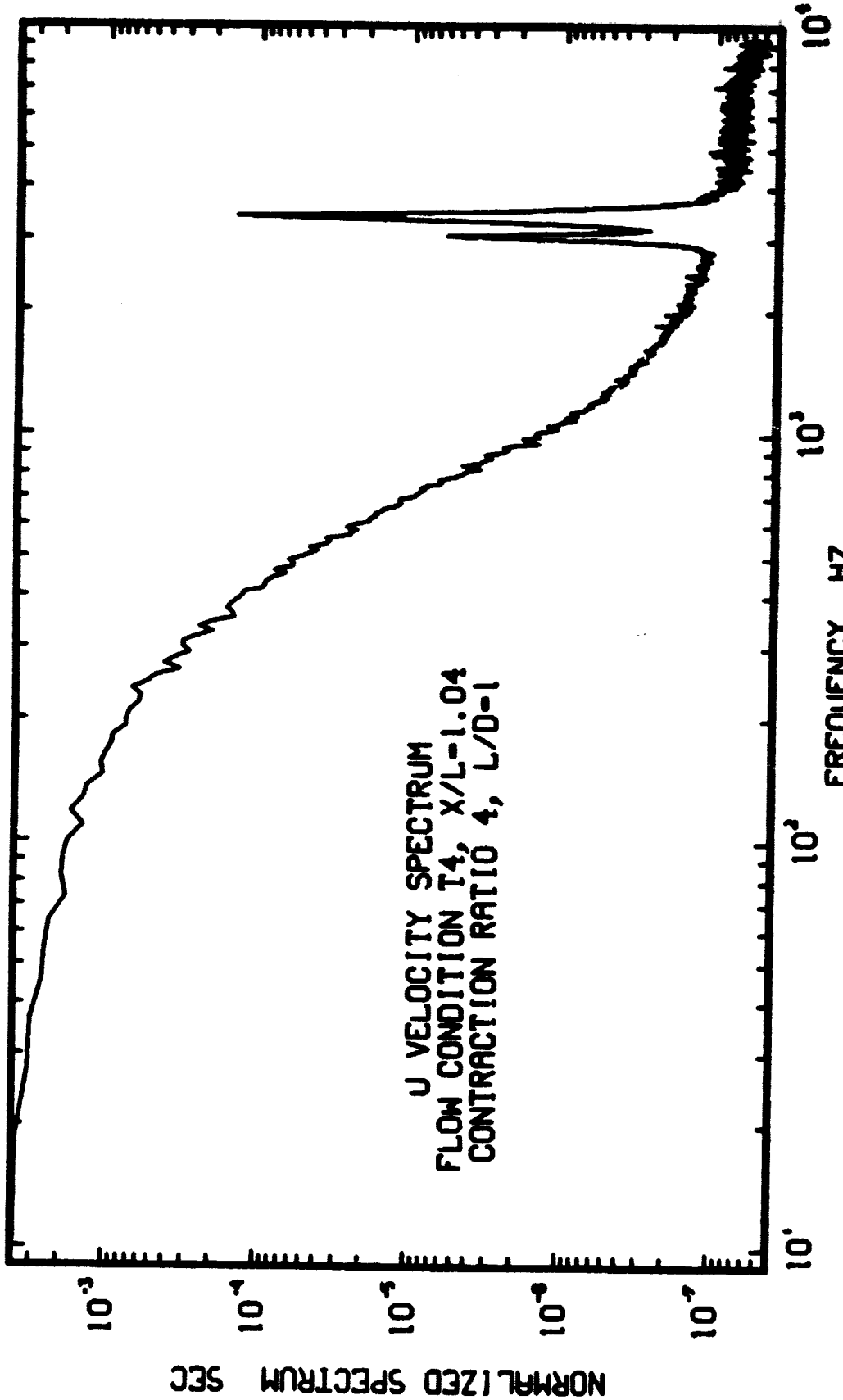

Figure 144. Normalized Streamwise-Velocity Spectrum Near Exit of a Mild Contraction in Flow Condition T4

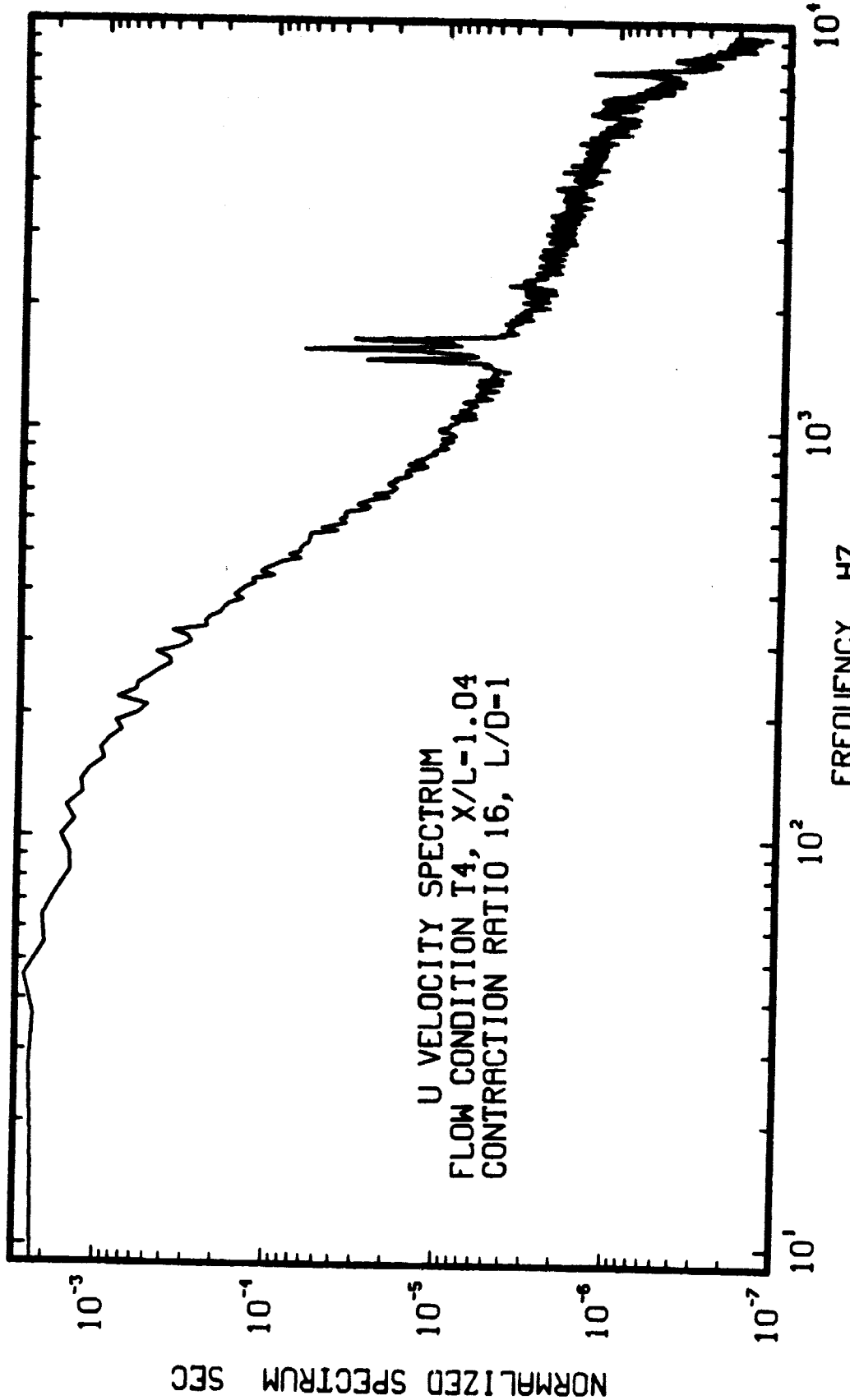

Figure 145. Normalized Streamwise-Velocity Spectrum Near Exit of a High Contraction in Flow Condition T4

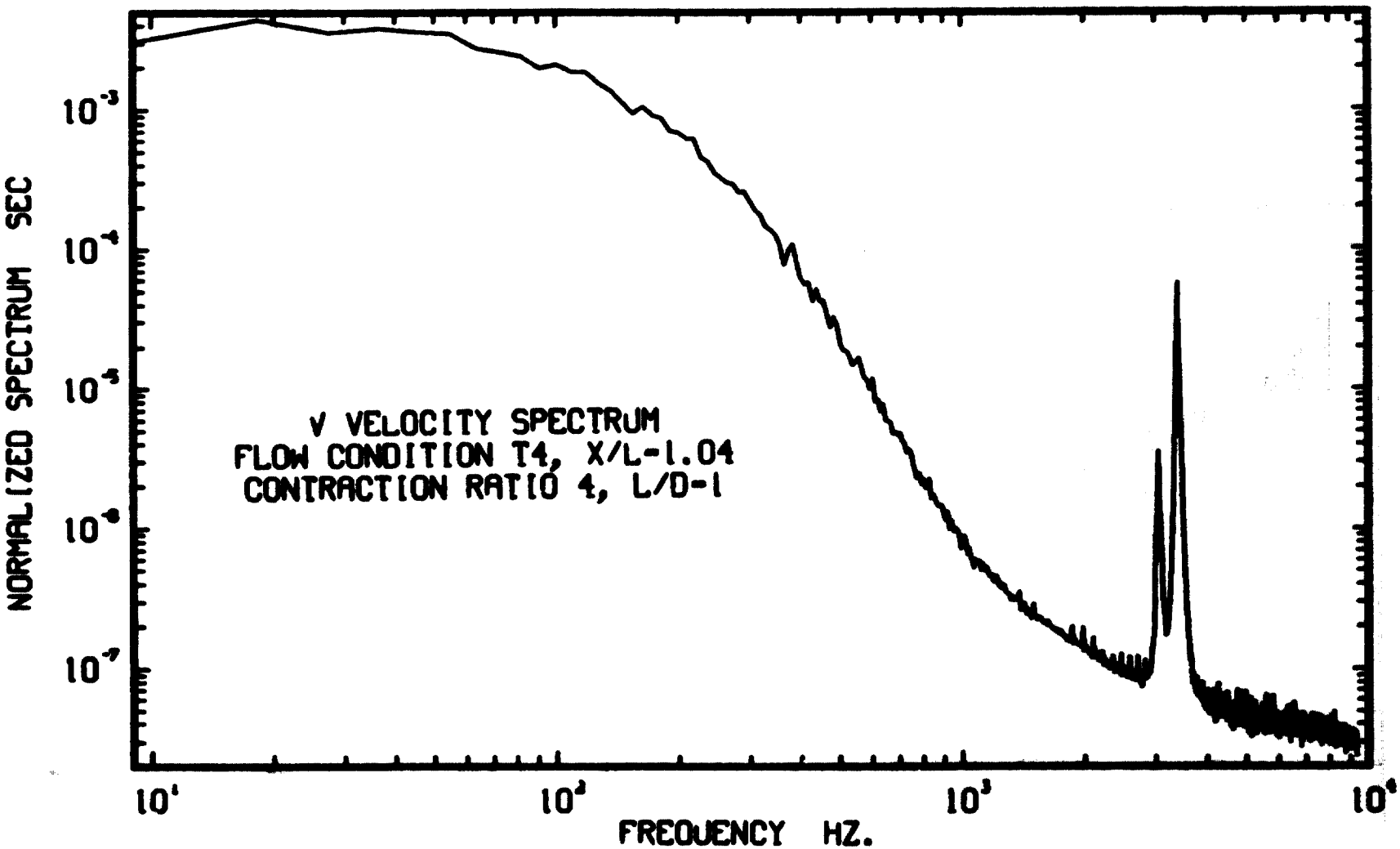

Figure 146. Normalized Radial-Velocity Spectrum Near Exit of a Mild Contraction in Flow Condition T4

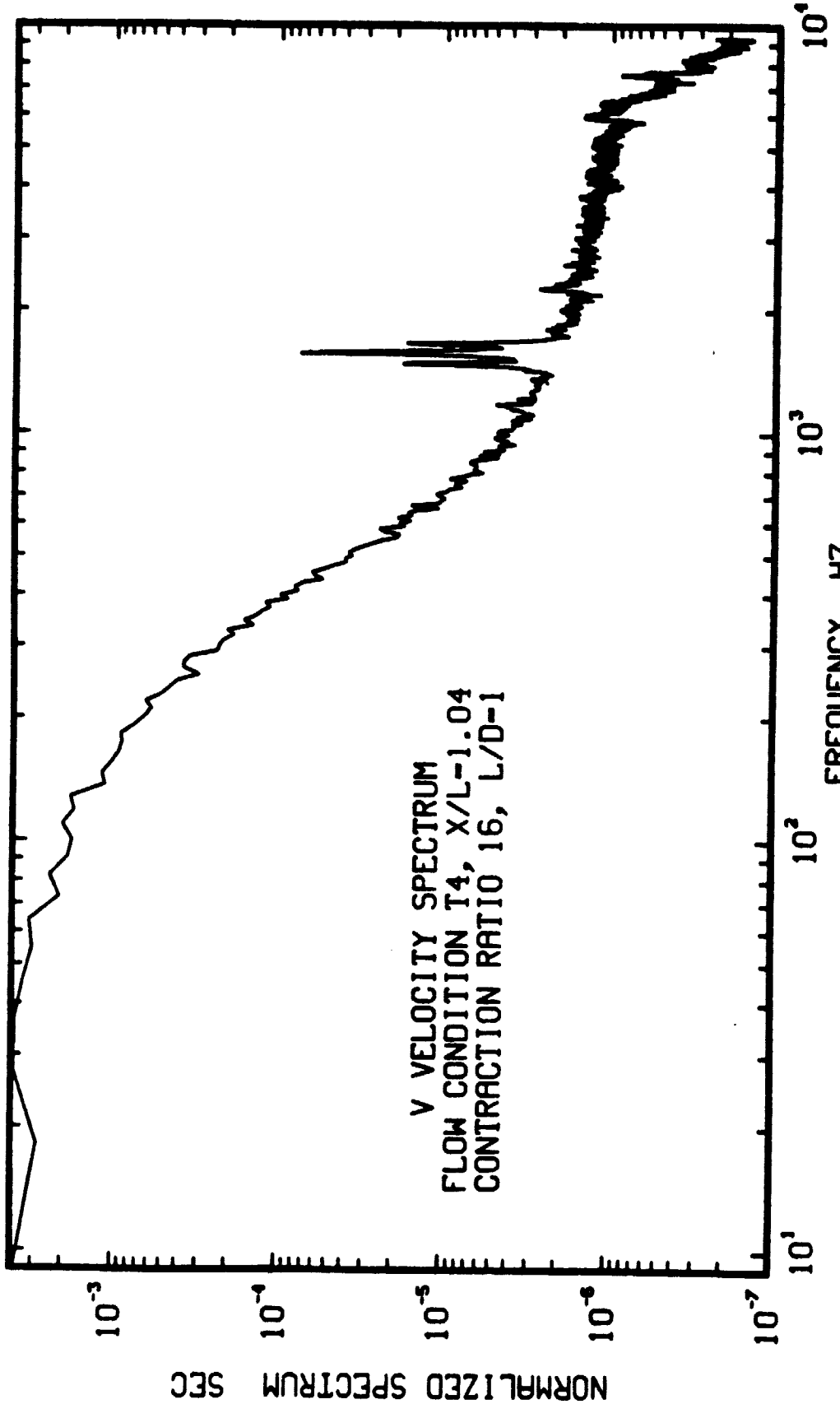

Figure 147. Normalized Radial-Velocity Spectrum Near Exit of a High Contraction in Flow Condition T4

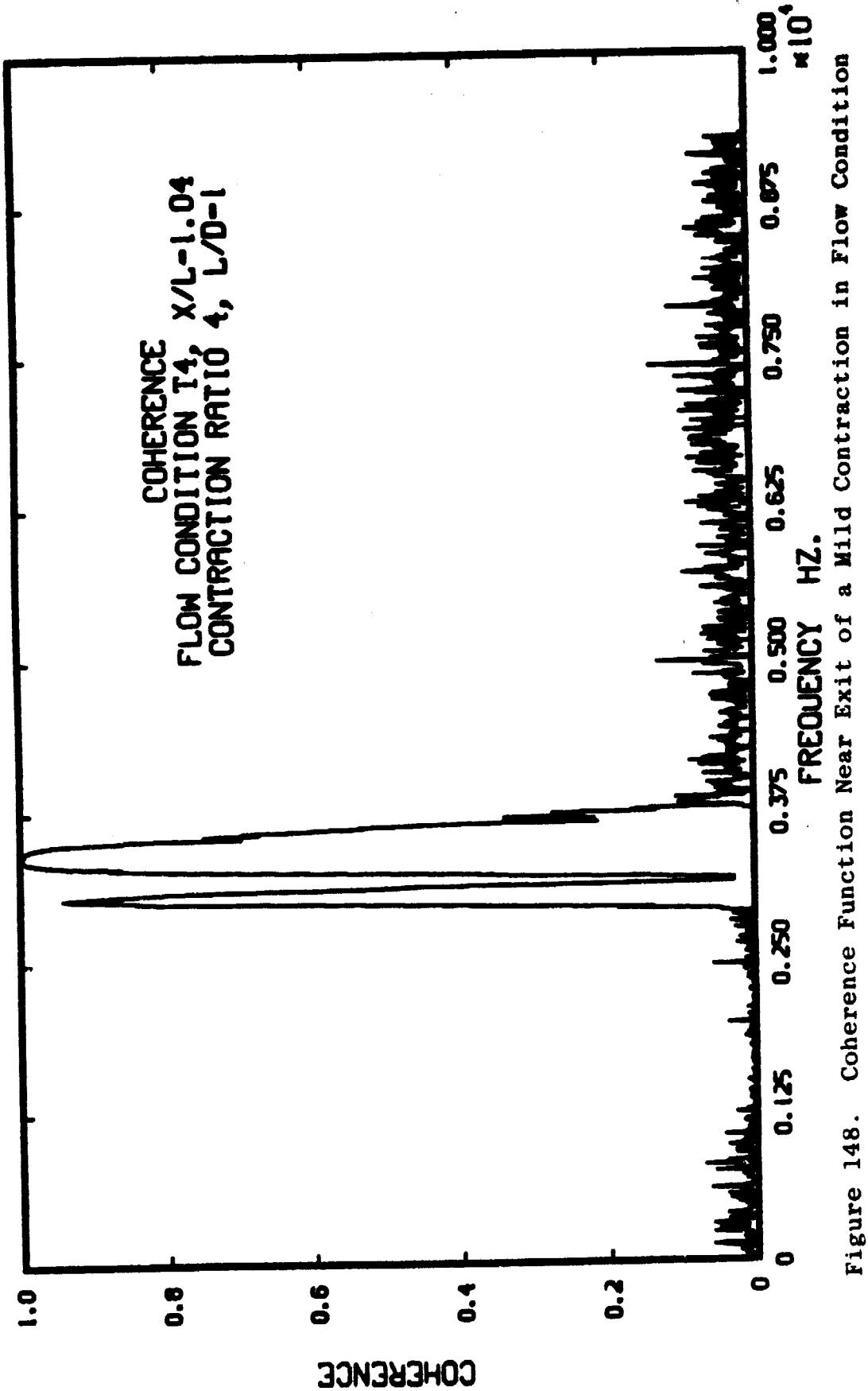

Figure 148. Coherence Function Near Exit of a Mild Contraction in Flow Condition T4

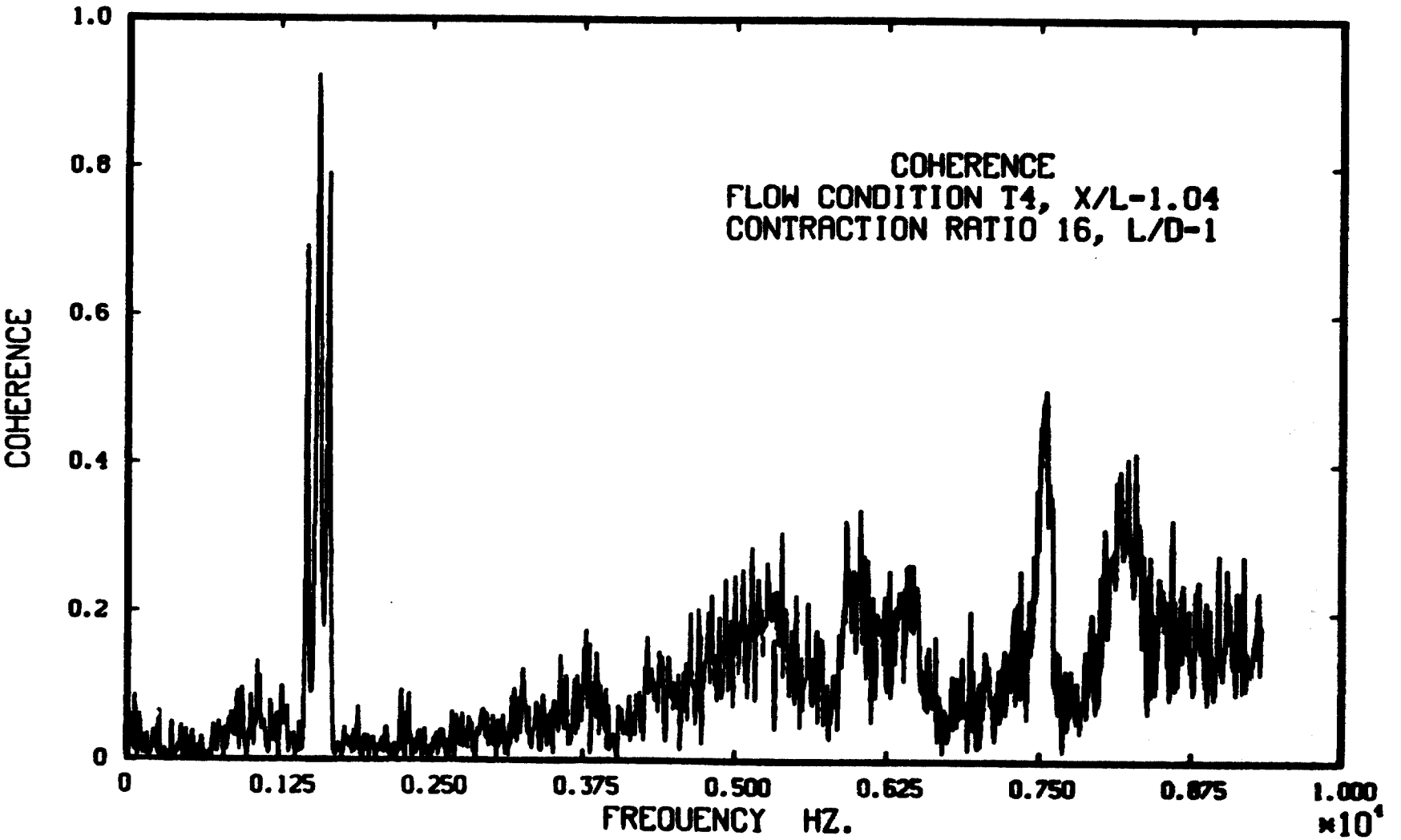

Figure 149. Coherence Function Near Exit of a High Contraction in Flow Condition T4

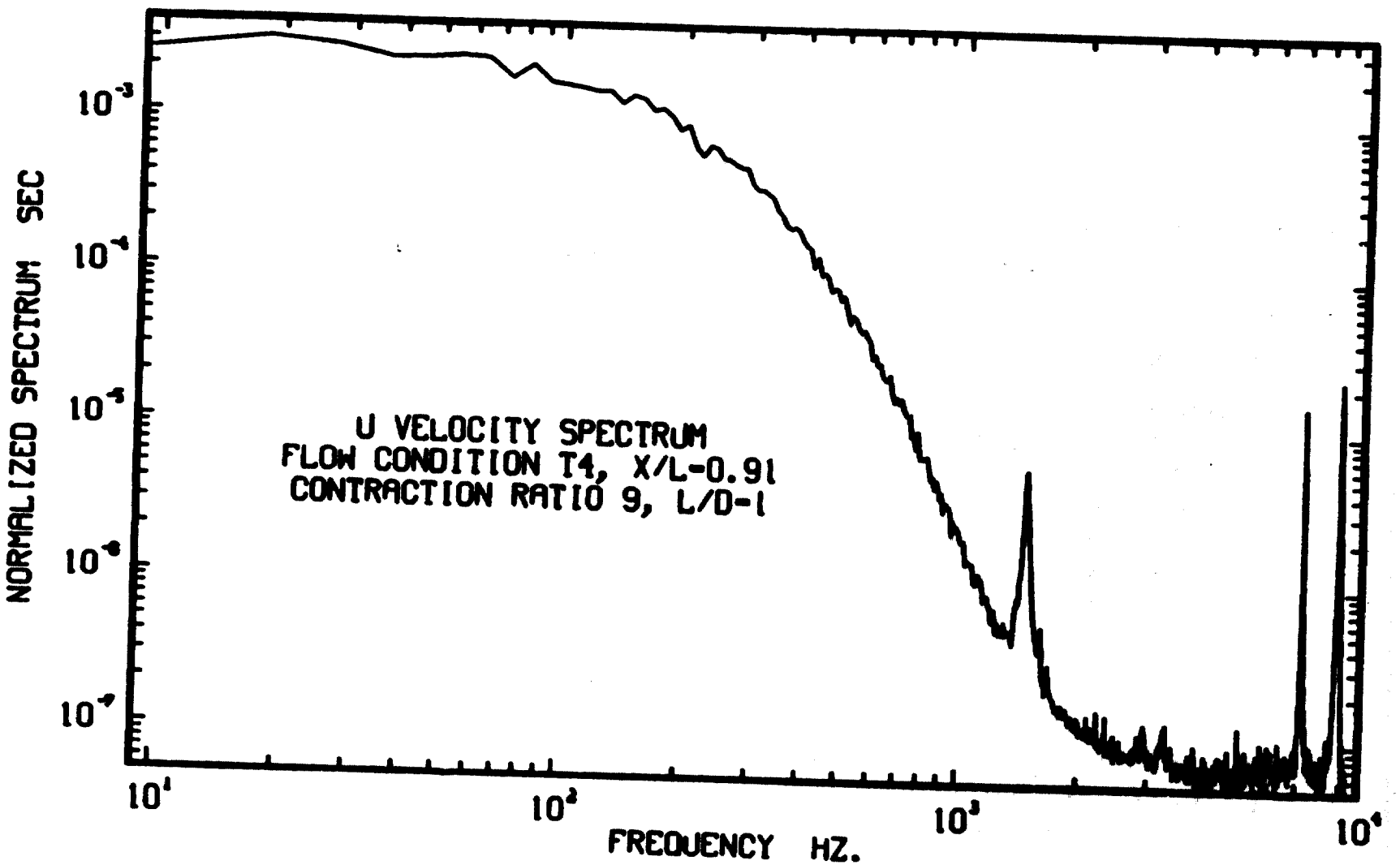

Figure 150. Normalized On-Axis Streamwise-Velocity Spectrum Before Exit of a Moderate Contraction in Flow Condition T4

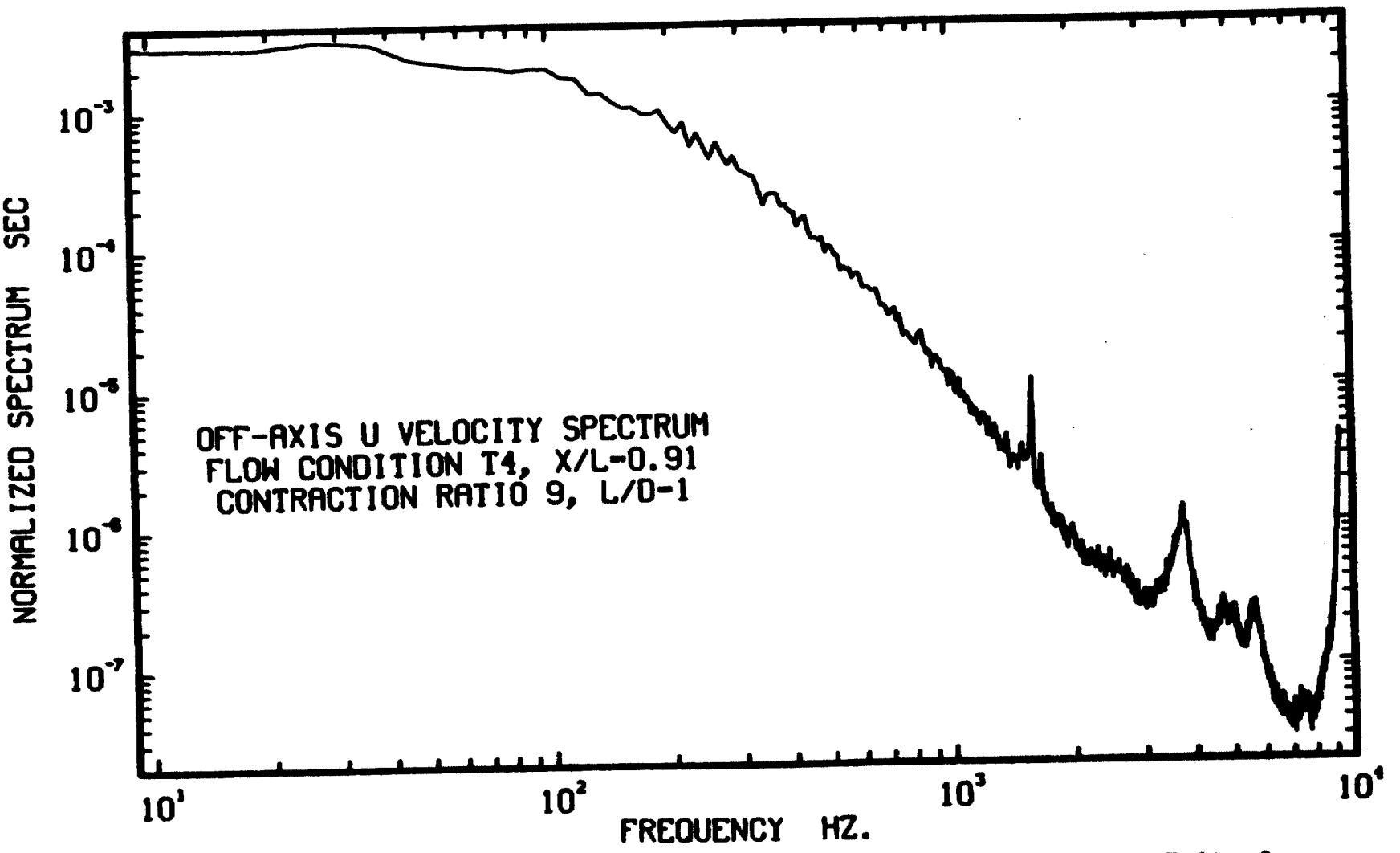

Figure 151. Normalized Off-Axis Streamwise-Velocity Spectrum Before Exit of a Moderate Contraction in Flow Condition T4

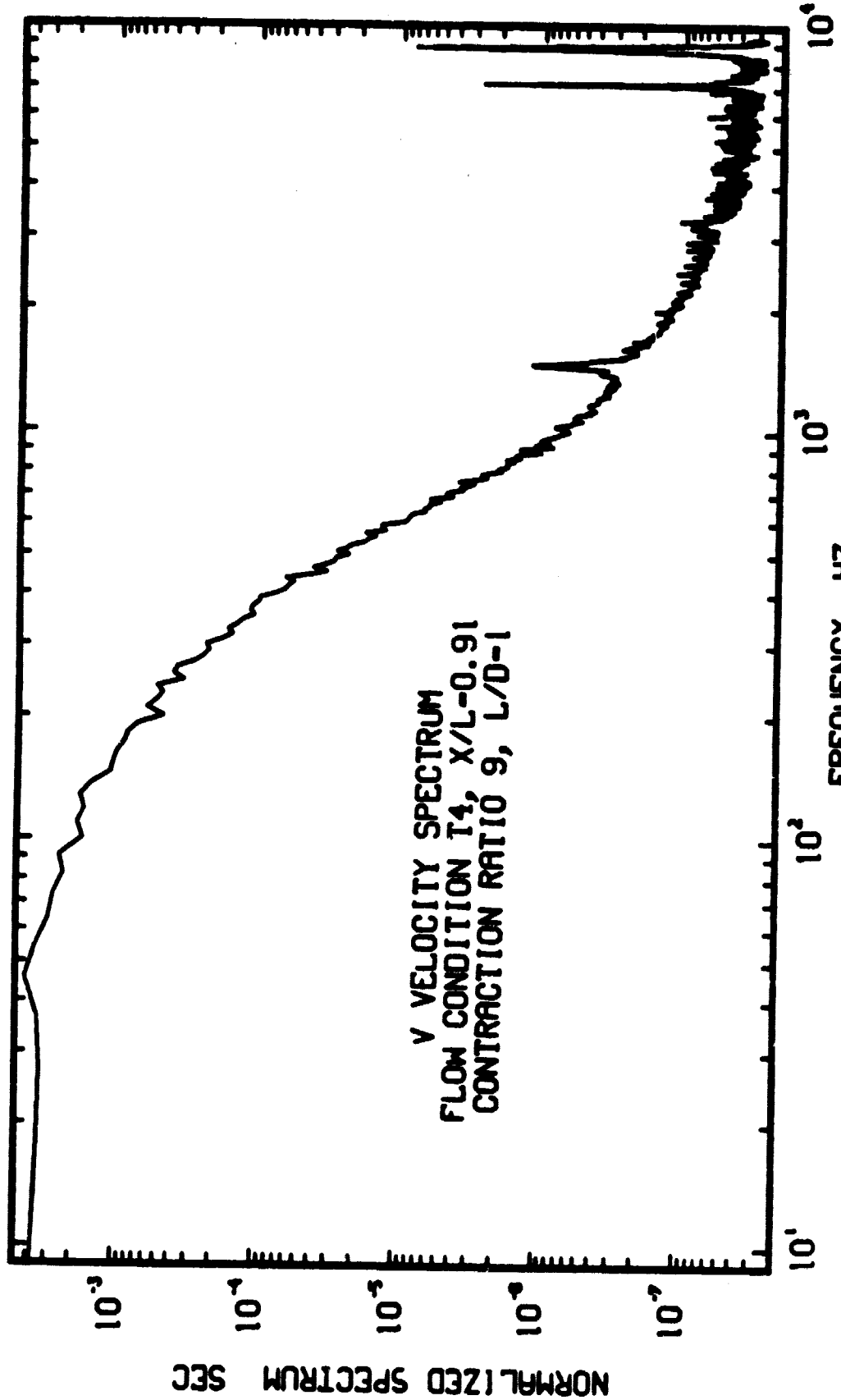

Figure 152. Normalized On-Axis Radial-Velocity Spectrum Before Exit of a Moderate Contraction in Flow Condition T4

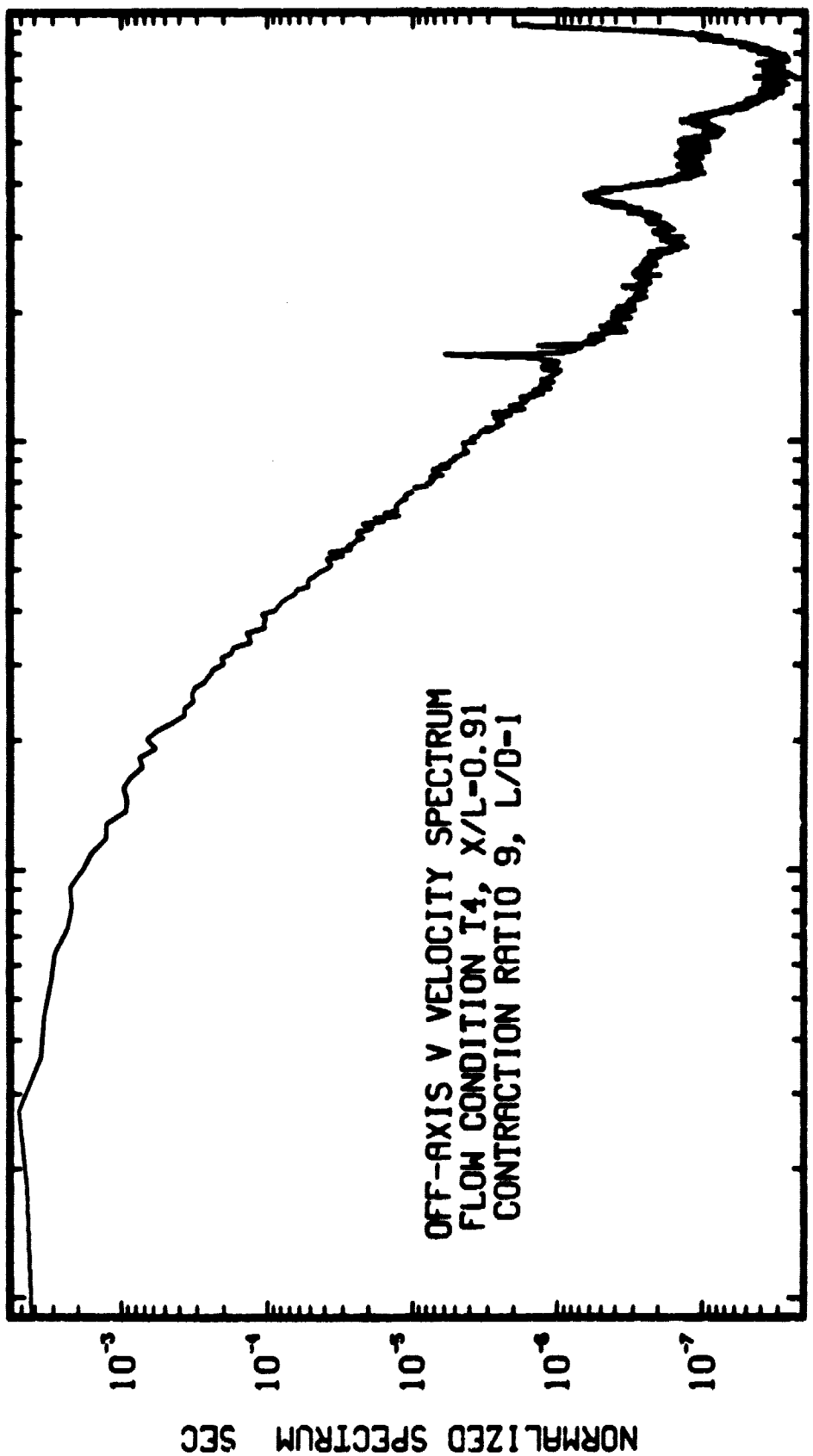

Figure 153. Normalized Off-Axis Radial-Velocity Spectrum Before Exit of a Moderate Contraction in Flow Condition T4

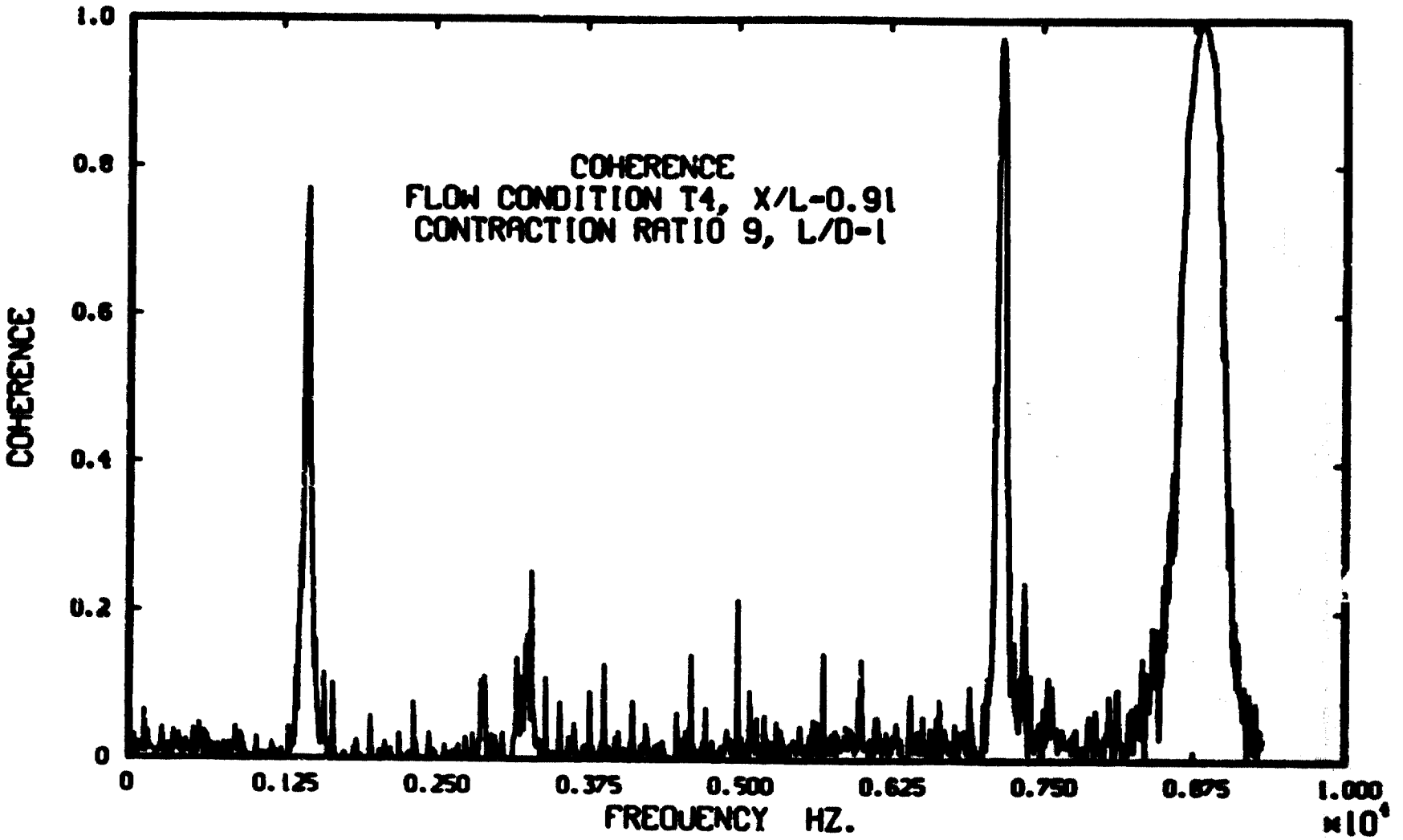

Figure 154. On-Axis Coherence Function Before Exit of a Moderate Contraction in Flow Condition T4

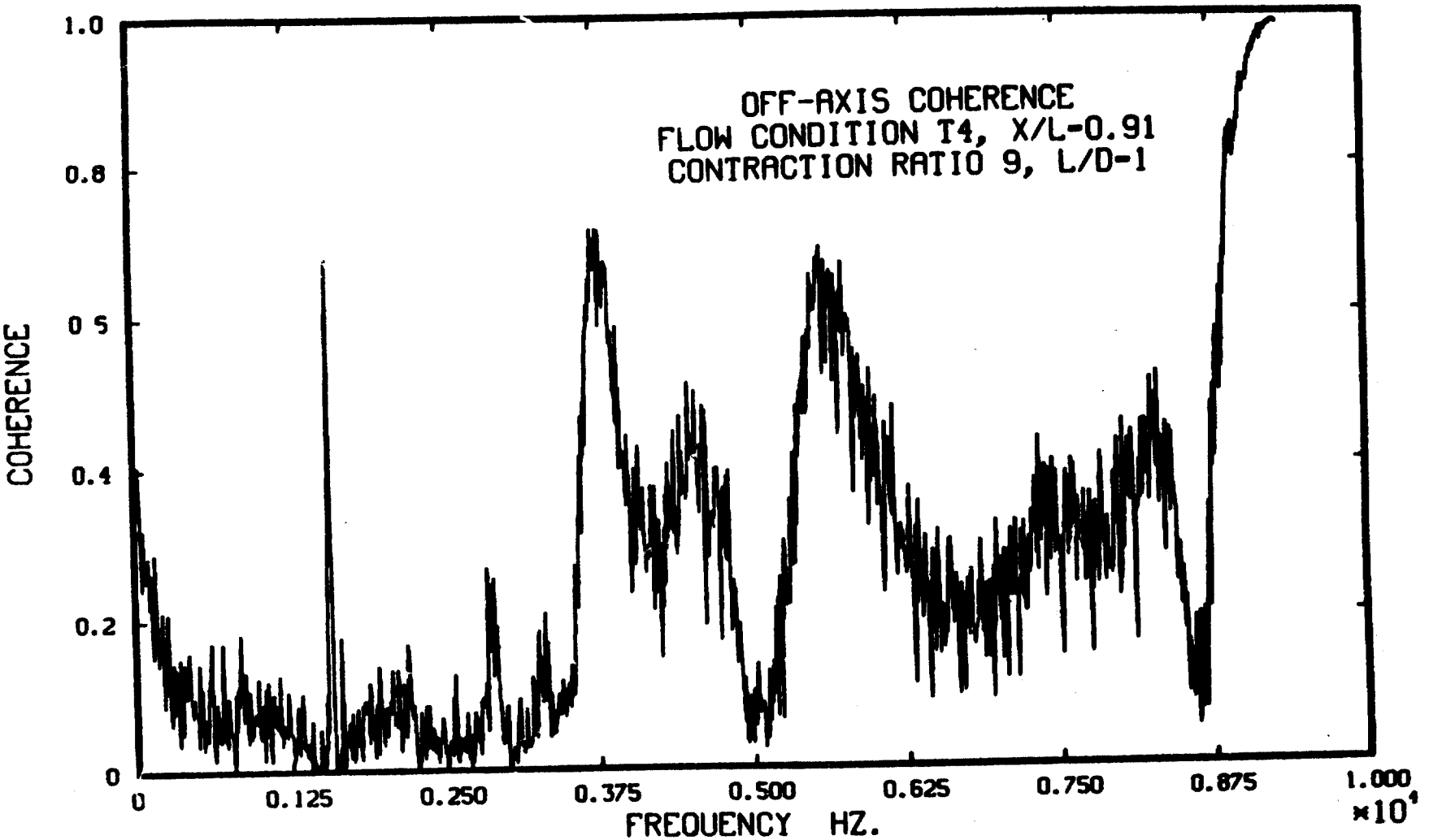

Figure 155. Off-Axis Coherence Function Before Exit of a Moderate Contraction in Flow Condition T4

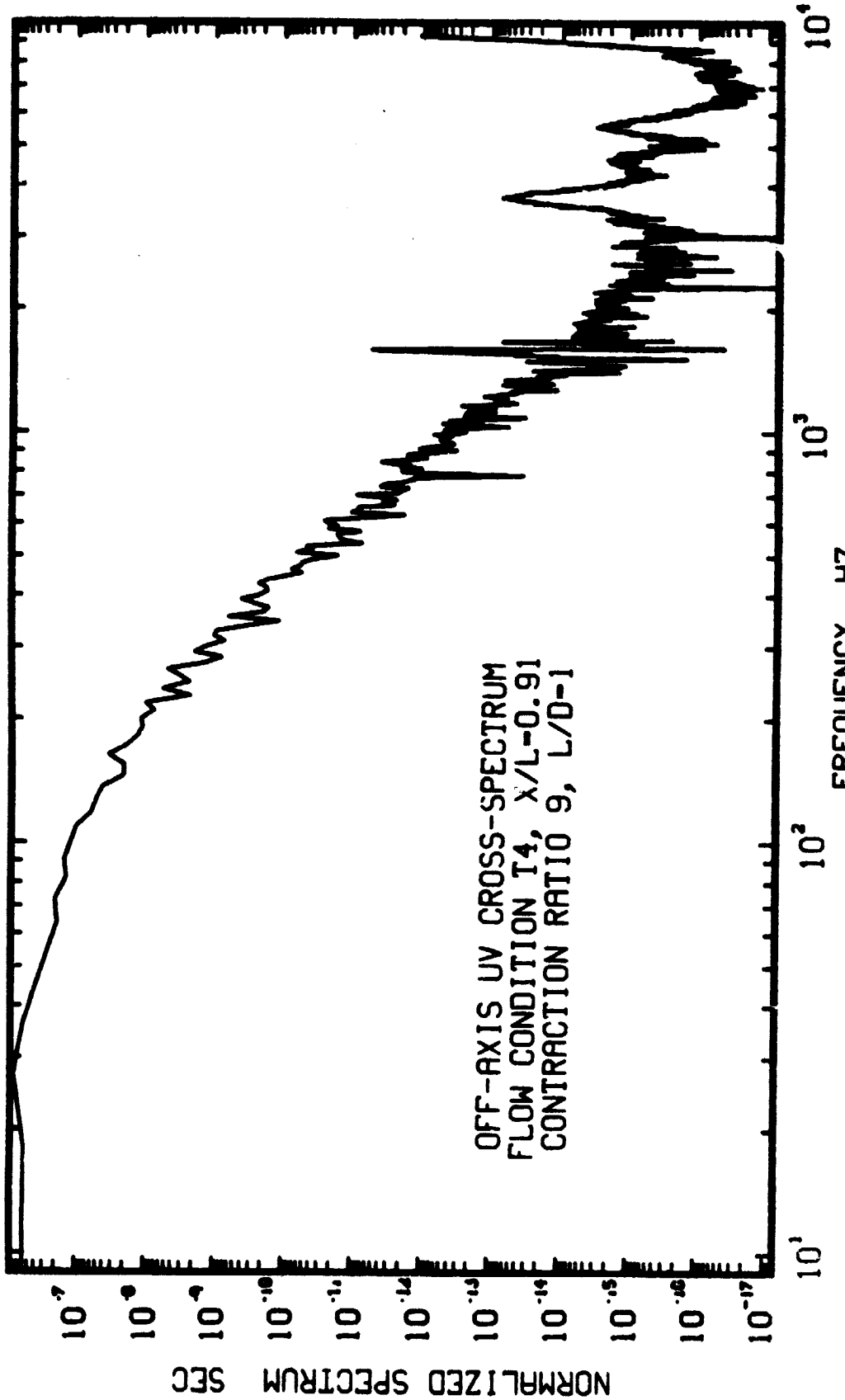

Figure 156. Normalized Off-Axis Cross-Spectrum Before Exit of a Moderate Contraction in Flow Condition T4

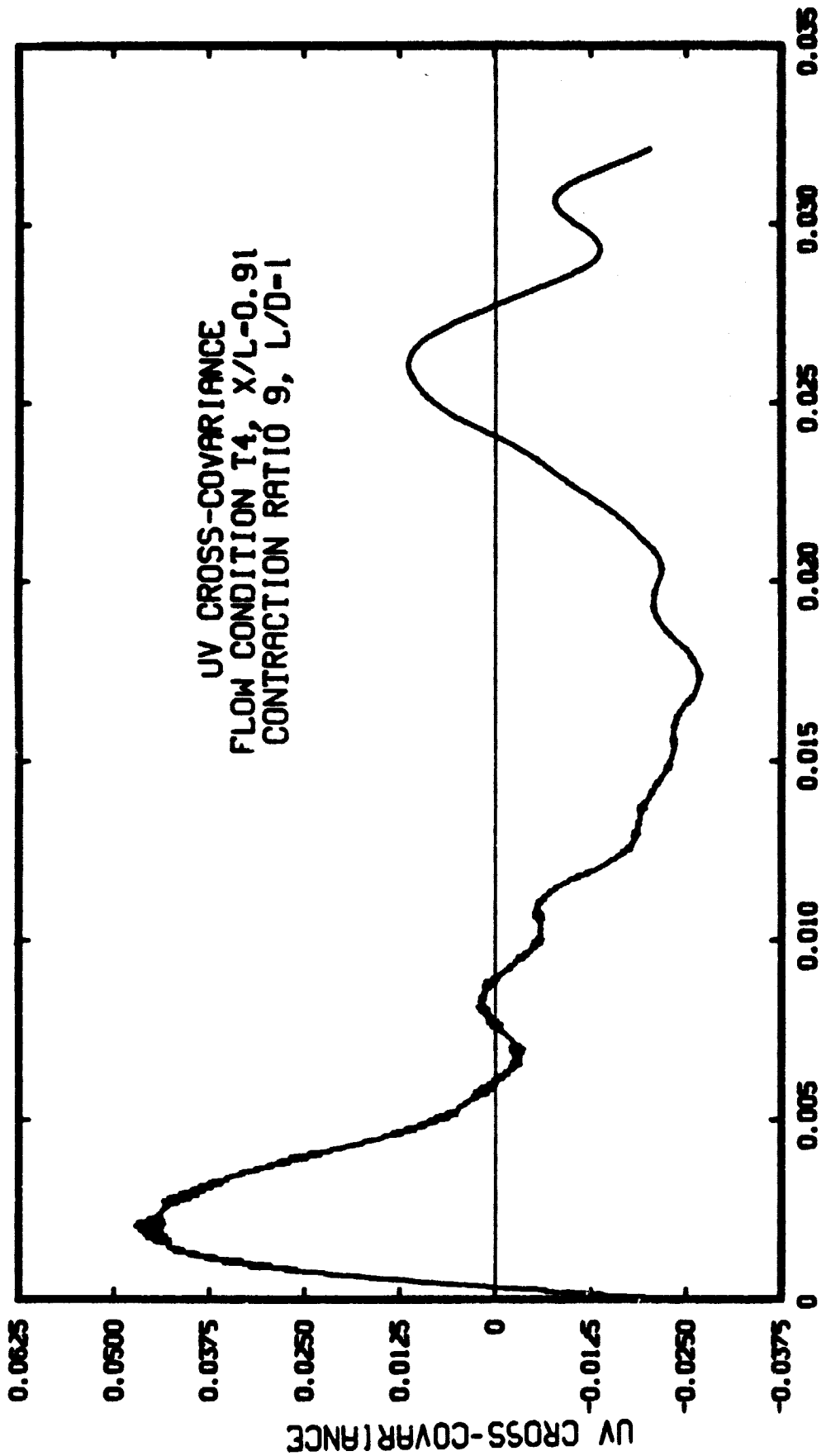

Figure 157. On-Axis Cross-Covariance Function Before Exit of a Moderate Contraction in Flow Condition T4

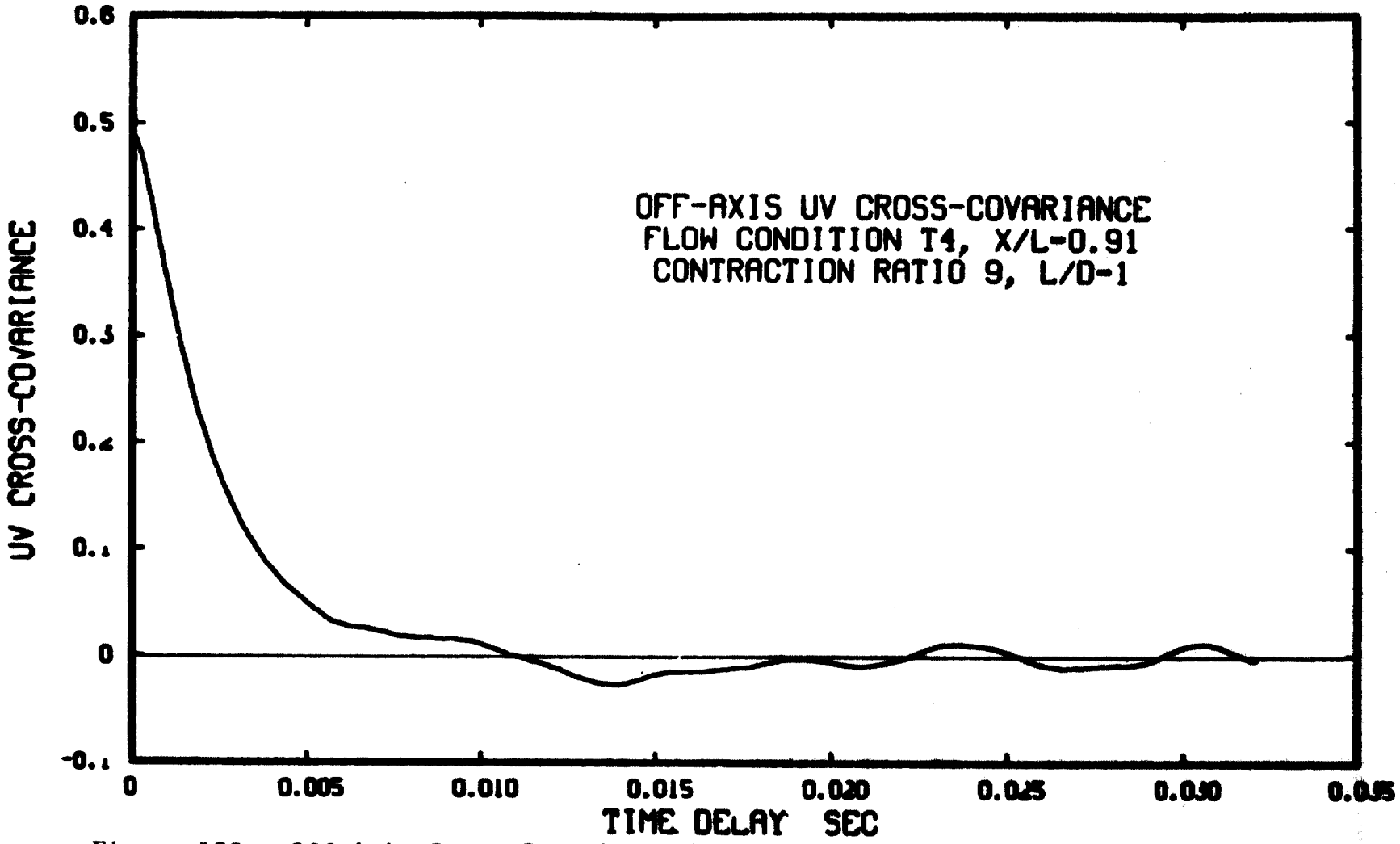

Figure 158. Off-Axis Cross-Covariance Function Before Exit of a Moderate Contraction in Flow Condition T4

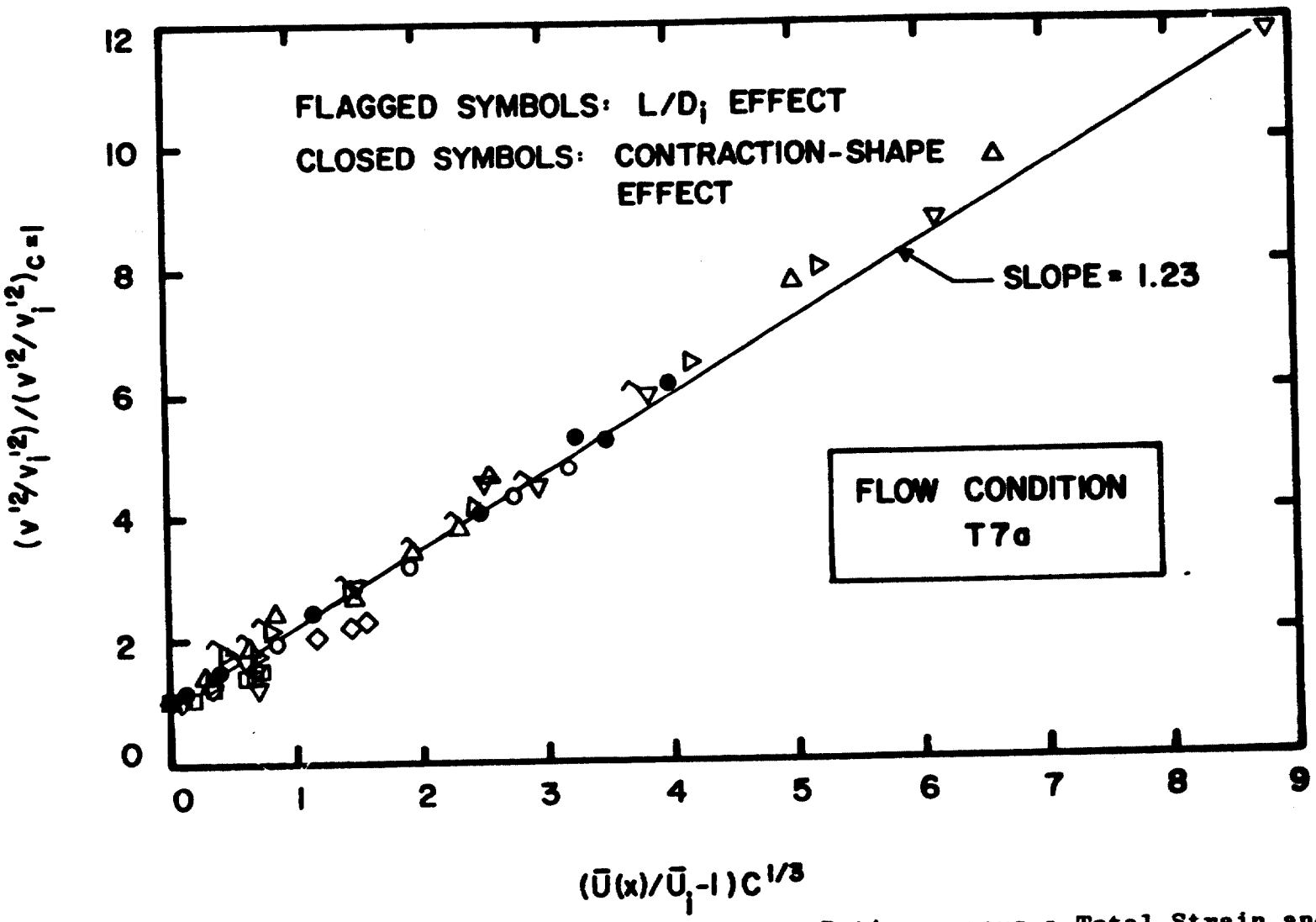

Figure 159. Corrected Radial Turbulence Energy Ratios versus a Total Strain and Contraction Parameter for Different Contractions in Flow Condition T7a

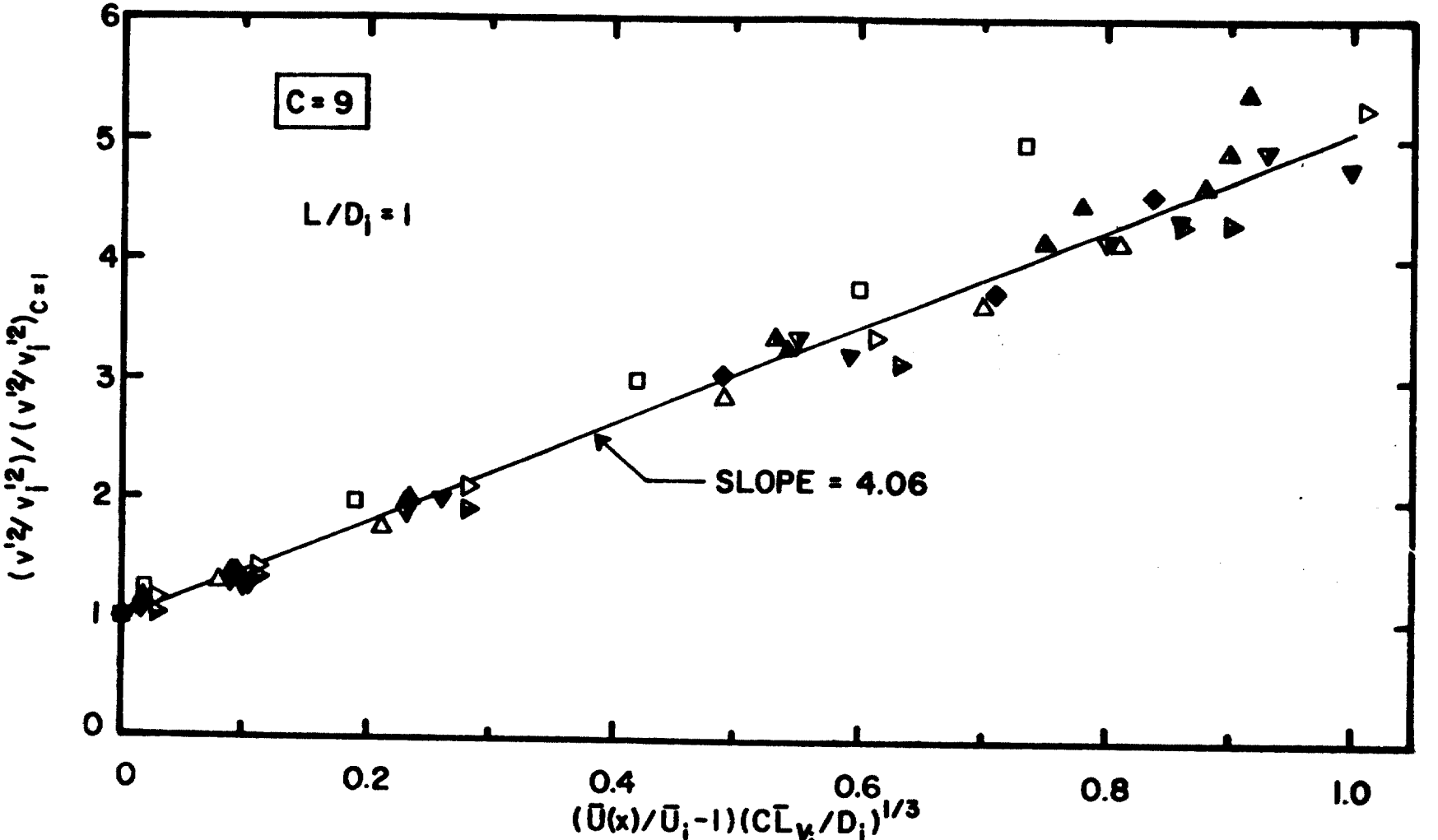

Figure 160. Corrected Radial Turbulence Energy Ratios versus a Total Strain, Contraction, and Turbulence-Scale Parameter for a Moderate Contraction in All Flow Conditions

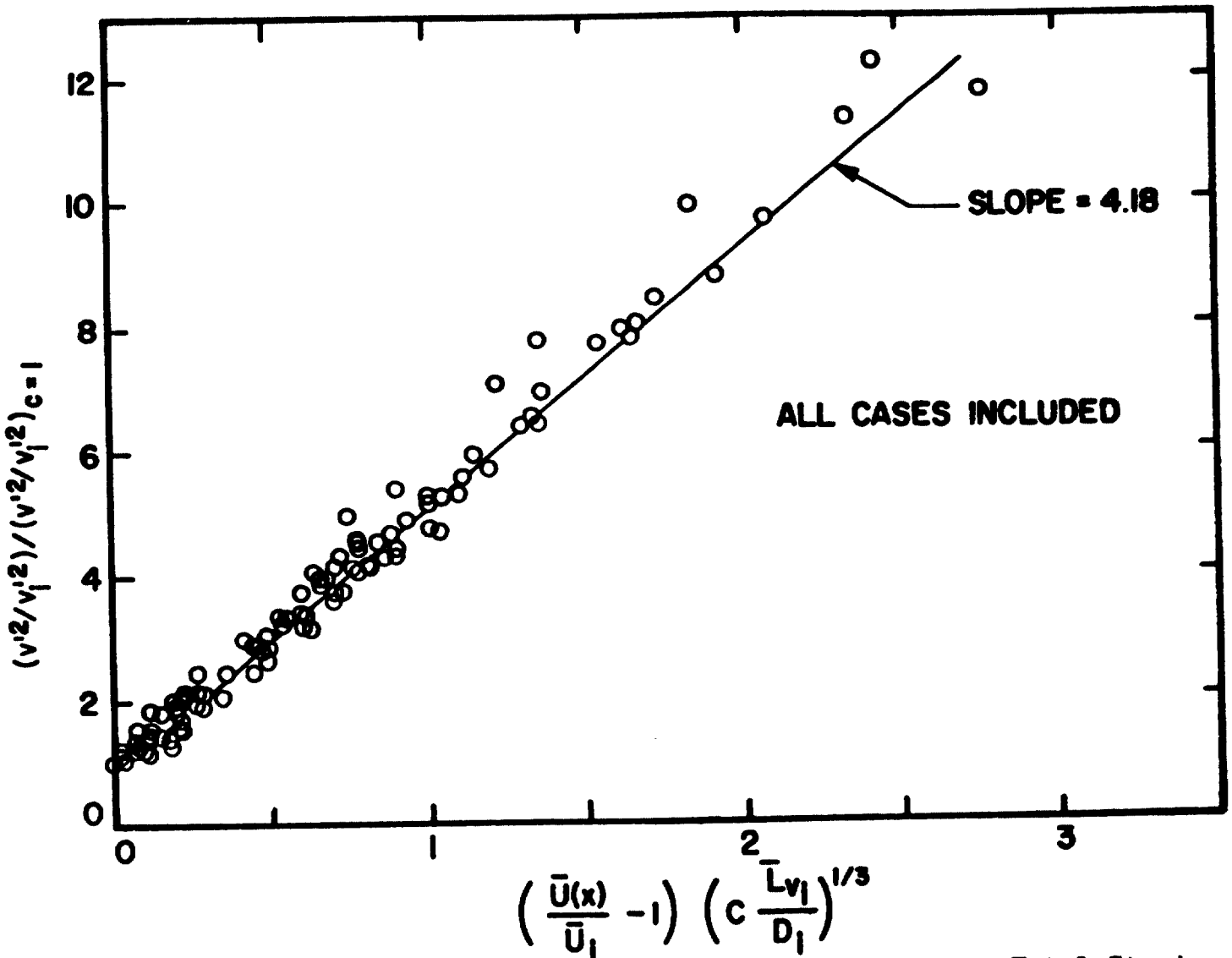

Figure 161. Corrected Radial Turbulence Energy Ratios versus a Total Strain, Contraction, and Turbulence-Scale Parameter for All Contractions in All Flow Conditions

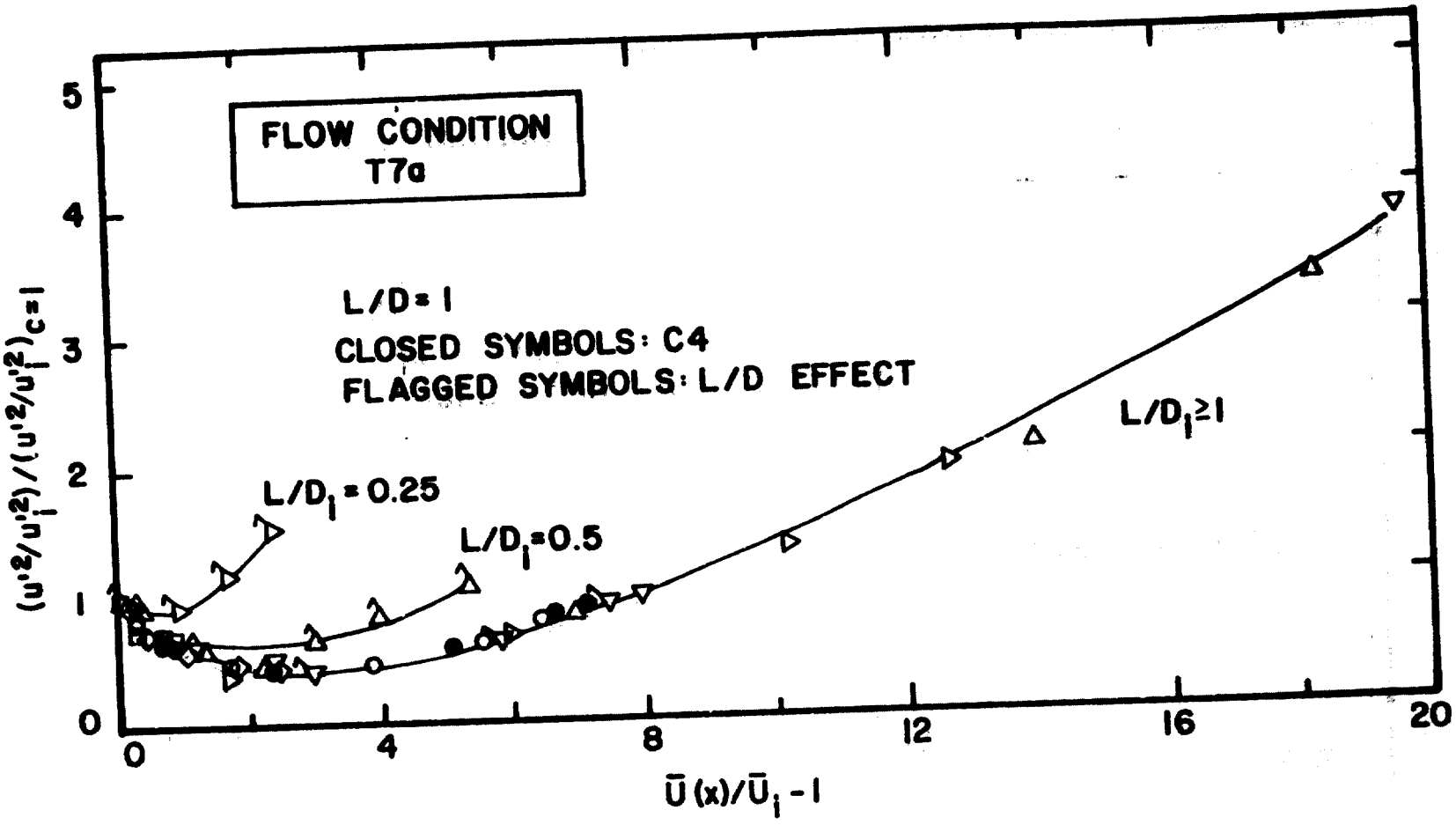

Figure 162. Corrected Streamwise Turbulence Energy Ratios versus Total Strain Parameter for All Contractions in Flow Condition T7a

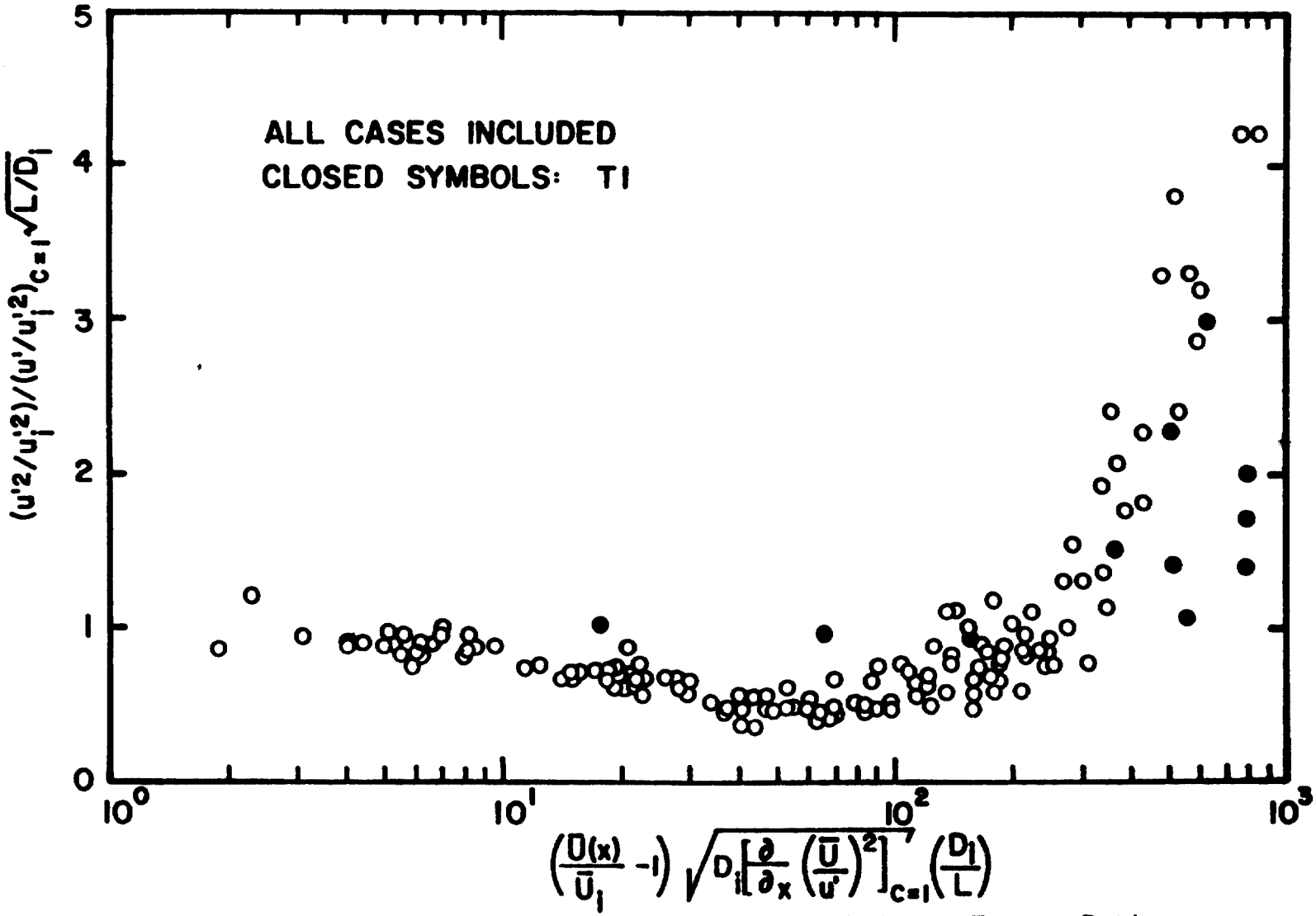

Figure 163. Corrected and Weighted Streamwise Turbulence Energy Ratios versus a Total Strain and Turbulence-Scale Parameter, Corrected for Precontraction Strain, for All Contractions in All Flow Conditions

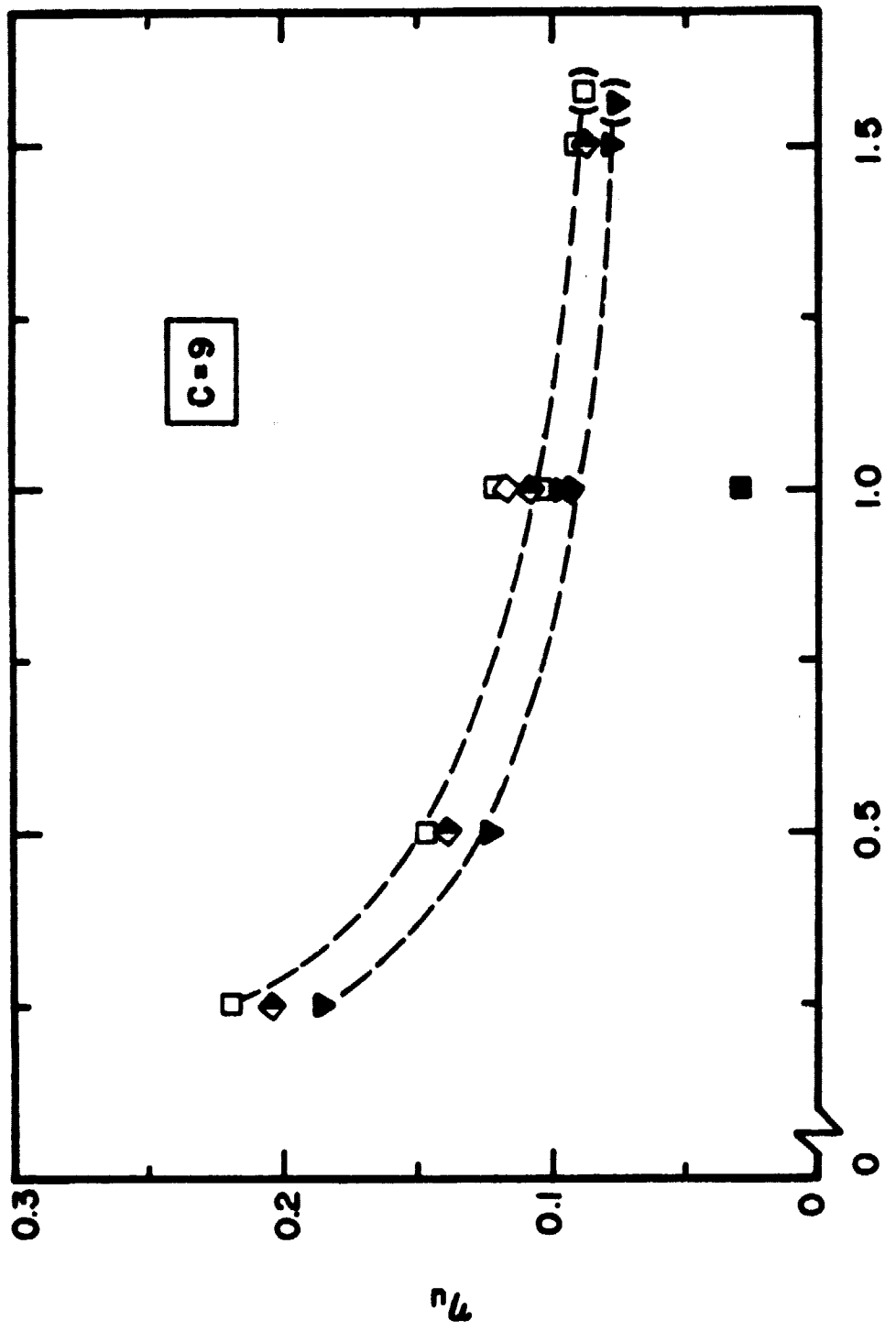

Figure 164. Streamwise Turbulence Intensity Reduction Efficiency for Different L/D Ratios

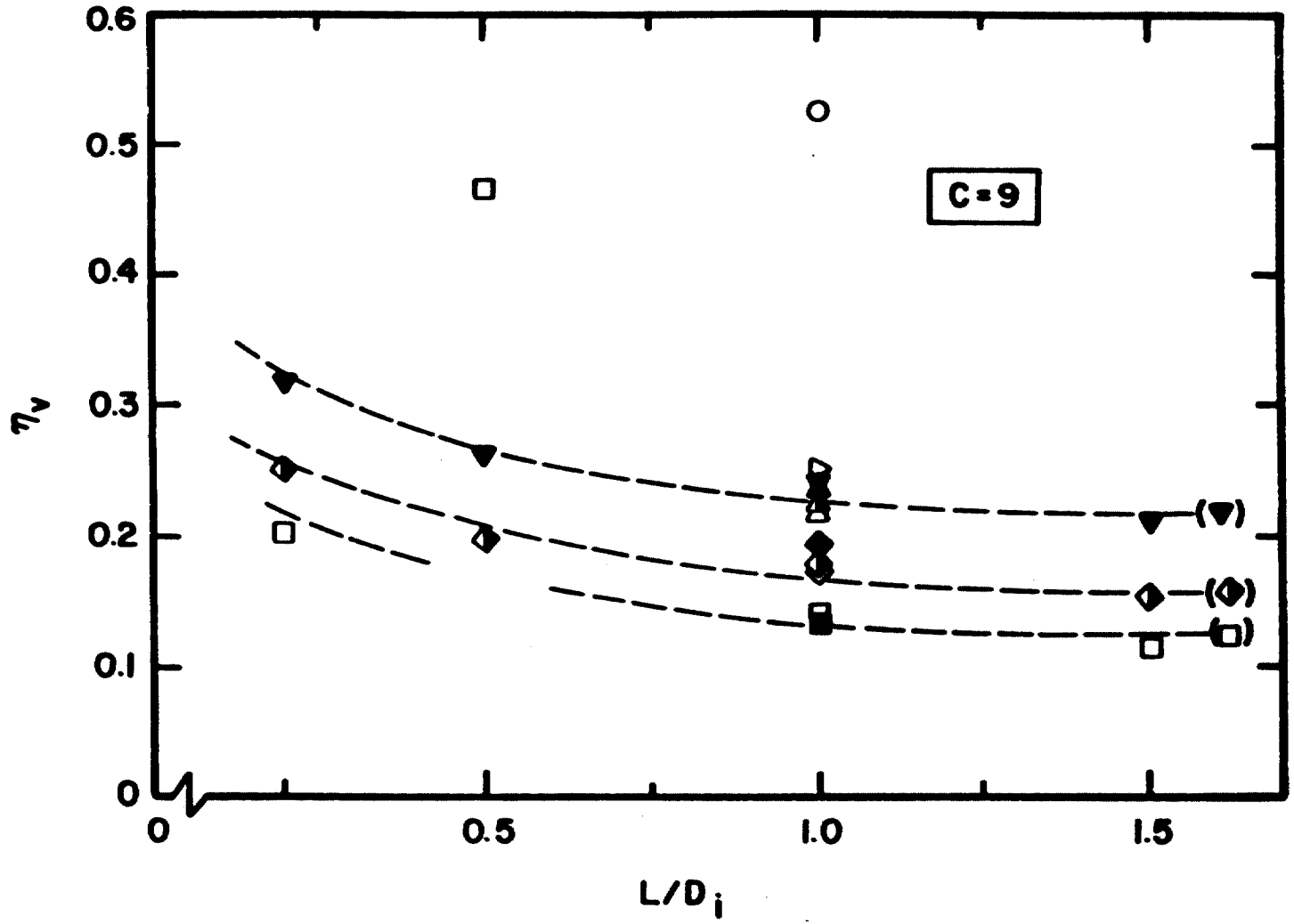

Figure 165. Radial Turbulence Intensity Reduction Efficiency for Different L/D Ratios

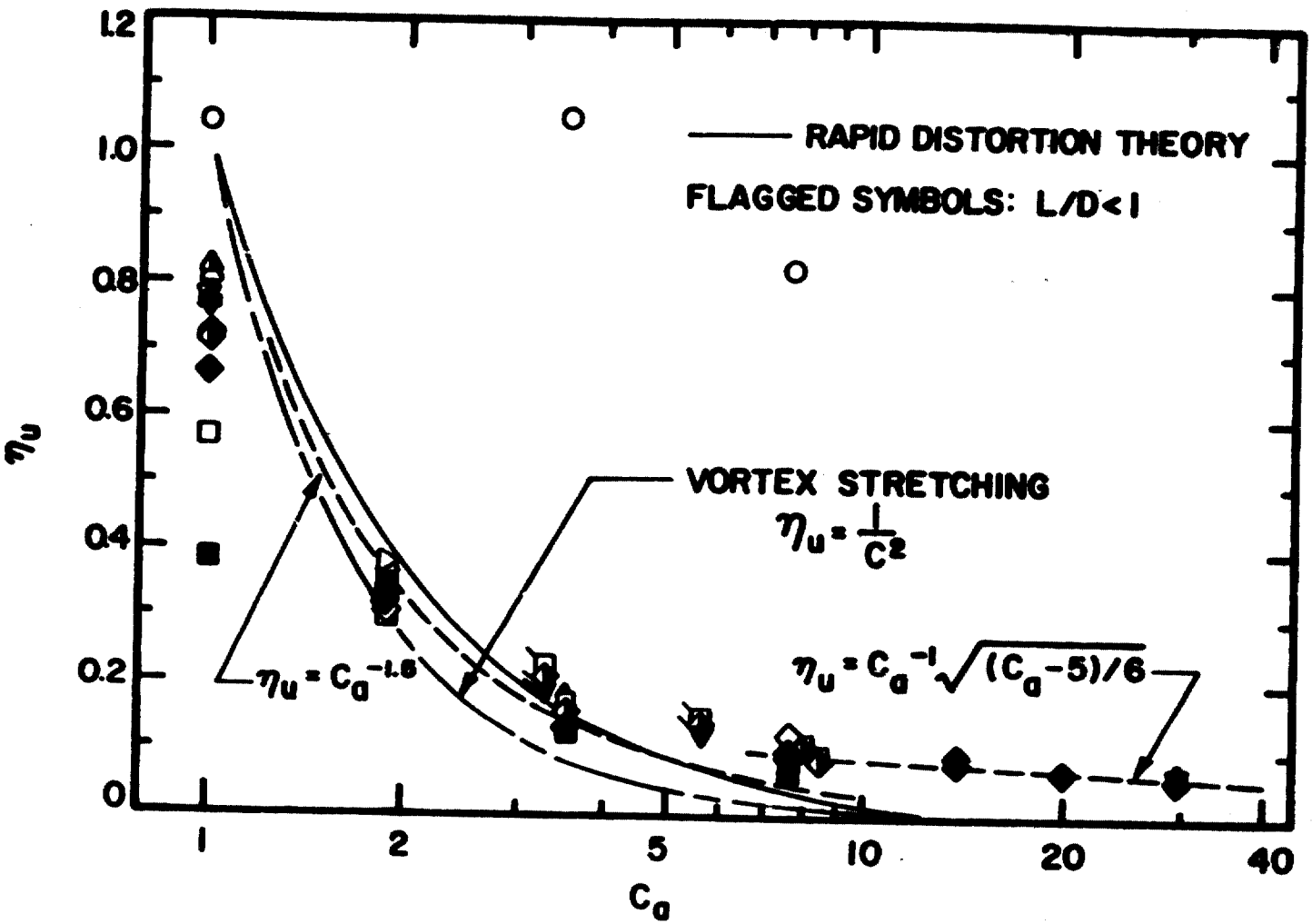

Figure 166. Streamwise Turbulence Intensity Reduction Efficiency for Different Contractions

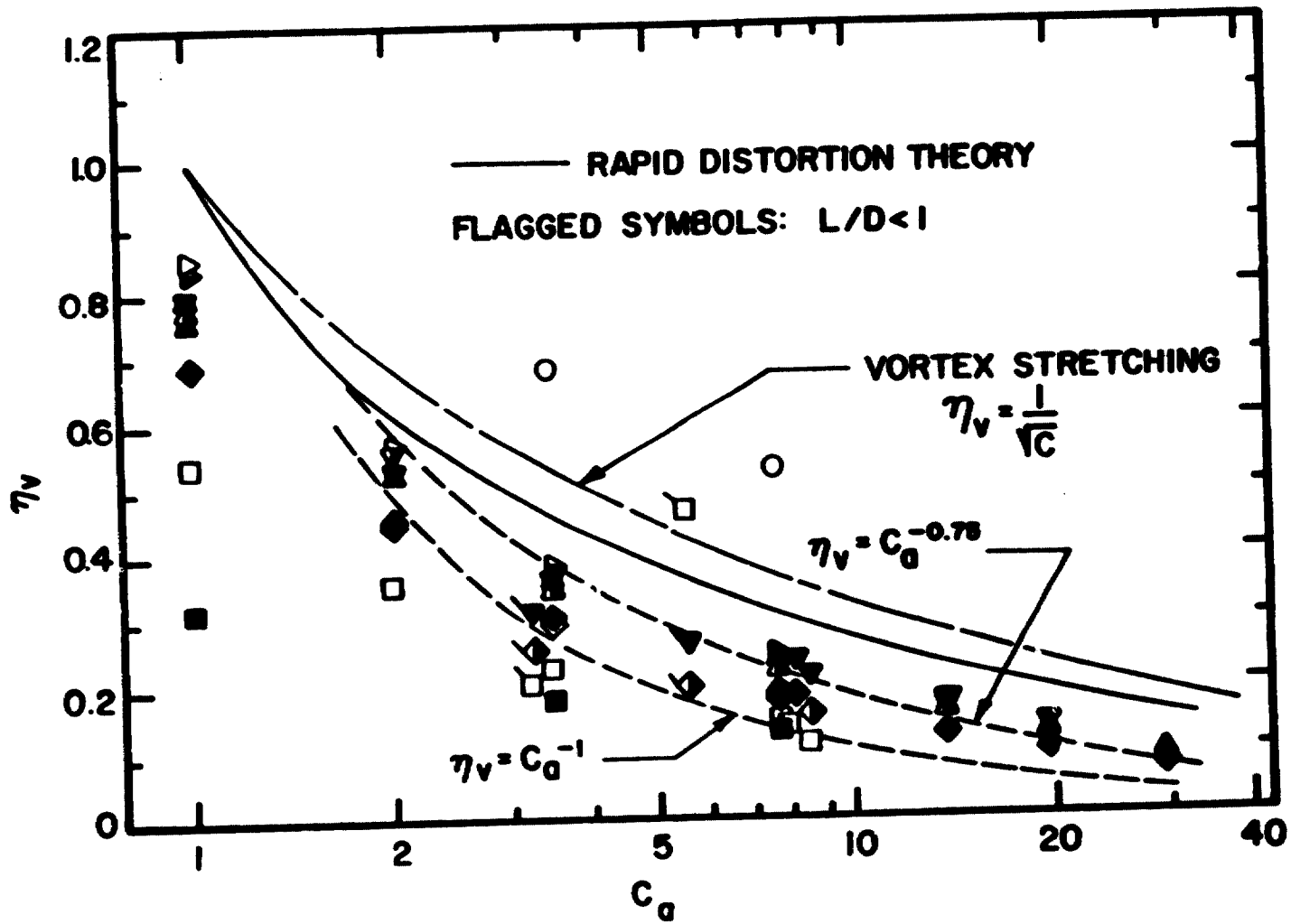

Figure 167. Radial Turbulence Intensity Reduction Efficiency for Different Contractions

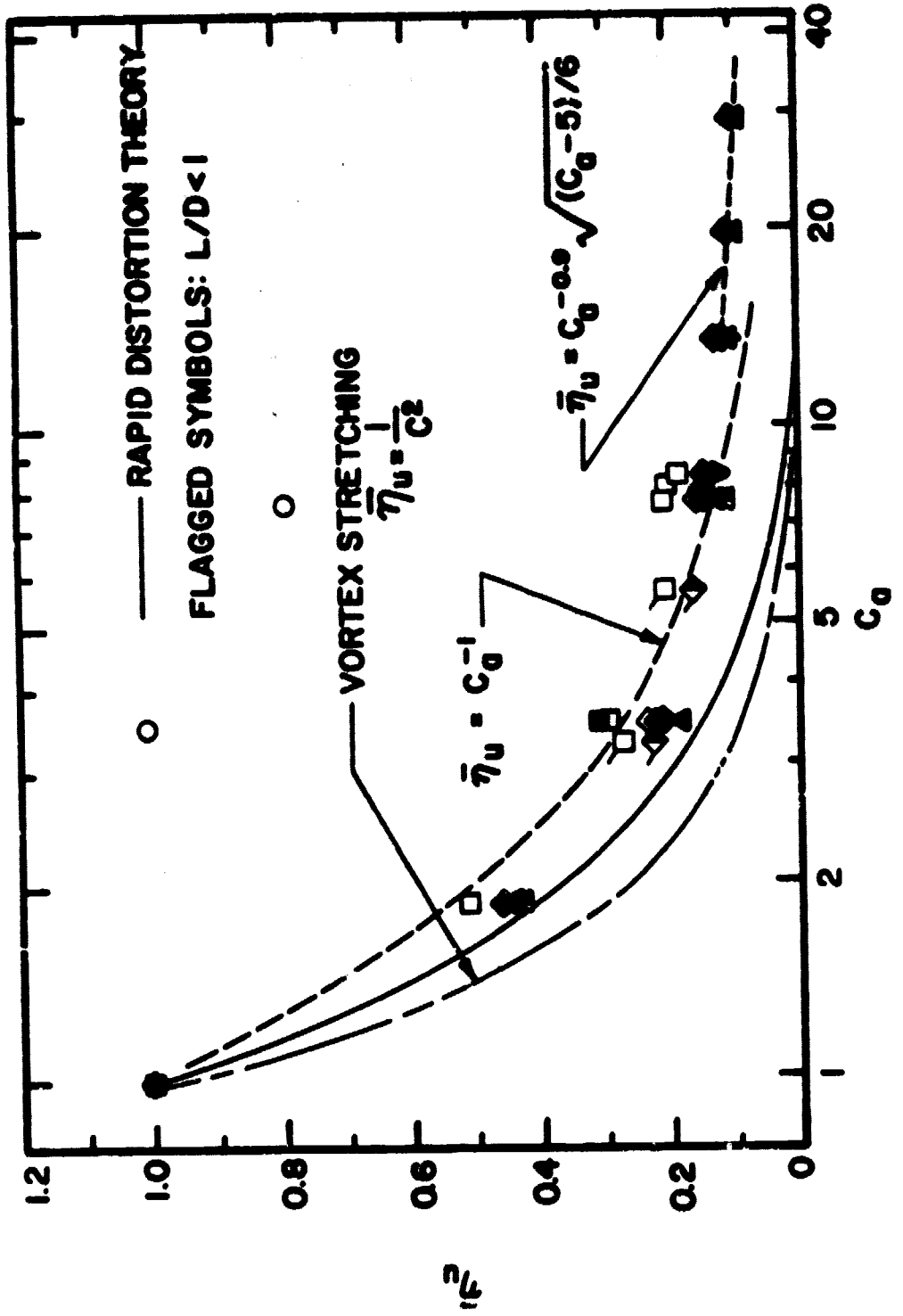

Figure 168. Corrected Streamwise Turbulence Intensity Reduction Efficiency for Different Contractions

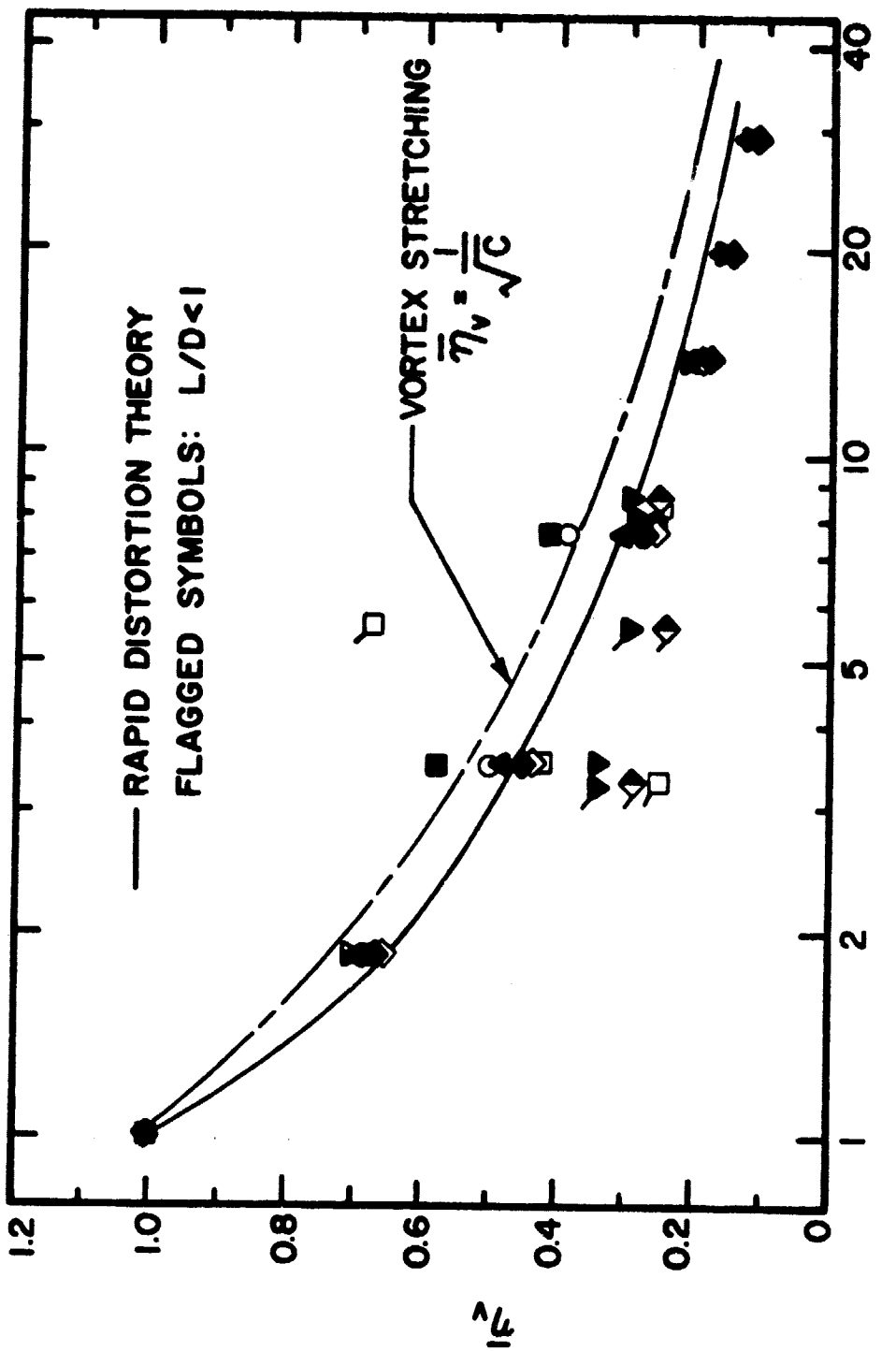

Figure 169. Corrected Radial Turbulence Intensity Reduction Efficiency for Different Contractions

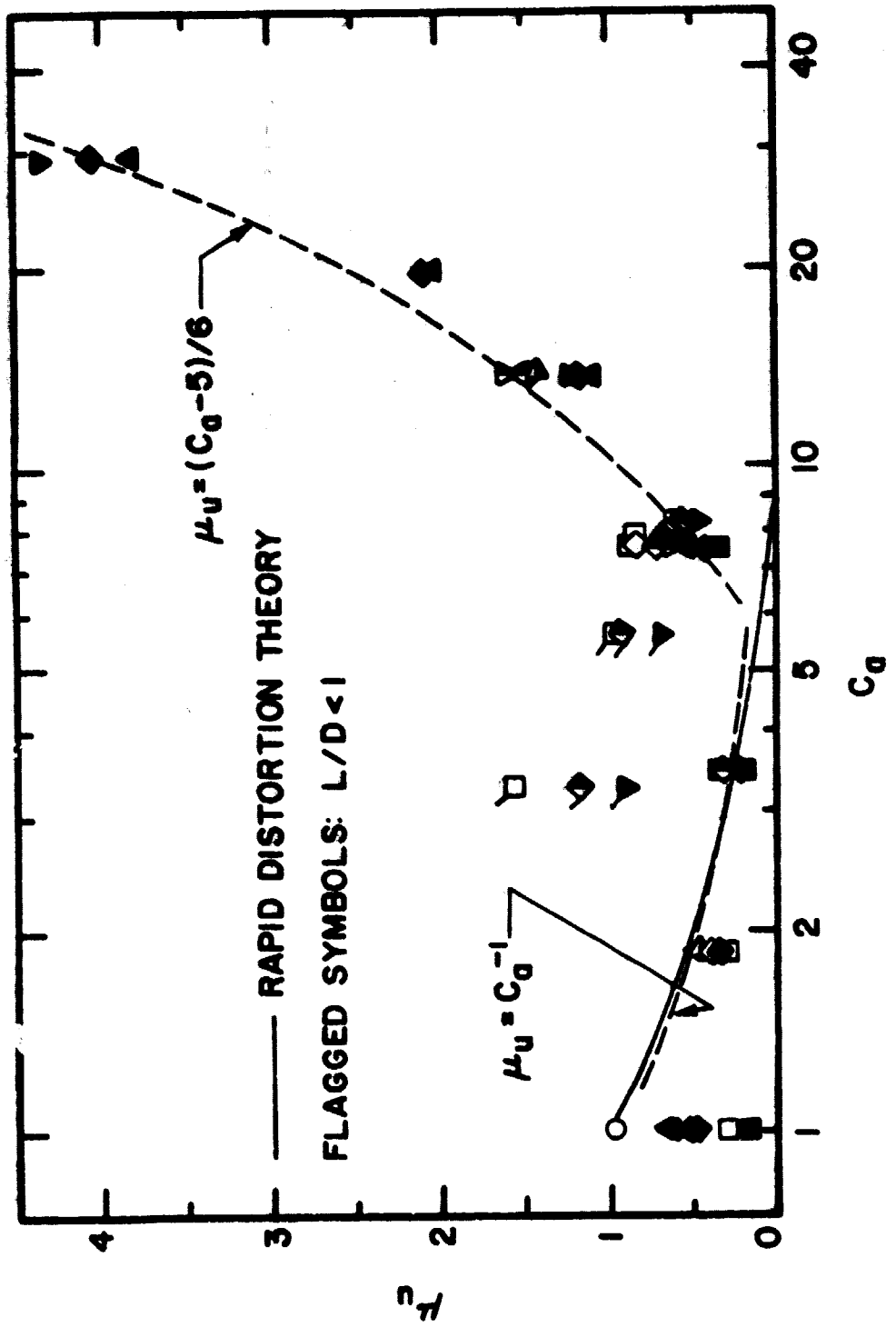

Figure 170. Streamwise Turbulence Energy Ratios for Different Contractions

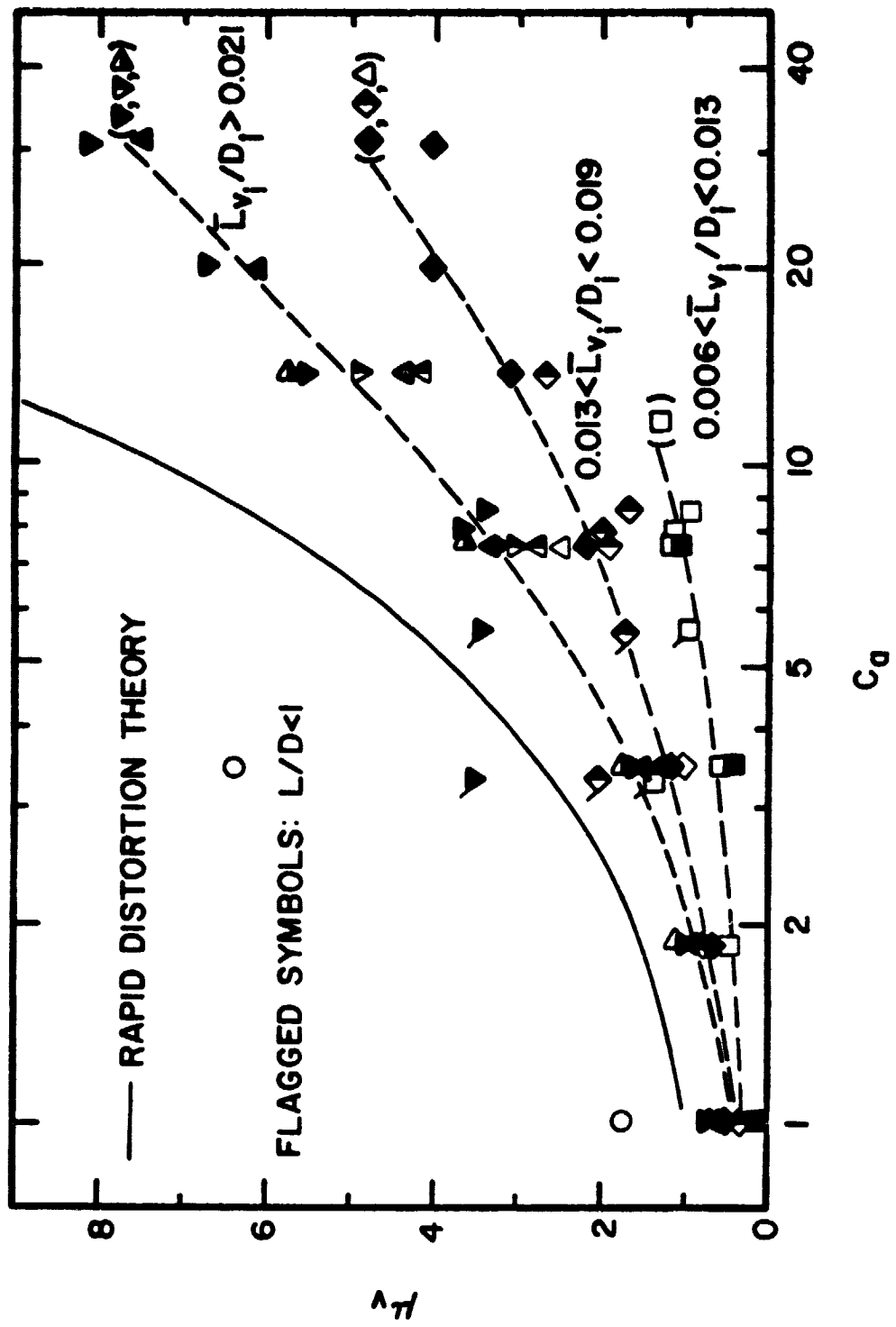

Figure 171. Radial Turbulence Energy Ratios for Different Contractions

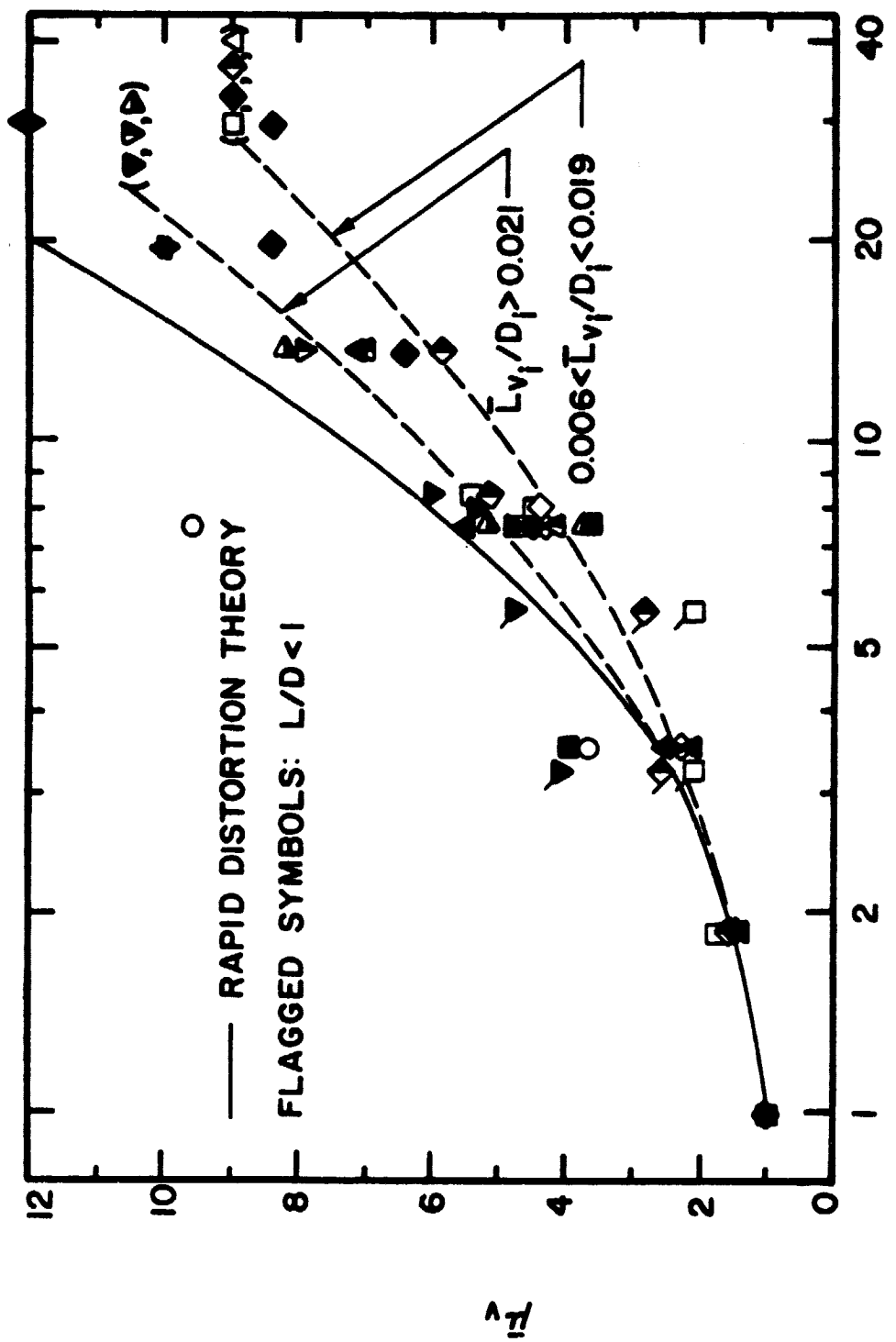

Figure 172. Corrected Radial Turbulence Energy Ratios for Different Contractions

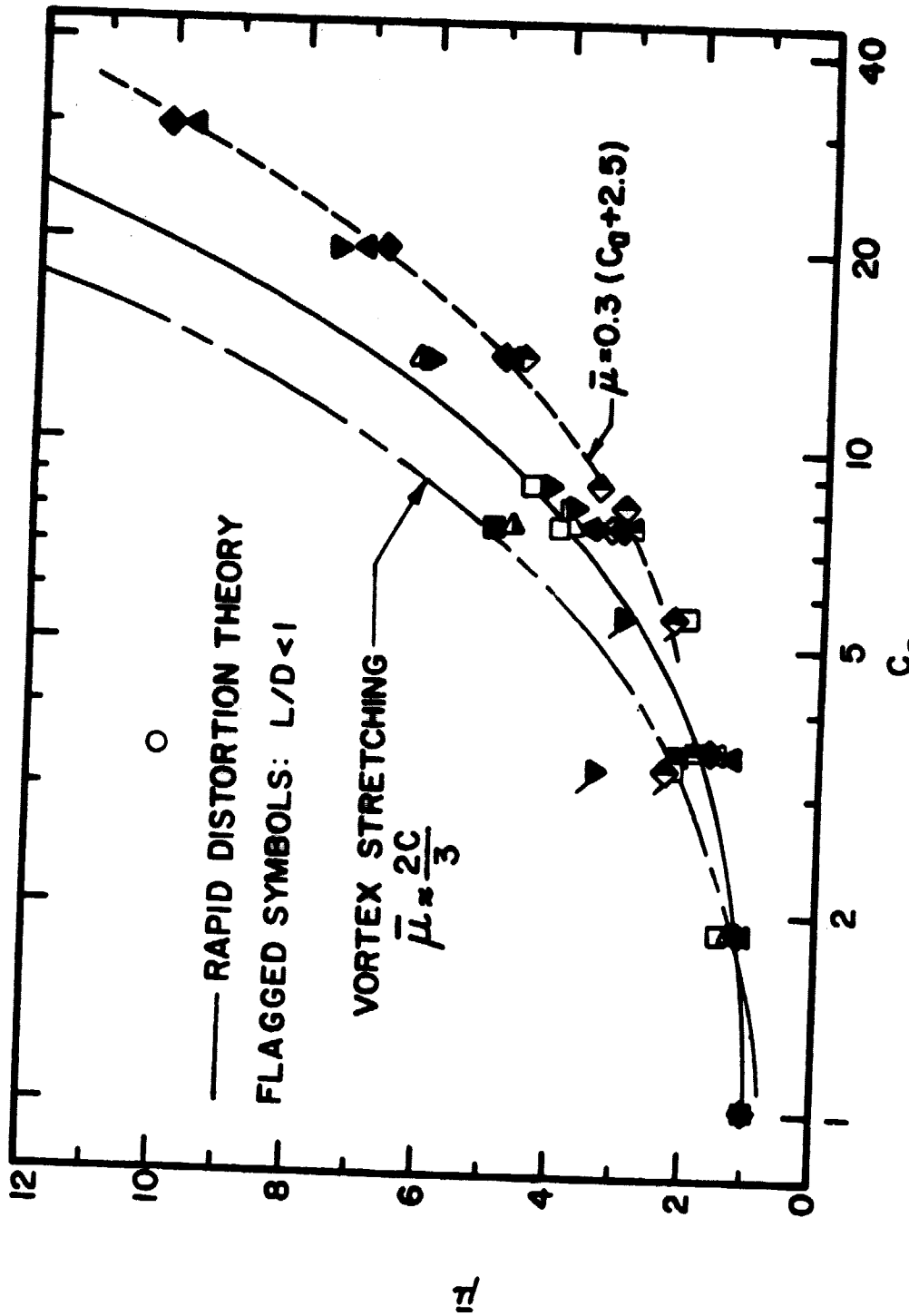

Figure 173. Corrected Total Turbulence Energy Ratios for Different Contractions

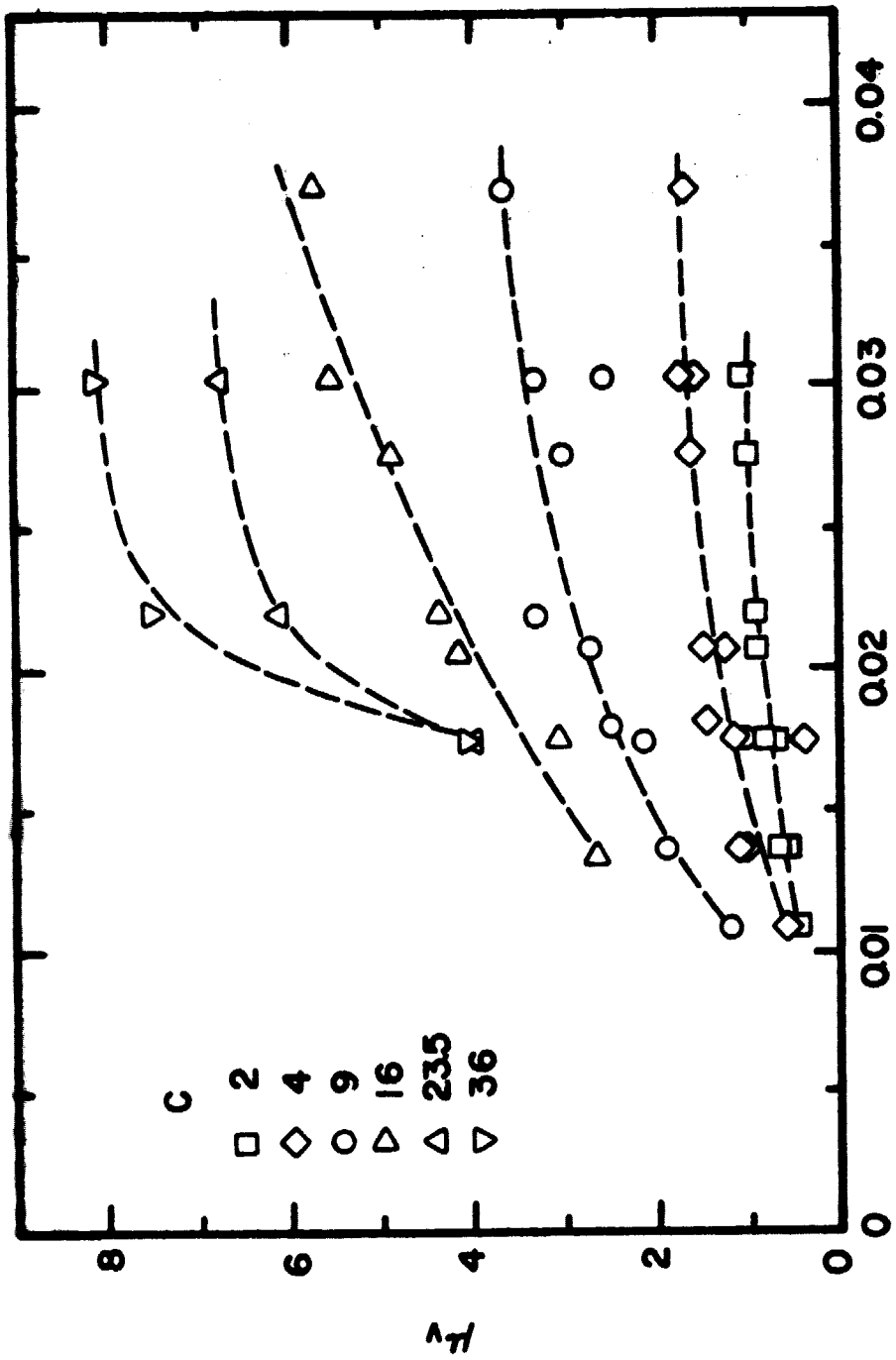

Figure 174. Radial Turbulence Energy Ratios versus Initial Turbulence Length Scales for Various Contractions

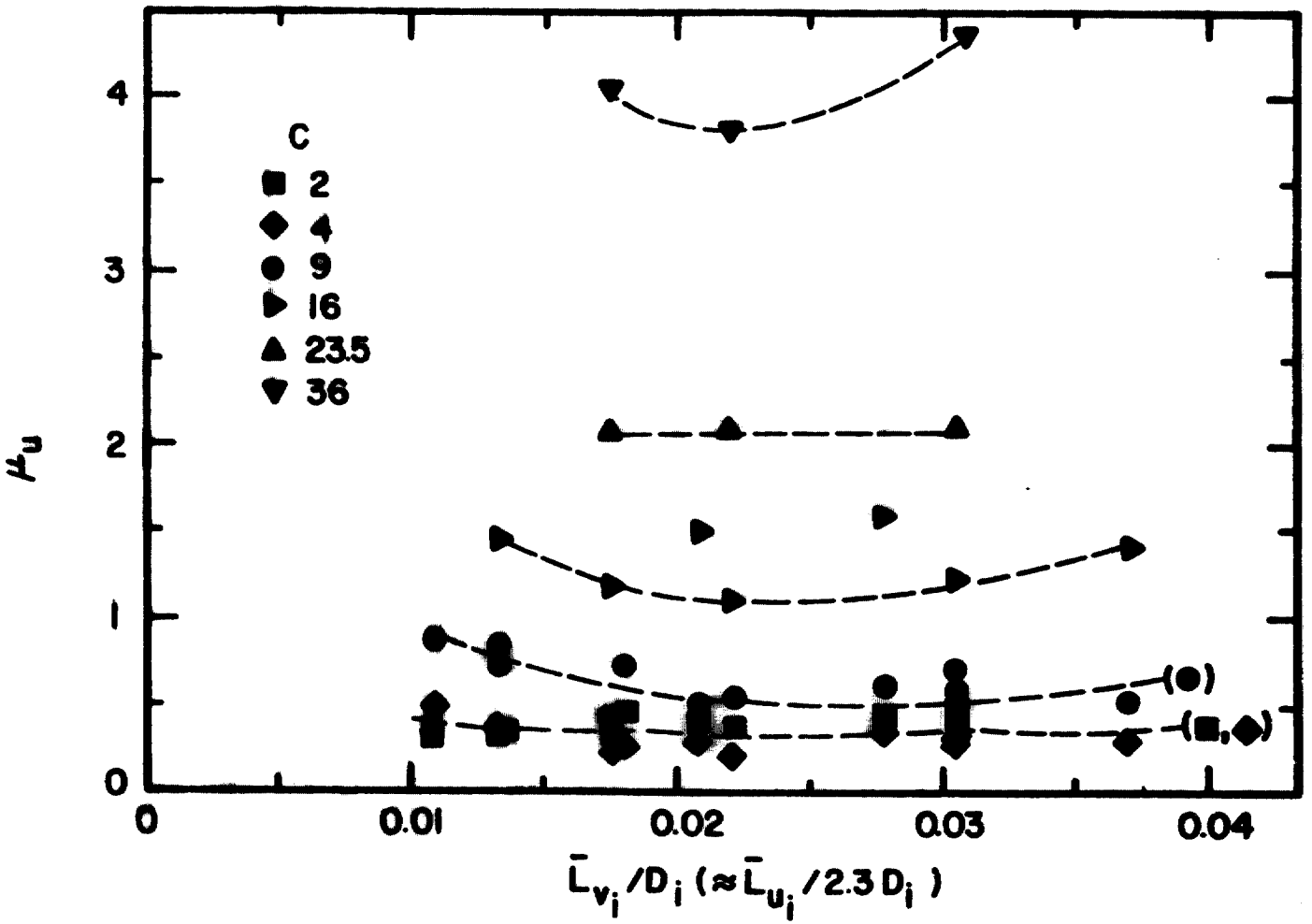

Figure 175. Streamwise Turbulence Energy Ratios versus Different Initial Turbulence Length Scales for Various Contractions

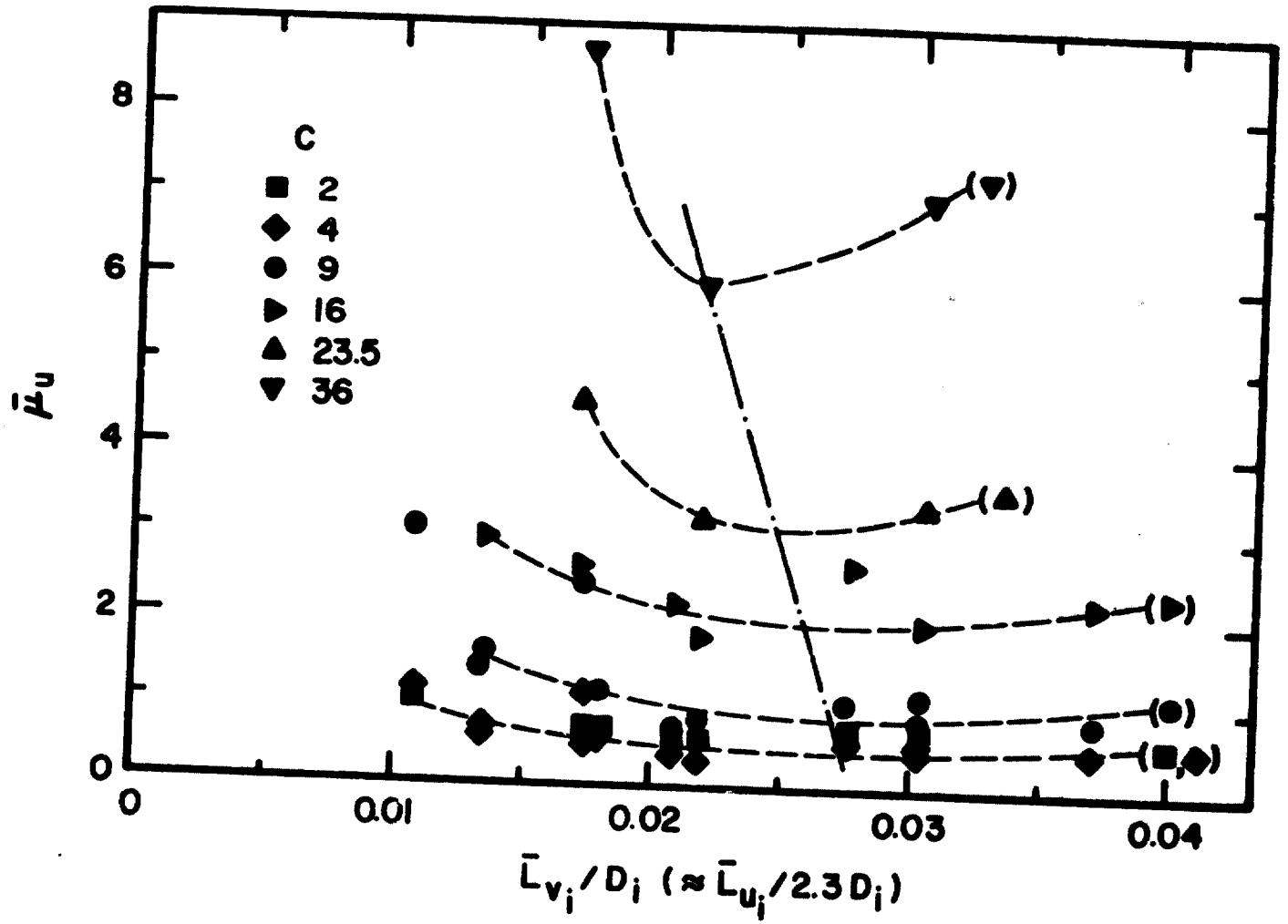

Figure 176. Corrected Streamwise Turbulence Energy Ratios versus Different Initial Turbulence Length Scales for Various Contractions

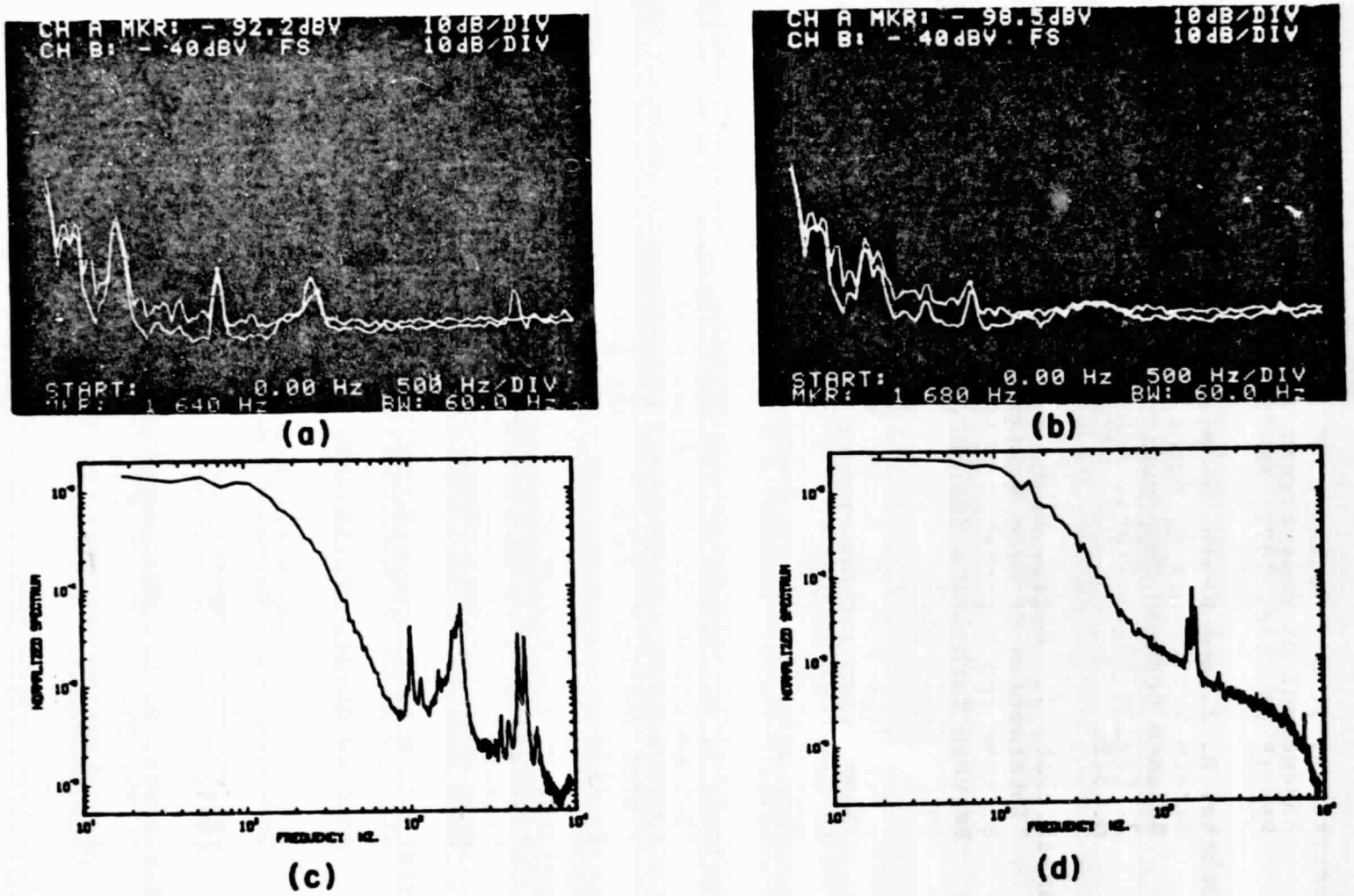

Figure 177. Spectra of X-Probe Signals Before (a,c) and After (b,d) Optimizating Probe-Vibration Damping

BIBLIOGRAPHY

[1] Loehrke, R. I. and Nagib, H. M., "Experiments on Management of Free Stream Turbulence", AGARD Report No. 598, 1972, AD-749-891.

[2] Loehrke, R. I. and Nagib, H. M., "Control of Free Stream Turbulence by Means of Honeycombs: A Balance Between Suppression and Generation", J. Fluids Eng., Trans. ASME, 98, 3, 1976, p. 342.

[3] Tan-atichat, J., Nagib, H. M. and Loehrke, R. I., "Interaction of Free Stream Turbulence with Screens and Perforated Plates: A Balance Between Turbulence Scales", Submitted to J. Fluid Mech.

[4] Ahmed, M., Wigeland, R. A. and Nagib, H. M., "Generation and Management of Swirling Flows in Confined Streams", I.I.T. Fluids and Heat Transfer Report R76-2, ARO-ITR-76-1, 1976.

[5] Wigeland, R. A., Ahmed, M. and Nagib, H. M., "Management of Swirling Flows with Application to Wind-Tunnel Design and V/STOL Testing", AIAA J., 16, 11, p. 1125.

[6] Wigeland, R. A., Tan-atichat, J. and Nagib, H. M., "Evaluation of a New Concept for Reducing Free-Stream Turbulence in Wind Tunnels", NASA C.R. No. 3196, 1979.

[7] Feiler, C. E. and Groeneweg, J. F., "Summary of Forward Velocity Effects on Fan Noise", NASA Technical Memorandum, TM 73722, 1977.

[8] Bradshaw, P. and Pankhurst, R., "The Design of Low-Speed Wind Tunnels", Progress in Aeronautical Sciences, 5, Pergamon Press, 1964, p. 1.

[9] Chmielewski, G. E., "Boundary-Layer Considerations in the Design of Aerodynamic Contractions", J. Aircraft, 11, 1974, p. 435.

[10] Gay, B., Spettel, F., Jeandel, D. and Mathieu, J., "On the Design of the Contraction Section for a Wind Tunnel", J. Appl. Mech., Trans. ASME, 40, 1973, p. 309.

[11] Cohen, M. J. and Ritchie, N. J. B., "Low-speed Three-dimensional Contraction Design", J. Roy. Aero. Soc., 66, 1962, p. 231.

[12] Smith, R. H. and Wang, C. T., "Contracting Cones Giving Uniform Throat Speeds", J. Aero. Sci., 11, 1944, p. 356.

[13] Tsien, H. S., "On the Design of the Contraction Cone for a Wind Tunnel", J. Aero. Sci., 10, 1943, p. 68.

[14] Jordinson, R., "Design of Wind Tunnel Contractions", Aircraft Eng., 33, 1961, p. 294.

[15] Morel, T., "Design of Two-Dimensional Wind Tunnel Contractions", J. Fluids Eng., Trans. ASME, 99, 1977, p. 371.

[16] Morel, T., "Comprehensive Design of Axisymmetric Wind Tunnel Contractions", J. Fluids Eng., Trans. ASME, 97, 1975, p. 225.

[17] Uberoi, M. S. and Wallis, S., "Small Axisymmetric Contraction of Grid Turbulence", J. Fluid Mech., 24, 1966, p. 539.

[18] Bennett, J. C. and Corrsin, S., "Small Reynolds Number Nearly Isotropic Turbulence in a Straight Duct and a Contraction", Phys. Fluids, 21, 1978, p. 2129

[19] Comte-Bellot, G. and Corrsin, S., "The Use of a Contraction to Improve the Isotropy of Grid-Generated Turbulence", J. Fluid Mech., 25, 1966, p. 657.

[20] Klein, A. and Ramjee, V., "Effects of Contraction Geometry on Non-Isotropic Free-Stream Turbulence", Aero. Quart., 24, 1973, p. 34.

[21] Hussain, A. K. M. F. and Ramjee, V., "Effects of the Axisymmetric Contraction Shape on Incompressible Turbulent Flow", ASME Paper, Presented at the Fluids Eng. Conf., May 5-7, 1975, Minneapolis, Minn.

[22] Uberoi, M. S., "Effect of Wind-Tunnel Contraction on Free-Stream Turbulence", J. Aero. Sci., 23, 1956, p. 754.

[23] Ramjee, V. and Hussain, A. K. M. F., "Influence of the Axisymmetric Contraction Ratio on Free-Stream Turbulence", J. Fluids Eng., Trans. ASME, 98, 1976, p. 506.

[24] Batchelor, G. and Proudman, I., "The Effect of Rapid Distortion of a Fluid in Turbulent Motion", Quart. J. Mech. and Appl. Math., 7, 1954, p. 83.

[25] Ribner, H. S. and Tucker, M., "Spectrum of Turbulence in a Contracting Stream", NACA Report No. 1113, 1953.

[26] Goldstein, M. E. and Durbin, P., "The Effect of Finite Turbulence Spatial Scale on the Amplification of Turbulence by a Contracting Stream", Submitted to J. Fluid Mech.

[27] Sreenivasan, K. R. and Narasimha, R., "Rapid Distortion of Axisymmetric Turbulence", J. Fluid Mech., 84, 1978, p. 497.

[28] Stratford, B. S., "The Prediction of Separation of the Turbulent Boundary Layer", J. Fluid Mech., 5, 1959, p. 1

[29] Wigeland, R. A., Grid Generated Turbulence With and Without Rotation About the Streamwise Direction, Ph.D. Thesis, Illinois Institute of Technology, 1978.

[30] Drubka, R. E. and Wlezien, R. W., "Efficient Velocity Calibration and Yaw-Relation Truncation Errors in Hot-Wire Measurements of Turbulence", Abstract published in the Bulletin of the American Physical Society, Fluid Dynamics Division, 24, 1979, p. 1142.

[31] Drubka, R. E., Nagib, H. M. and Tan-atichat, J., "On Temperature and Yaw Dependence of Hot-Wires", I.I.T. Fluids and Heat Transfer Report R77-1, 1977.

[32] Way, J. L., "Applications in Fluid Mechanics Research of a Portable Data Acquisition and Processing System", Proceedings of 5th Annual ICIASF, Ottawa, Canada, 1975.

[33] Thwaites, B., "On the Design of Contractions for Wind Tunnels", ARC, R & M 2278, 1946.

[34] Batchelor, G. K. and Shaw, F. S., "Consideration of Design of Wind Tunnel Contractions", Australian Council for Aeronautics, Report ACA-4, 1944.

[35] Tucker, H. J. and Ali, S. F., "Decay of Anisotropic Turbulence", Tech. Note, AIAA J., 11, No. 4, 1973, p. 546.

[36] von Kármán, T. and Howarth, L., "On the Statistical Theory of Isotropic Turbulence", Proc. Roy. Soc. A, 164, 1938, p. 192.

[37] Prandtl, L., Handbuch der Experimentalphysik, 4, Part 2, 1932, p. 73.